To the Graduate Council

I am submitting herewith a thesis written by Margaret Denise Duncan entitled "Investigation of Gas Porosity in Laser Melted Gray Iron." I have examined the final copy of this thesis for form and content and recommend that it be accepted in partial fulfillment of the requirements of the degree of Master of Science, with a major in Mechanical Engineering.

John A. Hopkins, Major Professor

We have read this thesis and recommend its acceptance:

Accepted for the Council:

Associate Vice Chancellor and
Dean of the Graduate School

INVESTIGATION OF GAS POROSITY IN LASER MELTED GRAY IRON

A Thesis
Presented for the
Master of Science
Degree
The University of Tennessee, Knoxville

Margaret Denise Duncan
May, 2000

Copyright © Margaret Denise Duncan, 2000
All rights reserved

Dedication

I would like to dedicate this thesis to my Lord and Savior, Jesus Christ, in whom I have placed my faith and trust and to whom I have pledged to follow as a disciple May His light always shine through me, and may He continually work on me and with me to be a vessel for His will

I would like to dedicate this thesis to my father, Jerry Duncan, who has taught me the most about patience, suffering, self-sacrifice and endurance I hope I have, and always will, make you proud Thanks, Dad I love you

I would like to dedicate this thesis to the memory of my mother, Sandy Duncan, who has finally found happiness, love, joy and peace in heaven I love you, Mom

I would like to dedicate this thesis to the memory of my dear friend, Pat Milam, who entered into heaven after a long battle with cancer In the brief time that I knew her, she valued me enough to recognize that it was important for me to finish. Thank you for teaching me about faith, Pat I miss you.

Acknowledgements

I would like to thank God for His wisdom, guidance and direction to bring me here, through the power of His Holy Spirit, to give me back an education which I had given to Him.

I would also like to thank the members of my thesis committee, namely Dr. Mary Helen McCay, Dr Firouz Shahrokhi, and my major professor, Dr. John A. Hopkins, the most longsuffering advisor and person I have ever met. Thanks, Dr. J, for being patient, understanding and encouraging, and for never allowing me to quit.

I would also like to thank all those individuals who provided technical help, either with the experiment or with the thesis, namely Arvind Agarwald, Kate Lansford, Marvis White, Scott Scarborough, Mike Sharp, Terri Tramel, Anuradha Godavarty, Anthony Turner, Leo Benetti-Longhini, Dan Thomas, Ivan Dors, Andrea Ciasullo, Pavlina Jeleva.

I would also like to thank my family, Jerry Duncan, Sandy Duncan, Patrick and Samantha Duncan, and my 'other' family, Stephen and Melody Smith, Shaun, Meleah, and Micayla, for their love, encouragement and support throughout these few years.

I would also like to thank my friends, especially Pavlina Jeleva, Holley Britton and Dennis Bunfield, Sherri and Scotty Smith, Anu Godavarty, Agatha Kotsonis, Beth Webster, Nadine Lashier, Judy Rudder, Dan and Jessica Thomas, Marcus and Judy March, Bill Weidner, Corey Hauer, Leo Benetti-Longhini, Arvind Agarwald, Sekhar Radhakrishnan, Mahesh Gopalan, and the members of Tuesday night's bible study group, for encouragement, affirmation, and friendship.

I would also like to thank King's Cross Church, especially David and Jana Benjamin, John and Faye Hartin, Charlie and Carolyn Neel, Rick and Jan Moore, Jim and Virginia Brown, Bob and Carol Donalson, Bob and Cyndi Hampton, John and Irma Troxler, Reggie and Annette Riddle, Norma Taylor, the Milam family and the Helms family for strength in Christ, prayers, discipleship and ministering to me when I was in need.

I would also like to thank the youth and volunteers at the Dossett Chapel Youth Program, especially Charles and Juanita Bair, and Jennifer and Scott Smith, for providing me with an opportunity to serve others and for ministering to me as well.

I would also like to thank the members of the UTSI Soaring Club, especially Dr. Peter Solies and Leo Benetti-Longhini for teaching me to fly gliders.

Abstract

Gray iron is one of the most common, versatile materials used today in the manufacturing world because it is inexpensive, yet strong and durable. If certain deficiencies in iron, specifically corrosion and wear in some applications, could be cost-effectively eliminated, then expensive alloys or composite materials would not be needed for some applications. Existing technology to improve the hardness and wear performance of iron has shown mixed results. A new technology, laser processing, is currently under development and shows great promise. Porosity is an identifiable problem when laser processing iron. Porosity, in general, can be traced to several sources. Some of the possibilities are shrinkage, trapped gases, material evaporation, and chemical reactions producing gases. In the case of laser melted iron, one reaction in particular is of interest. The oxidation of carbon in air is theorized to be a primary contributor to the porosity. Therefore this study investigates this hypothesis in order to verify the effect of oxygen on laser processed iron. For a specific set of processing conditions, inert shielding gases (nitrogen and argon) are compared with air to investigate the environmental effects, in particular the presence of oxygen, on the porosity. In addition, if oxygen is a problem, the possibility of using a deoxidizer to reduce porosity is considered. Titanium is chosen to be coated onto the gray iron to investigate this hypothesis. The current study investigates surface re-melting and alloying with titanium on gray iron. The results are presented quantitatively and qualitatively through metallurgical evaluation, gas chromatography, x-ray diffraction, SEM analysis, and microprobe analysis.

Table of Contents

Chapter	Page
I. Introduction	
A. Statement of problem	1
B. Gray Iron	1
B.1 Uses and Applications	1
B.2 General Characteristics of Gray Iron	2
B.2.1 Graphite Composition	2
B.2.2 Material Properties	3
B 3. Surface Hardening Techniques	3
B.3.1. Carburizing	6
B.3.2. Nitriding	7
B.3.3. Flame and Induction Processes	7
B.3.4. Electron Beam Hardening	8
C. Laser Processing Techniques	8
C.1 Surface Transformation Hardening	10
C.2 Laser Surface Melting	10
C.3 Laser Cladding	11
C.4 Laser Surface Alloying	11
D. Previous Research	11
D.1 Possible Sources of Porosity	11
D.1.1 Graphite Nodules – including Graphitization	12
D.1 2 Shrinkage	13
D.1.3. Material Evaporation	13
D 1.4. Trapped Gases / Solubility	15
D.1.4.1. Nitrogen	18
D.1.4.2. Oxygen	20
D.1.5. Carbon-Oxygen Reaction	21
D.2. Preliminary Work at UTSI	24
E. Thermochemical Reactivity	26
E.1. Thermochemistry	26
E 2. Derivation of Gibbs Free Energy of Formation	31
E.3. Chemical Equilibrium	32
E.4. Titanium as a Deoxidizer	36
II. Experimental Methods	37
A. Prior Research Conditions	38
B. Apparatus Set-up	39
B.1. Equipment	39
B.2. Shield Gas Flow Rate	43
C. Iron Sample Preparation	44
D. Laser Processing Conditions	45
E. Cross-sectional Sample Preparation	46
F. Image Analysis	47

F.1. Procedure 47
F.2. Scaling 48
III. Results and Discussion 49
A. Quantitative Analysis Results 49
B. Qualitative Description of Porosity 53
C. Histogram Porosity Comparison 62
D. Results – Width / Depth Ratios 70
E Gas Chromatograph Results 74
F. X- ray Diffraction Results 77
G. SEM Analysis 79
H. Microprobe Analysis 87
I. Results – Summary of Observations 96
IV. Conclusions 97
A. Primary Conclusions - Oxygen Effects 97
B. Secondary Conclusions - Titanium Effects 98
C. Other Conclusions 99
V. Recommendations 101
A Modify the Processing Conditions 101
B. Further Sample Testing and Analysis 101
C. Numerical Modeling 102
References 103
Appendices 108
A. Cross-sectional Photos of Gray Iron (GI) Samples 109
B. Cross-sectional Photos of Titanium on Iron (TI) Samples 122
C. Cross-sectional Photos of Binder on Iron (BI) Samples 135
D. X-ray Diffraction Analysis Report 145
E. SEM Analyses 161
F. Table of Past Experiments 188
Vita 192

List of Tables

Table	Page
Table 1: Graphite Form Classifications	3
Table 2: Forms of Flake Graphite	4
Table 3: Typical Mechanical Properties of Standard Gray Iron Test Bars	4
Table 4: Gibbs Free Energy for Possible Reactions	28-29
Table 5: Possible Chemical Reactions Based on Free Energy Change	33
Table 6: Chemical Reactions of Primary Interest	35
Table 7: Comparison Among UTSI Preliminary Laser Processing Conditions and Other Research Studies	40
Table 8: Total Porosity Data for Gray Iron	50
Table 9: Total Porosity Data for Titanium Coated Iron	50
Table 10: Total Porosity Data for Binder Coated Iron	50
Table 11: Percent Porosity in Melt Zone of Gray Iron	51
Table 12: Percent Porosity in Melt Zone of Titanium Coated Iron	51
Table 13: Percent Porosity in Melt Zone of Binder Coated Iron	51
Table 14: Width and Depth of Gray Iron Cross-sections	71
Table 15: Width / Depth Ratios of Gray Iron Cross-sections	71
Table 16: Width and Depth of Titanium Coated Iron Cross-sections	72
Table 17: Width / Depth Ratios of Titanium Coated Iron Cross-sections	72
Table 18: Width and Depth of Binder Coated Iron Cross-sections	73
Table 19: Width / Depth Ratios of Binder Coated Iron Cross-sections	73
Table 20: Gas Chromatograph Results	76
Table 21: SEM Results for Titanium Concentration in Air, Nitrogen, and Argon Tracks	85
Table 22: SEM Results for Investigating Titanium in Pores	86
Table 23: Microprobe Results on Sample TI9-1	95

List of Figures

Figure	Page
Figure 1: Carbon-Iron Phase Diagram	5
Figure 2: Laser Alloying in Progress	12
Figure 3: Rofin 020 Nd:YAG Laser	41
Figure 4: Experimental Box Apparatus Set-up	42
Figure 5: Iron Sample Cutting and Labeling	46
Figure 6: Olympus Microscope	47
Figure 7: Plan View of Laser Processed Gray Iron Sample	54
Figure 8: Plan View of Laser Processed Titanium on Gray Iron	54
Figure 9: Typical Cross-section of Laser Melted Gray Iron in Air	55
Figure 10: Typical Cross-section of Laser Melted Gray Iron in Nitrogen	56
Figure 11: Crack across sample Laser Processed in Argon	57
Figure 12: Typical Cross-section of Laser Melted Gray Iron in Argon	57
Figure 13: Plasma Effect in Air Track	59
Figure 14: Plasma Formation	59
Figure 15: Typical Cross-section of Laser Melted Titanium on Iron in Air	61
Figure 16: Typical Cross-section of Laser Melted Titanium on Iron in Nitrogen	61
Figure 17: Typical Cross-section of Laser Melted Titanium on Iron in Argon	62
Figure 18: Porosity Comparison Among Air Processed Samples	64
Figure 19: Porosity Comparison Among Nitrogen Processed Samples	65
Figure 20: Porosity Comparison Among Argon Processed Samples	66
Figure 21: Porosity Comparison for Gray Iron (GI) in Air, Nitrogen and Argon	67
Figure 22: Porosity Comparison for Titanium on Iron (TI) in Air, Nitrogen and Argon	68
Figure 23: Porosity Comparison for Binder Coated Iron (BI) in Air, Nitrogen and Argon	69
Figure 24: X-ray Diffractometer	78
Figure 25: X-ray Trace of Titanium Alloyed Iron	80
Figure 26: X-ray Trace of Gray Iron, Detecting Fe_5C_2 Phase	81
Figure 27: X-ray Trace of Gray Iron, Detecting FeC Phase	82
Figure 28: X-ray Trace of Titanium Powder	83

Figure 29: Scanning Electron Microscope 84
Figure 30: SEM Map for Sample Ti4-1 88
Figure 31: SEM Map for Sample Ti4-2 89
Figure 32: SEM Map for Sample Ti4-3 90
Figure 33: SEM Map for Sample Ti7 in Air 91
Figure 34: SEM Map for Sample Ti10 in Air 92
Figure 35: Cameca Camebax 286 Microprobe 93
Figure 36: Map of Data Points for Microprobe Analysis of TI9-1 94

Nomenclature

A	Chemical Substance
a	Stoichiometric Coefficient
B	Chemical Substance
b	Stoichiometric Coefficient
C	Chemical Substance
c	Stoichiometric Coefficient
D	Chemical Substance
d	Stoichiometric Coefficient
$d\varepsilon$	Differential Change in Extent of Reaction
dg	Differential Change in Gibb's Function
dG	Differential Change in Gibb's Function
dn	Differential Change in Number of Moles
dP	Differential Change in Pressure
dq	Differential Change in Heat
ds	Differential Change in Entropy
dT	Differential Change in Temperature
du	Differential Change in Internal Energy
dv	Differential Change in Specific Volume
dw	Differential Change in Work
ΔG	Gibbs Free Energy Change
ΔG_f	Gibbs Free Energy of Formation Change
$\Delta G_r°$	Reference state change in Gibbs Free Energy of Reaction
ΔH	Enthalpy Change
g	Gibb's function (unit mass basis)
g°	Reference State (25°C, 1 atm) gibbs function
h	Enthalpy
HAZ	Heat Affected Zone
K	Equilibrium Constant
μ	Chemical Potential
N	Number of moles of a substance
n	Number of moles of a substance
P	Pressure
p	Pressure
P_I	Partial Pressure of Substance I
PMZ	Partially Melted Zone
Q	Volumetric Flow Rate (ml/min)
ρ	Density

R	Universal Gas Constant
r	Radius of a bubble
σ	Surface Tension
S	Entropy
s	Entropy
SEM	Scanning Electron Microscope
T	Temperature
u	Internal Energy
V	Volume
v	Specific Volume
X_I	Mole Fraction of Substance I

I. Introduction

A. Statement of the Problem

Gray iron is a very common and versatile material used for automotive applications, such as engine blocks and crankshafts, as well as a variety of other industrial and machine parts. It is a very strong, durable and inexpensive material. However, iron has several detrimental properties such as poor wear performance and low fracture toughness, and a tendency to corrode. These properties can be enhanced by using a laser to modify the surface through re-melting and alloying. A significant problem with laser melting of iron is porosity, which can cause an irregular surface and serve as a source for stress risers. Determining the cause(s) of porosity and eliminating it from the laser melted iron will greatly improve the technique and make the process feasible for more applications. This paper focuses on the role of atmospheric oxygen in the production of gas porosity in laser melted iron.

B. Gray iron

B.1. Uses and applications

Gray iron is commonly used for automotive applications and machine and industrial parts in other industries. Some typical automotive parts made from gray iron include, but are not limited to, cylinder blocks, liners, and heads; clutch parts; brake parts; flywheels; transmission cases; gear boxes; pistons, camshafts, and tappets. The Society of Automotive Engineers (SAE) has designated automotive gray irons as J431. There are several grades within this category depending on the composition, and mechanical properties. American Society for Testing and Materials (ASTM) has several specifications for gray iron, depending on their use. These include A48 for test bars,

A159 for automotive, A126 for valves, flanges, and pipe fittings, A74 for soil pipe and fittings, A377 for pressure pipe, A278 for pressure containing parts at high temperatures, and A319 for non-pressure containing parts at high temperatures.

B.2. General Characteristics of Gray Iron

Cast iron is essentially an alloy of iron, carbon and silicon. Whereas carbon contents < 2% are considered steels or steel alloys, cast iron contains 2 to 4% carbon. The silicon content ranges from 1 to 3 %. For gray iron, the carbon content is hypereutectic, which means that there is more carbon in the mixture than can be dissolved into a solid solution. Therefore, the carbon precipitates out as graphite flakes. Graphite in iron can take one of seven forms, as described by ASTM A247. Flake graphite is further subdivided into five types by the same ASTM standard.

B.2.1 Graphite Composition

Basically, the seven types of graphite range from spheroidal (or nodular) graphite, type I, to flake graphite, type VII, with the types in between being some intermediate form. The ASM Metals Handbook describes these forms in Table 1. For type VII, flake graphite, ASTM categorizes the flakes by flake distribution and orientation. The ASM Handbook describes this in the Table 2.

The type of graphite is important because it has an effect on the properties of the iron. Graphite is a form of carbon that is soft and slippery and acts as a natural lubricant for the iron. This characteristic is one of the main advantages of iron. Graphite nodules make the iron more ductile, which is why this type of iron is called ductile iron. Graphite spheroids contribute to greater strength.

B.2.2 Material Properties

The mechanical properties of typical grades of gray iron are shown in Table 3, which is taken from the ASM Metals Handbook.

Also, a Fe-C phase diagram is included in Figure 1. The diagram shows the weight percent carbon, the eutectic point, and the temperature range over which the iron transition from a solid to a liquid. It is reprinted from the ASM Handbook, Volume 3 Alloy Phase Diagrams

B.3. Surface Hardening Techniques

Although iron is a reasonably hard metal, it is often desirable to increase the hardness to improve the wear resistance. Then, parts that come into contact with each other will be able to last longer. Parts such as gear teeth, camshaft lobes, tappets, pistons, rings and cylinder bores are all good candidates for hardening.

Ferrous metals, namely iron and steels, undergo a hardening process called martensitic transformation. In this process the temperature of the ferrite phase of the iron is raised to a critical temperature where a phase change from (δ) ferrite to (γ) austenite occurs. The critical temperature is called the austenization temperature and occurs around 1550°C. If the ferrous metal is subsequently cooled very rapidly, the austenite

Table 1 Graphite Form Classifications

ASTM Type	Description
I	Nodular (Spheroidal) Graphite
II	Nodular (Spheroidal) Graphite, imperfectly formed
III	Aggregate, or Temper Carbon
IV	Quasi – flake Graphite
V	Crab - Form Graphite
VI	Irregular or "Open" Type Nodules
VII	Flake Graphite

Table 2 Forms of Flake Graphite

Flake Type	Description
A	Uniform Distribution, Random Orientation
B	Rosette Grouping, Random Orientation
C	Superimposed Flake Size, Random Orientation
D	Interdendritic Segregation, Random Orientation
E	Interdendritic Segregation, Preferred Orientation

Table 3 Typical Mechanical Properties of Standard Gray Iron Test Bars

ASTM Class	Tensile Strength MPa	Torsional Shear Strength MPa	Compressive Strength MPa	Reversed Bending Fatigue Limit MPa	Transverse Load on Test Bar B kg	Hardness HB
20	152	179	572	69	839	156
25	179	220	669	79	987	174
30	214	276	752	97	1145	210
35	252	334	855	110	1293	212
40	293	393	965	128	1440	235
50	362	503	1130	148	1638	262
60	431	610	1293	169	1678	302

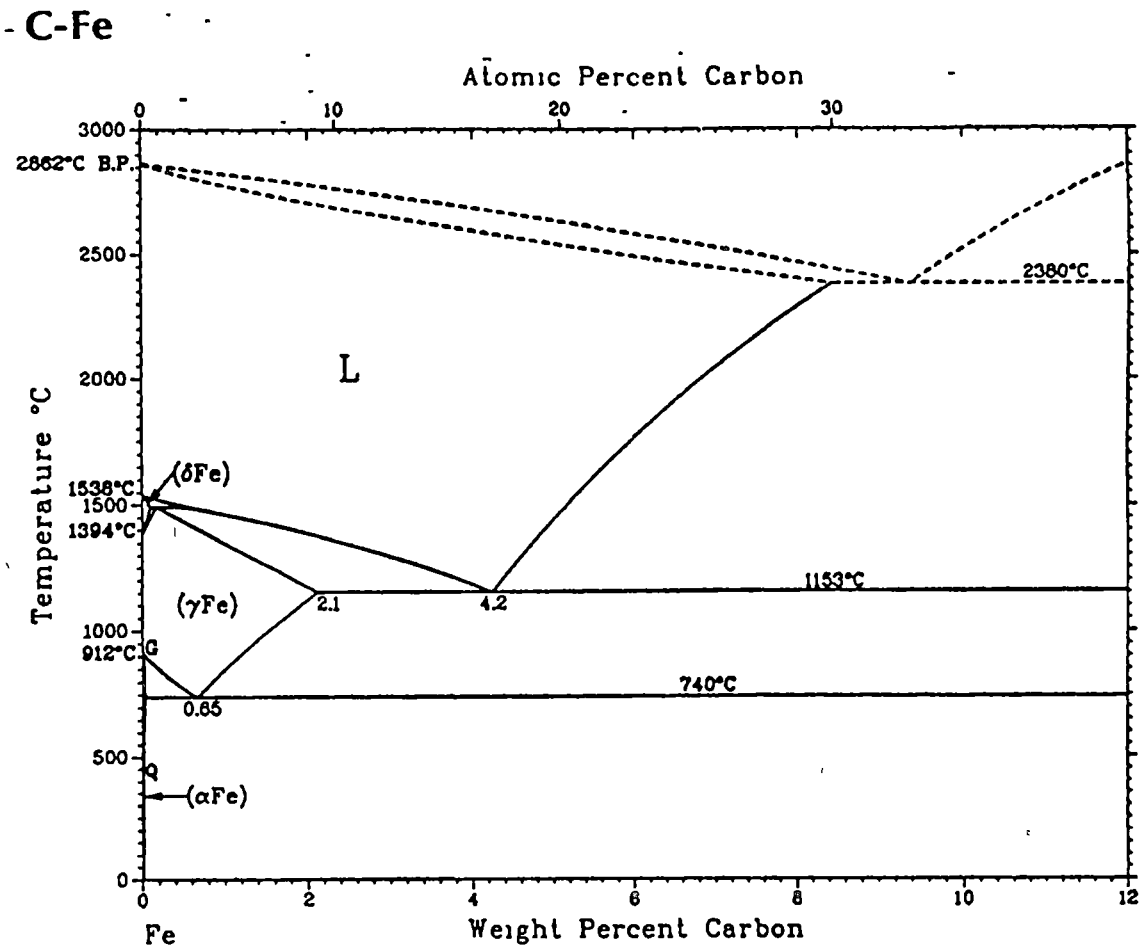


Figure 1. Carbon – Iron Phase Diagram

(fcc) back to ferrite (bcc) transformation results in a (bct) form called martensite. Martensite is a very hard and brittle metastable phase of iron. This is the primary type of process used to harden iron.

There are several industrial processes currently used in industry today that harden the surface of a part to a certain depth, while leaving the inside relatively soft. Frequently, these methods are used on low-carbon, low alloy steels, but high alloy steels and nonferrous metals can be surface hardened as well. The basic idea is that an agent is used to permeate the surface whose presence will cause a hardening effect on the metal as its concentration increases. Some of the most common methods of achieving this are carburizing, nitriding, flame and induction hardening, electron beam hardening and laser surface hardening. There are many others as well as combinations of the ones just mentioned, such as carbonitriding, which will not be discussed here.

B.3.1. Carburizing

Carburizing is a diffusion based hardening method by which a ferrous metal is heated above its austenization temperature (1550 °C) so that a carbon source is allowed to seep into the metal from the surface. The process is time and temperature dependent. Usually the temperature is increased to approximately 1700 - 2000 °C. The time required for sufficient hardening is on the order of hours (up to a day is typical, but it can take as long as three days). It depends on the degree and depth of hardening desired. The diffusion depth is proportional to the square root of time multiplied by a diffusion constant. The carbon can be introduced in the form of a solid such as packed charcoal, a gas such as carbon monoxide or a hydrocarbon gas, or a liquid such as a salt bath. The hardening is actually achieved when the carbon enriched part is quenched and a

martensitic transformation takes place. The case depths achieved can be up to 1.5 mm, and hardness values of 50-65 HRC can be achieved (ASM Handbook, vol. 4, p. 260).

B.3.2 Nitriding

Another diffusion case hardening process for alloy steels, stainless steels and cast irons is nitriding. In this process, nitrogen or a nitrogen compound is exposed to the metal at approximately 500°C. The most common form of nitrogen used for nitriding is ammonia gas. The nitrogen dissolves into solid solution with the ferrite phase of the iron. According to the ASM Handbook, the solid solubility of nitrogen in ferrite is 6% (ASM Handbook, vol. 4, p 261). The nitrogen can also form nitrides with the iron or with alloying elements such as aluminum, chromium, molybdenum and titanium. The advantage of this process is that the lower temperature (500°C) does not require any secondary heat treatment and distortions are minimized. Nitrided parts are case hardened to a depth up to 0.75 mm and hardened to a depth of 50-70 HRC (ASM Handbook, vol. 4, p. 260).

B.3.3 Flame and Induction Processes

Besides diffusion of an element or compound into the metal matrix, a simple heat and quench treatment can be used to harden the surface of steels. In the flame hardening process, a ferrous metal is heated beyond the austenization temperature (1550 °C) with a blowtorch, typically oxyacetylene, and then quenched with water. This causes a martensitic transformation to take place in the steel, which makes it much harder. In induction hardening, an electrical current is used to generate heat through an inductor coil instead of a torch. The parts are still quenched with water. The depth of hardening is related to the frequency of the alternating current used to generate the magnetic field.

Lower frequencies lead to deeper case depths. In both processes, the hardening is achieved selectively on a specific area of a part; whereas other processes harden the entire surface of the part.

B.3.4 Electron Beam Hardening

Another type of selective surface heat treatment process is electron beam hardening. For this process, an electron gun shoots electrons at a very high velocity through a focusing element (which concentrates the beam and accelerates the electrons) and onto the part to be hardened. The accelerated electrons have enough energy to transfer heat to the part. The temperature of ferrous alloys can be raised into the austenization range so that a martensitic transformation can take place. As the beam passes, the part is self-quenched in the ambient environment. A water or oil quench is not necessary as long as there is a sufficient amount of material to dissipate the heat through the part. Because of the localized heat input and self-quenching ability of electron beam hardening, distortions are minimized. Typical case depths are up to 1.5 mm, and hardness is up to 800 - 1000 HV to a reasonable depth (ASM Handbook, vol. 4, p. 304).

C. Laser Processing Techniques

Another selective surface hardening technique is laser surface heat treatment, which can take a variety of forms. The acronym LASER stands for Light Amplification by the Stimulated Emission of Radiation. Lasers have been in use for a number of years, with the first reported observation of a laser effect in 1960 [Duley, Laser Welding, 1999]. Throughout the 1960s, a number of different types of lasers were invented, each employing a different lasing medium. In order for a laser to 'lase', a material that has the

property of excitation must be used. Excitation is defined as 'the process of raising a species from a lower energy level to a higher one.' [Hecht, The Laser Guidebook, p.26] This occurs when energy is input by one of several ways. The excited molecules will then release that energy in the form of light emitted by photons when the excited molecules return to a stable state. This effect can be initiated by an outside energy source, and sustained by the outside source and by photons stimulating the emission of other photons. Mirrors are used to direct the emitted light back into the laser source.

Lasers may be solid-state - that is to say a solid crystalline substance is used as a medium to energize a laser beam. The medium can also be a mixture of gases in the case of a gas laser. Some typical solid-state lasers are ruby, Nd: YAG (Neodium-Yttrium Aluminum Garnet), Nd: Glass, and diodes. Some typical gas lasers are helium-neon, argon and krypton ion, helium-cadmium, CO2, and rare gas halides (excimers). Each of these types of lasers has different individual characteristics, such as a unique wavelength, but there are a few common characteristics of lasers that they all share. These common characteristics of lasers are monochromatic light, coherent emission, and a narrow beam.

Since their invention, lasers have found a number of applications, including material processing such as surface treatment, cutting, drilling, and welding. The actual technique depends largely on the type of laser used and the power settings used. Welding and drilling, for example, require a greater energy density because they involve both melting and vaporization. Some of these techniques are used to improve the surface properties of metals. Laser surface processing is a collective term encompassing numerous methods which includes hardening, melting (glazing), cladding, and alloying. This paper discusses these specific examples of laser material processing in greater detail.

The wear performance of the cast iron can be improved by using high powered lasers which transform the surface by techniques such as surface cladding, surface alloying, and surface transformation hardening. While each process differs procedurally, the net result is a change in the material properties at the surface.

C.1. Surface Transformation Hardening

Surface transformation hardening is basically a martempering process that uses a laser to heat the surface of ferrous metals to the austenization temperature so that the microstructure can turn into martensite upon rapid cooling. This is a solid-state transformation. The martensitic transformation is the primary process by which steels and iron are hardened. A typical beam intensity of ~10^4 W/cm^2 is required to heat treat (Duley, Laser Processing, 1983) The resulting martensitic microstructure is much harder than the original material. In the case of transformation hardening, the laser beam passes over the material and raises the temperature of a small area enough to cause a solid state phase transformation in the material.

C.2. Laser Surface Melting

Surface melting (glazing) is a surface treatment process that uses a laser to melt the surface to a shallow depth and heat the metal to beyond the austenizing temperature into a liquid form. Then the metal cools and rapidly solidifies and a martensitic structure results. For re-melt hardening, the laser beam causes a small area to melt and rapidly solidify. The effect of this re-melting and self-quenching operation is similar to a heat treatment process in that it produces a refined grain structure by "freezing" the material in a metastable state.

C.3. Laser Cladding

Cladding is a type of laser surface treatment that creates a new surface on top of the base metal surface that has different properties and composition than the base metal. A laser is used to melt the precursor elements into a new layer on the surface while leaving the substrate virtually unchanged. A cladded surface is essentially applied onto the base and there is very little if any mixing between the two surfaces. According to MacIntyre, (Dubrujeaud, 1997) laser cladding was first performed industrially in the United Kingdom in 1981 on turbine blades with a Co-based alloy. Also cited in Dubrujeaud (1997), cladding of Ni-Cr-Al-Hf has been researched in the U. S. for corrosion protection of aircraft engines.

C.4. Laser Surface Alloying

In the case of laser surface alloying, the alloying elements are placed on top of the base metal up to a certain depth. The laser beam melts the alloying elements and a portion of the substrate which mix and form a region with new properties near the surface. For surface alloying, an element, or several elements, is added to the metal substrate prior to making the laser passes that melt the powder into the metal to form a new matrix upon re-solidification. In this case, the alloying elements are dispersed into the new layer on the substrate An illustrative example of the technique is shown in Figure 2.

D. Previous Research

D.1. Possible Sources of Porosity

There have been a number of recent studies on laser processing of iron and steel. Most of these focus on the microstructure, hardness, and wear. However, as a

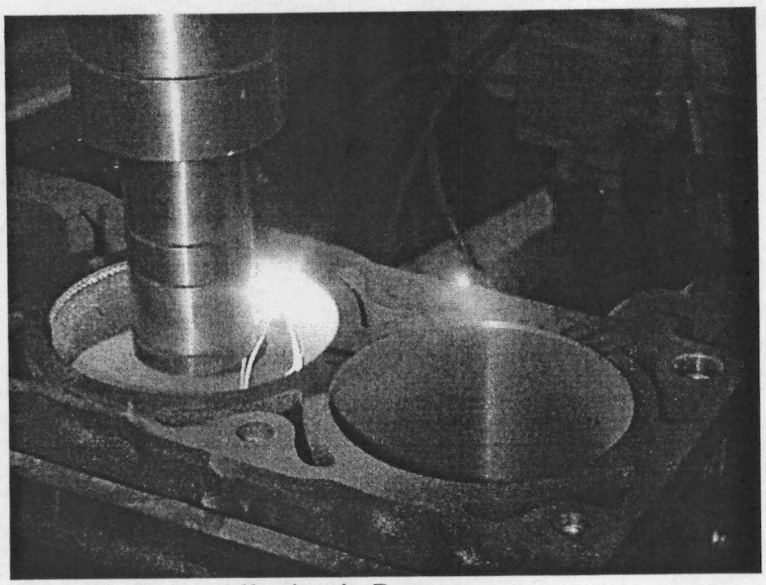


Figure 2: Laser Alloying in Progress

consequence of the remelting, alloying or cladding technique used, some type of porosity is often present. This porosity may be due to a number of sources, depending on the conditions and the material used. Porosity can be caused by shrinkage during solidification (as in castings), material evaporation/vaporization, entrapped gases that dissolve in the liquid and solid metal, and gases generated by a chemical reaction – in particular the carbon-oxygen reaction. Also, there are some things that look like porosity that are not pores at all. They could be graphite spheres, rust spots, or irregularly shaped microstructures that could appear to be porosity under a microscope. Therefore, it is instructive to define porosity, and identify what is and is not a pore. Then, this study can focus on the causes and elimination of gas porosity in iron.

D.1.1. Graphite Nodules - Including 'Graphitization'

In some instances, apparent porosity in the iron might be the result of graphite nodules formed in the melt zone through a process called graphitization. If an iron or steel undergoes this process during a heat cycle, the cementite (Fe_3C) dissolves into

graphite and some phase of iron. Certain conditions promote the process, and the presence of particular inoculants may cause or prevent graphitization. In particular, ferrosilicon has an effect on the size and shape of graphite formation (ASM Handbook, vol. 4, p. 80). Magnesium is also a well-known inoculant. In fact, magnesium combined with cerium is used to make spheroidal graphite iron – also called ductile iron. The graphite collects in spheroids, which may vary in size, interspersed between grains in the microstructure. These 'black dots' under the microscope or in pictorial images may appear to be pores. In fact, if the sample is well polished, the graphite nodules may be rubbed out of the metal and leave a hole behind. It is not known whether there are any sample preparation steps to prevent this, but the use of magnesium, cerium, or silicon as alloying elements is not recommended for laser alloying.

D.1.2. Shrinkage

Whenever a hot liquid metal cools and solidifies, there is a tendency for empty pockets to form where the solidification fronts merge. This occurs because the molten metal begins to freeze solid at the extremes, often before it has a chance to rejoin the other metal. The void space left behind is a shrinkage pore. It is typically oddly shaped and not round due to the nature of formation. Shrinkage pores are more common in castings, but they can also exist in a laser melted metal if the melt zone is large enough and the cooling rate is fast enough.

D.1.3. Material Evaporation

Another possible source of porosity in laser melted materials, as well as laser welded materials, is material evaporation. This can occur when there is enough energy input to vaporize the base metal and/or some of the alloying elements. Some researchers

have observed that for certain combinations of power and velocity, the laser heat input is sufficiently high that material evaporation can occur (Straus et al, 1990). As the material is vaporized, it leaves behind small cavities in the melted zone as well as on the surface where the gasified material escapes. Several studies on various types of iron, steel, and aluminum have observed this phenomenon. Luft et al (1991) noted the formation of cavities attributable to gas bubbles as a result of excessive overheating of the liquid pool in the laser treated iron. A study by Mordike and Bergmann (1986) on laser melted spheroidal graphite cast iron showed that elements in the surface of the castings, which were absorbed from the mold, can evaporate and cause porosity problems. Their study concluded that avoiding porosity required that no significant evaporation of alloying elements occurs. In a separate study by Mordike and Bergmann (1983) on iron-based alloys, the researchers concluded that degassing and pore formation will occur in phosphorous alloys (0.2-1.9 %). Straus et al (1990), when studying laser treated gray cast iron, noted the surface defects and distinct chainlet of small cavities in the re-melted zone which appear to be caused by material evaporation. According to Mordike (1990), if the energy density of the laser is very high the surface will boil and evaporate before the heat has penetrated the surface. A study by Arata and Oda (1984) on laser welded steel suggests that alloying elements such as silicon and manganese are oxidized or evaporated, while other alloy element concentrations remained the same. The laser welds in air had a noticeably lower concentration of silicon and manganese, while the laser welds in argon exhibited only a slight decrease in silicon and manganese compared to the base metal.

Material evaporation has also been observed in nonferrous laser welds. A study by Weckman et al (1997) cited previous work that vaporization of low vapor-pressure constituents such as magnesium in 5xxx series aluminum alloys causes porosity when laser welded. Further, the study noted that aluminum only requires about 6 x 10^6 KJ/kg for vaporization compared to 10 x 10^6 KJ/kg for stainless steel. However, due to the higher absorbtivity and lower thermal conductivity of steel, it will reach the vaporization temperature at a lower power density (Weckman et al, 1997).

D.1.4. Trapped Gases / Solubility

If a shielding gas is used while processing with the laser, it is possible that the gas flow might become mixed in with the melt and trapped in the re-solidified zone. During the process of steelmaking or welding, atmospheric gases are often trapped in the molten metal. These gases are not necessarily generated by a chemical reaction taking place; rather they are the result of gas concentrations which are greater than their solubility limit in the metal. There are a number of research studies, mainly related to welding which describe this type of porosity. A welding study on nickel-copper alloys by Ramirez et al (1994) indicates that 'dissolved gases such as hydrogen, oxygen, and nitrogen are always present, to some extent, in molten metal during welding. The solubility of these gases in the molten pool is generally more than their solubility in the solidified weld metal.' Further, Ramirez adds that the porosity is formed when the amount of dissolved gases exceeds the solubility limit when the metal solidifies. Specifically, porosity formation is a function of the solid and liquid solubilities, S^s and S^l, and the dissolved gas content Co. The gas concentration, Co, may be greater, less than, or in between the limits, S^s and S^l. Also, Ramirez noted that the pore formation is

influenced by the solidification rate (welding speed); faster rates can freeze the pores in the weld metal. Ramirez further stated that since gas solubility is limited, dissolved gases build up at the solidification front and the gas content in the solid increases until it reaches the saturation point. This type of porosity, where spherical pores result from supersaturated gases, is referred to as bulk porosity; whereas interdendritic porosity occurs when gas bubbles are formed or trapped between dendrite arms in the solidification structure.

Ramirez also states that pore formation is a 'nucleation and growth process' which occurs homogeneously or heterogeneously in molten metal supersaturated with gas. Atoms can diffuse either into the bulk liquid or into the existing gas, promoting the growth of these bubbles. The nucleation and growth process of gas bubble formation can be explained. The surface tension of the liquid causes a pressure that is exerted on the gas bubble. The relationship is

$P = 2\sigma/r$ where σ = the surface tension of the liquid

r = radius of the bubble

In other words, for a very small bubble, the pressure exerted on it is very high. This makes it very difficult for a bubble to grow. The liquid must be supersaturated with the gas in order to overcome this pressure It is not likely that gas bubbles will grow if the liquid is not supersaturated.

The nucleation process can arise from two primary ways. Vortices can develop in an agitated liquid. The center of the vortex has a negative pressure that encourages a bubble to form. Another way a bubble could start is at the location of a gas film. The

bubble grows off of the film and breaks loose. A stream of bubbles can be formed this way.

A study by Liu et al (1994) on welding suggests that hydrogen atoms can combine diatomically to form hydrogen gas which can be trapped to form pores. Liu also suggests that hydrogen can react with oxygen to form water molecules. Several other research studies on welding pointed to hydrogen gas as a cause of porosity. A study by Calder et al (1992) on welding aluminum-lithium alloy suggests that hydrogen gas is the underlying cause of spherical pores. A study by Weckman et al (1997) on aluminum and stainless steel welding suggests that porosity near the fusion boundary is caused by hydrogen gas evolving from the weld pool during solidification. In both the stainless steel and the aluminum welds, porosity and cratering occurred, and there was an increase in root porosity with increasing power density. In aluminum, the porosity was found close to the fusion boundary.

With welded aluminum some researchers have pointed to the collapsed keyhole effect as a contributor to pore formation. A study by Calder et al (1992) suggests that the irregular pores formed in partial penetration welds are related to the keyhole dynamics. In a study by Weckman et al (1997), 'large central pores were frequently observed in the keyhole-mode welds of aluminum, as in stainless steel; this type of pore may be due to the trapping of metal vapor as the keyhole collapses ' Also, Lee et al (1996) found that the large pores in the center of the weld might be caused by the collapsed keyhole effect and be the primary contributing factor to high porosity in the center of the weld. The same researchers (Lee et al, 1996) observed that among welds performed in an argon atmosphere, there were a few occasions where dendrite tips were not seen on the inner

surface of large pores, and in those cases oxides were formed on the inside walls of the pores. Furthermore, Lee et al (1996) noted

'as for the samples welded using nitrogen, considerable (elemental) N was detected on the inner surface of the large voids; whereas no apparent (elemental) N was found near small pores. This suggests that the inner surfaces of large voids must have absorbed nitrogen and formed nitrides during welding and such large holes might be filled with nitrogen gases. The inner surfaces might be the key-hole surfaces which were partially closed at the final stage so as to form individual large voids. These surfaces had extensively reacted with nitrogen gas during welding. In contrast, the small pores, without the detection of (elemental) N, should be originated from the interior by the evaporation of H_2, Li or Mg. Based on the current findings, the large and small pores seen in the laser beam welded specimens, for both the argon and nitrogen ones, might be formed by different mechanisms.'

D.1.4.1. Nitrogen

The presence of nitrogen gas during the solidification of iron or steel has some effects on the material properties. This effect has been studied extensively in the steel-making business, in which the primary source of nitrogen is the atmosphere. The diatomic atmospheric gas dissociates and dissolves into the metal as a single atom. The concentration of nitrogen in the steel is proportional to the length of exposure time to air. The solid-state solubility of nitrogen in iron is relatively low. According to the ASM Metals Handbook, for γ austenite, the solubility of nitrogen is nearly a constant 0.021 %. For δ ferrite, the solid-state solubility drops to 0.010 % at 1400 °C and increases slightly to 0 014 % at the solidification point. The solubility of nitrogen in liquid iron drastically increases to 0.039 % at the melting point. From that point the solubility continues to increase with increasing temperature.

Nitrogen also affects welding processes involving iron and steel. The nitrogen can either dissolve into the metal by itself, or it can form nitrides. This occurs mainly with self shielded metal arc welding since the protection from the atmosphere is not as

great. Some strong nitride formers which can be used for arc welding processes are Al, Ti, and Zr. These alloying elements are used in both welding and steel-making processes to remove the nitrogen.

It is known that nitrogen is soluble in iron in a liquid state. The solubility is a function of pressure and temperature, and obeys Sievert's law which states that, at a given temperature, the amount of nitrogen dissolved in liquid iron is proportional to the square root of the pressure (Welding Metallurgy, p. 4). According to Simmons and Wilson's study (1996), if the nitrogen concentration is less than 1 percent, its solubility in iron based alloys follows Sievert's Law. Also, the solubility of nitrogen in liquid iron decreases with increasing temperature. The result at higher temperatures is the entrapment of gas bubbles of nitrogen in the iron as it solidifies. This behavior can be observed particularly when the iron rapidly solidifies, as is the case with welding and laser melting processes.

Nitrogen has been used as a shielding gas in some research studies to prevent oxidation in laser melted iron specimens (Papaphilippou et al, 1996; Jianglong et al, 1996). The presence of nitrogen gas can have several effects on the molten metal. A small fraction of it can dissolve into the solid. According to Simmons and Wilson (1996) the solubility of nitrogen in pure liquid iron at atmospheric pressure is only 0.045 weight percent, which is greater than the solubility of carbon. The remaining nitrogen will bubble out of the liquid metal in gaseous form. Depending on the solidification rate, these nitrogen bubbles can become trapped and result in porosity. In a separate study by Arata and Oda (1984) on laser welding of structural steel, it was found that a relatively

small amount of nitrogen was absorbed into the molten metal under both of the air and argon gas conditions The content rose to about twice that of the base metal.

D.1.4.2. Oxygen

Oxygen is well-known in the steel industry as well as in the welding business to dissolve or chemically react with iron and steel. Like nitrogen, oxygen follows Sievert's law such that the amount of oxygen dissolved in liquid iron is proportional to the square root of the pressure. Depending on the solubility of the oxygen, and the presence of deoxidizers, the residual oxygen can be present as gas bubbles, dissolved as an oxide, or removed by a deoxidizing agent. Al, Ti, Zr, Si, Mn are all good oxidizing agents.

For laser alloying with pre-placed material, the mixture of alloying elements is typically mixed with an adhesive agent to fix the mixture to the metal prior to laser material processing. Another possible source of oxygen besides the atmospheric environment is the binder material. It is possible that this material is organic and contains various types of organic compounds that can be oxidized to produce gases that can be trapped in the melt zone upon solidification. A study on laser cladding by Yellup (1995) cited previous research by Abilsiitov et al (1983) that showed that contamination and gas porosity were a problem among various binder materials investigated. In the Abilsiitov et al. study (1983), high porosity was noted in the cases of paste mixed with boric acid or brazing flux and also in the case of a plasma sprayed coating of laser melted or laser alloyed steel. In a study by Liu et al. (1994) on welding, it was observed that the hydrogen content is greatly reduced when cellulosic and water-based organic binders were removed from the electrodes. Straus et al. (1990) observed absorptive coatings used

for preventing energy losses to be a source of impurities and structural defects of material remelted with a laser.

D.1.5. Carbon-Oxygen Reaction

The most important reaction that takes place involving oxygen is the reaction with carbon to form carbon monoxide. The concentration of carbon and oxygen in the molten metal determines the quantity of carbon monoxide produced. Frequently, with steels, there is excess undissolved oxygen after the carbon-oxygen reaction takes place. The carbon-oxygen reaction will always occur when producing steel, will occur for unshielded welding processes which expose the weld zone to oxygen, and in theory will also occur when a laser is used to melt iron, or steel, in the presence of oxygen. The extent to which this takes place depends on the activity of the carbon and oxygen dissolved in the iron. The reaction will be driven in the direction of the available excess free energy. The gas is generated inside the molten metal and bubbles out to the surface. However, as the metal cools and solidifies, some of these gas bubbles may be trapped, creating porosity. In rapid solidification processes such as welding and laser remelting and alloying, the metal solidifies so quickly that gases do not have time to escape.

Furthermore, in the case of iron, the carbon-oxygen reaction is also influenced by the type of graphite Other research has suggested that because lamellar graphite has a higher reactivity than spheroidal graphite (Ricciardi et al, 1983), lamellar graphite produces more bubbles than spheroidal graphite.

This chemical reaction occurs in the steel making process as well. Approximately ninety percent of the gas evolved in producing rimmed, capped or semi-killed steel ingots is carbon monoxide (Smith et al, 1952). Since the carbon-oxygen reaction is already well

documented to cause porosity in steel-making and welding processes, it is reasonable to extend the theory to laser melting techniques on irons and steels. The focus of this study is to examine and test the hypothesis and show that the theory is applicable. And also to investigate ways to prevent gas porosity from forming by removing the oxygen from the equation. Killed steel ingots are produced, by definition, without much gas being evolved in the manufacturing process. This is accomplished by the addition of deoxidizing agents such as silicon and aluminum, which react with the oxygen to produce silica and alumina (ref ASM). Since the oxygen is combined with the silicon or the aluminum, it is not available to react with the graphite to produce carbon monoxide. Knowledge of this reaction in the steel making process can give valuable insight into the laser re-melting process if the laser melt region can be a microsample of molten steel. Samples laser melted in pure nitrogen or pure argon environments are expected to be nearly pore free compared to the samples laser melted in air. Furthermore, the addition of titanium as a deoxidizer and nitride former is investigated in this study.

There are a number of examples in the literature where formation of carbon monoxide is cited as a possible source of porosity. For instance, Riccardi et al (1983) indicates that the presence of porosity in cast iron seems to be due to the formation of carbon monoxide and inferior quantities of carbon dioxide in the melted metal. A different research study (Samsonov et al, 1990) cites the previous work that associates pore formation with the evolution of carbon monoxide, carbon dioxide, or hydrogen gas. Also, Sedunov and Andriyakhiv et al (1980) have observed high porosity at the solidification boundary, and the spherical shape of the pores indicates that they are formed due to gas evolution by graphite during re-solidification of the cast iron. This

same observation was cited in a work by Chen (1984) with reference to gray iron. Another study by Luft and Reitzenstein et al (1991) cited graphite oxidation in the liquid melt pool that produces carbon monoxide, which especially at high temperatures, is more likely due to the increasing negative free reactive enthalpy, as opposed to the reduction of silicon or magnesium alloys in laser re-melted cast iron. In the case of spheroidal graphite remelted iron, one research study observed that 'coarse graphite rosettes have a size approximately equal to the length of the graphite inclusion; this also gives rise to the formation of pores of this diameter and depth ' (Samsonov et al, 1990). This suggests that the graphite rosette was vaporized or oxidized by the laser beam as it passed. In another study, Shibata (1991) cites an example where oxygen binds with carbon in the course of electron beam (EB) welding of spheroidal graphite iron and forms carbon monoxide.

Further insight into the carbon-oxygen reaction can be obtained by examining weld metal porosity. A study by Liu et al (1994) discussed the importance of the H-O and C-O reactions in great detail. These reactions are considered to be fundamental to control the amount of residual hydrogen and gas pores in the weld metal. According to Liu, carbon and hydrogen are the last ones to react with oxygen prior to the iron, and carbon monoxide and hydrogen were observed to be the primary constituents of the weld pores. This is true in spite of the fact that carbon and hydrogen will react with oxygen only if the amount of free oxygen exceeds that required to react with other alloying elements (such as Al, Mn and possibly Ti) (Liu et al, 1994). Furthermore, the Liu study concluded that the third major source of gas pores in steel welds is carbon monoxide. The carbon may have originated from organic ingredients and carbonates, that when

dissolved in the molten steel, can react to form carbon monoxide, which subsequently is trapped and will result in porosity.

D.2. Preliminary Work at UTSI

Contract work at the Center for Laser Applications on a project to laser-alloy cast iron flat plate samples to improve hardness and wear resistance provided the initial impetus for the current experimental work. For that project, numerous iron samples were alloyed using a Nd·YAG laser and various combinations of alloying elements, as well as simply laser treating the bare iron itself. A common problem among these samples was porosity. Porosity is undesirable to have in metal because it can lead to failure of a component due to the stress concentrations around the holes and the limited strength because of the reduced cross-sectional area. After a brief review of steel-making and welding information, this knowledge base was then extended to laser material processing. Several samples that were produced under an air environment with titanium and zirconium did not exhibit much porosity. The success of these samples provided the inspiration for determining the root cause of the porosity.

The emerging hypothesis was that something in the ambient air environment reacted with something in the iron to generate a gas which was trapped in the melt zone upon solidification. To test the hypothesis that developed out of the contract work, some experiments were set up using flat plate samples of gray iron and a specially designed box to control the gas environment. Initially, both a CO2 laser and a Nd:YAG laser were used for the preliminary experiments. The goal was to melt tracks in the iron in a controlled air, nitrogen and argon environment and evaluate the porosity found in the

cross-sections. It was expected that the air samples would have the most porosity, and that the nitrogen and argon samples would have none.

A total of four experiments of laser remelting of gray iron were performed. One experiment was performed using a titanium coated sample. In all cases the laser power was set at 1850 W, primarily because this was the maximum power setting available on the Rofin-Sinar Nd:YAG laser used for the experiments. In all but one case, the translation speed used was 1000 mm/min. In all but one case, the iron samples were processed inside a specially designed chamber, or 'box' which contained the appropriate shielding gas. The box was purged for a half hour with the desired shielding gas. This was done in an effort to control the processing environment as best as possible. Some of these samples were processed using a nozzle to direct the shielding gas while others were not.

The sample preparation and analysis is the same for these trials. The pieces of gray iron were cut from a plate, degreased and wire brushed before laser processing. After laser processing, the samples were labeled and photographed. Then the samples were cross-sectioned, mounted in bakelite and polished to a mirror like finish, and etched with nital to reveal the microstructure and the porosity. Photographs were taken under the microscope using image analysis software and examined to quantify the porosity.

The result varied and were somewhat inconclusive. Generally speaking the air tracks had a greater amount of porosity than the nitrogen and argon tracks. However, it was expected that the oxygen free environments would be nearly porosity free, but that was not the case. Many samples did have quite a few pores. There was also a variation in the porosity of samples within the same laser track. Also, the set of samples produced

using the nozzle to flow the gases had significantly higher porosity counts. It is possible that the wire brushing method of cleaning the samples deposited some undesirable oxides or organics, which subsequently led to the higher porosity. For future experiments, samples would be sandblasted and rinsed with acetone to avoid this problem.

E. Thermochemical reactivity

E.1. Thermochemistry

If the porosity is caused by a gas generated by a chemical reaction in the melt zone, it is important to identify and understand what reactions could possibly occur, and what reactions are probable To do this, one must look at the set of all possible products which can be generated from iron, carbon, the constituents of air (nitrogen, argon and especially oxygen), and also titanium. If a gaseous product can be formed, then it is a candidate for porosity formation. The product of the reaction might also be a solid that precipitates out of solution. These solids can sometimes be identified through x-ray diffraction or scanning electron microscopy (SEM) investigation or microprobe analysis.

From the first law of thermodynamics, the energy equation can be used to derive an enthalpy of formation equation and a Gibbs free energy equation for all of the likely gas producing reactions. One can investigate the chemical equilibrium and kinetics of the most relevent reactions. Using a compilation of reactions such as found in the CRC Handbook of Chemistry and Physics, a list of possible products of the constituent elements can be identified. From this list of products, a list of pertinent reactions is made that can be used to determine the enthalpy change and Gibbs free energy change for those reactions at the standard state. The enthalpy change, ΔH, is a measure of energy transfer occurring for the reaction. The greater the enthalpy change, the more energy is

transferred in the reaction. By convention, -ΔH corresponds to exothermic reactions and +ΔH corresponds to endothermic reactions. The enthalpy change can be derived from the first law of thermodynamics and will be discussed in greater detail later. The Gibbs free energy change, ΔG, is a measure of how far away from equilibrium the reaction is. -ΔG indicates that the reaction will proceed in that direction at that temperature and pressure. +ΔG indicates that the reaction is not possible under those conditions of temperature and pressure. The free energy is related to the chemical potential of the species. The derivation and explanation of these relationships will be discussed later. Furthermore, chemical kinetics relationships may be used to determine equilibrium concentrations of products and reactants. This analysis is, however, rather complex and beyond the scope of this paper. But an explanation of the equilibrium constant and its relationship to the Gibbs free energy of formation will be useful in discussing the reaction rates for the most important reactions and will be discussed later.

The primary reactions of interest, along with their Gibbs free energy of formation values at the melting and boiling points of iron at the standard state are shown in the following table, created from the JANAF Thermochemical Tables.

The free energy of formation change, ΔG_f, for the set of reactions listed in Table 4 indicates whether the reaction is possible or not in that direction. If ΔG_f is negative, the reaction is possible and will proceed in that direction If $\Delta G_f = 0$, then an equilibrium condition exists and the reaction proceeds until the equilibrium concentration of products and reactants is reached. If ΔG_f is positive, the reaction is not possible in that direction at that temperature. More energy is required for the reaction to proceed.

Table 4: Gibbs Free Energy for Possible Reactions

Chemical Reaction	ΔG_f° (1808 K) KJ / mol	ΔG_f° (3023 K) KJ / mol
$O_2 \rightarrow 2O$	134.371	52.775
$O_2 \rightarrow 2O^+ + 2e^-$	1391.523	1240.056
$O_2 + 2e^- \rightarrow 2O^-$	66.963	67.930
$O_2 \rightarrow O_2^+ + e^-$	1095.997	1018 820
$O_2 + e^- \rightarrow O_2^-$	14.573	83.717
$N_2 \rightarrow 2N$	359 141	277 384
$N_2 \rightarrow 2N^+ + 2e^-$	1682.248	1514.245
$N_2 + 2e^- \rightarrow 2N^-$	422.157	410.271
$N_2 \rightarrow N_2^+ + e^-$	1423.859	1337.008
$N_2 + e^- \rightarrow N_2^-$	198.239	258.596

Table 4: Gibbs Free Energy for Possible Reactions Continued

Chemical Reaction	ΔG_f° (1808 K) KJ / mol	ΔG_f° (3023 K) KJ / mol
$Ar \rightarrow Ar^+ + e^-$	1429 414	1333.918
$C + 1/2O_2 \rightarrow CO$ (g)	-269 915	-369.655
$C + O_2 \rightarrow CO_2$ (g)	-396.353	-395.423
$3C + O_2 \rightarrow C_3O_2$ (g)	-198.087	-265.781
$C + 1/2N_2 \rightarrow CN$ (g)	410 878	526.697
$Fe + 5(CO) \rightarrow Fe(CO)_5$	-516.148	-359.496
$Fe + 1/2O_2 \rightarrow FeO$ (s)	156 403	NA
$Fe + 1/2O_2 \rightarrow FeO$ (l)	-158.734	-94.177
$2Fe + 3/2O_2 \rightarrow Fe_2O_3$ (s)	-363 055	NA
$1/2N_2 + 1/2O_2 \rightarrow NO$ (gls)	67.503	52.152
$N_2 + 1/2O_2 \rightarrow N_2O$ (gls)	214.273	297.753
$1/2N_2 + 3/2O_2 \rightarrow NO_3$ (g)	341.638	515.698
$1/2N_2 + O_2 \rightarrow NO_2$ (gls)	147.002	223.508
$N_2 + 3/2O_2 \rightarrow N_2O_3$ (gls)	422.914	642.014
$Ti + O_2 \rightarrow TiO_2$ (s)	-610 046	-428.902
$Ti + 1/2O_2 \rightarrow TiO$ (l)	-370.405	-288.835
$Ti + 1/2O_2 \rightarrow TiO$ (g)	-107.461	-188.266
$2Ti + 3/2O_2 \rightarrow Ti_2O_3$ (s)	-1039.653	-727.309
$3Ti + 5/2O_2 \rightarrow Ti_3O_5$ (l)	-1020.595	-766.546
$4Ti + 7/2O_2 \rightarrow Ti_4O_7$ (s)	-2298.386	-1696.492
$4Ti + 7/2O_2 \rightarrow Ti_4O_7$ (l)	-2282 221	-1696.492
$Ti + 1/2N_2 \rightarrow TiN$ (s)	-167.309	-47.053
$Ti + 1/2N_2 \rightarrow TiN$ (l)	-136.15	-42.899
$Ti + C \rightarrow TiC$ (s)	-161.13	-131.368
$Ti + C \rightarrow TiC$ (l)	-127.140	-125.490

The ΔG_f values in the table are listed for 1808 K and 3023 K, which are the melting and boiling points of iron. These two temperatures in particular are chosen because even though the temperature will vary within the melt zone of the laser melted iron, the melting and boiling points represent the two extremes during the process.

Based on the $-\Delta G_f$ values, it is apparent that oxides of carbon, iron, and titanium are all possible products. Nitrogen oxides are not possible based on the $+\Delta G_f$ values for these equations. Also, the dissociation and ionization reactions of O_2, N_2, and argon are not possible within the temperature range (1808 K – 3023 K) under consideration. Based on the $\Delta G_f°$ data for diatomic oxygen gas, ionization into positively charge ions (O^+, O_2^+) would require significantly more energy. However, ionization into negatively charged ions (O^-, O_2^-) require only slightly more energy and, in fact, is nearly at equilibrium within this temperature range. At equilibrium conditions, both products and reactants can exist in concentrations determined by the equilibrium constant. For nitrogen and argon gases too much energy would be required to dissociate or ionize these gases; therefore the reaction is not possible at these temperatures.

If the reactions were written in the reverse direction, however, the signs on the $\Delta G_f°$ would become negative and the reactions would proceed spontaneously in that direction. This means that oxygen, nitrogen, and argon gas could be generated if monatomic or ionic forms of oxygen, nitrogen and argon were available. The only possible source of these free atoms or ions is if they were dissolved in the iron in the form of an oxide or nitride when the metal was cast or due to atmospheric oxidation since that time. The likelihood of this occurring on a large enough scale to significantly alter the results is small. Any dissolved oxygen or nitrogen in the iron would be bound up with

another element and would require energy to release it from the bond. It would be difficult to speculate whether this would occur or not, since the exact compounds are not known and not known to be present. Besides, if any surface oxides or nitrides were present, they would most likely be removed during the cleaning and sample preparation process.

E.2. Derivation of Gibbs Free Energy of Formation

The gibbs function, g, is defined as $g \equiv h - Ts$ and enthalpy is $h \equiv u + pv$ on a unit mass basis. One can differentiate both expressions and substitute into the differential expression of the first law, $dq = du + dw$ where q is heat and w is work. Assuming reversible work, $dw = pdv$, and applying the second law, $dq = Tds$, the resulting expression, $Tds = du + pdv$ is one of Maxwell's equations which relates three properties if two are known. Further substitutions can produce the other Maxwell equations. The particular one of interest here is $dg = vdP - SdT$ which relates the gibbs free energy change to volume and entropy (on a mass basis) if T and P are known. From this relationship, and assuming ideal gas behavior.

$$dg = RT/P\ dP - SdT. \qquad (1)$$

If temperature is held constant, standard pressure is assumed to be 1 atm and integration with respect to P is carried out, one obtains the gibbs function:

$$g = g^{\circ} + RT\ln P \qquad (2)$$

The chemical potential is defined as $\mu_I \equiv (\partial u/\partial N_I)_{S,V,N(J+1)}$ which relates the change in internal energy of the system to the change in moles of a component of the system. In this case, $\mu_I = g_I$, which will be important later

In general, a chemical reaction can be written as $aA + bB = cC + dD$ where A and B are the reactants and C and D are the products. a,b,c,d are the stoichiometric coefficients of the equation. Whether the reaction will proceed in the forward or reverse direction, or be at a state of chemical equilibrium, is determined by the free energy change of the system. This free energy change, or Gibbs free energy of formation change can be defined as ΔG. G is the Gibbs function that describes the chemical availability of the substance.

Based on the free energy change, it is possible to reduce the number of reactions under consideration to those whose Gibbs free energy change is negative for the temperature range under consideration. Granted, it is possible to write the equations in reverse for those chemical reactions that have a positive free energy change in Table 4 and they would become possible. However, to simplify the set of products under consideration as cause of porosity, these decompositions will be excluded. This assumes that a decomposed compound or gas does not contribute to pore formation. The simplified list of reactions, along with their free energy change, $-\Delta G$, is shown in Table 5.

E.3. Chemical Equilibrium

For chemical equilibrium to exist, $dG=0$. Since $dG = VdP - SdT + \Sigma\mu_i dN$ from section E.2. For a general chemical equation, $dG = -SdT + Vdp + \mu_A dn_A + \mu_B dn_B + \mu_C dn_C + \mu_D dn_D$. If the temperature and pressure are held constant, $dG = \mu_A dn_A + \mu_B dn_B + \mu_C dn_C + \mu_D dn_D$ If $d\varepsilon$ is defined as the increment of the reaction, then $dn_A = ad\varepsilon, \ldots dn_D = dd\varepsilon$. After substituting, $dG = (-\mu_A a + \mu_B b + \mu_C c + \mu_D d)d\varepsilon$. Imposing equilibrium and rearranging $a\mu_A + b\mu_B = c\mu_C + d\mu_D$ which is the equilibrium condition. Recall that

Table 5: Possible Chemical Reactions Based on Free Energy Change

Chemical Reaction	ΔG_f° (1808 K) KJ / mol	ΔG_f° (3023 K) KJ / mol
$C + 1/2O_2 \rightarrow CO$ (g)	-269.915	-369.655
$C + O_2 \rightarrow CO_2$ (g)	-396.353	-395.423
$3C + O_2 \rightarrow C_3O_2$ (g)	-198.087	-265.781
$Fe + 1/2O_2 \rightarrow FeO$ (l)	-158.734	-94.177
$2Fe + 3/2O_2 \rightarrow Fe_2O_3$ (s)	-363.055	NA
$Ti + O_2 \rightarrow TiO_2$ (s)	-610.046	-428.902
$Ti + 1/2O_2 \rightarrow TiO$ (l)	-370.405	-288.835
$Ti + 1/2O_2 \rightarrow TiO$ (g)	-107.461	-188.266
$2Ti + 3/2O_2 \rightarrow Ti_2O_3$ (s)	-1039.653	-727.309
$3Ti + 5/2O_2 \rightarrow Ti_3O_5$ (l)	-1020.595	-766.546
$4Ti + 7/2O_2 \rightarrow Ti_4O_7$ (s)	-2298.386	-1696.492
$4Ti + 7/2O_2 \rightarrow Ti_4O_7$ (l)	-2282.221	-1696.492
$Ti + 1/2N_2 \rightarrow TiN$ (s)	-167.309	-47.053
$Ti + 1/2N_2 \rightarrow TiN$ (l)	-136.15	-42.899

$\mu_I = g_I = g^\circ + RTlnP_I$. Substituting this expression into the equilibrium condition obtains:

$$a(g_A^\circ + RTlnP_A) + b(g_B^\circ + RTlnP_B) = c(g_C^\circ + RTlnP_C) + d(g_D^\circ + RTlnP_D) \quad (3)$$

Rearranging terms gives:

$$a\,g_A^\circ + b\,g_B^\circ - c\,g_C^\circ - d\,g_D^\circ = RTln(P_C^c\,P_D^d / P_A^a\,P_B^b) \quad (4)$$

The left hand side is ΔG_r° and the quantity in parenthesis can be defined as the equilibrium constant K. $P_A = X_AP$, $P_B = X_BP$, ... $P_D = X_DP$, etc.

$$K = X_C^c\,P^c\,X_D^d\,P^d / X_A^a\,P^a\,X_B^b\,P^b = X_C^c\,X_D^d / X_A^a\,X_B^b\,P^{c+d-a-b} \quad (5)$$

For $C + 1/2O_2 \rightarrow CO$ $\qquad K = X_{CO} / X_C\,(X_{O2})^{1/2}\,P^{-1/2}$ (6)

For $C + O_2 \rightarrow CO_2$ $K = X_{CO2} / X_C X_{O2} P^{-1}$ (7)

For $3C + O_2 \rightarrow C_3O_2$ $K = X_{C302}/X_C^3 X_{O2} P^{-3}$ (8)

For $Ti + 1/2O_2 \rightarrow TiO$ $K = X_{TiO}/X_{Ti}(X_{O2})P^{-1/2}$ (9)

Since it is difficult to speak of these properties without establishing some reference state, standard temperature and pressure are taken to be 25°C and 1 atm. Any element in its standard reference state is assigned an enthalpy value of zero by convention. Similarly, the Gibbs free energy of formation is assigned a value of zero at the standard reference state.

When referring to the Gibbs function at the reference state, a superscript ° is used, as in G°. If talking about the chemical availability required to form a substance from its elemental components, a subscript $_f$ is used, as in G_f. Since the Gibbs function is an expression of energy, it can be expressed in KJ And further it is useful to express the free energy, G, on a molar basis to be consistent with the stoichiometry of the reaction. Thus, G = H – TS (KJ/mol)

Also, since energy is relative to the reference at which it is established, and exact values of the properties cannot be known, it is only useful to compare changes in free energy. Thus, one considers $\Delta G_f°$ when speaking of the relative energy change between the reference state and the state at a temperature, T, for a substance being formed of its constituent elements Tabulated values of $\Delta G_f°$, $\Delta H_f°$, K_f and select other thermodynamic properties can be found in the Journal of Physical and Chemical Reference Data, also known as JANAF Thermochemical Tables. In JANAF, the choice of reference states for the elements important to this study are monatomic argon, diatomic nitrogen, diatomic

oxygen, and graphite (Acheson-spectroscopic grade) for carbon, and the solid-state form of iron at room temperature.

Keeping in mind that the focus of this investigation is gas porosity in remelted iron, and that only products which have a negative free energy change (-ΔG) are possible, the chemical reactions of primary interest can be narrowed to a select few. The chemical equilibrium of the overall system is assumed to be limited to these reactions. This also assumes that no intermediate or catalytic reactions are taking place. Solid products such as TiN, TiC, FeC, etc, will undoubtedly be part of the chemical equilibrium as well. However, since they are solids, not gases, they will excluded as a possible cause of porosity for simplification. Thus, the simplified list of reactions and free energy change data are shown in Table 6.

This table represents the gaseous products, which are thermochemically possible based on the assumptions that were made These are all likely to contribute to gas porosity if they are trapped in the solidified melt zone. In competing for the available oxygen, it is more likely that carbon will be oxidized to carbon dioxide or carbon monoxide, since the free energy change is more negative.

Table 6: Chemical Reactions of Primary Interest

Chemical Reaction	ΔG_f° (1808 K) KJ / mol	ΔG_f° (3023 K) KJ / mol
$C + 1/2O_2 \rightarrow CO$ (g)	-269.915	-369.655
$C + O_2 \rightarrow CO_2$ (g)	-396.353	-395.423
$3C + O_2 \rightarrow C_3O_2$ (g)	-198.087	-265.781
$Ti + 1/2O_2 \rightarrow TiO$ (g)	-107.461	-188.266

E.4. Titanium as a Deoxidizer

It has been suggested that small amounts of titanium when added to a molten metal, can act as a deoxidizer. This has been done with steels, iron, and for welding. The addition of titanium causes certain chemical reactions to occur, and depending on the conditions, nitrides, oxides or carbides of titanium can result. According to Mordike (1990) titanium can react with nitrogen or methane to form a coherent layer of TiN or TiC.

If the titanium behaves as a nitride or carbide former, the titanium could not be contributing directly to porosity since TiN and TiC are solids. It is unclear how the presence of these compounds could influence porosity caused by other sources, such as material evaporation, carbon oxidation.

In the following experimental work, one objective is to use titanium as a deoxidizer and porosity inhibitor. The goal is to have titanium react with oxygen to prevent the oxygen from reacting with carbon and producing a gas. In order for this objective to be completely successful, the titanium must react in such a way as to produce a solid. If the titanium-oxygen reaction results in the production of a gas, its use would seem to be counterproductive. To investigate these possibilities, the second part of this experiment will use titanium coated iron for the laser processing in air. For consistency with the gray iron cases, the titanium coated samples would also be laser processed in the nitrogen and inert argon environments. It is expected that the samples coated with titanium before laser processing will have less porosity.

II. Experimental Methods

The hypothesis under investigation is that the porosity present in iron samples laser-processed in ambient air is caused by a reaction between the flake graphite (carbon) in the gray iron and the oxygen in the air which produces a gas, probably carbon monoxide, which is trapped in the melt zone upon re-solidification. According to the thermochemical data, carbon mono-, di-, or sub- oxides are all possible products of carbon oxidation To prevent the oxygen from oxidizing the carbon, several approaches were being investigated. One approach involved operating the laser in a controlled environment under an inert gas, such as argon, so that the graphite oxidation is eliminated. The laser processing was also done in a pure nitrogen environment in order to verify that the gas pores are not the result of a nitrogen reaction. It is possible that the nitrogen behaves as an inert gas, giving similar results to argon. This is relevant because nitrogen is less expensive than argon.

Another approach is to alloy a deoxidizing element such as titanium or zirconium into the iron to act as an oxidation inhibitor. Adding these elements is supposed to prevent the formation of carbon monoxide or dioxide gases that cause the porosity. Essentially, the deoxidizer will react preferentially with the carbon, or the oxygen, to use it/them up before the carbon reactions can take place According to the thermochemical data, most titanium compounds of oxygen, nitrogen or carbon are solids; therefore they will not contribute to porosity. However, TiO, Titanium Oxide is a gas within the melting and boiling points of iron. Since TiO is a possible product, based on the negative free energy change, it might actually contribute to porosity, instead of reducing it. At any rate, titanium samples were also laser processed in air (~ 20 % oxygen) and nitrogen and

argon inert environments to determine if the addition of titanium has a positive or negative effect on the porosity with and without the presence of oxygen.

Also, the titanium was applied as a coating on the iron samples before laser processing. A binder material was mixed with the titanium and sprayed onto the sample. Therefore, to determine if the binder, which contains organics, causes porosity, samples will be coated with binder only and laser-processed in air, nitrogen and argon.

The laser processing of all samples in this study was performed with an Nd:YAG laser. The Nd:YAG laser is a continuous beam of light with an output wavelength (1.06 μm) in the infrared range. J. Folkes (1997) has determined that surface modification with infrared lasers mainly occurs through heating, and the wavelength interaction with the substrate is also a contributing factor. This interaction time may affect the reactions that occur and the ability of any gases, which are produced, to escape. The thermodynamics of the reaction chemistry within the melt pool must be understood.

A. Prior Research Conditions

In order to determine the best conditions to use for the laser processing of the iron, other research studies on laser processed iron and steel were investigated. While most of these research studies focused on microstructure and wear performance, some insight was given as to the quality of the melted layer. In some cases the porosity was evident by photographs or stated explicitly to be present or not present. While most of the laser conditions were given by the researchers, some were inferred or derived from the information given. A table was created summarizing the research conditions and results to facilitate the comparisons among the research studies. This table includes information about the type of material, kind of laser, type of laser process and conditions

used Other information noted in the table were the use of shielding gas, occurrence of porosity, and research study where the information was obtained The complete table is included in the appendix of this paper Based on inferences drawn from this table, and the preliminary work performed at UTSI, the conditions for the current experiment were decided. A table was created to compare quantitatively the information from other research studies and the preliminary work performed at UTSI based on specific criteria. In this table, occurrences of porosity were sorted by the conditions used in previous research relative to the preliminary conditions used by UTSI. Therefore, a better understanding of what conditions are favorable or unfavorable for porosity generation was obtained. Once the laser processing conditions were selected, they remained constant throughout the current experiment. Optimizing the laser processing conditions by varying the power, speed, beam diameter or type of laser, is beyond the scope of the current experimental investigation, although it is possible that these variables can alter the results. However, if it is assumed that the selected conditions are optimal, then the effects of these factors are minimized and do not contribute to greater porosity The UTSI preliminary conditions are listed in table 7 as 1 m/min, 44,527 W/cm^2, 8905.4 J/cm/cm^2 for the re-melting or alloying process. The purpose of Table 7 was to determine which conditions, relative to the previous work, seemed to have the most porosity. Then, the conditions could be changed slightly for the current experiment to obtain better results. This comparison is shown in Table 7.

B. Apparatus Set-up

B.1. Equipment

The equipment used for the apparatus set-up of the experiment consisted of a

Table 7 : Comparison Among UTSI Preliminary Laser Processing Conditions and Other Research Studies

Laser Process:		melting or alloying	
# remelted	23	# hardened	9
porosity	6	yes	1
	11	no	4
	6	?	4

Translation rate:		1 m/min.	
# faster	32	# slower	37
porosity	2	yes	9
	21	no	21
	9	?	7

Power density:		44,527 W/cm^2	
# higher	19	# lower	38
porosity	7	yes	4
	5	no	27
	7	?	7

Shielding gas used:		yes	
# using	30	# not using	18
porosity	10	yes	2
	16	no	10
	4	?	6

Vol. Energy Input:		8905 4 J/cm/cm^2	
# higher	38	# lower	19
porosity	12	yes	0
	18	no	13
	8	?	6

Shield gas breakdown			Porosity	
	# of uses	yes	No	?
Argon	15	4	9	2
Helium	7	3	3	1
Nitrogen	7	2	4	1
CO_2	1	1	0	0

Rofin Nd:YAG laser, model 020, with round beam optics, a CNC computer controlled X-Y motion system, an aluminum and plexiglass box, cylinders of argon, nitrogen and air, a flowmeter, adequate tubing and nozzles, an oxygen analyzer, gas sampling bags, and gray iron samples.

The Rofin Nd:YAG laser, shown in Figure 3, is a 2 kW laser operating in a continuous mode. The beam is delivered through a flexible fiber optic cable. The end of the cable has the round beam optics attached. The beam delivered through the fiber is somewhat homogenized and has an approximate "top hat" intensity profile. There is a high energy spot in the middle surrounded by a low energy ring which is in turn

surrounded by a high energy ring. Higher TEM modes can have additional rings and/or a different shape altogether. As a consequence of this beam shape, the energy distribution is not exactly constant across the beam cross-section, and the center and outside edges of the beam do not receive the same amount of energy input. This may affect the results.

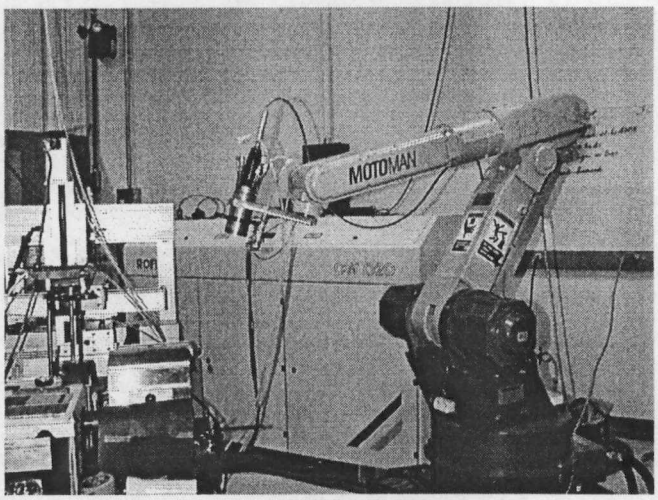


Figure 3: Rofin 020 Nd:YAG Laser

The next important item for the apparatus set-up is the X-Y motion system. A Unidex CNC machine is used to move the sample inside the "box", relative to the laser beam (which is held in a fixed position) at the prescribed translation rate. A computer program input into the Unidex system enables the stage, on which the "box" sits, to run and reset for each laser track that is made.

The aforementioned "box", shown in Figure 4, is 10 3/4" L x 6 3/4" W x 7" H. Three sides and the bottom are made of 3/8" aluminum plate. The fourth side of the box is made of 3/8" plexiglass to allow for viewing and picture taking. The sides are screwed together. A special 3/8" aluminum cover plate functions as a lid to the box, which is sealed to the underside of the plate by a lubricated o-ring. The cover plate is modified so that it houses the optical end of the laser in a fixed position at a 15° angle with the plate

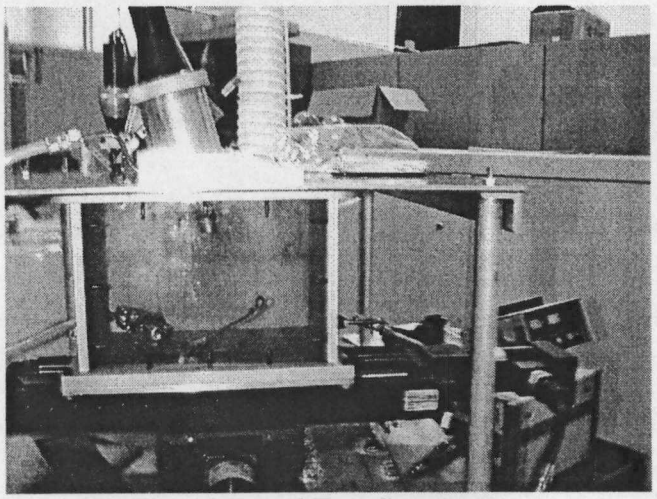


Figure 4: Experimental Box Set-up

at a depth sufficient for the appropriate focal depth of the beam on the sample inside the box. This coverplate also has a nozzle built into the laser optics housing so that the shielding gas can be introduced co-axially with the laser beam.

Shielding gases are necessary to determine the effect of gaseous environment on pore formation. In this experiment, cylinders of argon, nitrogen, and air were used to provide the desired environments for the laser processing. Argon was chosen because it is inert and not expected to react with the iron or the graphite. Argon also provides an oxygen-free environment in which to test the theory that oxygen in the air environment contributes to the oxidation of graphite in the gray iron. Nitrogen was chosen because it would also provide an oxygen-free environment and would be cheaper than argon if the results were similar. Also, the nitrogen gas might be more reactive and result in the formation of nitrides or other nitrogen compounds. The air environment was basically the control case to compare what would result if no shield gas were used. The oxygen present in the air was expected to permit oxidation of the graphite and contribute to porosity. A flowmeter was used to control the rate at which the gas enters the processing

chamber, and a flow rate of 30 units was used for argon and nitrogen. The flow for the air samples was directed across the optics, not at the sample.

B.2. Shield Gas Flow Rate

The volumetric flow rate of the shielding gases inside the box for all trials was held constant at 30 units. A Cole-Parmer flowmeter, model NO64-63G with a glass float was used to control the flow. According to the flowmeter calibration data, a scale factor of 30 corresponds to an air flow rate of 10,170 ml/min. For the cases of nitrogen and argon, a correction factor must be used to express the flow rate in ml/min. According to Arata and Oda (1984), the adjusted flow rate is proportional to the square root of the density ratio of the two gases. For example, the unknown flow rate, Q_1 is expressed as:

$$Q_1 = Q_{AIR} * \sqrt{\frac{\rho_{AIR}}{\rho_1}}$$

Therefore, the flow rate for nitrogen is 10,437 ml/min., and the flow rate for argon is 8,282 ml/min.

In order to verify that the shield gas is the only gas present in the chamber and that any oxygen or other gases present are evacuated by purging the chamber for a period of time prior to processing, an oxygen analyzer is attached to the outlet valve of the box. The analyzer was calibrated for oxygen content in ordinary air. When attached to the box, the oxygen concentration was measured as the argon or nitrogen was purged through the box. When the analyzer reading drops to less than 1% oxygen, one can be reasonably confident that the oxygen has been pushed out and the box contains the desired shield gas. Then it is safe to commence the laser processing experiment.

As an additional check of the gas environment to test for the presence of oxygen, nitrogen, argon, or any combustion gases which may be a by-product of the laser processing, gas samples were taken in sampling bags which could later be analyzed through a gas chromatograph. The gas chromatograph can be calibrated to detect the presence of oxygen, nitrogen, carbon monoxide, carbon dioxide, argon, and other gases that are suspected to be present.

The last item required for the experiment is the gray iron samples. Gray iron was chosen because of its common usage and also for the type of graphite it has. The flake graphite, as opposed to a nodular (spheroidal) graphite, was not expected to produce graphite nodules after processing which could be confused with porosity. According to (Riccardi et al, 1983), the flake graphite (near lamellar graphite) has a tendency to produce more bubbles than the near spheroidal graphite. This is because lamellar graphite has a higher reactivity than the spheroidal type.

C. Iron Sample Preparation

Preparation of the iron samples began with cutting a suitably sized sample, approximately 6 3/8" L x 3" W from the gray iron plate. The gray iron used was ASTM A48 class 83. The sample was sandblasted to remove any surface oxides and impurities. Then the surface was rinsed with acetone to remove any residue or oils. The sample was then sealed in a plastic bag to prevent any surface contamination from the air or from handling it. The sample must be laser treated within a few hours of being prepared so that oxidation (rusting) does not have time to occur.

In the case of the titanium coated samples, a thin layer of titanium was sprayed onto the sample after the acetone cleaning. The composition of this coating consisted of

a mixture of titanium powder (-325 mesh) and a binder material. The binder material consisted of LISI 100, a licensed product of Warren chemicals and water. The ratio used for the mixture was 100 Ti / 25 LISI 100 / 30 water. Once these quantities were mixed, a spray gun was used to spray the mixture onto the surface. The desired coating thickness was 100 microns +-20. The coating was allowed to dry and then the sample was sealed in a plastic bag until laser processing.

For the binder only samples, a thin layer of the binding agent was sprayed onto the sample after the acetone cleaning. Its composition consisted of a mixture of 25 LISI 100 / 30 water. The same spray procedure was used for the binder only as was used with the titanium mixture. The sample was then allowed to dry. Since the binder is a relatively transparent material, spots of surface oxidation on the iron, caused by the water in the mixture, were evident. The purpose for testing the binder was to determine if the organics or hydrocarbons contributed significantly to porosity.

D. Laser Processing Conditions

The power of the Nd·YAG laser was set at 1850 Watts, which is the maximum setting for this laser. The selected speed of the CNC motion system was 500 mm/min. The laser remained stationary while the X-Y stage moved beneath it. The iron samples were contained inside the box attached to the stage (in the cases using nitrogen or argon gas). The samples laser processed in ambient air remained stationary while the laser moved. The beam diameter was 2.3 mm based on the width of the melt zone of an air sample. This corresponds to an energy density of 44,527 W/cm^2. These conditions were chosen after consideration and comparison of other research efforts and preliminary conditions used by UTSI.

E. Cross-sectional Sample Preparation

After all three of the tracks were made under the desired conditions for both samples, they were marked, labeled and photographed in plan view. For both cases, the set of tracks were cut out of the sample plate and cut transversely to the laser track direction. A total of six cross-sections were made from each plate. The sections were cut at approximately ½" intervals. The sections were numbered starting from the beginning end of the laser track with '1' and continuing until six at the end of the track. Each cross-sectional sample contains an air track, a nitrogen track, and an argon track. All samples were mounted with the same plane facing outward. These pieces were then mounted and labeled. The gray iron samples were given the designation GI, and the titanium alloyed samples were given the designation TI. The next number in the label indicated the cross-sectional slice that was followed by a dash and a number indicating the gas environment. 1 is air, 2 is nitrogen, 3 is argon. For example, the fourth cross-sectional sample of gray iron laser processed in nitrogen was labeled GI4-2. A drawing showing how the laser tracks were cut is shown in the Figure 5.

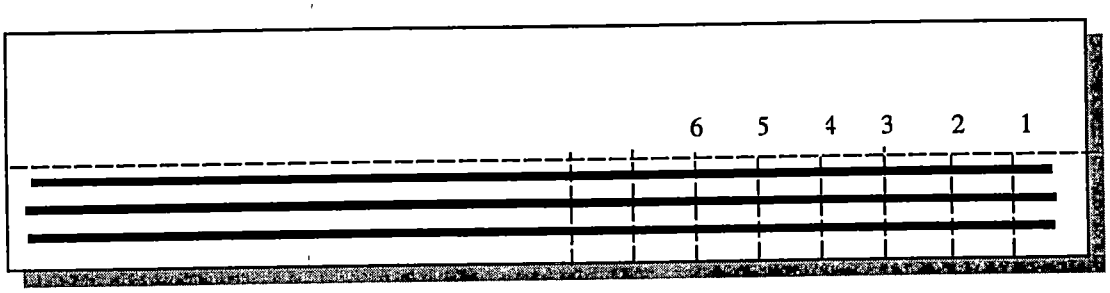


Figure 5: Iron Sample Cutting and Labeling

The properly labeled samples were then wet sanded with 180, 240, 320, 400, 600, 800 grit sandpaper. Then the samples were successively polished with 5.0, 1.0 and 0.3 micron AL_2O_3 micropolish. Samples were subsequently etched with 2% nital (Nitric

Acid) for 20-30 seconds. Then the samples were examined under a microscope to identify gas porosity.

F. Image Analysis

F.1. Procedure

Pictures of all cross-sections were taken at 5x magnification using an Olympus BX60M microscope, refer to Figure 6, which had a video camera attachment. In some cases, additional pictures were taken at 10x or 50x magnification for specific cases to show a crack or pore or graphite structure. The bakelite samples were placed under the microscope. The live image was then sent to a pentium/133 MHZ computer equipped with a frame grabber and image analysis software, IA3001 Image Analysis Application, version 1.25 by LECO Corporation. The focused live image of the cross-section was displayed on a computer screen. The image was then digitally stored by copying the image and bitplanes to a bitmap file, 640 x 480 pixels.

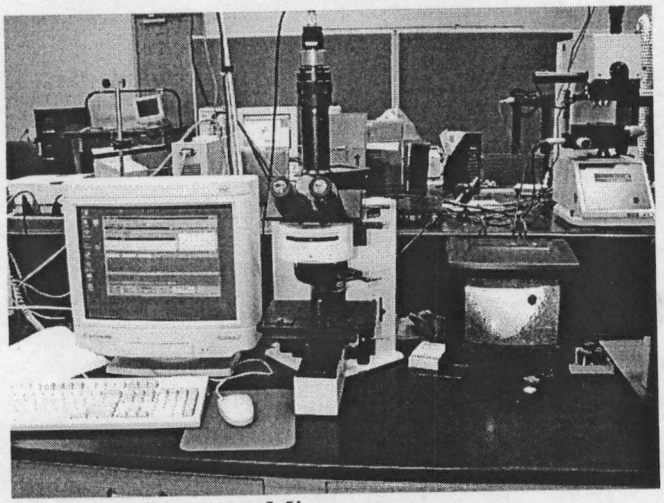


Figure 6: Olympus Microscope

The bitmap files were then opened in the Matrox Inspector 2.0, made by the Matrox Electronic Systems Ltd. This software package has the capability to perform a

blob analysis on the image This feature operates on the basis of the threshold of light and dark areas. The threshold can be adjusted and set so that only the pores are black and the background area is white. A region of interest, ROI, can be selected to perform the blob analysis only on the area specified. Once the light threshold is set, the program can count the dark spots and the areas of each.

The resulting blob count can be checked for false marks that should not be included in the analysis. Extraneous blobs are deleted form the results. These blob analysis data for each track of each sample were saved in a spreadsheet so that statistical comparison between conditions can be made.

F.2. Scaling

In order to determine the scale of the digital pictures at each magnification that was used, a digital image was made of a specified dimension on a vernier scale. A 2 mm gap was used for the 5x magnification scale and a 1 mm gap was used for the 10x magnification scale. When these images were viewed with the Matrox Inspector software, a line could be drawn to measure the gap in pixels. Therefore, a relationship between mm and pixels could be established at each magnification.

@ 5 x, 1 mm = 166 pixels

@ 10x, 1 mm = 341 pixels

@ 50x, 100 μ = 168 pixels (estimated)

With that established, a scale could be attached to each image. To do this, the appropriate length line (in pixels) was drawn in yellow overlay with a thickness of 3 pixels.

III. Results and Discussion

For the set of samples overall, the air tracks consistently had more porosity than the nitrogen and argon samples. This is on the basis of the average number of pores, total area of pores and percentage of porosity in the melt zone. Even though the cross-sections of the melt zone of samples were typically twice the size of the nitrogen and argon, they still had a higher percentage of porosity. The most porous samples by far were the titanium coated (TI) samples processed in air, which was on average 25% of the melt zone. The gray iron (GI) and the binder on iron (BI) samples both had an average of 3% porosity. Among the nitrogen and argon samples, the titanium (TI) again produced the most porosity in the melt zone - 4% for nitrogen and 2% for argon. The gray iron (GI) and the binder on iron (BI) produced very similar results in terms of porosity. In both these cases, the percentage of porosity in argon was 1%. Similarly, the porosity in the (GI) and (BI) samples with nitrogen was 1% and 2% respectively. It seems that the binder material has little or no effect on porosity, since the results seem to be nearly the same as for the laser melted gray iron. The titanium coated samples unexpectedly produced the greatest amount of porosity under any conditions (air, nitrogen, and argon) on all of the iron surfaces. The results of the quantitative analysis are shown in tables 8-13.

A. Quantitative Analysis Results

After the iron samples were laser-processed, cut and polished, digital photos of the cross-sectioned surface were taken and the porosity quantified. The total number, total area and percentage of porosity in the melt zone were calculated for all of the cross-

Table 8: Total Porosity Data for Gray Iron

	Total Number of Pores				Total Areas of Pores (pixels^2 @ 5x)			
Gray Iron	(1) Air		(2) Nitrogen	(3) Argon	(1) Air		(2) Nitrogen	(3) Argon
GI-7	7	GI -1	7	4	3,529	GI -1	406	2,355
8	9	2	4	3	2,527	2	597	209
9	2	3	6	2	249	3	1,634	1,309
10	9	4	1	3	3,385	4	33	210
11	13	5	4	3	2,817	5	1,339	116
12	7	6	3	6	399	6	272	2,186
Total	47		25	21	12,906		4,281	6,385
Avg	8		4	4	2,151		714	1,064
Std Dev.	4		2	2	1,462		633	1,034
Min	2		1	2	249		33	116
Max	13		7	6	3,529		1,634	2,355

Table 9: Total Porosity Data for Titanium Coated Iron

	Total Number of Pores				Total Areas of Pores (pixels^2 @ 5x)			
TI on Iron	(1) Air		(2) Nitrogen	(3) Argon	(1) Air		(2) Nitrogen	(3) Argon
TI-7	21	TI-1	15	4	46,386	TI-1	6,601	1,076
8	39	2	29	4	7,960	2	5,681	1,807
9	30	3	15	8	47,720	3	3,356	3,690
10	33	4	15	14	28,627	4	1,791	2,475
11	30	5	19	9	21,966	5	5,927	1,973
12	26	6	13	6	13,439	6	4,206	952
Total	179		106	45	166,098		27,562	11,973
Avg.	30		18	8	27,683		4,594	1,996
Std Dev	6		6	4	16,594		1,818	1,007
Min	21		13	4	7,960		1,791	952
Max	39		29	14	47,720		6,601	3,690

Table 10: Total Porosity Data for Binder Coated Iron

	Total Number of Pores			Total Areas of Pores (pixels2 @ 5x)		
BI on Iron	(1) Air	(2) Nitrogen	(3) Argon	(1) Air	(2) Nitrogen	(3) Argon
BI-1	12	1	2	6,585	43	115
2	9	6	2	4,558	381	187
3	8	1	2	1,506	255	1,119
4	5	3	2	1,419	201	208
5	6	4	1	994	3,061	20
6	5	4	1	3,118	161	53
Total	45	19	10	18,180	4,102	1,702
Avg.	8	3	2	3,030	684	284
Std. Dev.	3	2	1	2,193	1,170	416
Min.	5	1	1	994	43	20
Max	12	6	2	6,585	3,061	1,119

Table 11: Percent Porosity in Melt Zone of Gray Iron

	Total Area of Melt zone (pixels^2 @ 5x)				Percent Porosity in Melt Zone			
	(1)		(2)	(3)	(1)		(2)	(3)
Gray Iron	Air		Nitrogen	Argon	Air		Nitrogen	Argon
GI-7	98,910	GI -1	98,070	92,930	4%	GI -1	0%	3%
8	88,500	2	102,900	83,750	3%	2	1%	0%
9	95,520	3	77,250	80,530	0%	3	2%	2%
10	81,920	4	66,630	69,850	4%	4	0%	0%
11	74,880	5	64,950	66,640	4%	5	2%	0%
12	74,880	6	59,610	67,490	1%	6	0%	3%
Total	439,730		469,410	461,190	15%		6%	8%
Avg	87,946		78,235	76,865	3%		1%	1%
Std Dev	9,810		18,225	10,588	2%		1%	1%
Min	74,880		59,610	66,640	0%		0%	0%
Max.	98,910		102,900	92,930	4%		2%	3%

Table 12: Percent Porosity in Melt Zone of Titanium Coated Gray Iron

	Total Area of Melt zone (pixels^2 @ 5x)				Percent Porosity in Melt Zone			
	(1)		(2)	(3)	(1)		(2)	(3)
TI on Iron	Air		Nitrogen	Argon	Air		Nitrogen	Argon
TI-7	116,000	TI-1	113,000	125,900	40%	TI-1	6%	1%
8	104,900	2	125,100	128,400	8%	2	5%	1%
9	112,500	3	113,920	112,840	42%	3	3%	3%
10	109,000	4	106,400	108,300	26%	4	2%	2%
11	109,000	5	100,990	104,310	20%	5	6%	2%
12	102,000	6	103,570	89,670	13%	6	4%	1%
Total	442,800		662,980	669,420	149%		25%	11%
Avg	110,700		110,497	111,570	25%		4%	2%
Std. Dev	4,908		8,791	14,375	14%		2%	1%
Min	104,900		100,990	89,670	8%		2%	1%
Max.	116,400		125,100	128,400	42%		6%	3%

Table 13: Percent Porosity in Melt Zone of Binder Coated Gray Iron

	Total Area of Melt zone (pixels^2 @ 5x)			Percent Porosity in Melt Zone		
	(1)	(2)	(3)	(1)	(2)	(3)
BI on Iron	Air	Nitrogen	Argon	Air	Nitrogen	Argon
BI-1	96,330	44,620	48,300	7%	0%	0%
2	93,810	47,140	43,940	5%	1%	0%
3	93,530	40,240	46,470	2%	1%	2%
4	89,380	41,930	43,050	2%	0%	0%
5	83,870	41,710	48,060	1%	7%	0%
6	79,790	39,090	40,720	4%	0%	0%
Total	536,710	254,730	229,820	20%	10%	4%
Avg	89,452	42,455	45,964	3%	2%	1%
Std. Dev.	6,441	2,956	2,382	2%	3%	1%
Min	79,790	39,090	43,050	1%	0%	0%
Max	96,330	47,140	48,300	7%	7%	2%

sections. The cross-sections were then compared based on the conditions. There were basically three sets of samples – gray iron (GI), binder on iron (BI) and titanium on iron (TI) which included binder. A track was made in air, nitrogen, and argon for each sample. All of the nitrogen and argon tracks were made inside the box. Initially, the air tracks were also done inside the box.

The shield gas flow inside the box was directed coaxially with the laser optics. However, the air flow rate used to shield the optics was very high. It was believed that this rate provided excess oxygen to fuel the reactions taking place in the melt zone. Also, because the air flow was directly impinging the melt region, it could have been altering the heat transfer in the melt pool. Besides, an air environment does not need to be specially 're-created' in the box. Most of the time, laser processing is done in an ambient air environment. Therefore, the samples were redone in ambient air with an air gas flow rate that was used to protect the optics. An air knife, which directed the air flow across the optics to cool them, was used instead of the coaxial nozzle. This is why the samples corresponding to GI and TI are numbered 7-12 in the results, instead of 1-6 like the other samples. In order to compare and contrast the differences among the samples in this study, it is helpful to know that all of the nitrogen and argon samples were processed in the box with a gas flowing coaxially with the optics. The previous data set of air samples (GI and TI) were retained in the appendix, but they are not used for comparative purposes here.

After the tracks were made and the soot on the surface was brushed off, the surface was observed. The soot was dark gray in color when processed in nitrogen and argon. The soot was reddish brown when processed in air. The tracks made in the

nitrogen and argon environments have a silvery surface appearance. They were narrow and relatively flat. There were no visible surface holes. Some very fine transverse cracks were seen. In contrast, tracks made in air were wider and had a dark gray appearance. The surface was dull and relatively flat. Some very fine transverse cracks can be seen. The edges of the air tracks had a wide, dark band surrounding it. This band was noticeably wider in air than in the nitrogen or argon environments. The width of the band might be associated with the partially melted zone (PMZ). A photo showing the appearance of the tracks in plan view is shown in figure 7.

For the titanium coated samples, the soot was again brushed off after each track was made. The surface of the tracks made in nitrogen and argon is silvery and somewhat bumpy. The tracks are narrow with some fine cracks. The tracks made in air were dark gray, narrow, bumpy and full of holes. The surface was raised, not flat. Some fine, transverse cracking was evident. There was a dark band surrounding the track. A photograph of the surface is shown in figure 8.

B. Qualitative Description of Porosity

For the set of gray iron samples laser melted in air, series GI7-1 through GI12-1, there were several medium to large sized pores and many more smaller sized pores visible in the melt zone. The larger pores were generally found at or near the edge of the partially melted zone (PMZ). The smaller pores were typically distributed throughout the entire melt zone. The shape of the cross-section was half-moon shaped, wide at the top and rounded at the bottom, while the surface interface was basically flat. On average, these samples were 3% porous, varying from 0 – 4 % from section to section within the air track. A typical gray iron section processed in air is shown in Figure 9.

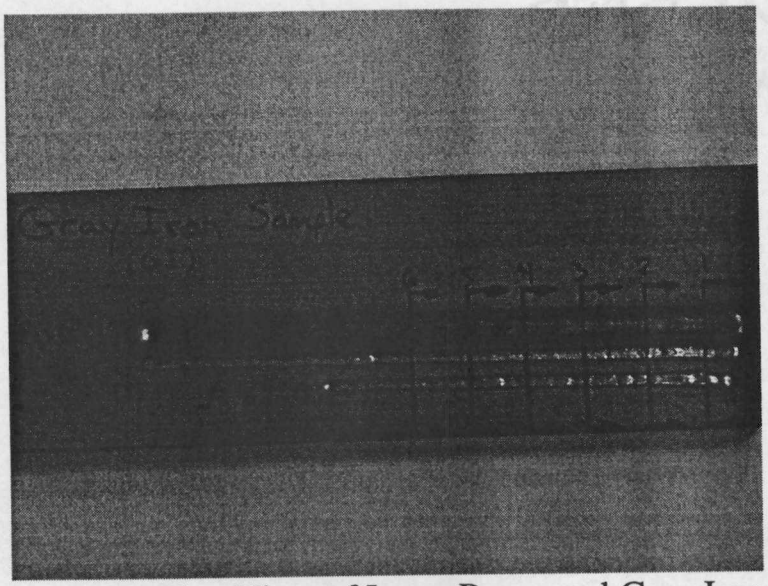


Figure 7: Plan View of Laser Processed Gray Iron Sample

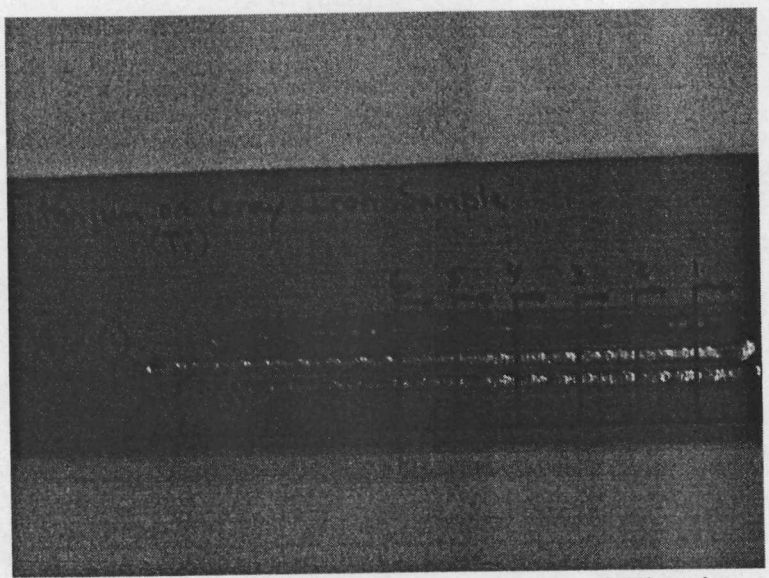


Figure 8: Plan View of Laser Processed Titanium on Gray Iron

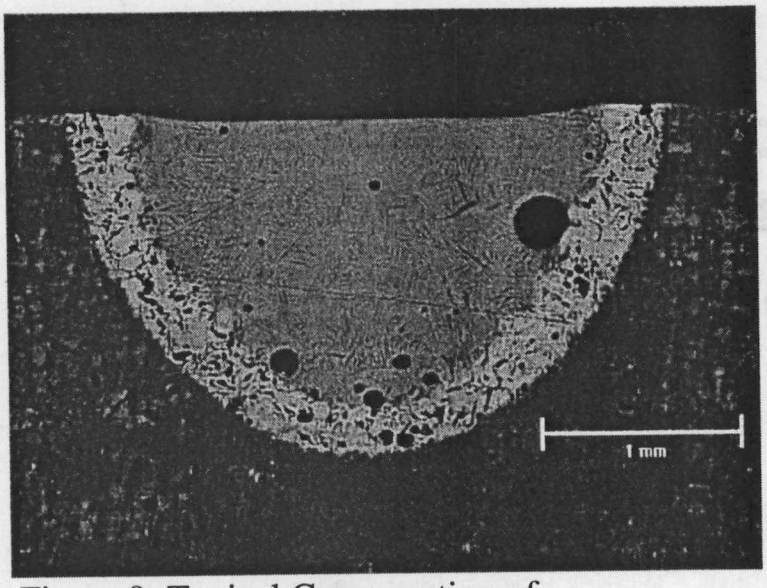


Figure 9: Typical Cross-section of
Laser Melted Gray Iron in Air

For the set of gray iron samples laser melted in nitrogen, series GI1-2 through GI6-2, there were few to several very small pores, or none at all. A few small and medium sized pores are mainly located near the edge of the PMZ. The shape of the cross-section was narrow at the top and continued basically straight down, except for some slight necking, to a rounded bottom. The necking caused the minimum width to occur about one third of the way down. The surface interface was basically flat. On average, these samples were 1% porous, varying from 0 – 2 % from section to section within the track. A typical gray iron section laser processed in air is shown in Figure 10.

For the set of gray iron samples laser melted in argon, series GI1-3 through GI6-3, there were a few small to medium sized pores, or just a few small pores. The medium sized holes were typically found at or near the PMZ, while small pores were typically found at or near the PMZ or in the middle. The shape of the melt zone was narrow at the top and fairly straight down to a rounded bottom. There was also some necking in these

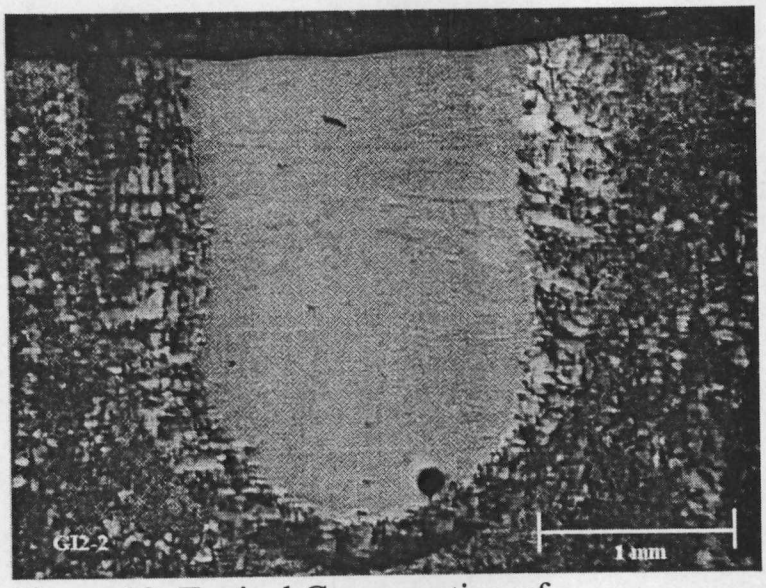


Figure 10: Typical Cross-section of
Laser Melted Gray Iron in Nitrogen

samples which occurs around one-third to halfway down. The surface interface was basically flat. Sample GI5-3 had a wide horizontal crack cutting through the mid-section, which can be seen in Figure 11. On average these samples were 1% porous, varying from 0 – 3 % from section to section within the air track. A typical gray iron section processed in argon is shown in Figure 12.

In comparing all the samples of the three sets, several observations can be made. It is obvious that the biggest differences are between the air samples and the nitrogen or argon samples; since the resulting porosity for the nitrogen and argon samples was very similar. The samples laser melted in air were always greater in total number and volume than the samples laser melted in nitrogen or argon. Refer back to Table 8 for quantitative porosity data. The air tracks were consistently both wider and deeper than the nitrogen and argon. In fact, the total area of the melt zone for the air tracks was double the size of either the nitrogen or argon, which were both nearly the same size. Refer back to Table 9

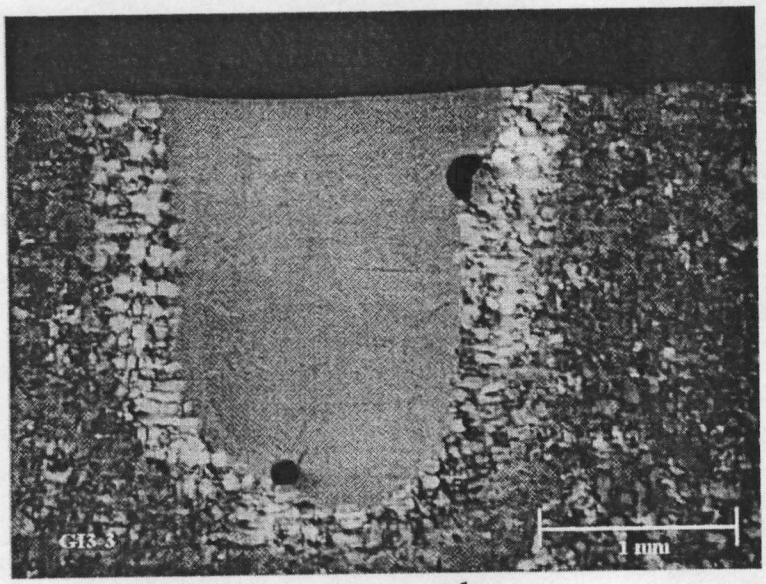


Figure 11: Crack across sample
Laser Processed in Argon

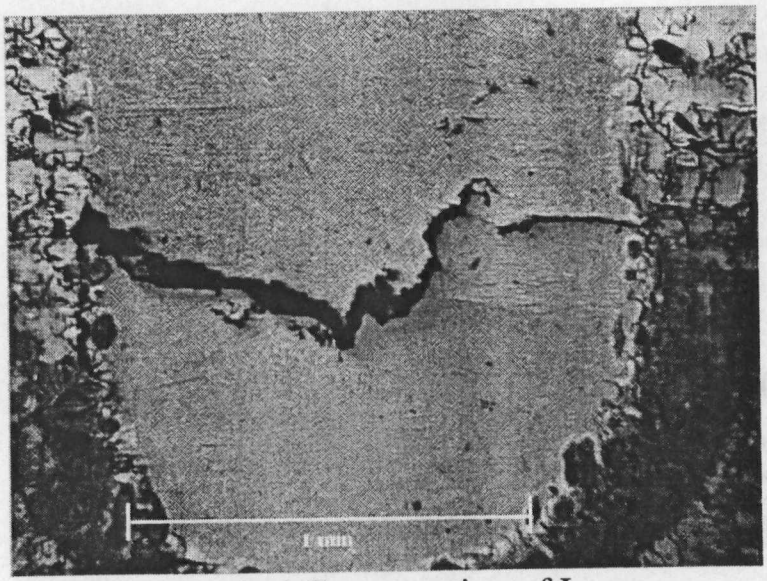


Figure 12: Typical Cross-section of Laser
Melted Gray Iron in Argon

for specific values of the areas The surface of the track was relatively flat in all cases. One reason for such a large difference in cross-sectional area between air and the other gas environments was the difference in shape of the melt zones. The air samples looked like wide mouth wine glasses, while the nitrogen and argon samples had a classic shape The reason for this was theorized to be directly linked to the presence of oxygen in the air that was ionized by the laser beam just above the iron plate. From the CRC handbook of Chemistry and Physics, the first ionization potential for diatomic oxygen is 12.1 eV, nitrogen is 15.6 eV, and argon is 15.8 eV. The laser energy is most likely between 12.1 and 15.6 eV. A plasma, by definition, is an ionized gas. To form a plasma, the gas would need to lose an electron to become ionized. The resulting plasma formation disperses the laser energy over a wider area; consequently, a wider section of the surface was melted than would have been without the plasma formation. Refer to Figures 13 and 14 which shown this effect.

Furthermore, even though some of the input energy was probably dissipated at the surface, the oxidation of carbon reaction, because it is exothermic, possibly generates enough energy to more than compensate for the surface plasma effect. There appears to be enough excess energy to penetrate to a slightly greater melt depth in the air tracks

For the set of titanium coated gray iron samples that were laser melted in air, series TI7-1 through TI12-1, there were several large pores and many small to medium sized pores. Many of the pores were at or near the PMZ, while many of the smaller pores were near the surface interface, but there was porosity throughout the melt zone. Most of the pores are not perfectly round. In fact, a few of them are crescent shaped. The surface interface was mounded instead of flat for these tracks. That shape of the cross-section

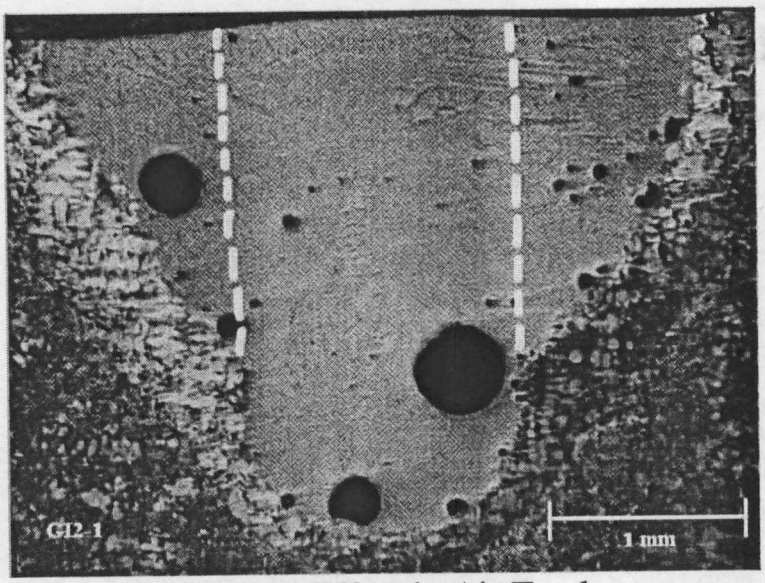


Figure 13: Plasma Effect in Air Track

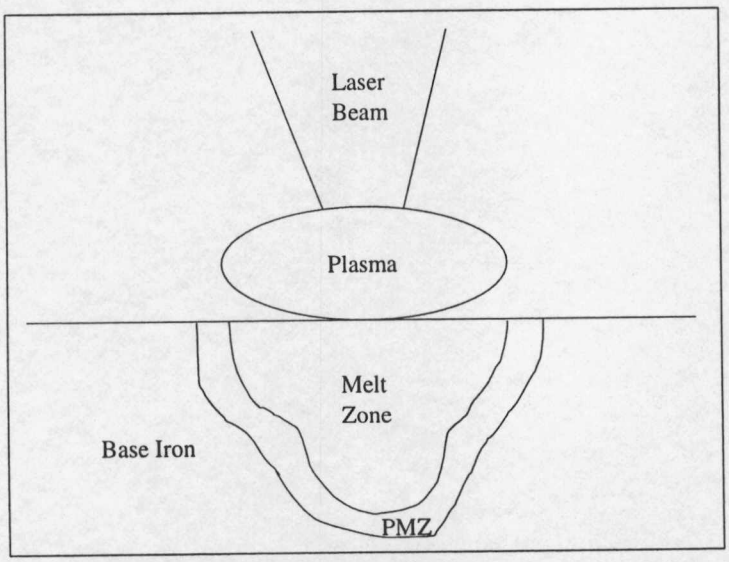


Figure 14: Plasma Formation

was wide at the top and narrowing gradually until it rounded out the bottom. On average, these samples were 13% porous, varying from 4 – 27 % from section to section within the track. A typical titanium on iron section is shown in Figure 15.

For the set of titanium on iron samples laser melted in nitrogen, series TI1-2 through TI6-2, there were several small to medium sized pores and a few medium sized pores. Several pores were irregularly shaped. Some pores were at or near the PMZ; others were not. The melt zone shape was narrow near the surface and remained narrow until the bottom of the melt zone. At the surface, however, there was evidence of a slight widening of the melt zone at the surface. This suggests that there may have been some plasma formation caused by a residual amount of oxygen, or the titanium, or another source. The surface interface was essentially flat, as opposed to being mounded. On average, these samples were 4 % porous, ranging from 2 – 6 % from section to section within the nitrogen track. A typical titanium on iron section laser processed in air is shown in Figure 16.

For the set of titanium on iron samples laser melted in argon, series TI1-3 through TI6-3, there were a few small to medium sized pores. Most of them were found at or near the HAZ. Some of the pores are irregularly shaped. While the surface interface was relatively flat, the shape of the melt zone was narrow near the surface and stayed narrow until the bottom. There is a slight widening near the surface as there was with the nitrogen samples, which suggests plasma formation. On average, the argon samples had 2 % porosity, ranging from 1 – 3 % from section to section within the argon track. A typical titanium on iron sample processed in argon is shown in Figure 17.2 % porosity, ranging from 1 – 3 % from section to section within the argon track. A typical titanium

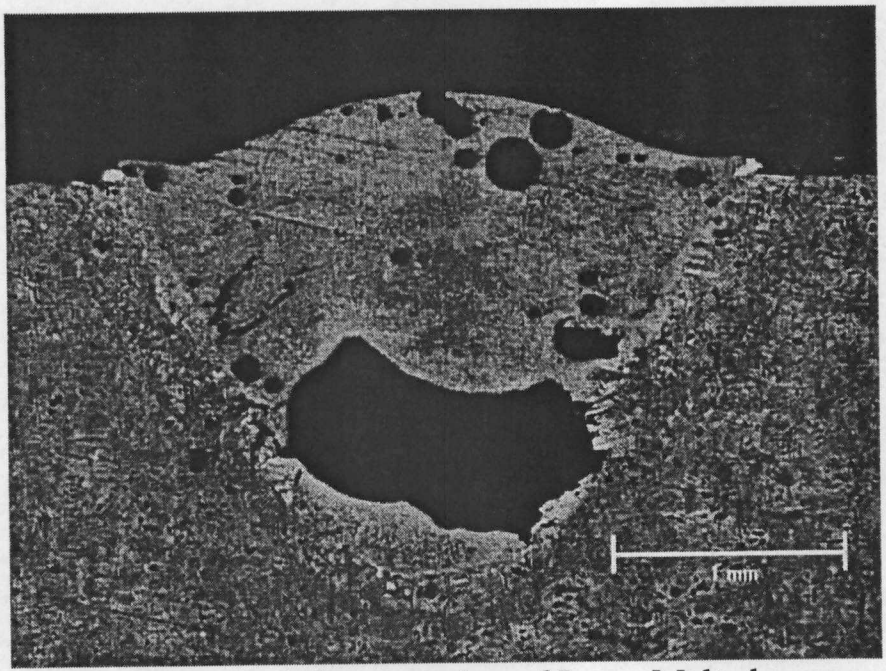


Figure 15: Typical Cross-section of Laser Melted Titanium on Iron in Air

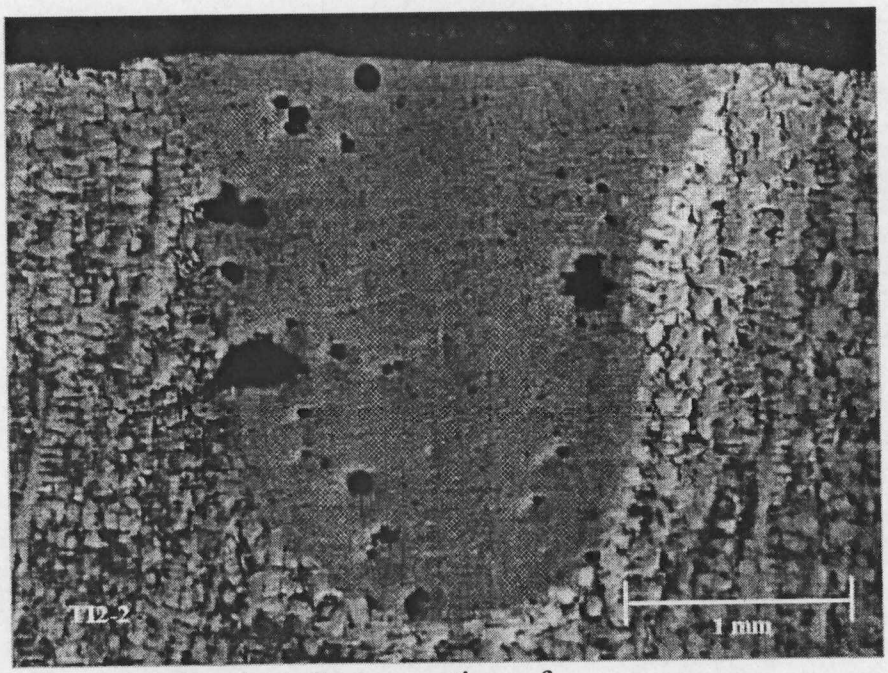


Figure 16: Typical Cross-section of Laser Melted Gray Iron in Nitrogen

on iron sample processed in argon is shown in Figure 17.

When comparing results of the titanium coated samples in three gas environments, several observations can be made. Once again, the air tracks were more porous than the nitrogen or argon tracks, and the pores were larger in air as well. The melt zone of the air samples was wider and deeper than for the other gas environments. The surface of the air samples was mounded, while the nitrogen and argon samples were flat. Overall, the titanium coated samples had consistently more porosity than the gray iron samples for the corresponding gas environments. This porosity is directly linked to the titanium, since the binder only samples showed results similar to the gray iron samples in all cases.

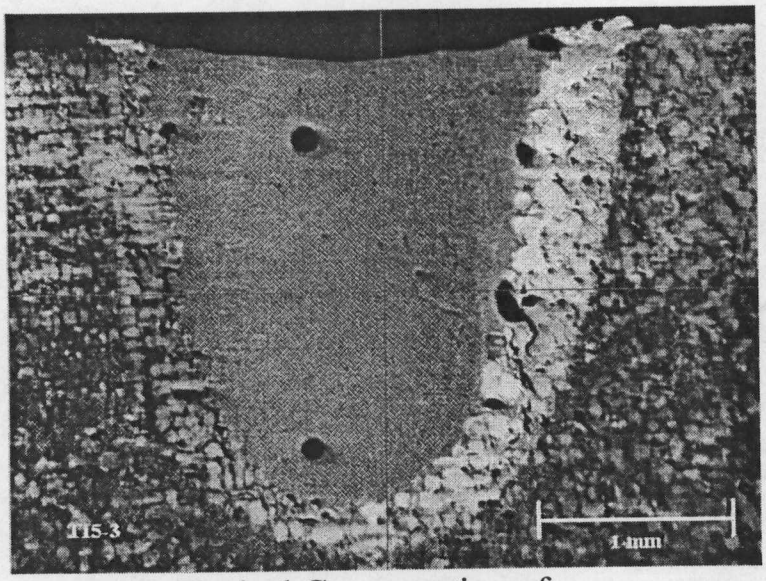


Figure 17: Typical Cross-section of
Laser Melted Titanium on Iron in Argon

C. Histogram Porosity Comparison

In order to facilitate the comparison among groups of samples based on pore size and frequency, histogram charts were created from the pore area data. Since the pore

area data is given in square pixels, it was necessary to use a scale to convert these units into square millimeters. The frequency ranges chosen are based on order of magnitude increments mostly for convenience. The ranges are < 0.002, 0.0021 < 0.02, 0.021 < 0.2, 0.21 < 2. The number of occurrences in each category was counted for all of the samples. Then charts making comparisons among materials for each gas are created.

In comparing all of the samples laser processed in air, it is obvious that the titanium samples have the most porosity by far, with over 100 occurrences in the 0.0021 < 0.02 mm^2. This does not occur with GI or BI samples in any environment. This suggests that there is a link between air, titanium, and porosity in iron. The occurrences of porosity in GI and BI samples were comparatively low and nearly the same.

When comparing among nitrogen samples, again the TI samples have by far the most porosity, although the quantity is less than in air. The GI and BI samples are roughly the same. Most of the TI porosity is in the smaller frequency range. This is also true for the GI and BI samples. Among the argon processed samples, the occurrences are nearly the same as for nitrogen except the totals in each category are lower.

If one compares among gray iron (GI) samples in the different gaseous environments, it is obvious that the most porosity occurs in air, then nitrogen, then argon. The total number of occurrences is relatively high, especially for the TI samples. Once again most porosity is concentrated in the smaller size ranges. The air case is the only one that has any porosity occurring in the highest range.

Among BI samples in different gas environments, the air once again had the most, followed by nitrogen and argon. In any case, however, the total number of occurrences is still low. The highest case is in air with 22 occurrences. Refer to figures 18-23.

Figure 18: Porosity Comparison Among Air Processed Samples

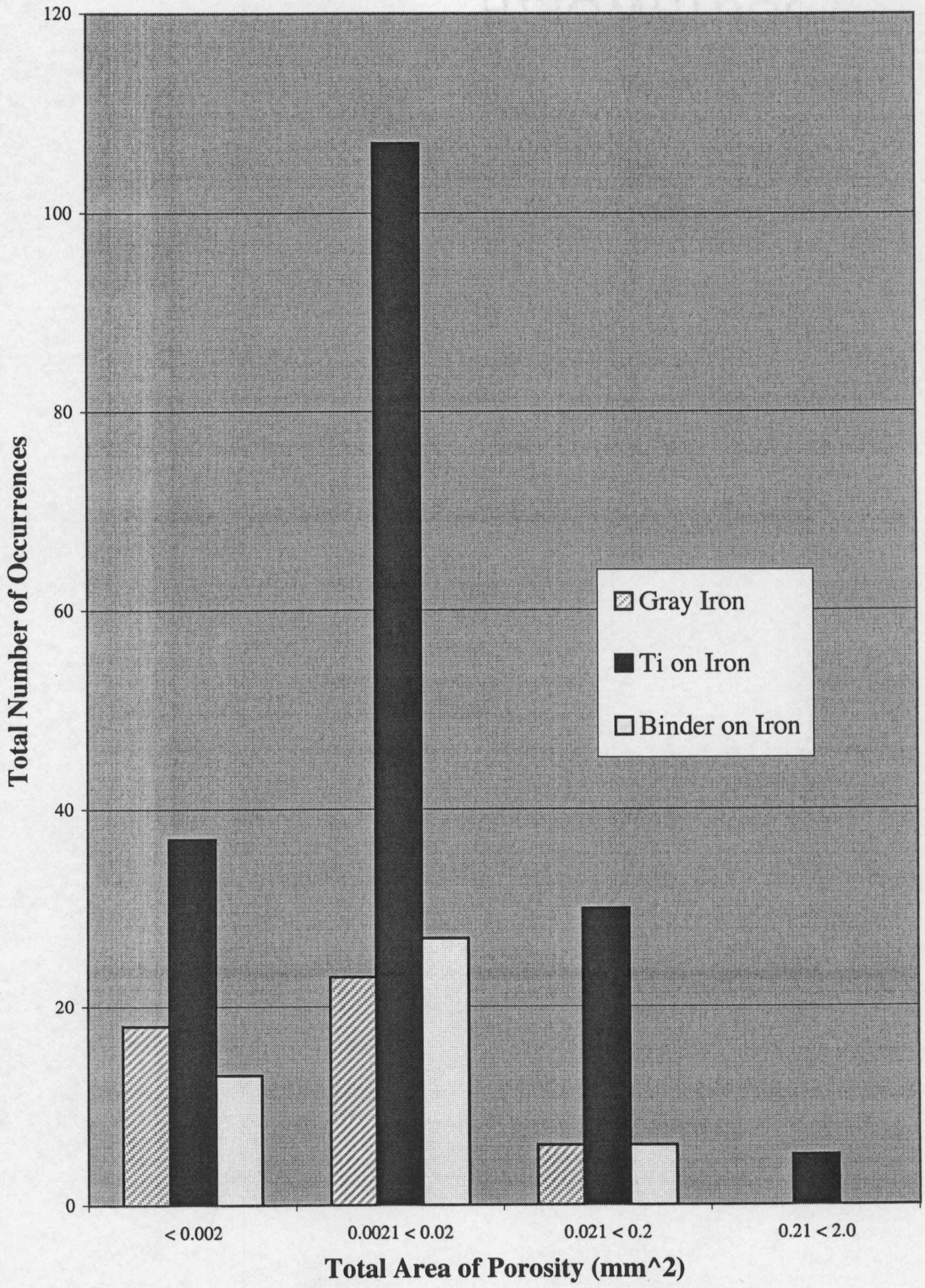


Figure 19: Porosity Comparison Among Nitrogen Processed Samples

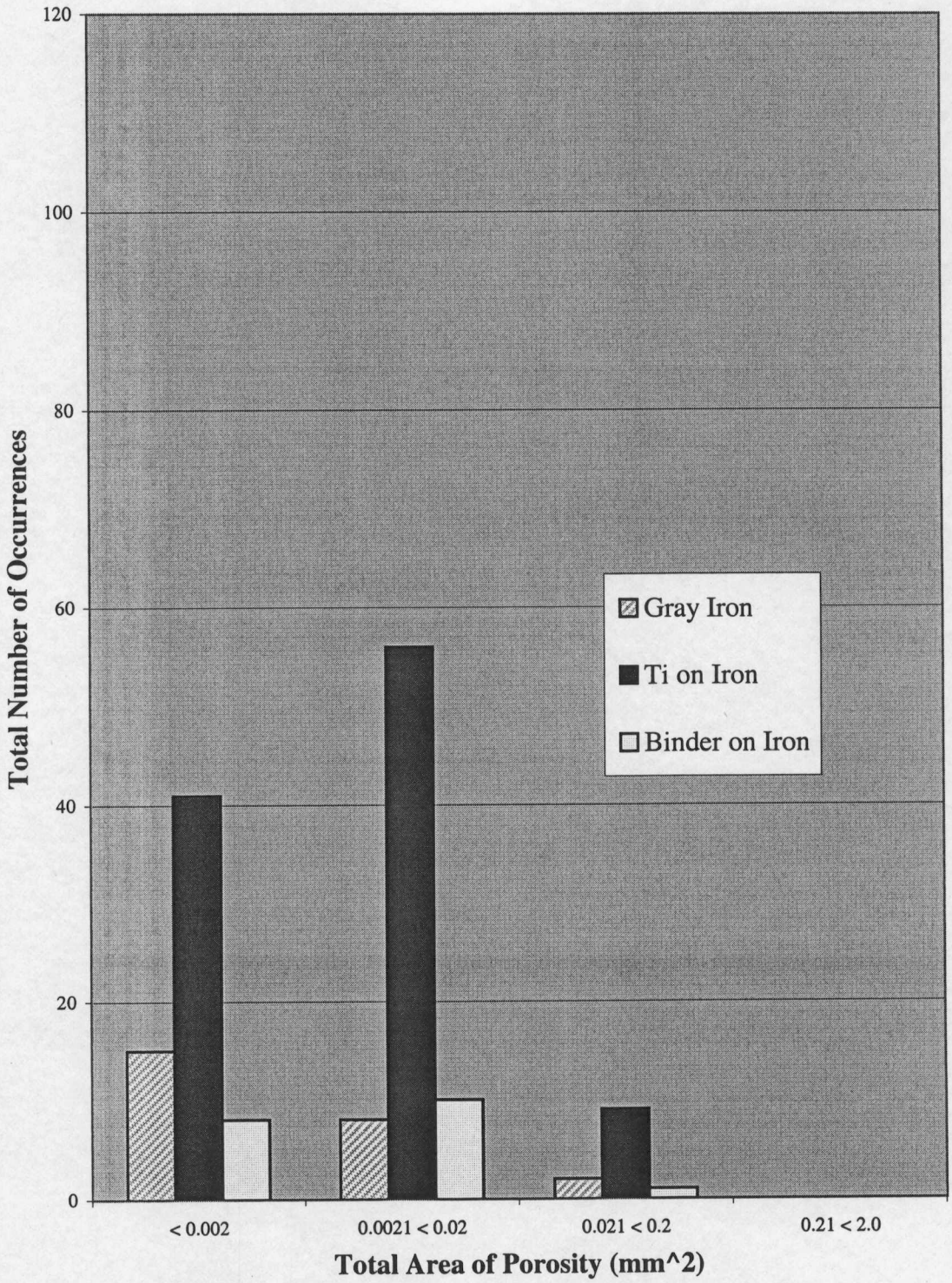


Figure 20: Porosity Comparison Among Argon Processed Samples

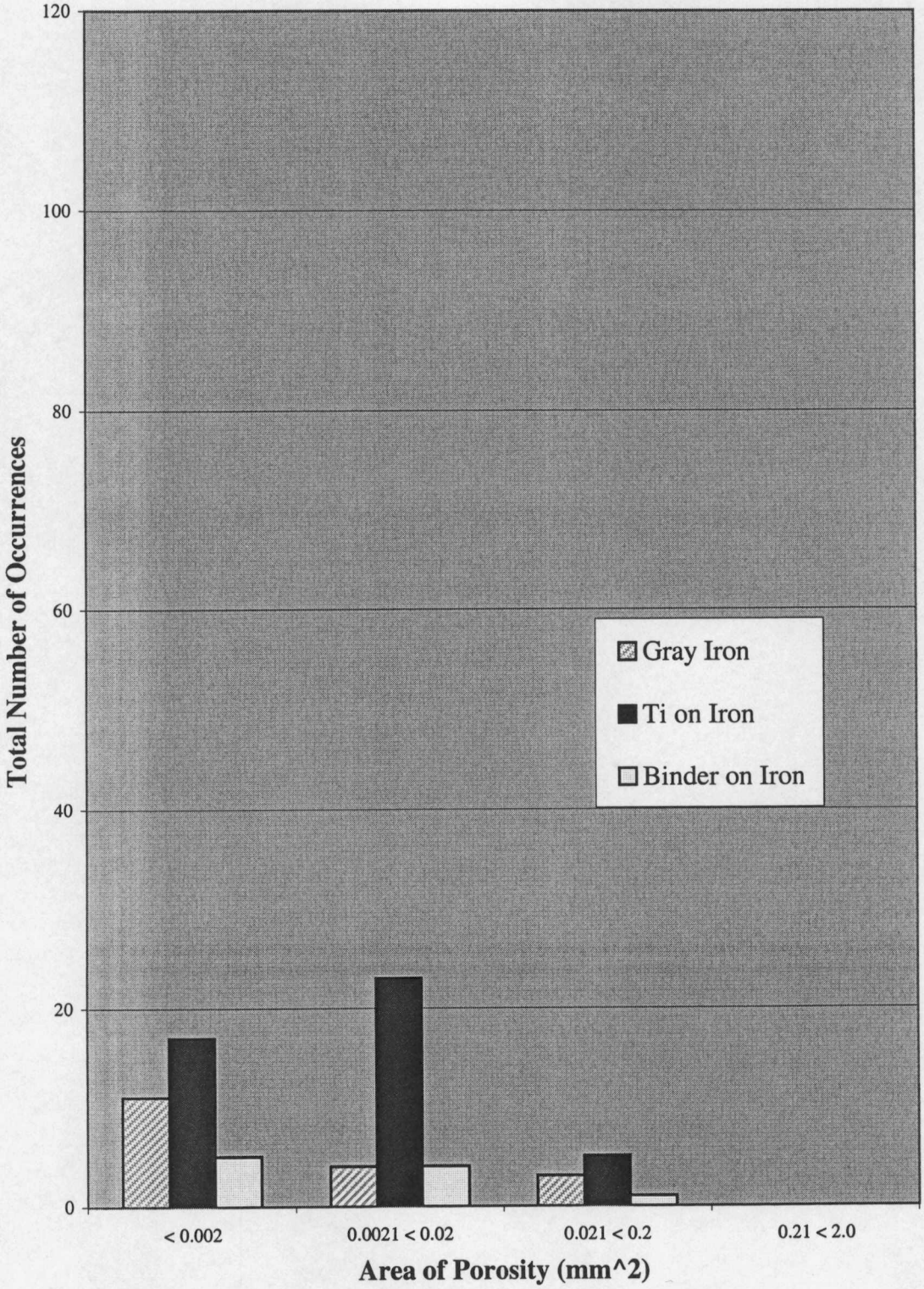


Figure 21: Porosity Comparison for Gray Iron (GI) in Air, N_2 and Argon

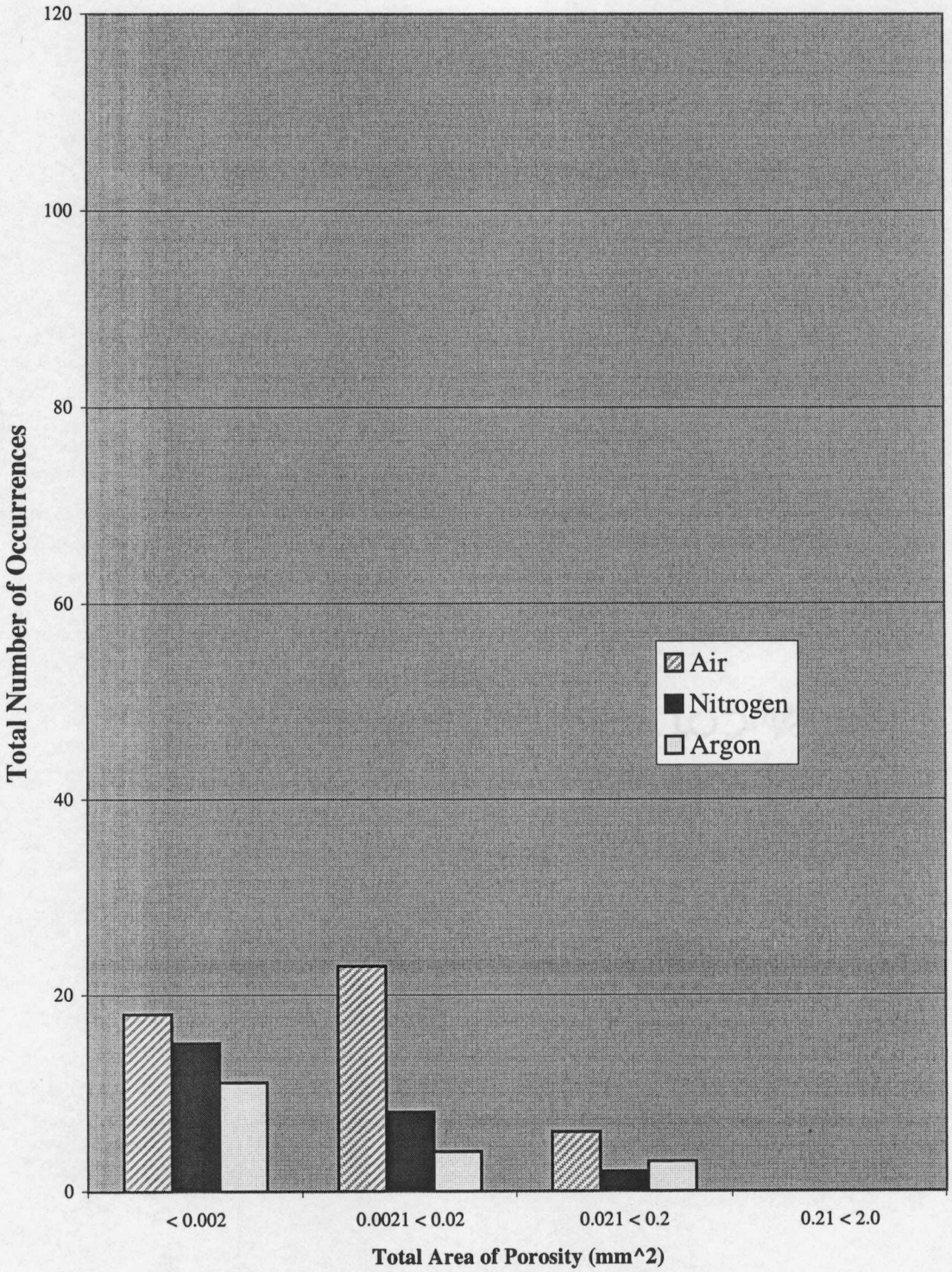


Figure 22: Porosity Comparison for Titanium on Iron (TI) in Air, N_2 and Argon

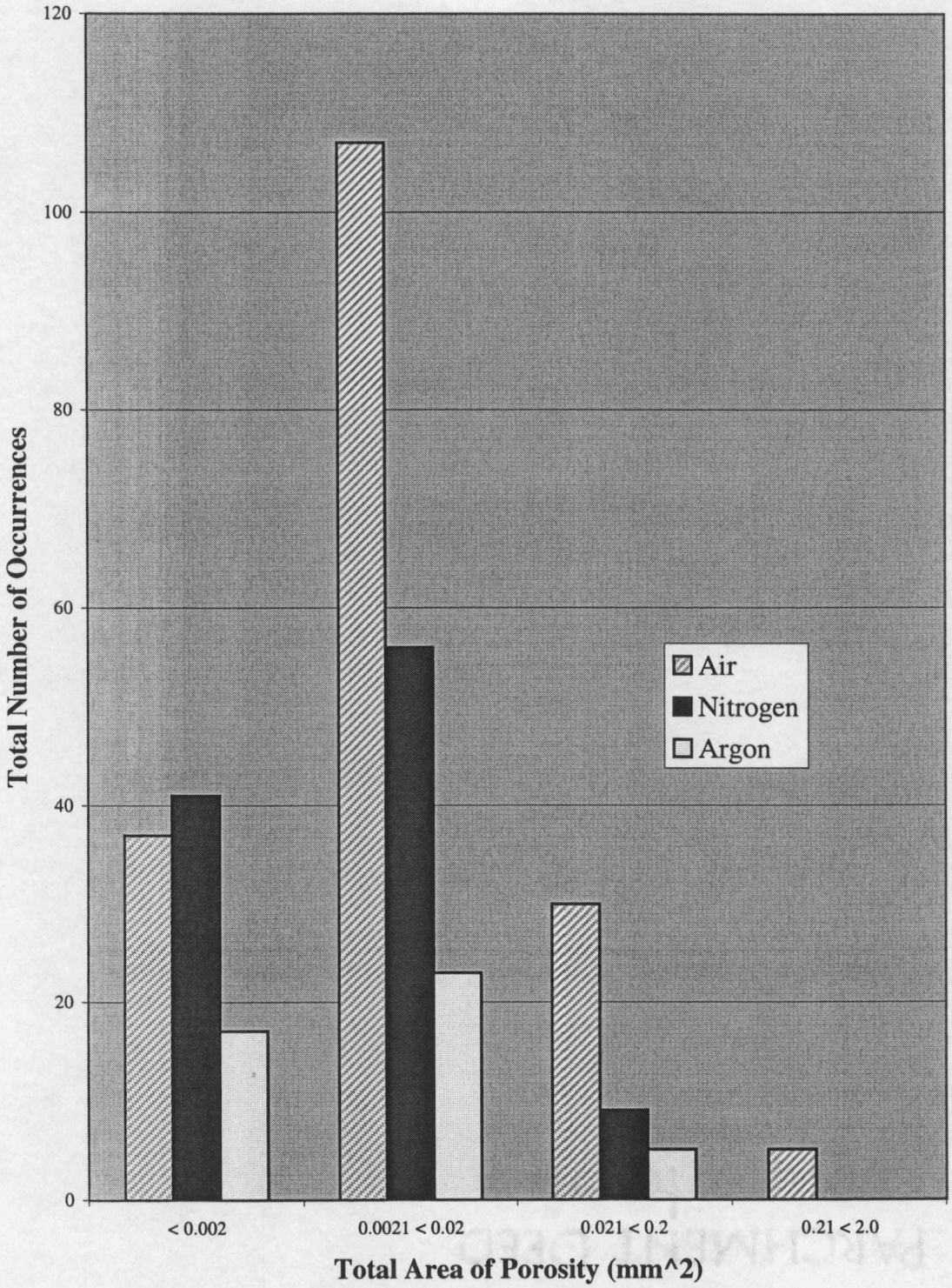
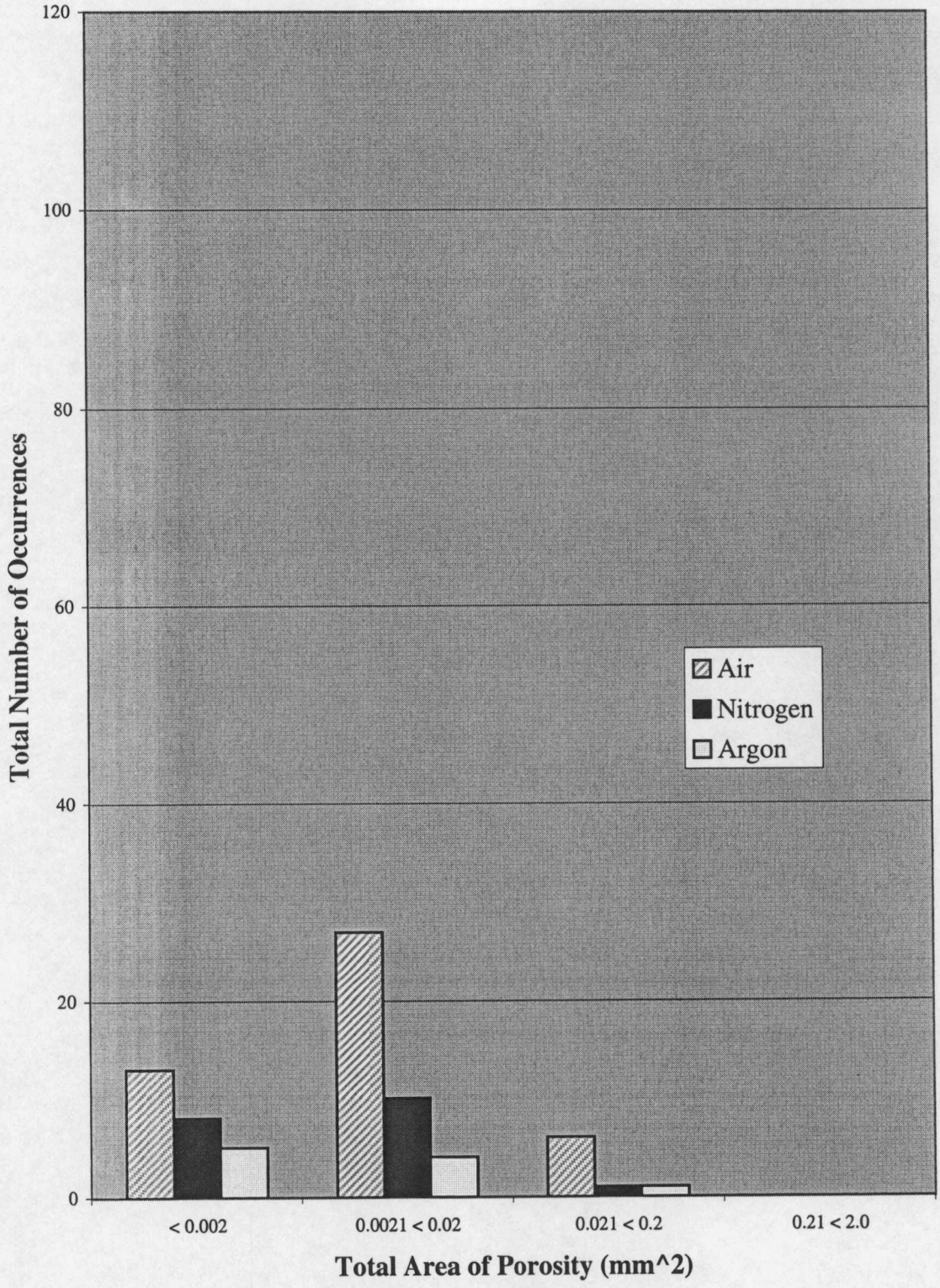


Figure 23: Porosity Comparison for Binder Coated Iron (BI) in Air, N_2 and Argon



D. Results – Width /Depth Ratios

Measurements of the width and depth of all of the cross-section samples were made using the Matrox Inspector image analysis software. The width measurements were made at the top surface of the sample between the inside edges of the heat affected zone (HAZ) in order to reflect the actual width of the melt zone. Typically, this is also the maximum width, as in the case of all of the air samples that are wide at the surface and narrow with depth. The width of the nitrogen and argon samples is nearly constant with depth, except for a slight necking that can be observed approximately one third of the way from the top. All depth measurements reflect the maximum depth of the melt zone and were made at the center of the sample between the surface interface and the maximum melt penetration depth.

The width, depth and width/depth ratios of the GI, TI and BI samples are given in tables 14-19 on the following pages. For the GI and BI samples, the air processed tracks are nearly twice as wide as the nitrogen or argon processed tracks. Even for the TI samples, the air track is wider than the other two by about 25%. The width of the nitrogen track is nearly identical to the width of the argon track for all samples GI, BI and TI.

Similarly, when examining the depths of the laser tracks, the nitrogen and argon cases show nearly identical results for all of the GI, BI and TI samples. Except for the binder coated iron, BI, the depth of the air track is somewhat less than the depth of the air track is somewhat less than the depth of the nitrogen and argon processed tracks. These observations can be clearly seen when one examines the width / depth ratios for all of the samples – GI, TI and BI. Consistently, the air tracks have a w/d ratio greater than one,

Table 14: Width and Depth of Gray Iron Cross-sections

	Width of Laser Track (mm)				Depth of Laser Track (mm)			
	(1)		(2)	(3)	(1)		(2)	(3)
Gray Iron	Air		Nitrogen	Argon	Air		Nitrogen	Argon
GI-7	2 75	GI-1	1.66	1 57	1.95	GI-1	2 40	2 39
8	2 70	2	1.73	1.46	1 87	2	2.37	2.35
9	2.70	3	1.58	1.75	1.88	3	2 01	2.08
10	2.60	4	1.33	1.46	1.63	4	1 97	1.89
11	2.40	5	1 48	1.43	1.46	5	1.80	1.84
12	2 49	6	1.44	1.48	1.47	6	1.77	1.83
Total	15 65		9.217	9.163	10.25		12.31	12 386
Avg	2.61		1 536	1 527	1.71		2.05	2.06
Std. Dev.	0.14		0 15	0.12	0.22		0.27	0.26
Min.	2 40		1.33	1.43	1.46		1.77	1.83
Max	2.75		1 73	1 75	1.95		2.40	2.39

Table 15: Width / Depth Ratio of Gray Iron Cross-sections

	Width/Depth Ratio for Laser Tracks			
	(1)		(2)	(3)
	Air		Nitrogen	Argon
GI-7	1.41	GI-1	0.69	0.66
8	1.44	2	0.73	0.62
9	1 44	3	0.78	0.84
10	1.60	4	0 68	0.77
11	1.64	5	0 83	0 78
12	1 70	6	0.81	0 81
Total	9.23		4 52	4 48
Avg.	1.54		0.75	0 75
Std. Dev.	0.12		0.06	0 09
Min	1.41		0.68	0 62
Max.	1.70		0.83	0 84

Table 16: Width and Depth of Titanium Coated Iron Cross-sections

	Width of Laser Track (mm)				Depth of Laser Track (mm)			
	(1)		(2)	(3)	(1)		(2)	(3)
TI on Iron	Air		Nitrogen	Argon	Air		Nitrogen	Argon
TI-7	2.60	TI-1	1 99	2.45	2.44	TI-1	2.54	2.46
8	2 65	2	2.43	2.26	2 17	2	2.49	2.63
9	2.76	3	2 01	1 98	2.30	3	2.36	2.45
10	2 72	4	2.01	1 99	2.15	4	2.26	2.30
11	2.69	5	2 09	2.26	2.20	5	2.24	2 27
12	2 57	6	2.14	1 92	2 11	6	2.28	2 13
Total	15.98		12.67	12 86	13.36		14.17	14.24
Avg.	2.66		2.11	2 14	2.23		2.36	2.37
Std Dev.	0 07		0.17	0.21	0.12		0.13	0.18
Min.	2.57		1.99	1 92	2.11		2.24	2.13
Max.	2.76		2 43	2.45	2.44		2 54	2.63

Table 17 : Width / Depth of Titanium Coated Iron Cross-sections

	Width/Depth Ratio for Laser Tracks			
	(1)		(2)	(3)
	Air		Nitrogen	Argon
TI-7	1 06	TI-1	0.78	1.00
8	1.22	2	0.98	0 86
9	1.20	3	0.85	0.81
10	1.27	4	0.89	0.86
11	1.22	5	0.93	1.00
12	1.22	6	0.94	0.90
Total	7.20		5 37	5.42
Avg.	1.20		0.90	0 90
Std. Dev.	0.07		0.07	0.08
Min	1 06		0 78	0.81
Max.	1 27		0 98	1 00

Table 18: Width and Depth of Binder Coated Iron Cross-sections

	Width of Laser Track (mm)			Depth of Laser Track (mm)		
	(1)	(2)	(3)	(1)	(2)	(3)
Bl on Iron	Air	Nitrogen	Argon	Air	Nitrogen	Argon
Bl-1	2.71	1 29	1 25	1 94	1 58	1.59
2	2 77	1 34	1 22	1 85	1.54	1 57
3	2 64	1 18	1.37	1 89	1.48	1.50
4	2 60	1 27	1.27	1 86	1 45	1.49
5	2 58	1 27	1 37	1 56	1 39	1 46
6	2 34	1.19	1.27	1 61	1 36	1.40
Total	15.65	7 53	7 74	10,70	8.81	9 02
Avg	2.60	1 26	1 29	1 78	1 47	1.50
Std Dev	0.15	0 06	0 07	0.16	0.08	0 07
Min	2 34	1.18	1.22	1.56	1 36	1.40
Max	2 77	1.34	1.37	1 94	1 58	1 59

Table 19: Width / Depth Ratios of Binder Coated Iron Cross-sections

	Width/Depth Ratio for Laser Tracks		
	(1)	(2)	(3)
	Air	Nitrogen	Argon
Bl-1	1.39	0.82	0 78
2	1 50	0 87	0 78
3	1 40	0 79	0 92
4	1.40	0 87	0.85
5	1 66	0.91	0 93
6	1 46	0 88	0 91
Total	8 81	5 14	5 16
Avg.	1.47	0 86	0 86
Std. Dev	0 10	0.04	0 07
Min.	1 39	0 79	0 78
Max	1 66	0 91	0 93

while the nitrogen and argon tracks are less than one. Since there was oxygen present in the air processed tracks, but not in the inert environment, it is reasonable to suggest that oxygen causes the air tracks to be so much wider. The reason for this behavior could be due to the oxygen plasma that diverted the laser beam energy over a greater surface area. Also, chemical reactions such as carbon oxidation, which is exothermic, might assist in generating a wider melt area.

E. Gas Chromatograph Results

An SRI 8610C gas chromatograph machine was used to determine the gas composition of the gas samples that were taken before and after the laser tracks were processed. Specially sealed 0 5 L capacity sample bags, made by SKC,were used to capture the gas from the outlet of the box through a tube that connected to the vent on the side of the box. After the box was purged for a half hour, and the oxygen analyzer showed that the oxygen content dropped to less that 1%, a plastic sample bag was attached to the tube to obtain a gas sample of the pre-process environment. This was done to verify that the environment contained only the shielding gas (nitrogen or argon) and no other gases The gas chromatograph can also be used to detect any oxygen that might be present in the processing environment Then, immediately after the laser track was made, another gas sample was taken of the post-processing environment. The gas chromatograph can also be used to detect any CO, or CO_2 produced, in air conditions, after the laser-processing step. There was not expected to be any CO or CO_2 produced under the inert conditions, since the oxygen was removed. This analysis was done to detect, if possible, any gases that were generated or evolved by the laser process and also to verify that the environment contained primarily the shielding gas (nitrogen or argon).

It is worth noting that the post-track bags filled up faster than the pre-track bags. This could be due to gas generation during the laser processing step which causes an increase in pressure within the box.

To analyze the gas samples using the gas chromatograph, a carrier gas is used along with the sample gas. The machine detects the gases. The Peak Simple software on the computer connected to the machine plots the peaks corresponding to the various gases that are present. The peaks correspond to millivolts that measure correlates to the concentration of the gases. Different gases peak at different points. If these points are known, then a gas can be identified. The area under the peak represents the amount of that gas present. Once all the peaks are identified, then the areas under the curve can be calculated and summed to determine the percentage of each gas present in each sample bag.

For this study, helium was used as a carrier gas for all samples, with the exception of detecting oxygen in the argon samples. When helium was used as the carrier gas, the oxygen and argon peak at the same place, therefore it was nearly impossible to detect the presence of oxygen for the gas samples taken in an argon environment. But if argon was used as a carrier gas for the argon gas samples, the oxygen peaks could be separated out. And, if helium was used as a carrier gas for the argon gas samples to detect the presence of other gases, a reasonable estimate of the percentages of each gas could be obtained. The results of the gas chromatograph analysis are shown in Table 20.

The results show that in all cases the concentration of oxygen in the box, although not completely eliminated by purging, was reduced to less than 1%. This is consistent with the readings given by the oxygen analyzer as the experiment was proceeding. It is

Table 20 : Gas Chromatograph Results

	Nitrogen purge gas samples			Argon purge gas samples			
Conditions	Gas Detected	Peak Area	Approx %	Conditions	Gas Detected	Peak Area	Approx %
Gray Iron Pretrack	O2	98.554	0 72%	Gray Iron Pretrack	O2	132 588	0 84%
	N2	13681 78	99 28%		Argon	15647.51	99 14%
					CO	1 764	0.01%
					CO2	1.948	0.01%
					H2	0.141	0.00%
Gray Iron Postrack	O2	56 424	0.41%	Gray Iron Postrack	O2	118.011	0.75%
	N2	13739.60	99 58%		Argon	15762 66	99 87%
	CO	0 429	0 00%		CO	0.7	0.00%
	CO2	1 476	0 01%		CO2	2 945	0 02%
					H2	0 241	0.00%
Ti on Iron Pretrack	O2	56 77	0.41%	Ti on Iron Pretrack	O2	144 976	0.92%
	N2	13743 53	99 58%		Argon	15696 16	99 44%
	CO	0 26	0 00%		CO	0.681	0 00%
	CO2	0 448	0 00%		CO2	2.016	0 01%
					H2	0 136	0 00%
Ti on Iron Postrack	O2	38.516	0 28%	Ti on Iron Postrack	O2	145.718	0.92%
	N2	13583 02	99.71%		Argon	15472.26	98 03%
	CO	0.208	0 00%		CO	0 631	0 00%
	CO2	1 097	0 01%		CO2	2.53	0.02%
	H2	0 215	0 00%		H2	0.132	0 00%
Binder on Iron Pretrack	O2	161 896	0 97%	Binder on Iron Pretrack	O2	137.878	0.90%
	N2	15879.87	94 90%		Argon	18151 61	95 75%
Binder on Iron Postrack	O2	149 732	0.88%	Binder on Iron Postrack	O2	140.017	0 91%
	N2	16389 69	96 86%		Argon	18233.14	98 07%
	CO	1 367	0 01%		CO2	188.284	1.01%

Helium carrier gas was used

Helium carrier gas used (except for O2)
Argon carrier gas used to detect O2

difficult to remove all of the air from the box and replace it completely with the inert gas. Even with the half hour purge time allowed, there were still trace amounts of oxygen left in the box. Although oxygen was present, the quantity is not likely to have significantly affected the results

As for the shield gas (nitrogen or argon) concentrations, they were consistently found to be greater than 98%, which is to be expected The gas chromatograph also detected trace amounts of carbon monoxide (CO) and carbon dioxide (CO_2) as well as hydrogen (H_2) in some cases The concentrations, however, were nearly zero. In fact, the maximum percentage recorded was 0.02%. With such a small amount, it was difficult to determine if the gases were actually present or if the concentration was within the experimental error of the machine. Also, given the fact that there were traces of CO and CO_2 in both the pretest and posttest samples, it was impossible to determine if either of these gases was generated during the experiment Theoretically, in a nitrogen or argon environment, in the absence of oxygen, there would be no CO or CO_2 generated.

For the analysis of the argon samples, two separate analyses had to be made to determine the gases present. First, helium was used as a carrier gas to detect the argon, CO, CO_2, and H_2 Since this requires two samples to be analyzed for the argon cases, the percentages do not add up to exactly 100 percent.

F. X-ray Diffraction Results

X-ray diffraction analysis was performed in order to detect the presence of nitrides, oxides or carbides that may have formed as a result of the laser processing. If any are detected, that is supporting evidence that the chemical reactions under investigation have

taken place. The samples to be analyzed were not cleaned before being analyzed. The procedure used for the X-ray diffraction analysis was as follows.

Using the Philips Norelco diffractometer, the incident beam divergence slit was narrowed so that the beam just covered the narrowest of tracks, and a scan was done on the surface of each individual track with the divergence slit. The scans were done from 20 to 100 degrees 2Theta in steps of 0.05 degrees with 5 seconds counting time per step. Additionally, a scan was run on the unprocessed gray cast iron for comparison. However, that scan was done with variable divergence slit and with the beam covering a 0.5" wide area of the sample. A photo of the diffractometer is shown in Figure 24.

The x-ray analysis was done on both a gray iron (GI3) and a titanium on iron (TI3) sample processed in air, nitrogen, and argon environments. The binder on iron (BI) samples were not x-rayed. The x-ray results on the GI3 and TI3 samples showed that most of the iron is ferrite. There was evidence of retained austenite as well. There was evidence of FeC, Fe_5C_2, and nonstoichiometric Fe_3C of varying concentrations in both GI

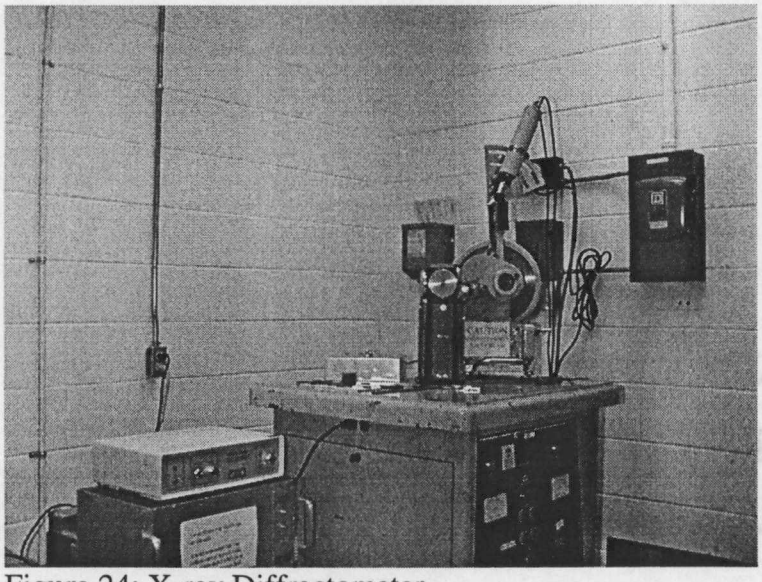


Figure 24: X-ray Diffractometer

and TI samples in all gas environments. The profile for GI3-1, gray iron laser melted in air shows several large peaks, which are unidentified but assumed to be carbides. The nitrogen and argon tracks also peak at this location, but they are not as high. The same is true for the TI3 sample in all gas environments; the unidentified peaks are small and assumed to be carbides. The x-ray analysis report does not mention the detection of any oxides or nitrides in any of the samples. Several typical x-ray profiles are shown on the following pages. The rest of the profiles and the report, can be found in Appendix D.

Also, a sample of the titanium precursor that was sprayed onto the gray iron was placed in the x-ray diffractometer to check for titanium oxides. It was believed that since titanium is so reactive with oxygen, the sprayed sample would begin to oxidize in ordinary air if left to sit for a day. If this happens, oxygen can be introduced into the laser processing environment in the form of oxides. It is possible that these oxides could be subsequently reduced and the oxygen freed to react with something else, such as carbon Or, the other possibility is that the oxides will remain intact and be left behind on the surface or in solid solution. Most likely, however, they would be involved in some sort of chemical reaction.

The results of the x-ray diffraction analysis indicate that Ti_2O, $Ti_{10}O_{19}$ and Ti_4O_7 are present. These are all metastable titanium oxides. The plots of intensity counts for the analyses are shown in Figures 25-28.

G. SEM Analysis

Scanning Electron Microscopic (SEM) analysis was performed on the titanium alloyed samples to detect the presence, distribution, and concentration of titanium in the laser processed sample. The Super IIIA model made by International Scientific

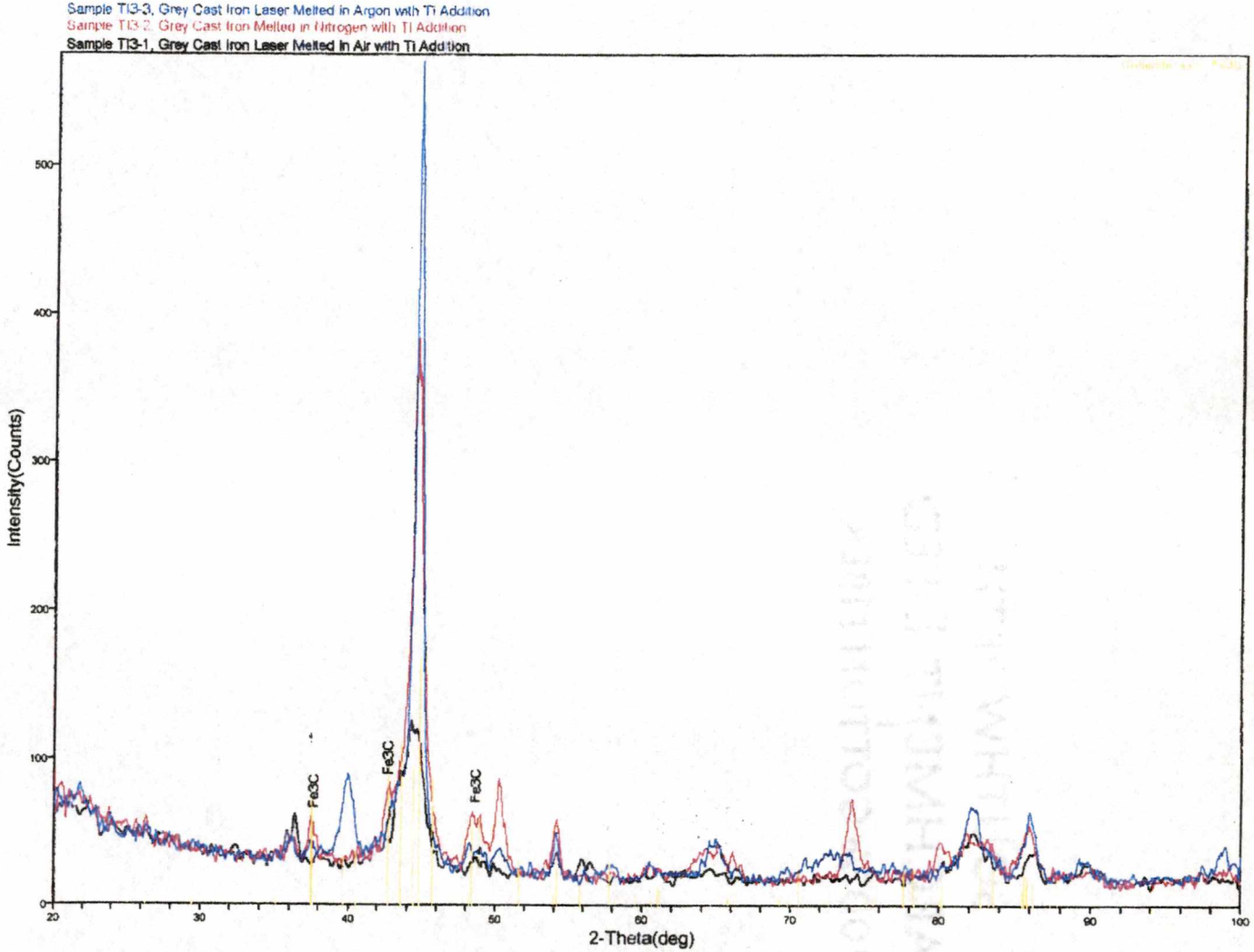


Figure 25: X-ray Trace of Titanium Alloyed Iron

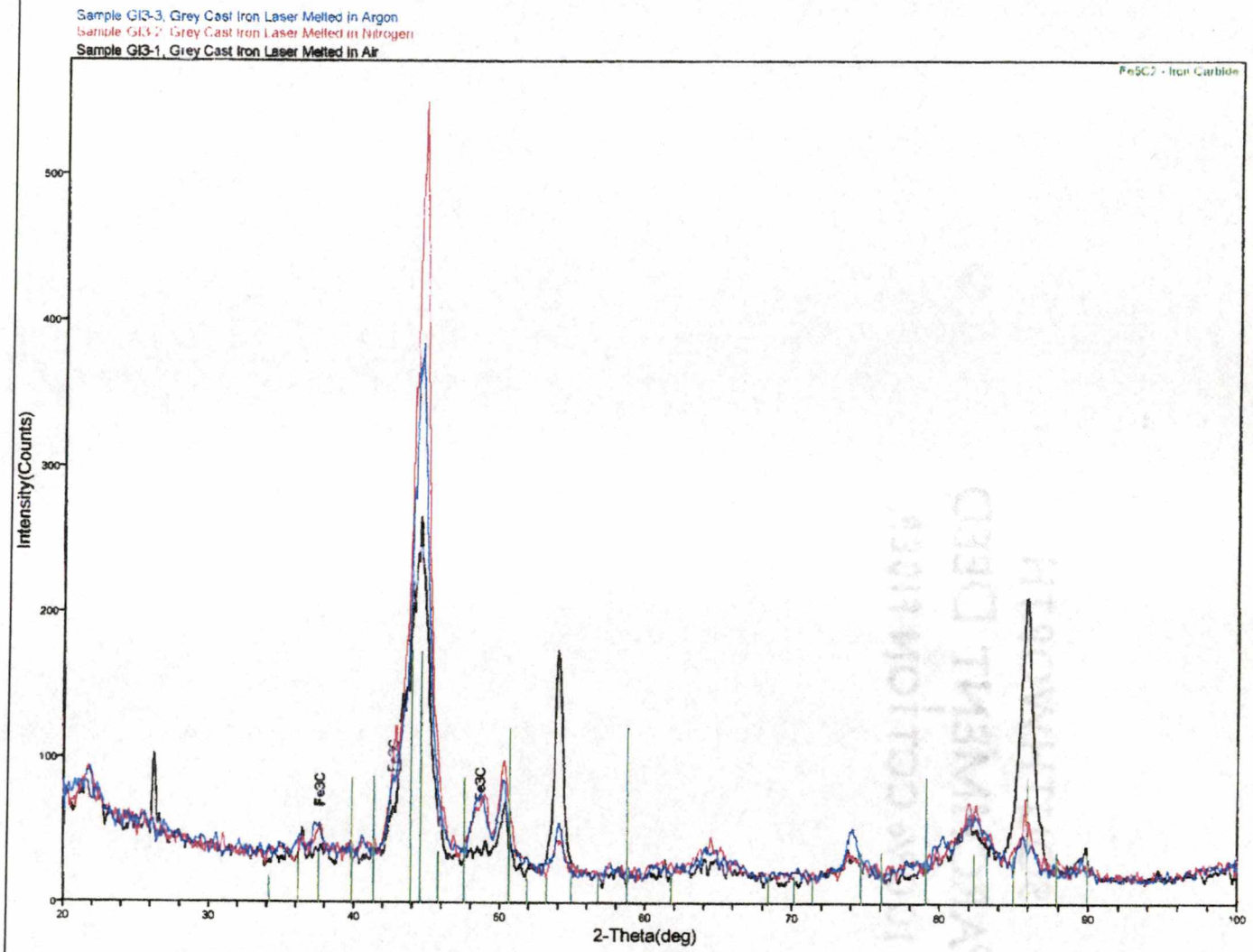


Figure 26: X-ray Trace of Gray Iron Detecting Fe_5C_2 Phase

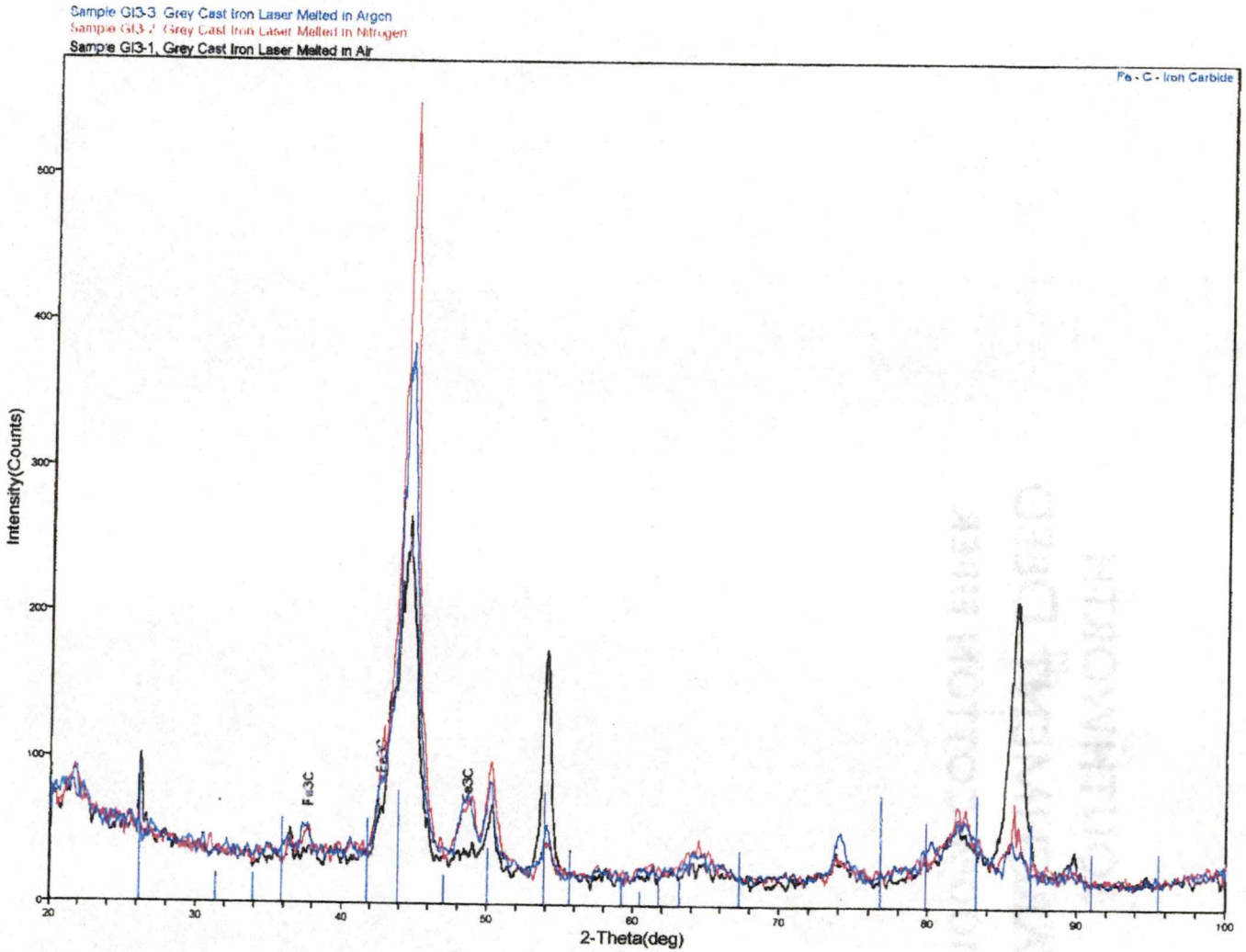


Figure 27: X-ray Trace of Gray Iron Detecting FeC Phase

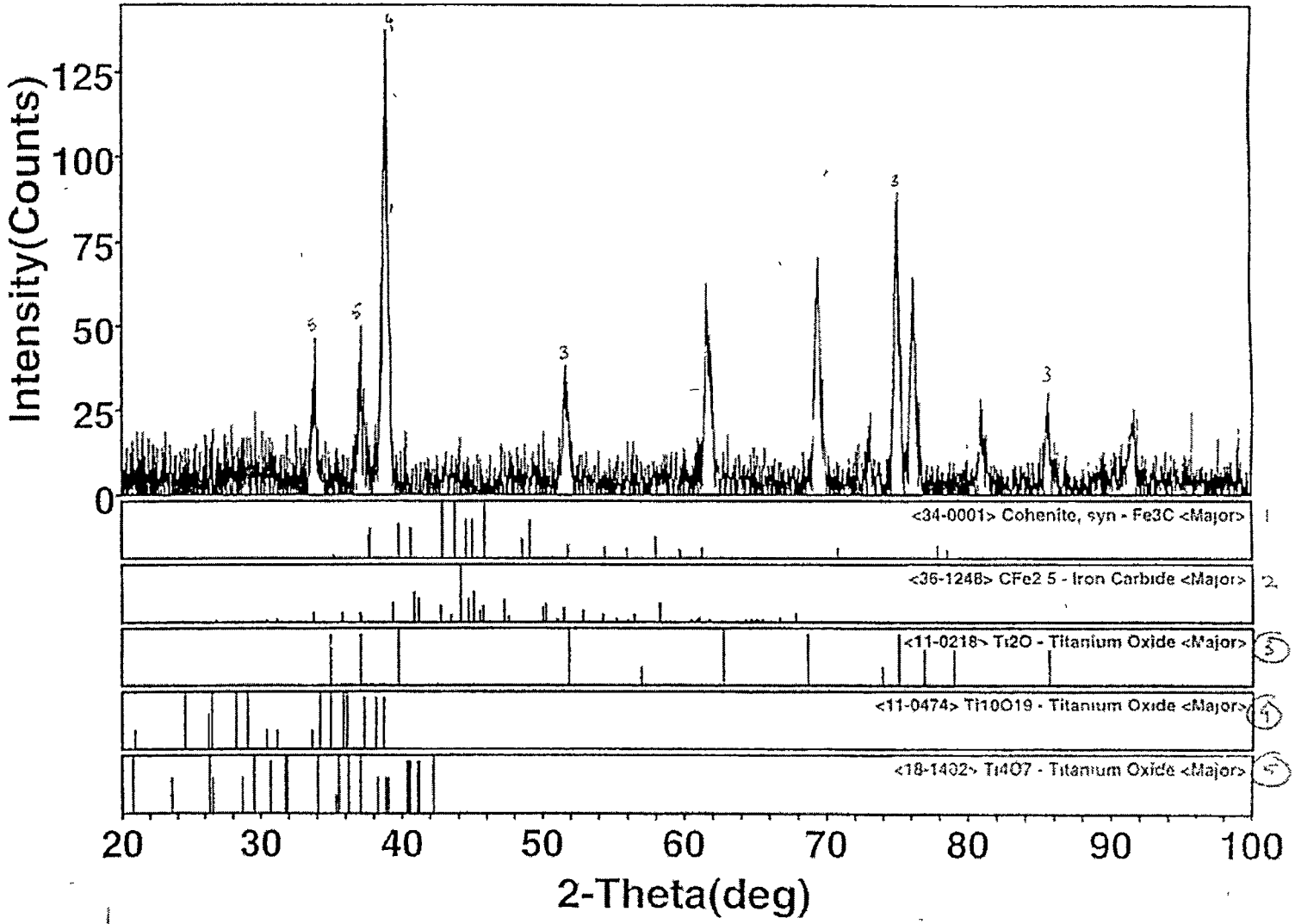


Figure 28: X-ray Trace of Titanium Powder

Instruments was used. The accompanying analysis software was Iridium v.5.14 made by IXRFSystems. A picture of the SEM is shown in Figure 29.

The SEM is a highly sophisticated microscope that can be used for material elemental analysis. The SEM with spectroscopic capabilities can detect the presence and concentration of certain elements in a material sample. A small tungsten filament gives off electrons like a light bulb radiates light. These electrons flow through a small aperture and down a tube through another aperture lens and then strike the material. The electrons reflect off the sample with a particular speed, which corresponds to a certain voltage, depending on the element that the electrons strike. A detector 'catches' the electrons and assimilates the information relating voltage to elemental concentration.

Using the SEM as an analysis tool, the samples laser-alloyed with titanium were investigated for the presence and concentration of titanium. If the titanium is oxidizing and forming Ti_xO_y compounds, which are solids, they will be left behind as alloys in the iron. While the SEM cannot detect oxygen (or other elements naturally existing as a

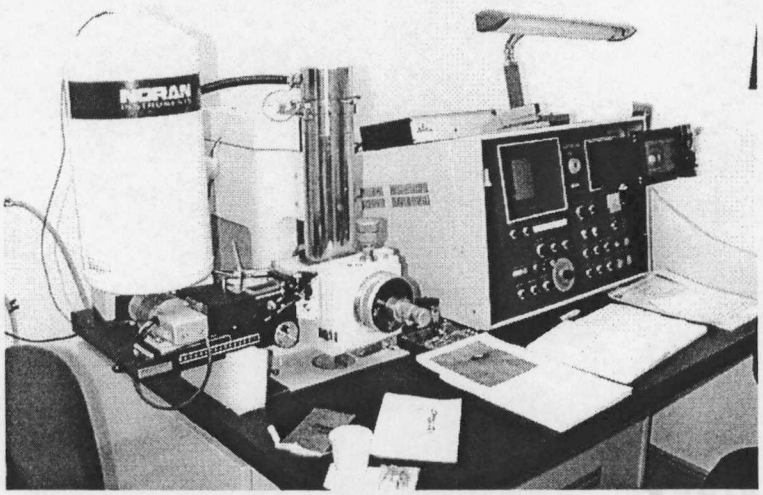


Figure 29: Scanning Electron Microscope

diatomic gas), or compounds, it can detect elemental titanium.

The SEM analysis consisted of making multiple point measurements in the melt zone of a typical slice of the titanium alloyed iron laser processed under air, nitrogen, and argon conditions. The concentration of titanium, if detected, can be noted. Also, the relative distribution can be inferred by taking multiple points and using the SEM to map a picture of the titanium distribution. The results of the SEM work are summarized in Table 21 below.

The SEM analyses of the air, nitrogen, and argon tracks of sample TI4 indicate that the concentration of titanium in air processed samples ranges from 0.2 – 2.4 % and generally increases with depth. Analysis points 1- 6 are taken with increasing depth from the surface of the track. Titanium concentration in the nitrogen processed samples ranges from 0.7 – 3 1 % and does not necessarily increase with depth. Titanium concentration in the argon processed samples ranges from 0.3 – 2.4 % and does not necessarily increase

Table 21: SEM Results for Titanium Concentration in Air, Nitrogen and Argon Tracks

		Track Ti4-1 Air	Track Ti4-2 Nitrogen	Track Ti4-3 Argon
		Conc. Wt %	Conc Wt %	Conc Wt %
1	Ti	0 234	3 13	0 447
	Fe	99 766	96 87	99.553
2	Ti	0 975	0 676	0 203
	Fe	99 025	99 324	99 797
3	Ti	0 61	1 852	0 458
	Fe	99 39	98 148	99 542
4	Ti	1 153	3 042	2 471
	Fe	98 847	96 958	97.529
5	Ti	0 844	1 904	1 618
	Fe	99 156	98 096	98 382
6	Ti	2 394	1 472	1.863
	Fe	97 606	98 528	98.137
Base	Si	2 383	Accuracy 3%	
	Mn	0 618	Sample Ti4 used for analysis	
	Fe	96 999	6 points taken per track	

with depth Given that the accuracy of the analysis is 3 % it is reasonable to conclude that the percentage of titanium alloyed into the iron in any of the gas environments is approximately 2 %.

In an effort to determine if the concentration of titanium was greater inside the surface of the pores, additional SEM analyses were performed. Also, a microprobe analysis was performed If the concentration of titanium inside the pores is greater than in the melt zone, that is evidence that some of the pores are caused by titanium. The titanium might have been a gaseous compound such as TiO during melting, which precipitated to a solid at room temperature. The gas cannot be directly detected in these circumstances; so evidence must be inferred. For the SEM analysis, samples Ti7 and Ti10 processed in air were used. These samples were chosen because they had several large and small pores The results of these supplemental analyses are shown in Table 22.

Table 22: SEM Results - Investigating Titanium in Pores

		TI7-1 Air			TI10-1 Air
# Description	Element	Conc Wt %	# Description	Element	Conc Wt %
1 Lg Pore	Ti	2 323	Ti Std	Al	5 248
	Fe	97 677		Si	6 252
2 Lg. Pore	Ti	2 443		Ti	85 156
	Fe	97 557		V	3 345
3 Sm Pore	Ti	0 952	1	Al	1.724
	Fe	99 048		Si	4.745
4 Sm Pore	Ti	2 668		Ti	3 138
	Fe	97 332		Fe	90 394
5 Melt Zone	Ti	3 662	2 Lg Pore	Ti	11 179
	Fe	96 338		Fe	88 821
6 Sm Pore	Ti	2 813	3 White Blob	Ti	10 987
	Fe	97 187		Fe	89 013
7 Base Iron	Si	3 022	4 White Blob	Ti	10 037
	Mn	0 652		Fe	89 963
	Fe	96 326	5 Melt Zone	Ti	2 029
				Fe	97 971
			Base Iron	Si	3.87
Tracks Ti7, 10 in air used for analysis				Fe	96 13

For the concentration of titanium in the various pores of samples TI7 and TI10, the SEM analysis shows that for sample TI7, the titanium concentration ranges from 1-2.8 %, which is consistent with (slightly less than) the concentration of titanium in the melt zone. The melt zone concentration for this sample was 3.6 %. However, for sample TI10, several locations had titanium concentrations greater than 10 %, while the concentration of titanium in the melt zone was found to be 2 %. This suggests that, in some pores, additional titanium was present. Figures 30-34 show the locations of the SEM analyses performed on samples TI4, TI7 and TI10.

Further analyses into titanium concentrations in the pores were performed on another sample using an SEM microprobe. The analysis and results of which are subsequently described.

H. Microprobe Analysis

In order to determine the presence and/or concentration of titanium in the pores, a Cameca Camebax 286 Microprobe was used to detect the element. Also referred to as EPMA, electron probe microanalysis, the instrument uses an electron beam to excite x-rays in the sample. The x-rays are diverted to a crystal and then to detectors in the wavelength dispersive spectrometer. The detector processes the x-rays to determine which elements are present. Different elements will have different x-ray spectra. The electron beam is generated by an electron gun that uses a tungsten filament. The beam is accelerated through two lenses and an aperture towards the sample. The microprobe is similar to the SEM, but the microprobe can focus the beam on a smaller area of the sample. A photo of the equipment in use is shown in Figure 35.

Image: Ti4-1.imx

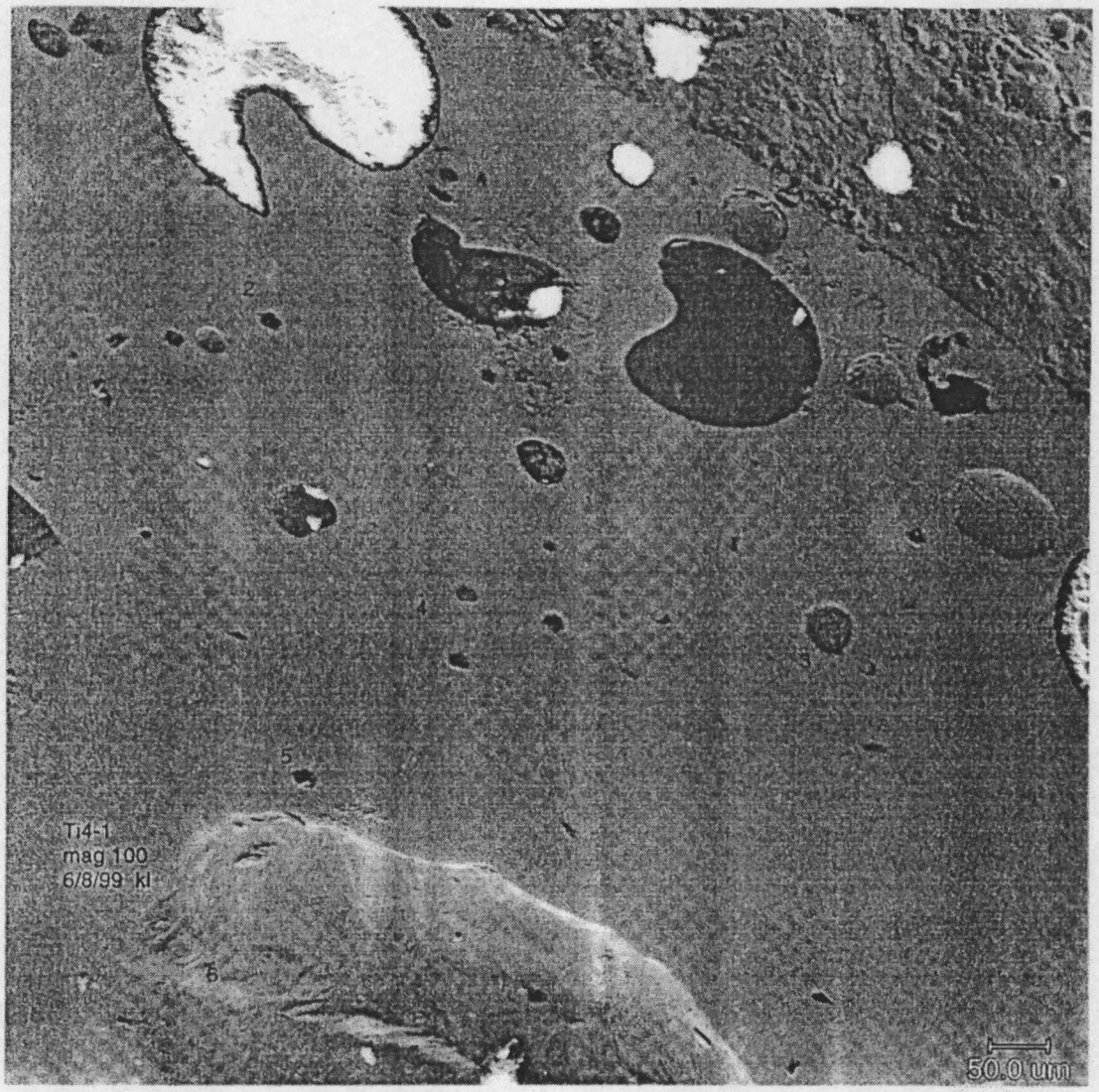


Figure 30: SEM Map for Sample TI4-1

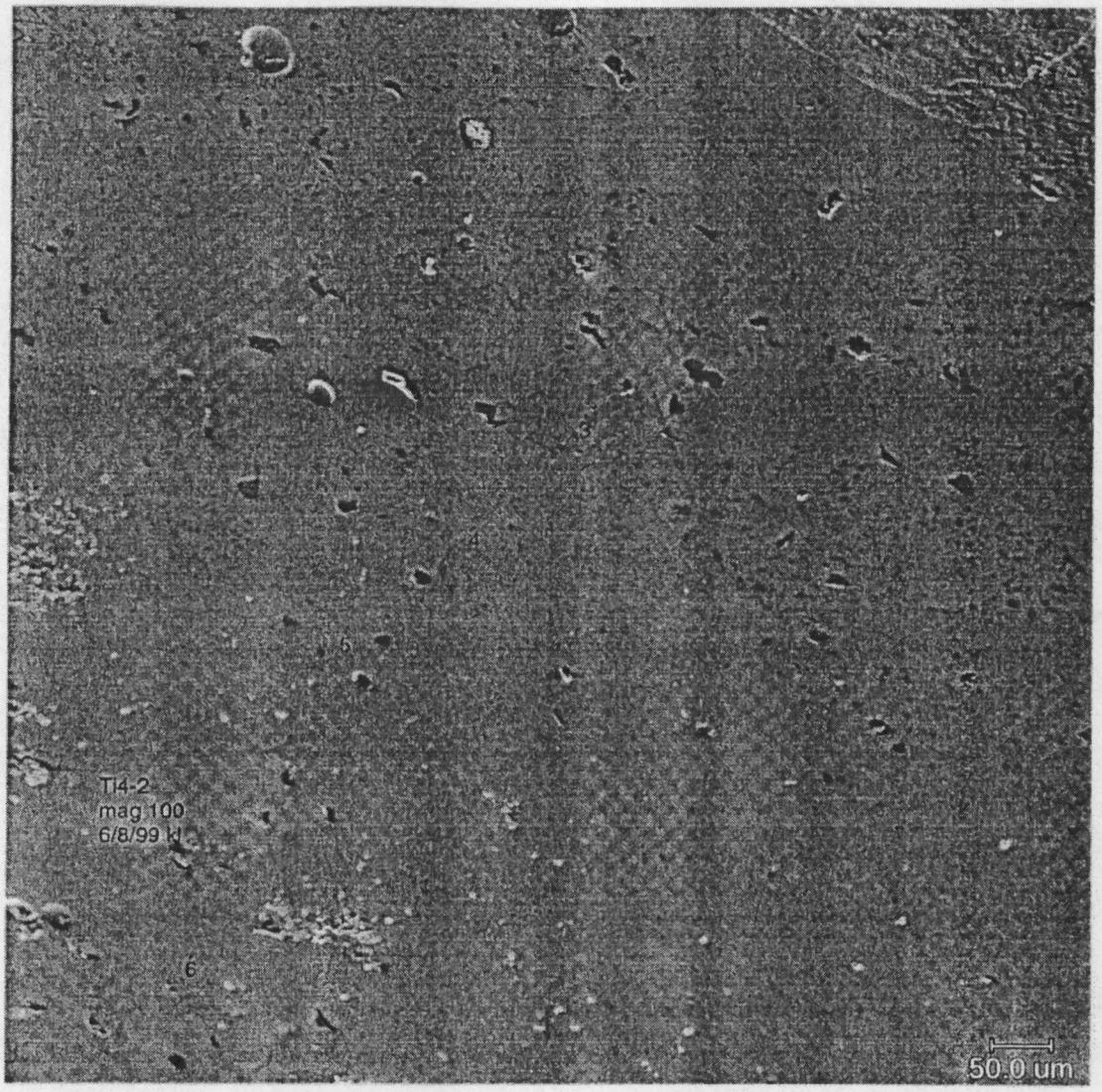


Figure 31: SEM Map for TI4-2

Image: Ti4-3-imx..imx

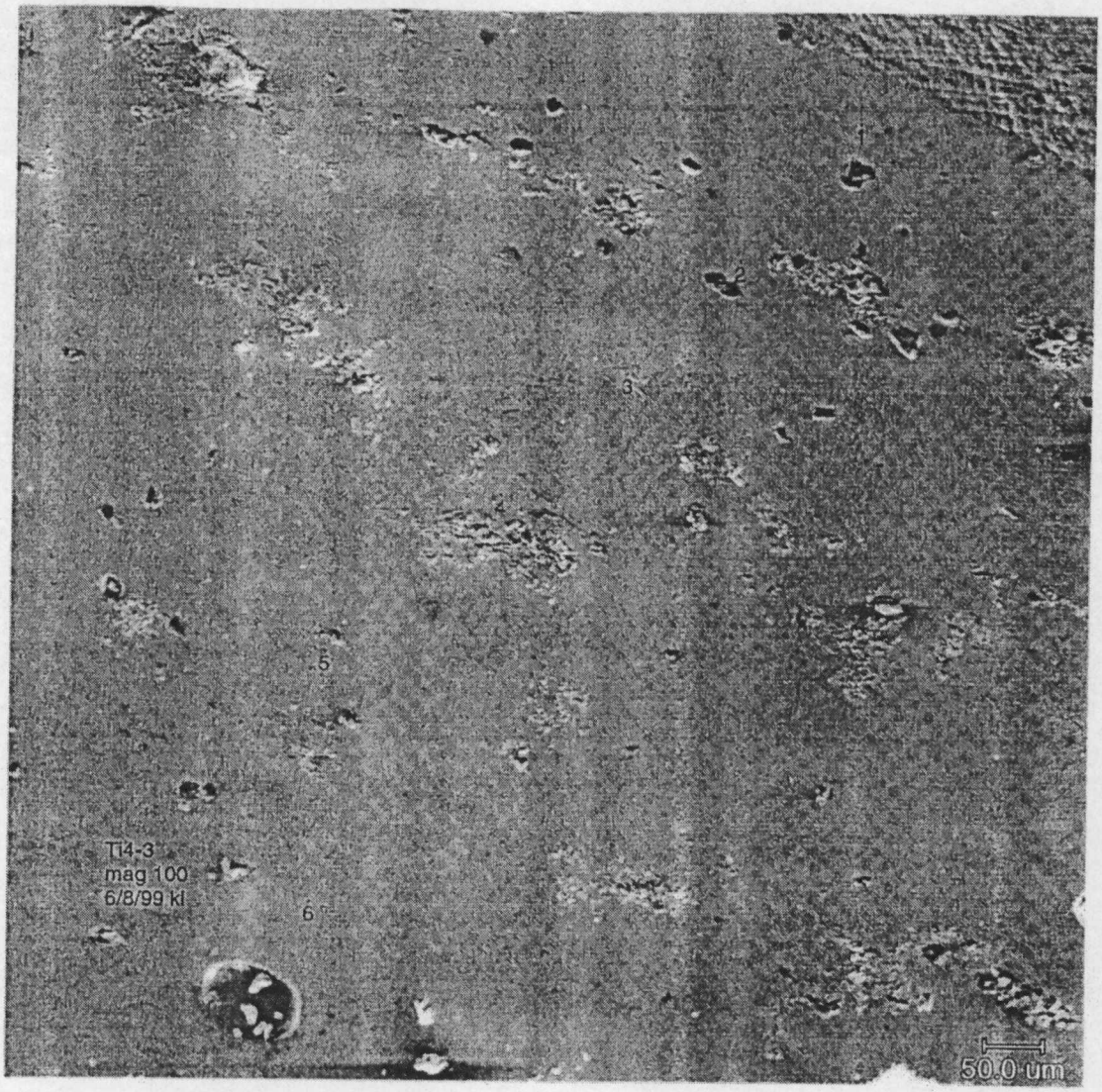


Figure 32: SEM Map for TI4-3

Image: Ti7.imx

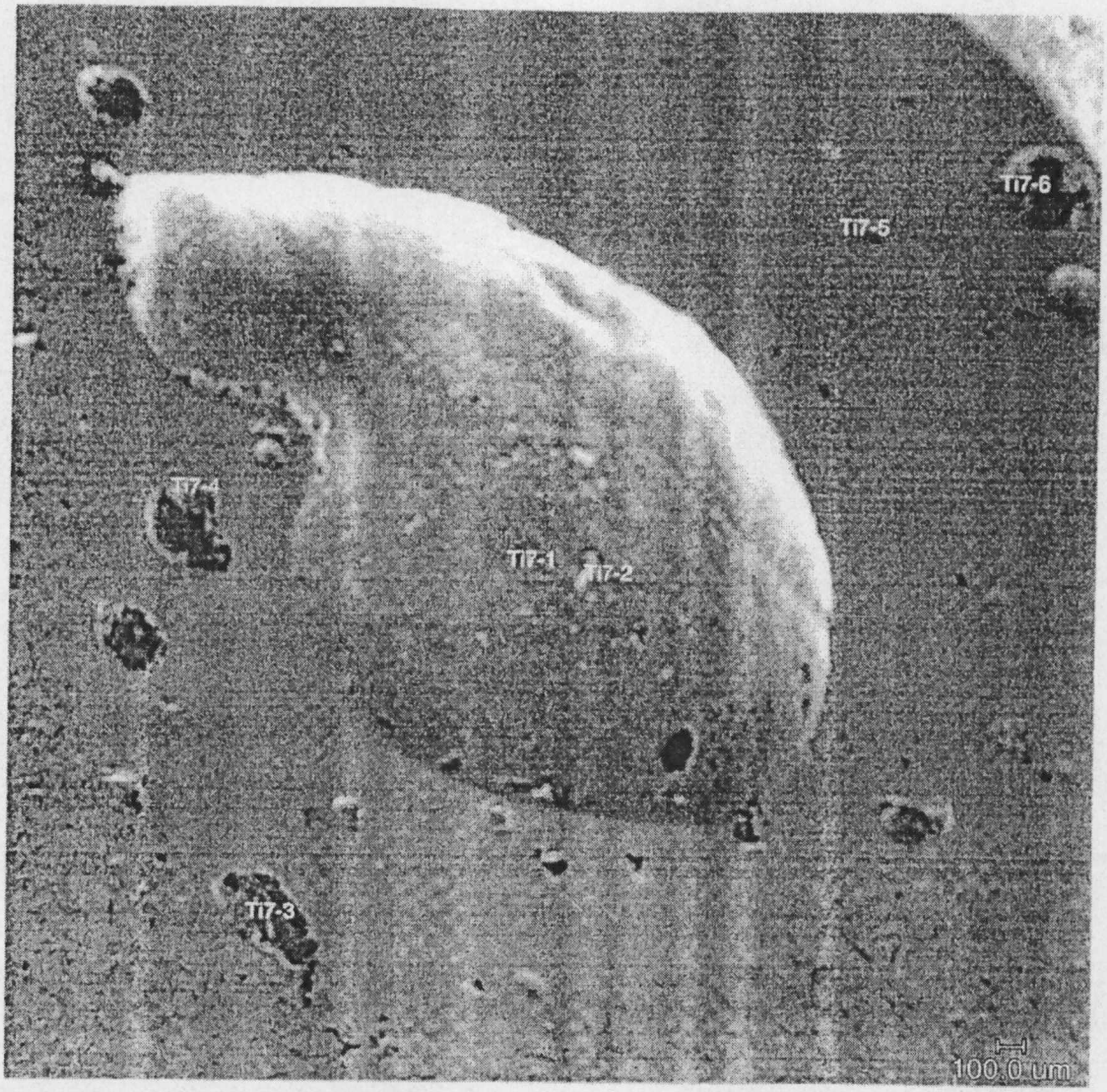


Figure 33: SEM Map for Sample TI7

Image: Ti10LP.imx

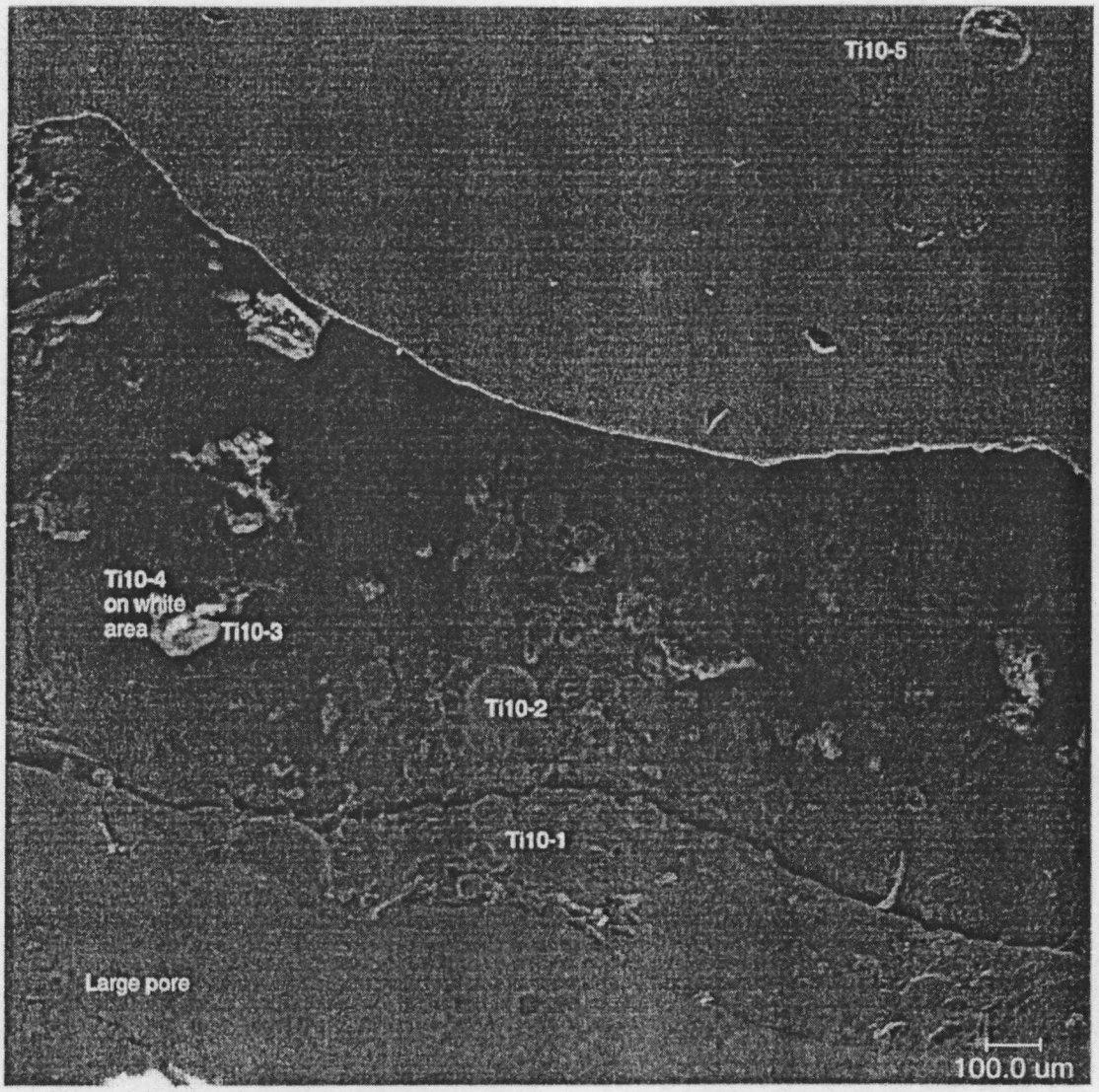
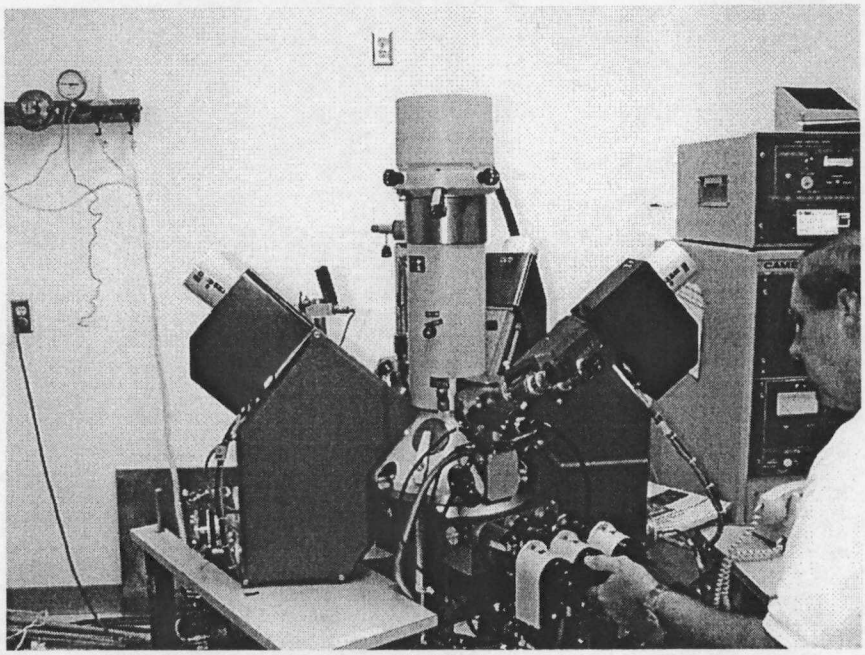


Figure 34: SEM Map for Sample TI10


Figure 35: Cameca Camebax 286 Microscope

A titanium alloyed sample (TI9-1) laser alloyed in air was chosen for this analysis. To calibrate the machine, a standard piece of pure titanium was used. Once calibrated, the beam was focused on the sample to be analyzed. A coordinate system was set up on the sample in order to locate specific points to analyze. Various sites within the large pore, as well as several small pores, were analyzed for titanium concentration. Some data points were also taken in the melt and heat affected zones. A photo of sample TI9-1 with the coordinate points and the data points is shown in Figure 36.

The concentration of titanium ranged from 0-25% in some of the pores. Typically, the higher concentrations of titanium were found in smaller pores. The large central pore had only trace amounts of titanium detected – less than 1%. The melt zone had approximately 2-3% titanium. There was no trace of titanium in the partially melted zone (PMZ), which was to be expected since it did not completely melt; therefore it could not be alloyed with titanium.

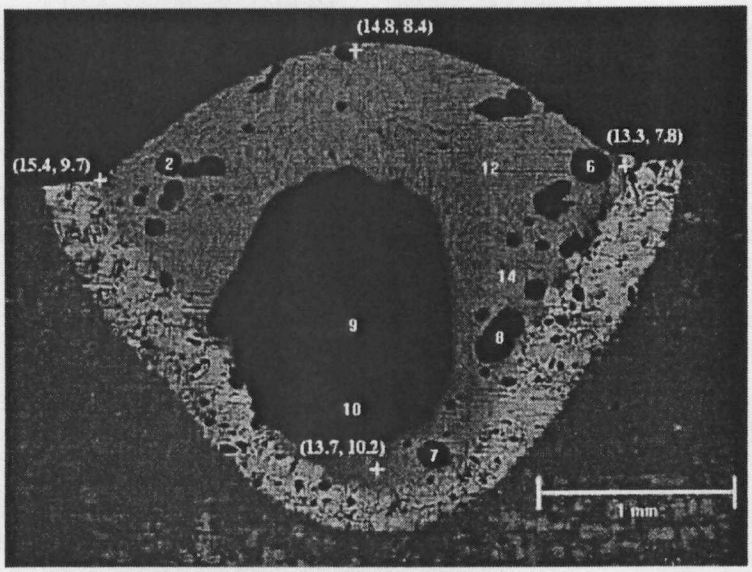


Figure 36: Map of Data Points for Microprobe Analysis of TI9-1

The results of the microprobe analyses are shown in Table 23.

The 2-3% titanium found to be alloyed in the melt zone was a reasonable hypoeutectic amount to expect. 14 - 25% titanium, however, was hypereutectic, or a supersaturated condition. The eutectoid point of a system occurred at 14% titanium for a binary Fe-Ti system. Titanium was present in greater amount at some locations, and some form of it may precipitate out as the metal solidifies. Whether this was pure titanium or some titanium compound, was presently unknown. It was possible that the precipitate was left behind as a residue that can be rinsed off during the polishing process. This would explain why the largest pores were free from titanium residue. The large pores were easily rinsed out.

Another possibility was that titanium or a titanium compound was degassing at the time it was trapped in the metal. Upon solidification, the compound may have undergone a phase change into a solid that created a residue on the inside surface of the small pores.

Table 23: Microprobe Results on Sample TI9-1

Test Number	X	Y	Z	% Ti	Description
1	10.2	40 1	3 9	99.77%	Titanium Standard
2	15.1	9.35		24.50%	Inside Surface of Small Pore
3	10.2	40.1	3.9	97.00%	Ti std (beam current to 15 namps)
4	10 2	40.1	3.9	100.30%	Titanium Standard
5	15.1	9.35	3.04	25.30%	One of Smaller Pores (repeat of 2)
6	13 4	7.95	2.98	14.89%	Inside Surface of Small Pore
7	13.08	9.65	3.05	3 60%	Inside Surface of Small Pore
8	13 2	8 9	3 01	2.25%	Inside Surface of Small Pore
9	14 2	9 2	2 75	0.71%	Inside Surface of Large Pore
10	13.9	9 15	2.7	0.33%	Inside Surface of Large Pore
11	10.2	40 1	3.9	99.30%	Post Run Titanium Standard
12	13.9	8.2		2.81%	Melt Zone
13	15.15	9.95		0.005%	Heat Affected Zone
14	13.45	8.65		3.01%	Melt Zone
After the sample was polished down to decrease the depth of the large pore					
100				99 83%	Titanium Standard
101				99 96%	Titanium Standard
102	11 4	12.1	3 03	0 8%	Large Pore
103	11.1	12 52	3 13	24 6%	Small Pore
104	11 2	13 24	3.14	18.4%	Another Small Pore
105	10 85	12.28	3.2	2.5%	Melt Zone
106	10.75	11.78	3.2	0.04%	HAZ
107	11.85	12.7	3.14	2.2%	SP3
108	10 85	12.1	3.15	9.9%	SP4
109	11.6	12.3	3.1	0.23%	LP2
110	11.62	11.71	2.94	1 9%	LP3
111	12.35	13.24	2 98	14 6%	SP5

The present analysis is inconclusive. Some techniques to sample the inside pore surface prior to the grinding and polishing operation would need to be devised in order to make certain that the residue is not rinsed off.

It is also possible that the gas trapped to form the pore remains in a gaseous state upon solidification. In this case, the gas escapes undetected when the cross-sectional sample is cut. It is virtually impossible to detect what type of gas it might have been.

I. Results – Summary of Observations

- Air samples have greater porosity than nitrogen and argon samples on gray iron, titanium on iron, binder on iron.
- The results of the nitrogen and argon samples are nearly identical; therefore, if an inert environment is required, the less expensive nitrogen can be used instead of argon.
- Air samples were consistently wider and slightly deeper than nitrogen or argon samples, possibly due to a plasma effect with oxygen.
- Binder only samples do not have significantly more porosity than the gray iron samples.
- Titanium samples in air have ~2% titanium alloyed into the melt zone.
- The titanium concentration in the pores, large and small, varied from 0-25%, which suggests that titanium contributes to the porosity.

IV. Conclusions

The results of this experiment indicate that porosity in laser melted gray iron is difficult to eliminate completely. Under the current conditions, porosity is reduced in an oxygen-free environment. However, the attempt to use titanium as a deoxidizer failed to reduce porosity, which can be caused by a number of things. Basically, some general conclusions can be made about how an oxygen or oxygen-free environment, addition of titanium, and experimental conditions can contribute to porosity. Sources of porosity include dissolved gases such as nitrogen or oxygen, shrinkage, vaporized elements, or gases produced by oxidation within the melt zone. It is evident that in some situations porosity is decreased, while in others it increases. The following general conclusions can be made.

A. Primary Conclusions – Oxygen Effects

- Most of the porosity in the air samples is caused by carbon monoxide or carbon dioxide gas.
- Oxygen is the primary factor contributing to porosity in laser melted iron in air.
- Oxygen-free environments, such as nitrogen or argon, reduce the porosity.
- The oxygen content, 1% max by volume in the nitrogen and argon environments detected by the oxygen analyzer and gas chromatograph, does not significantly contribute to porosity.
- Not all porosity is attributable to oxygen in air.
- Trace porosity in the air samples is caused by shrinkage, dissolved gas (nitrogen, oxygen, argon) or vaporized elements.

B. Secondary Conclusions – Titanium Effects

- The greatest contributing factor to the porosity was, unexpectedly, the titanium because it is not an effective oxidizer under the conditions used in this study.
- Titanium contributes to porosity directly or indirectly through chemical reactions caused mainly by carbon monoxide, carbon dioxide or a reaction with titanium producing a gas.
- Titanium coating oxidizes in the atmosphere into metastable Ti_xO_y compounds prior to processing, which can provide an additional source of oxygen.
- The precise amount of titanium could be a factor in the deoxidation and pore formation process.
- Chemical reactions of the Fe/C/O/N/Ti combination contribute the greatest amount of porosity.
- For the Fe/C/O/N/Ti combination, it is possible that intermediate metastable compounds are formed then reduced or oxidized to produce other gases.
- Intermediate reactions could be taking place where nitrogen, carbon monoxide or carbon dioxide gases are possible products. These types of reactions might include:

$$2TiN + 2C \rightarrow 2TiC + N_2$$

$$TiC + 2O_2 \rightarrow CO_2 + TiO_2$$

$$TiO_2 + 3C \rightarrow TiC + 2CO$$

$$TiN + O_2 \rightarrow TiO_2 + 1/2N_2$$

C. Other Conclusions

- Surface preparation is important to prevent porosity caused by contaminants.
- Sandblasting and rinsing with acetone removed surface impurities that could cause porosity (Preliminary samples were wire-brushed only; porosity results were erratic).
- Laser processing conditions may have an effect. It might be possible to adjust the laser power and speed settings to allow bubbles to escape from the melt pool.
- The binder, or hydrocarbons or oxides in binder, does not significantly contribute to porosity in air or argon.
- The binder appears to be reactive with nitrogen to increase porosity in titanium on iron (TI) samples and binder on iron (BI) samples.
- Blowing the shielding gas directly at the melt zone can entrap it and cause more porosity, such as in GI1-6, TI1-6 samples.

These are a generalized set of conclusions based on the current experimental work, preliminary experimental work, and other research efforts into this field. The possibility of producing porosity free laser melted iron surfaces is realistic provided that the conditions are optimized. Ambient air does not provide the best environment because of the oxygen content. As for an oxygen-free environment, given that nitrogen and argon produce similar results, it is reasonable to conclude that pure nitrogen is preferable because it is the cheaper gas. Also, a side effect of using nitrogen is more retained austenite after the self-quenching process, which could contribute to greater hardness if

subsequently supercooled. It is also likely that some nitrogen is dissolved into the iron. Since the temperature range is at least 500°C during laser processing, the resulting microstructure is similar to nitriding.

Deoxidizing the iron with titanium does not eliminate porosity under the conditions used in this study Titanium makes the situation worse, possibly due to the production of a Ti_xO_y titanium oxide gas, additional CO_2, CO, or nitrogen gas. Given that it costs time and money for the extra step of using the titanium, it is difficult to rationalize reasons to attempt to deoxidize the iron with titanium. However, it is theoretically possible that the amount of titanium used, relative to the other constituent elements, could alter the results.

V. Recommendations

Although some results were unexpected since some experimental work did not proceed as anticipated, the basic investigation into porosity in laser melted iron produced useful information. Since it is not possible to actually sample the gas inside the pores directly to determine its composition, indirect methods must be used and simplifying assumptions must be made. Some of these assumptions pertained to the laser processing conditions like power, speed, beam size and energy density. For this study, they were assumed to be optimal. Also, the reaction chemistry in the melt zone was assumed to be a system of reactions where only two reagents combine to form a single product. The possibility of intermediate reactions or decompositions was not addressed. The actual chemical system would be more difficult to model and numerical methods should be considered for equilibrium and non-equilibrium compositions The iron sample preparation and handling prior to laser processing is critical to prevent contamination by impurities. With this information in mind, recommendations for future work in this area are as follows.

A. Modify the Processing Conditions

- The laser power, speed, focus could be further varied to optimize the processing conditions for complete degassing and less shrinkage It is possible that the optimum processing conditions for gray iron are not the same for titanium coated iron, for example.

B. Further Sample Testing and Analysis

- X-ray or SEM analysis could be performed on the post laser process soot to further determine what is being oxidized or reduced.

- The thickness of the titanium layer can be varied in further tests.
- Multiple tracks for each condition should be made so that X-ray diffraction results would be easier to obtain. The single track cross-section is too narrow for the wide X-ray beam to give good results.

C. Numerical Modeling

- The chemical equilibrium of the Fe/C/O/N/Ti system deserves further study – particularly with respect to products and for various concentrations of reactants and at different temperatures.
- The NASA chemical equilibrium program could be used to assist in studying the Fe/C/O/N/Ti system.
- For the Fe/C/O/N/Ti system, run a chemical analysis several times with each element being a different limiting reagent and see what different products and or concentrations of products are produced. This type of sensitivity analysis could help determine the delicate balance between titanium and oxygen, for example, that produces the least amount of porosity.

Assuming that the laser processing conditions can be optimized, and numerical modeling of the complex chemical system within the melt region is possible, the technique could be applied to actual machine parts instead of flat plate samples. The technique would require additional experimentation on corners and rounded surfaces in order to become applicable to such parts as camshafts, tappets, pistons, cylinder blocks and liners, brake and clutch parts, and much more. The applications are endless.

References

References

Abılsiitov, G. A., A. N. Safonov, V. V. Shıbaev, A.G. Grıgor'Yants. "Introductıon of Laser Technology – An Effective Method of Improving Welding Productıon: Laser Depositıon and Treatment of Wear Resistant Coatings". Weldıng Productıon. No. 9. Weldıng Institute. 1983. pp. 21-23.

Arata, Yoshiaki, and Tatsuharu Oda, "Fundamental Research on Laser Welding of Structural Steel". Transactions of JWRI. Vol. 13:2. Weldıng Research Institute. Osaka: 1984. pp. 55-61.

ASM Handbook Vol. 1: Properties and Selection: Irons and Steels. Amerıcan Society for Metals. Metals Park,OH. 1995.

ASM Handbook Vol. 3: Alloy Phase Diagrams. American Socıety for Metals. Metals Park,OH. 1995

ASM Handbook Vol. 4 Heat Treating. Amerıcan Socıety for Metals. Metals Park,OH. 1995.

Bergmann, H. W., B. L. Mordıke, T. Bell. "Laser Melting of Cast Irons". Optoelectronics in Engıneering: 6th. Intl. Congress. 1984. pp. 335-349.

Calder, Neil J., Iaın R. Whitaker, D. Graham McCartney, Wılliam M Steen. "Laser Weldıng of Aluminum Lıthıum Alloy 8090". ICALEO 1992: Laser Material Processıng. SPIE 1992. pp. 565-573.

Chase, M.W. Jr., C. A. Davıes, J. R. Downey, Jr , D J. Frurip, R. A. McDonald, and A. N Syverud. JANAF Thermochemical Tables 3rd. ed. Part 1. 1985.

Chase, M.W. Jr., C. A. Davies, J. R. Downey, Jr., D. J. Frurip, R. A. McDonald, and A. N. Syverud. JANAF Thermochemıcal Tables 3rd. ed. Part 2. 1985.

Chen, C. H., C. J. Altstetter, J. M. Rıgsbee. "Laser Processıng of Cast Iron for Enhanced Erosıon Resistance". Metallurgical Transactions A. Vol. 15A. Mınerals, Metals, & Materıals Society. 1984. pp. 719-728.

Darken, L. S. and R. W Gurry. Physical Chemıstry of Metals. McGraw-Hıll. New York: 1953.

Dubrujeaud, B., A. Fontes, P. Forget, C. Papaphilıppou, C. Saınte-Catherine, M. Vardavoulıas, M. Jeandın. "Surface Modıfıcation Using Hıgh Power Lasers: Influence of Surface Characterıstics on Properties of Laser Processed Materıals". Surface Modificatıon Technologies X. Institute of Materials. London: 1997. pp. 153-176.

Duley, W. W. Laser Welding. John-Wiley & Sons, Inc. New York: 1999.

Duley, W. W. Laser Processing and Analysis of Materials. Plenum Press. New York. 1983.

Folkes, J. "Surface Modification and Coating with Lasers". Materials Science Forum. Vol. 246. 1997. pp. 261-278.

Grossman, M. A. and E. C. Bain. Principles of Heat Treatment. 5th. Ed. American Society of Metals. Metals Park,OH. 1964.

Hecht, Jeff. The Laser Guidebook. 2nd Ed. TAB Books. Blue Ridge Summit, PA. 1992. p. 26. 1992.

Huang, Francis F. Engineering Thermodynamics, Fundamentals and Applications. 2nd. Ed. Macmillian Publishing Company. New York. 1988.

Jianglong, Liu, Zhou Chuanguang, Ding Peidao. "A Study of the Solidification Characteristics of Metallic Surfaces Melted by High Power Laser". Lasers in Engineering Vol. 5. Overseas Publishers Association. 1996. pp. 43-50.

Kou, Sindo. Welding Metallurgy. John Wiley & Sons. p. 61-89. 1987.

Lee, M. F., J. C. Huang and N. J. Ho. "Microstructural and Mechanical Characterization of Laser-beam Welding of a 8090 Al-Li Thin Sheet". Journal of Materials Science Vol. 31:6. Chapman and Hall Ltd. pp. 1455-1468. 1996.

Liu, S., and D. L. Olson, and S. Ibarra. "Electrode Formulation to Reduce Weld Metal Hydrogen Porosity". Proceeding of the 13th International Conference on Offshore Mechanics and Arctic Engineering. Vol. 3. OMAE. 1994. pp. 291-298.

Luft, Arnold, Wolfgang Reitzenstein, Niva Zarubova, Jan Cermak. "Investigations into Laser Beam Remelt Hardening of Cast Iron". Welding and Cutting. Vol. 3. 1991 pp. E44-48.

Mordike, B. L., and H W. Bergmann. "Properties of Surface Melted SG Iron". Materials Research Society Symposia Proceedings. Vol. 58. Materials Research Society. Pittsburgh: 1986. pp. 429-435.

Mordike, B. L., and H. W Bergmann. "Metallurgical Considerations in the Laser Surface Melting of Iron-base Alloys". Z. Werkstofftech. Vol. 14. Weinheim: 1983. pp. 228-236.

Mordike, B. L. "Recent Developments in the Surface Treatment of Materials". CO_2 Lasers and Applications II. Vol. 1276. SPIE. Bellingham: 1990. pp. 332-342.

Papaphilippou, C., M. Vardavoulias, M. Jeandin. "Effects of CO_2 Laser Surface Hardening in the Unlubricated Wear of Ductile Cast Iron Against Alumina". Transactions of the ASME: Journal of Tribology. Vol. 18. ASME. 1996. pp. 748-752.

Ramirez, J.E., B. Han, S. Liu "Effect of Welding Variables and Solidification Strúcture on Weld Metal Porosity"; Metallurgical and Materials Transactions A: Physical Metallurgy and Materials Science. Vol. 25A:10. Minerals, Metals, & Materials Society 1994. pp. 2285-2294.

Ricciardi, G., F. Pasquini, S. Rudilosso. "Remelting Surface Hardening of Cast Iron by CO_2 Laser". Proceedings of the 1st. International Conference on Lasers in Manufacturing North-Holland Publishers. 1983. pp. 87-95.

Samsonov, V. I., V. S An, A. G. Shnypkin, P Yu. Boitsov. "Laser Hardening of Cast-Iron Machine Components". Metal Science and Heat Treatment. Vol 31:11-12. Plenum Publishing Corporation. 1990. pp. 807-810.

Sedunov, V. K., V. M. Andriyakhin, N. T. Chekanova, V. M. Belov. "Changes in the Structure and Properties of Cylinder Sleeves of Internal Combustion Engines after Laser Treatment" Metal Science and Heat Treatment. Vol. 22. Plenum Publishing Corporation. 1980. pp. 630-634.

Shibata, Fumio. "Effects of Insert Metal on Some Properties of Spheroidal Graphite Cast Iron Welds: Study on Electron Beam Welding of Spheroidal Graphite Cast Iron (report 2). Transactions of the Japan Welding Society. Vol 22:1. JWS. 1991. pp. 40-44.

Simmons, J. W., and R. D. Wilson. "Joining of High-nitrogen Stainless Steel by Capacitor Discharge Welding". Welding Journal. Vol. 75·6. American Welding Society. 1996. pp. 185-190.

Smith, D. P., D. J. Carney, L. W. Eastwood, C. E. Sims. Gases in Metals. American Society of Metals. 1952. pp. 69-114.

Straus, J., L. Szylar, W. Golebiewski, "Laser Treatment of Grey Cast Iron". Key Engineering Materials. vol. 46 & 47. Trans Tech Publications. Switzerland: 1990. pp. 369-380.

Van Wylan, Gordon, Richard Sonntag, Claus Borgnakke. Fundamentals of Classical Thermodynamics. 4th. Ed. John Wiley & Sons, Inc. New York. 1994.

Wark, Jr., Kenneth. Advanced Thermodynamics for Engineers. McGraw-Hill. New York: 1995

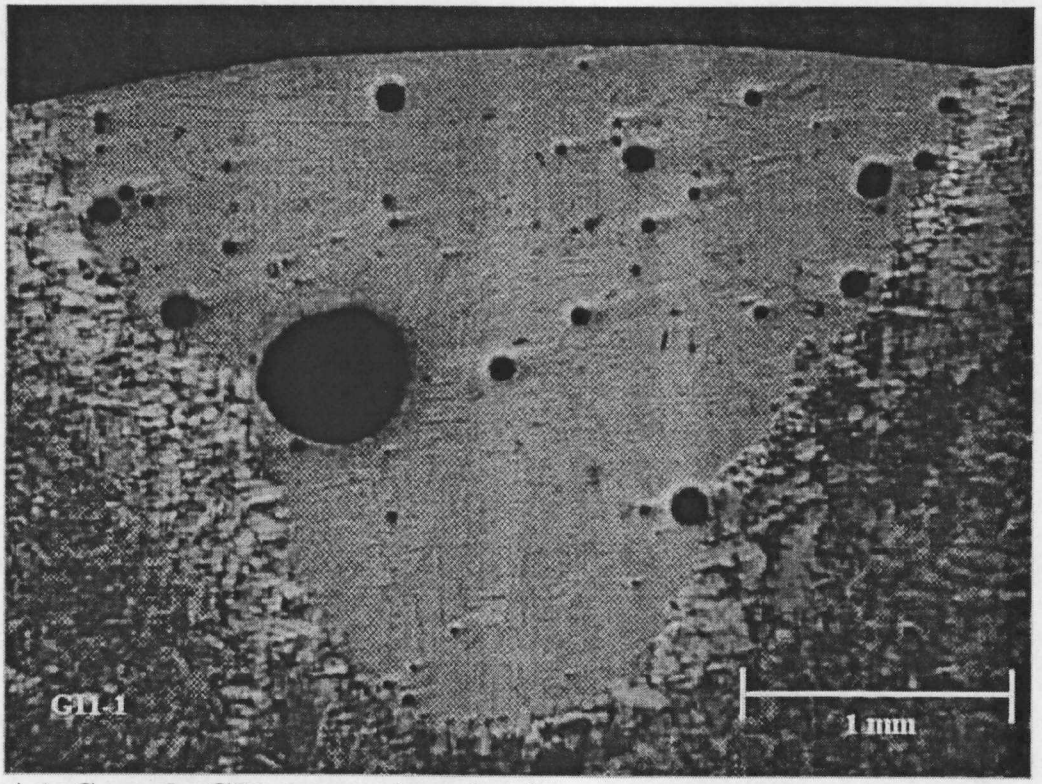
Weast, Robert C. ed. in chief, Melvin J. Astle, William H. Beyer. CRC Handbook of Chemistry and Physics 64th. Ed. CRC Press, Inc. Boca Raton 1984.

Weckman, D.C., H.W. Kerr, J T. Liu "Effects of Process Variables on Pulsed Nd:YAG Laser Spots Welds· Part II. AA1100 Aluminum and Comparison to AISI 409 Stainless Steel". Metallurgical and Materials Transactions B: Process Metallurgy and Materials Processing Science. Vol. 28:4. Minerals, Metals, & Materials Society. 1997. pp. 687-700.

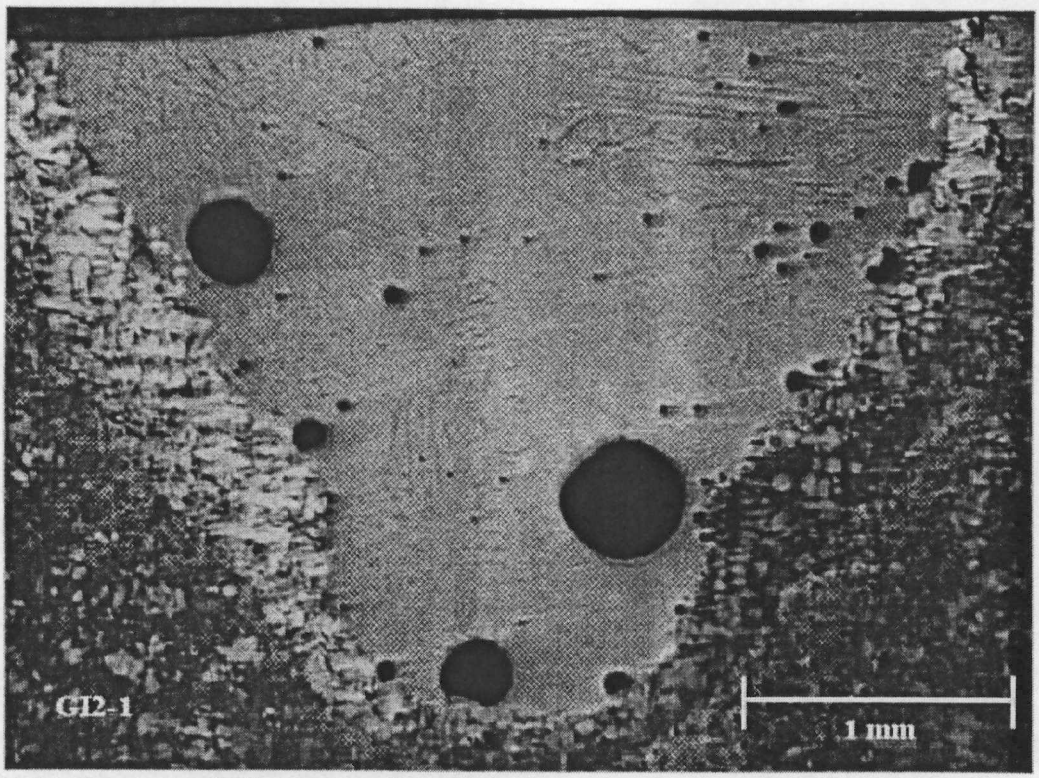
Yellup, J. M. "Laser Cladding Using the Powder Blowing Technique". Surface and Coatings Technology. Vol. 71. Elsevier Science. 1995. pp. 121-128.

Appendices

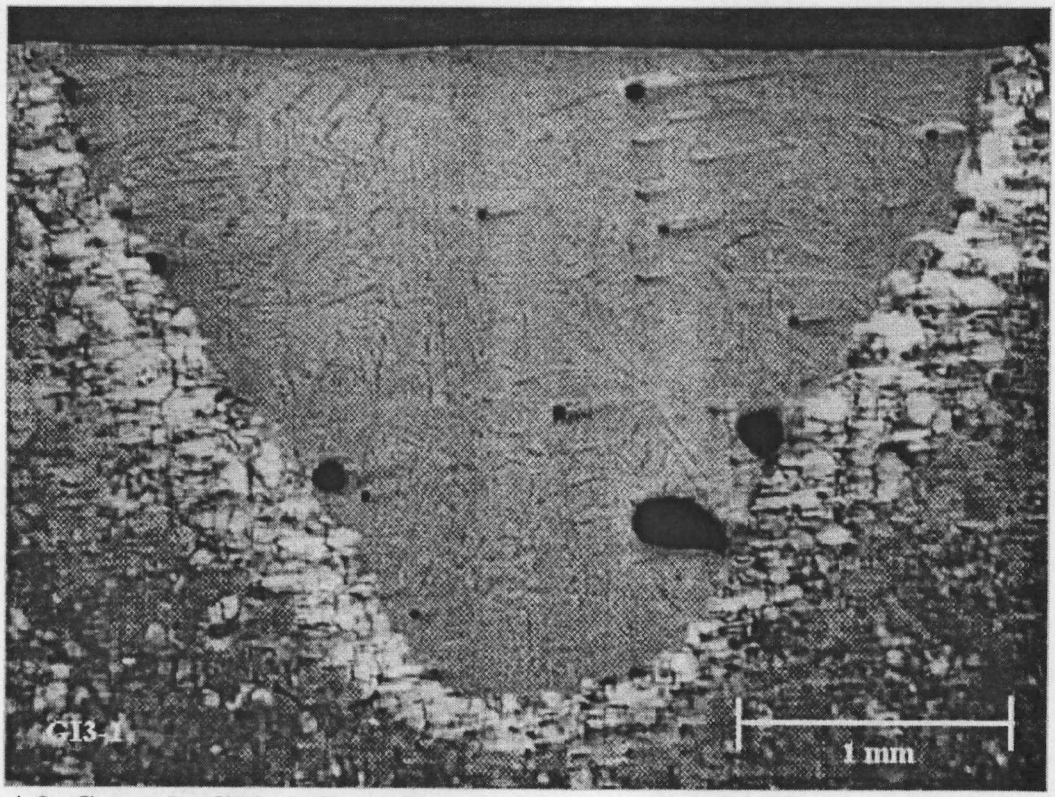
Appendix A
Cross-sectional Photos of Gray Iron (GI) Samples



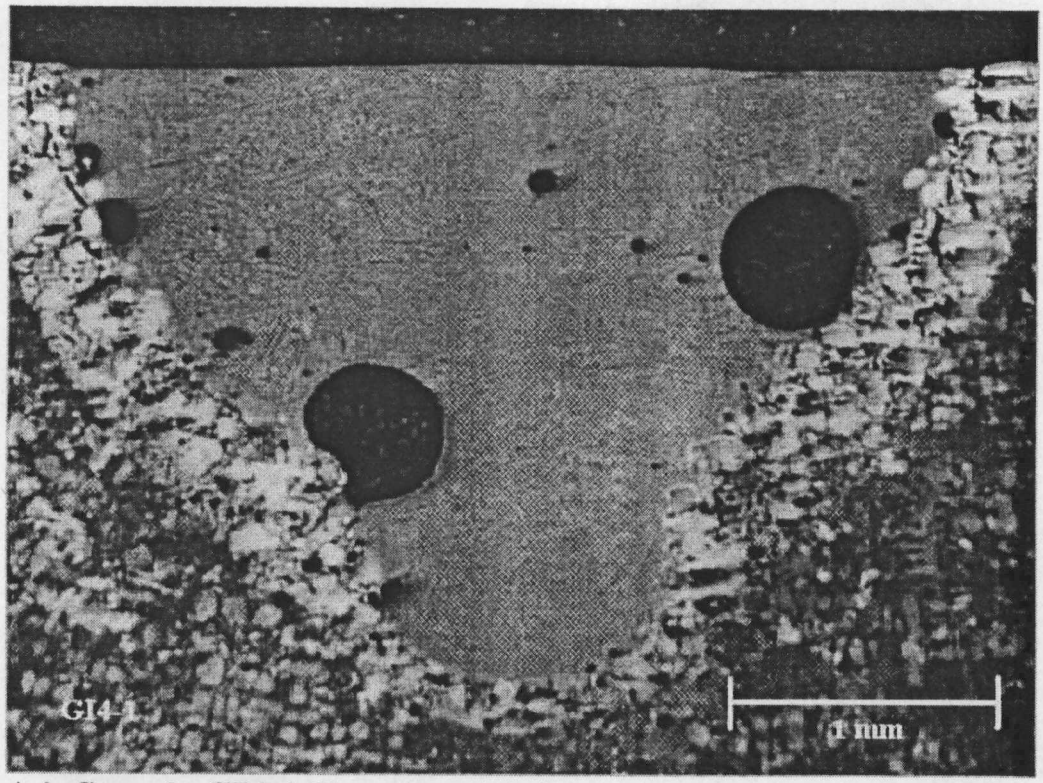
A1: Sample GI1-1 gray iron in air



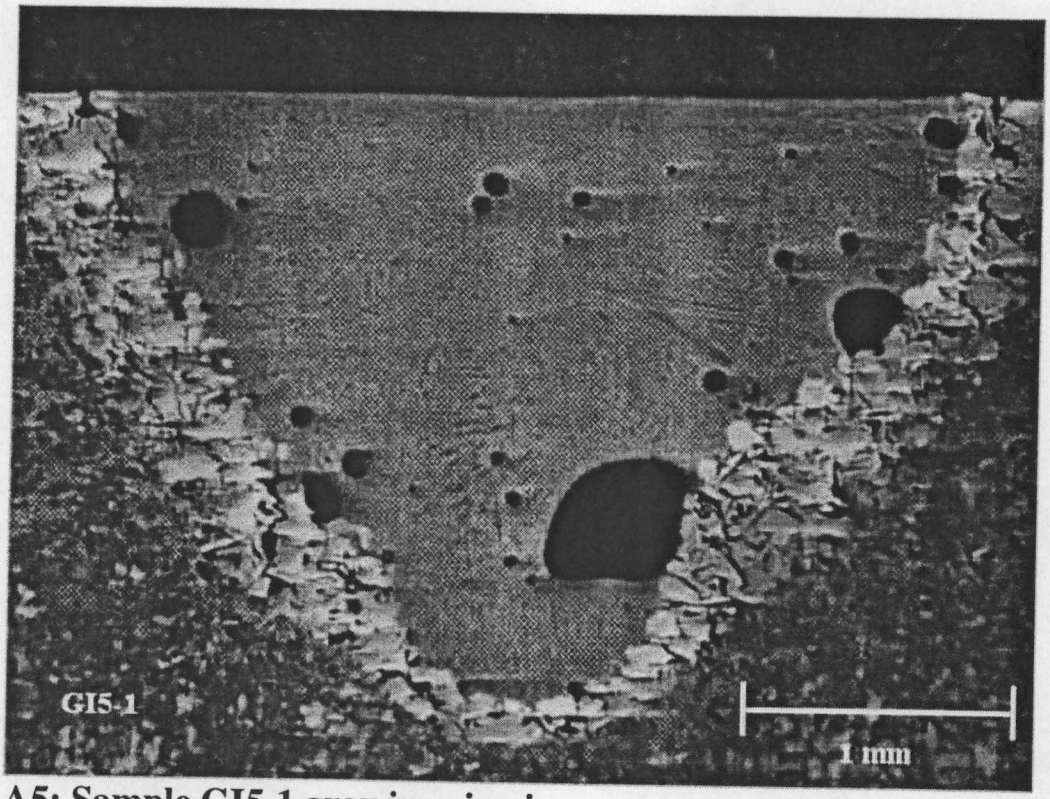
A2: Sample GI2-1 gray iron in air



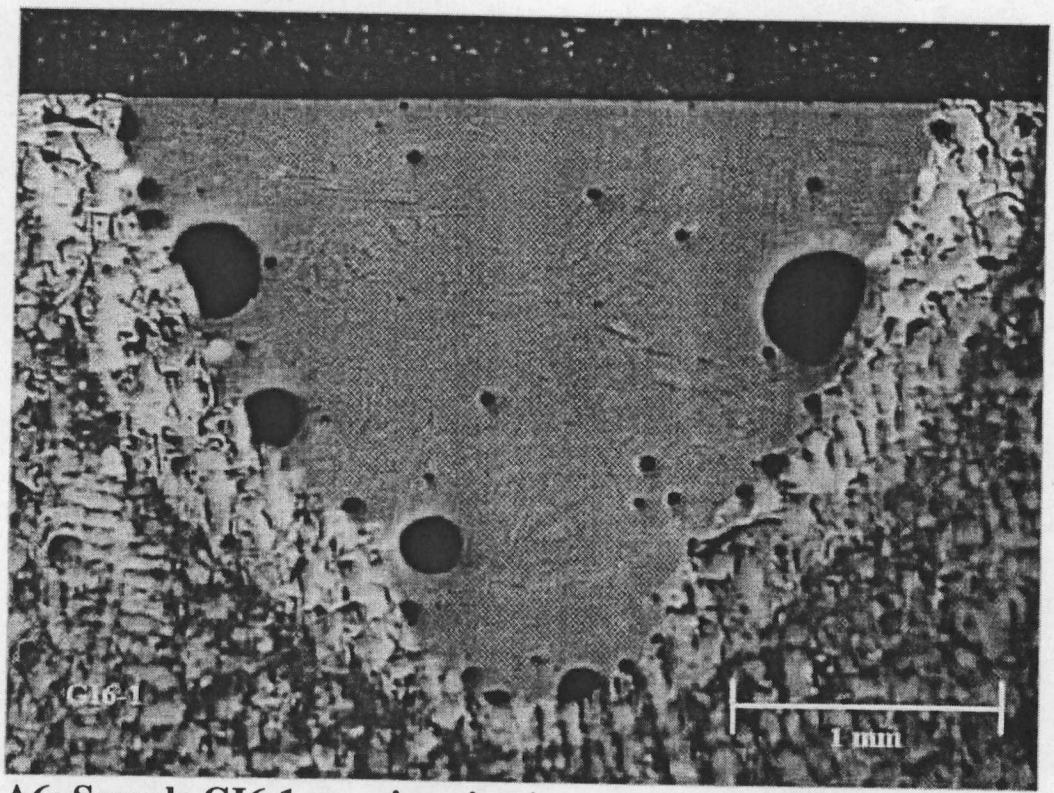
A3: Sample GI3-1 Gray iron in air



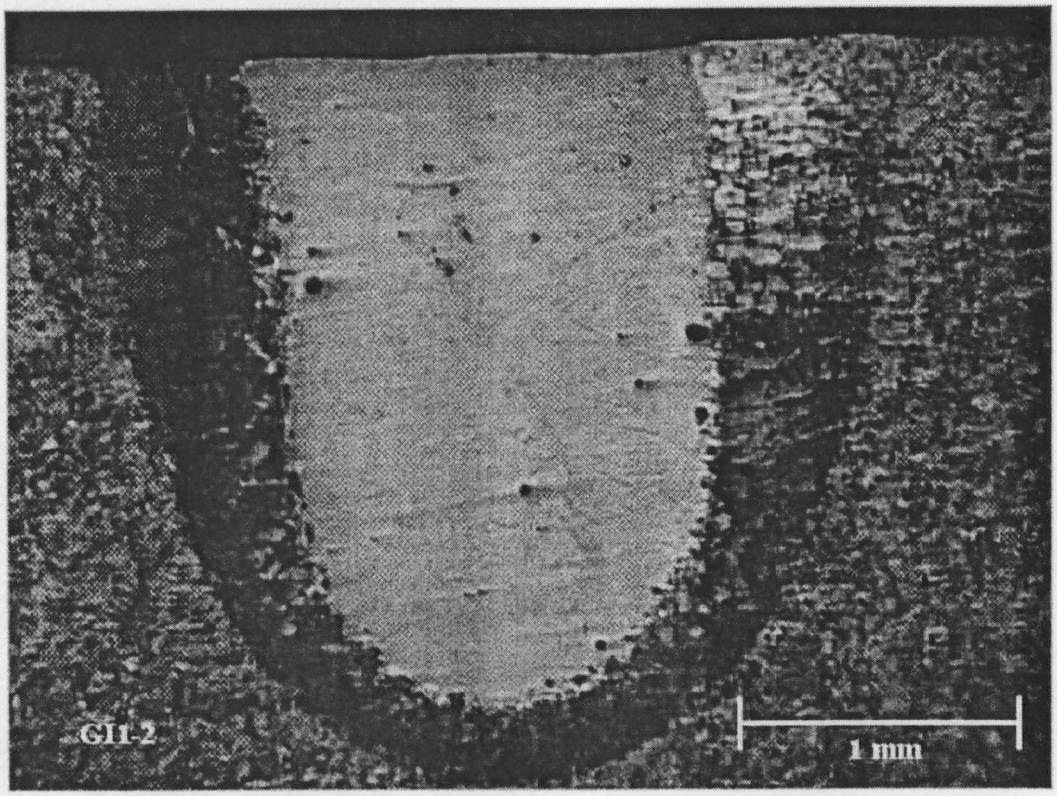
A4: Sample GI4-1 Gray iron in air



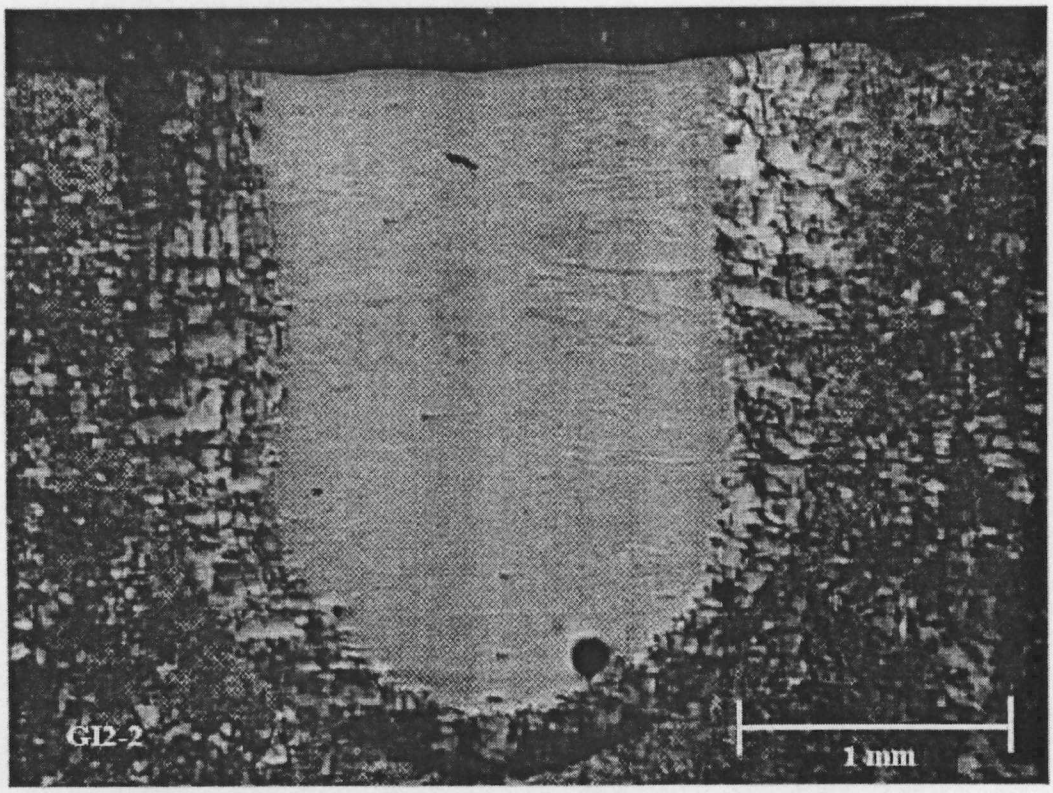
A5: Sample GI5-1 gray iron in air



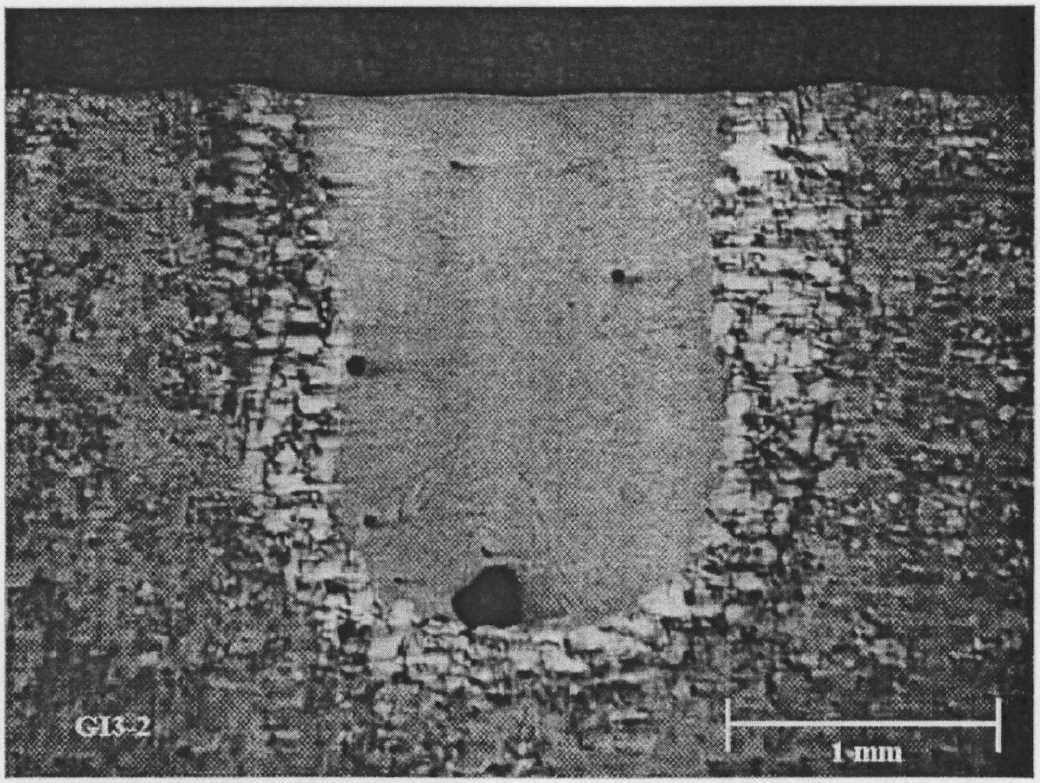
A6: Sample GI6-1 gray iron in air



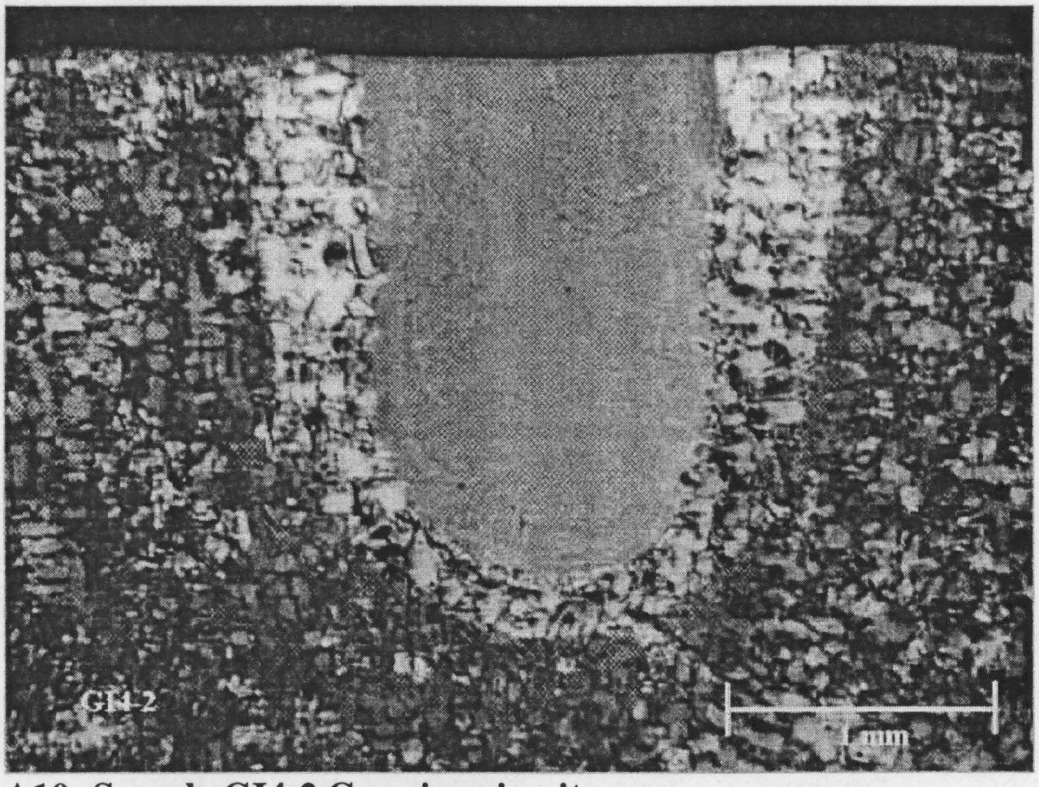
A7: Sample GI1-2 gray iron in nitrogen



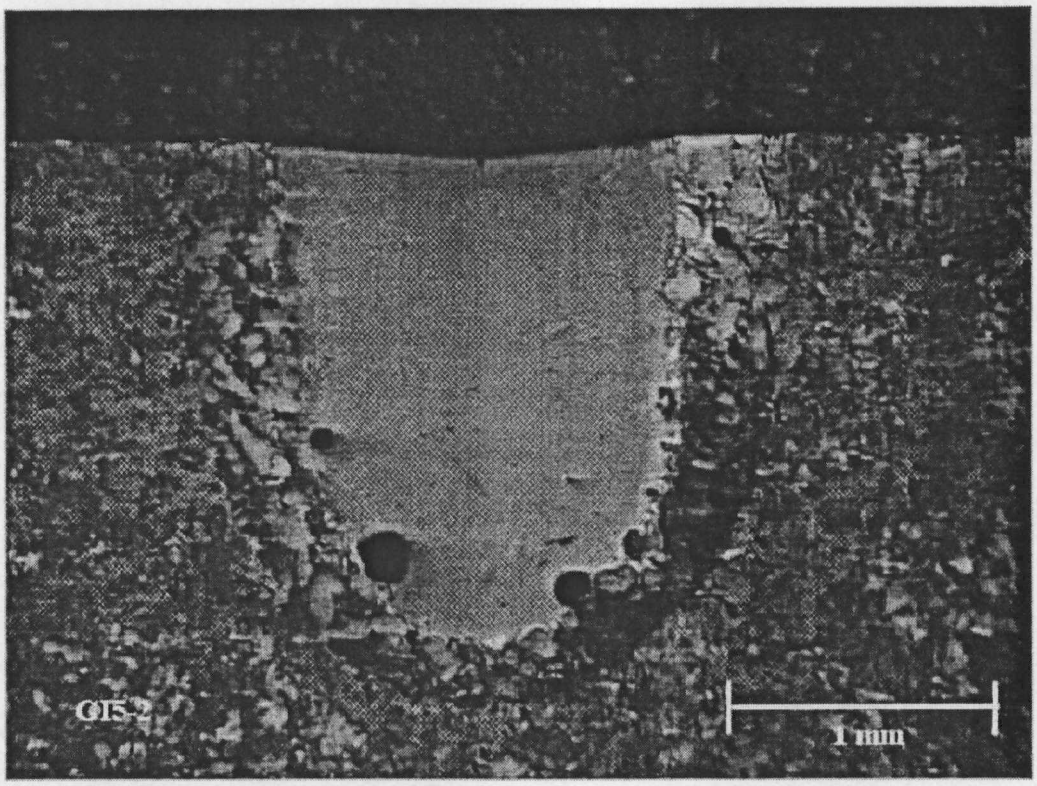
A8: Sample GI2-2 gray iron in nitrogen



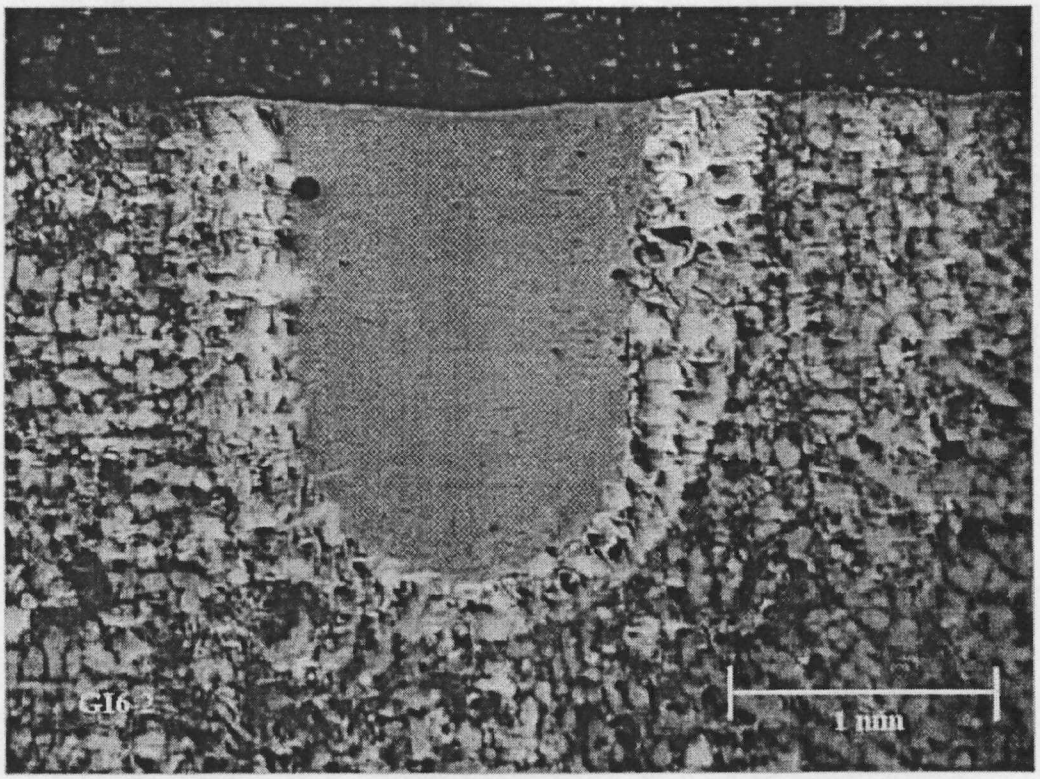
A9: Sample GI3-2 Gray iron in nitrogen



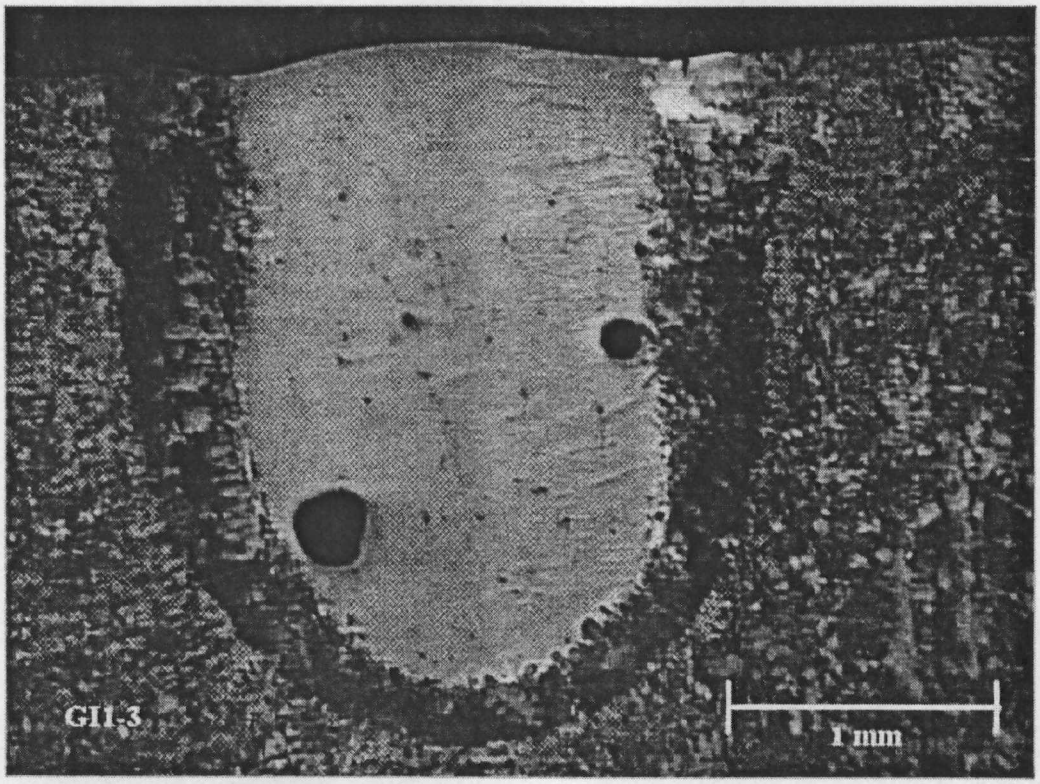
A10: Sample GI4-2 Gray iron in nitrogen



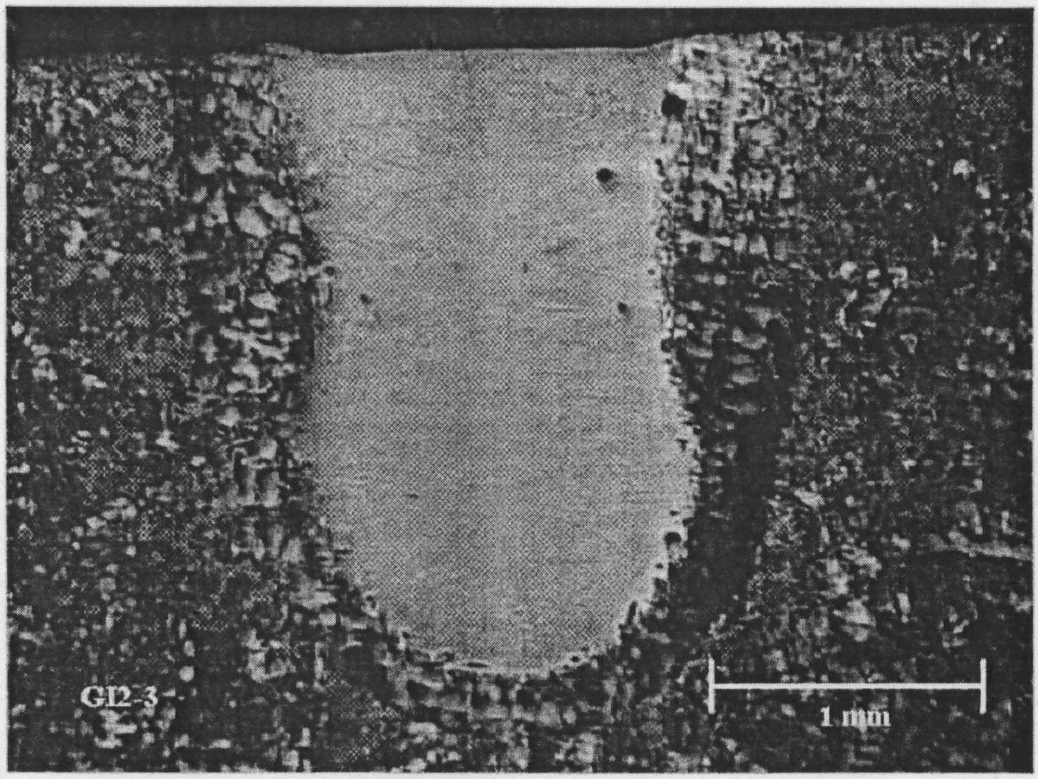
A11: Sample GI5-2 gray iron in nitrogen



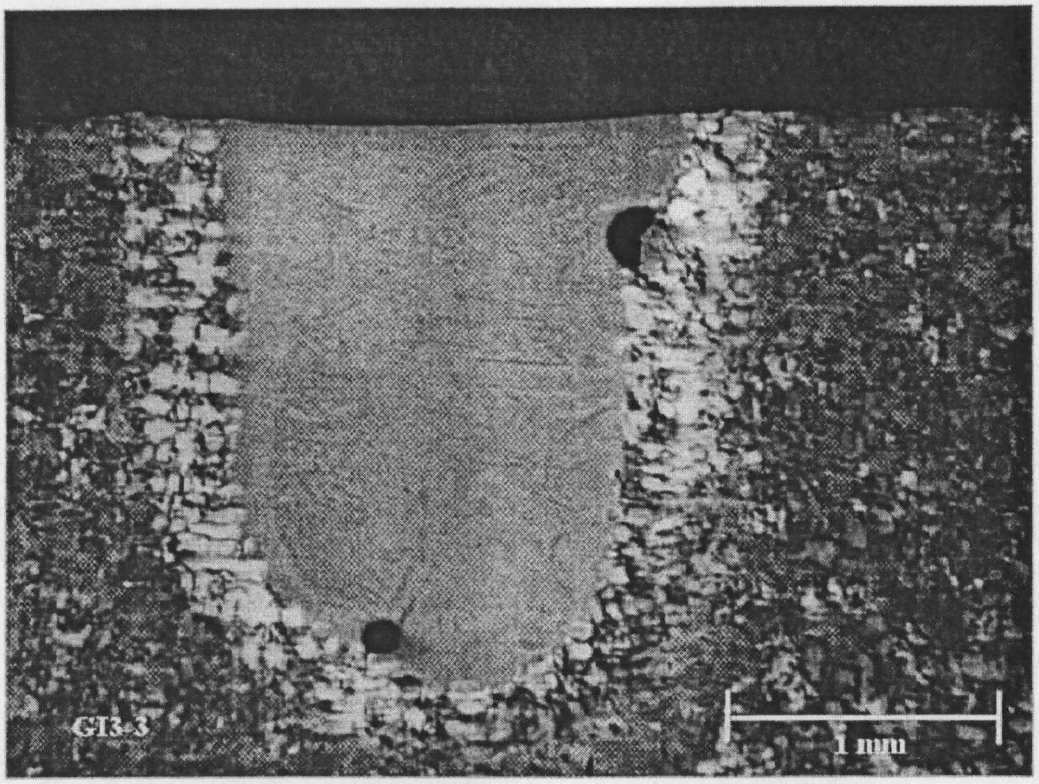
A12: Sample GI6-2 gray iron in nitrogen



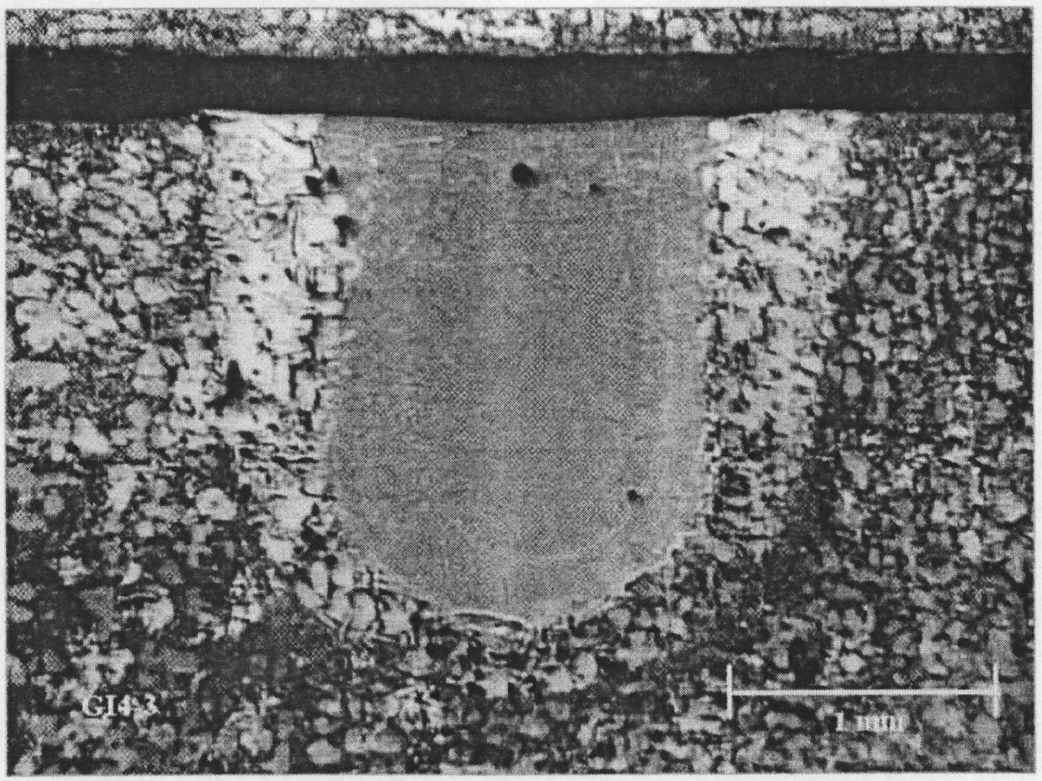
A13: Sample GI1-3 gray iron in argon



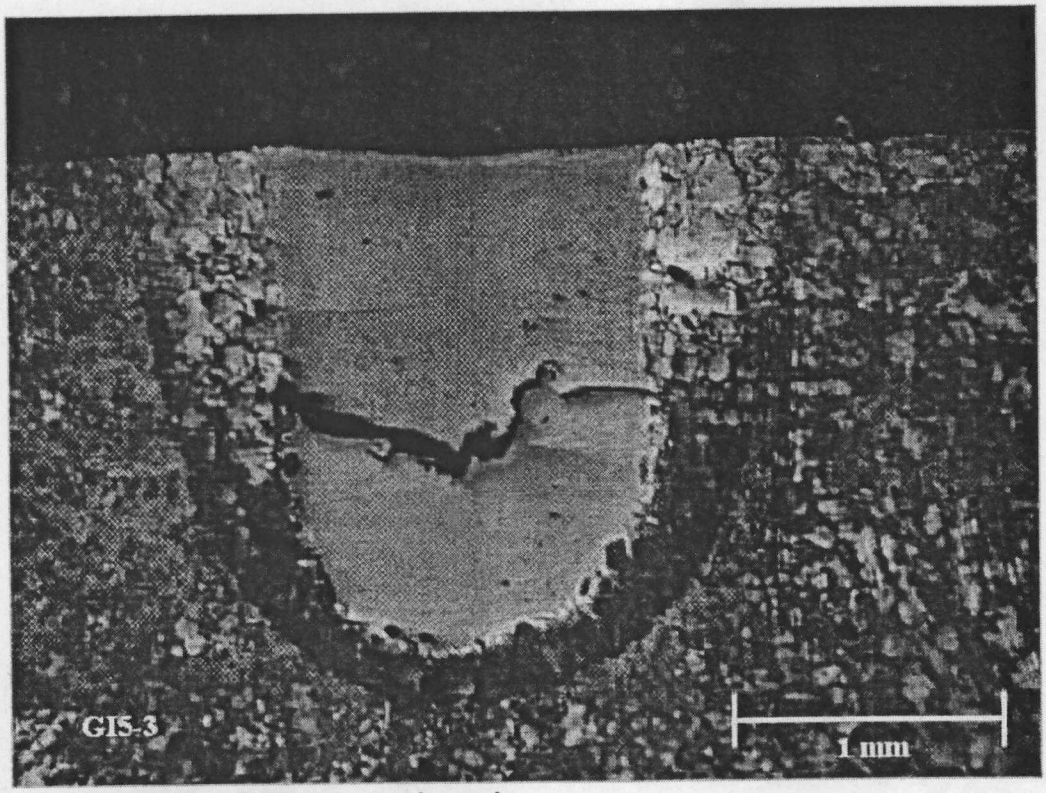
A14: Sample GI2-3 gray iron in argon



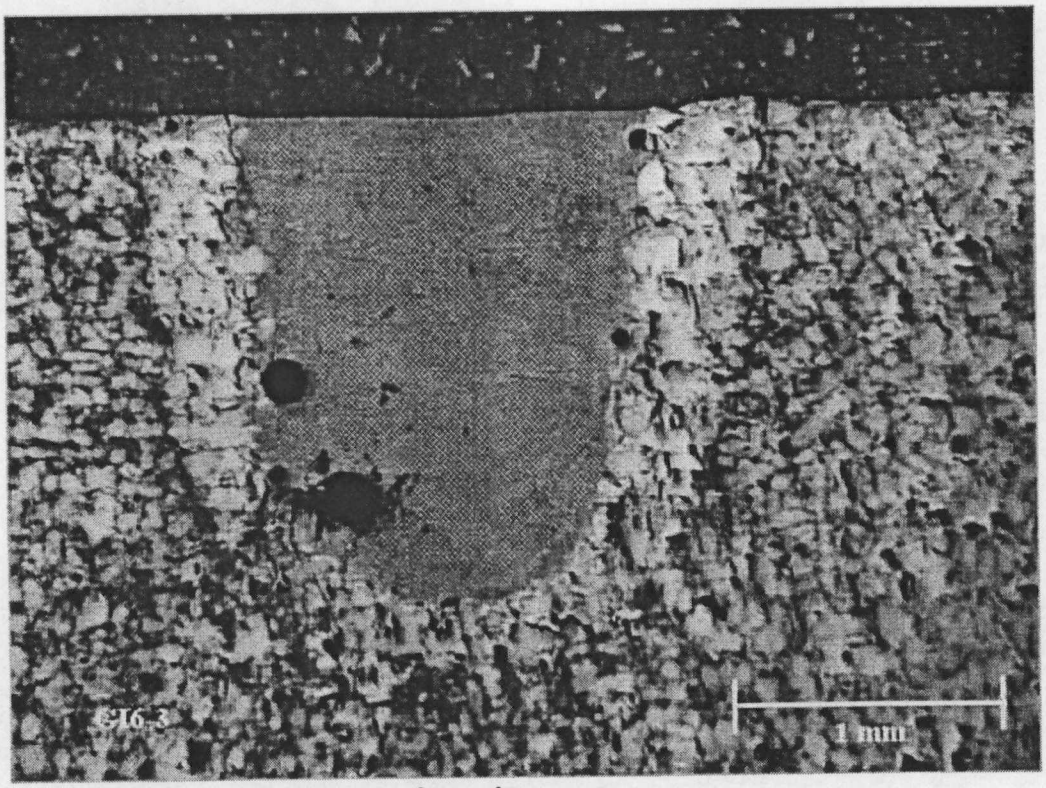
A15: Sample GI3-3 gray iron in argon



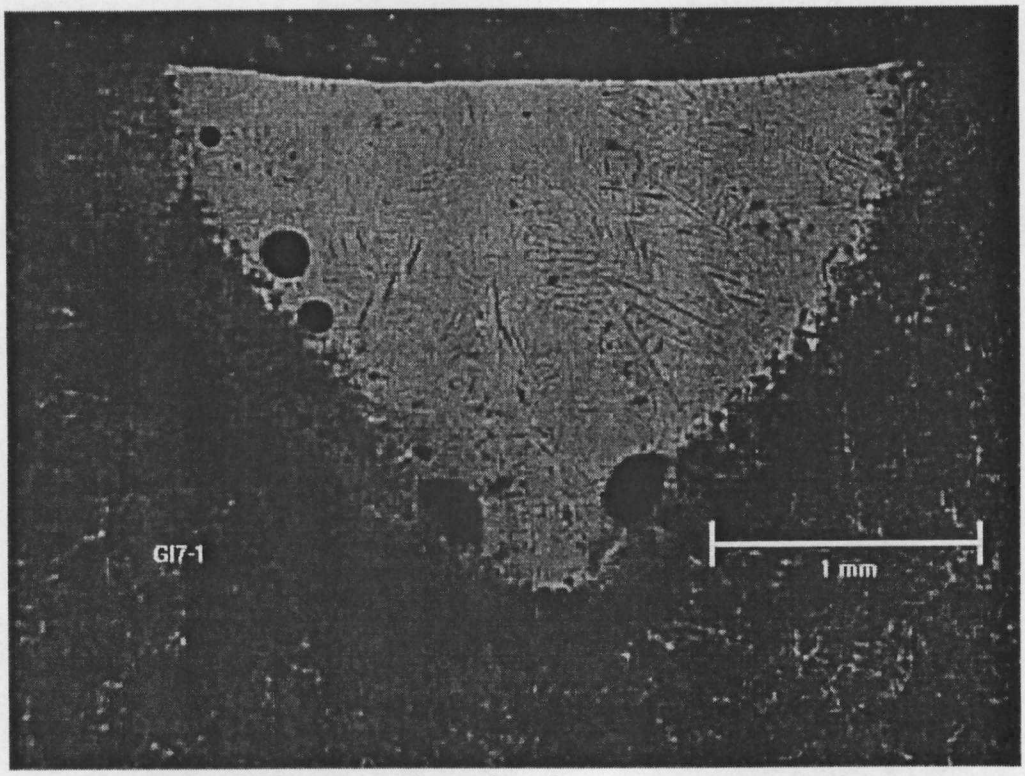
A16: Sample GI4-3 gray iron in argon



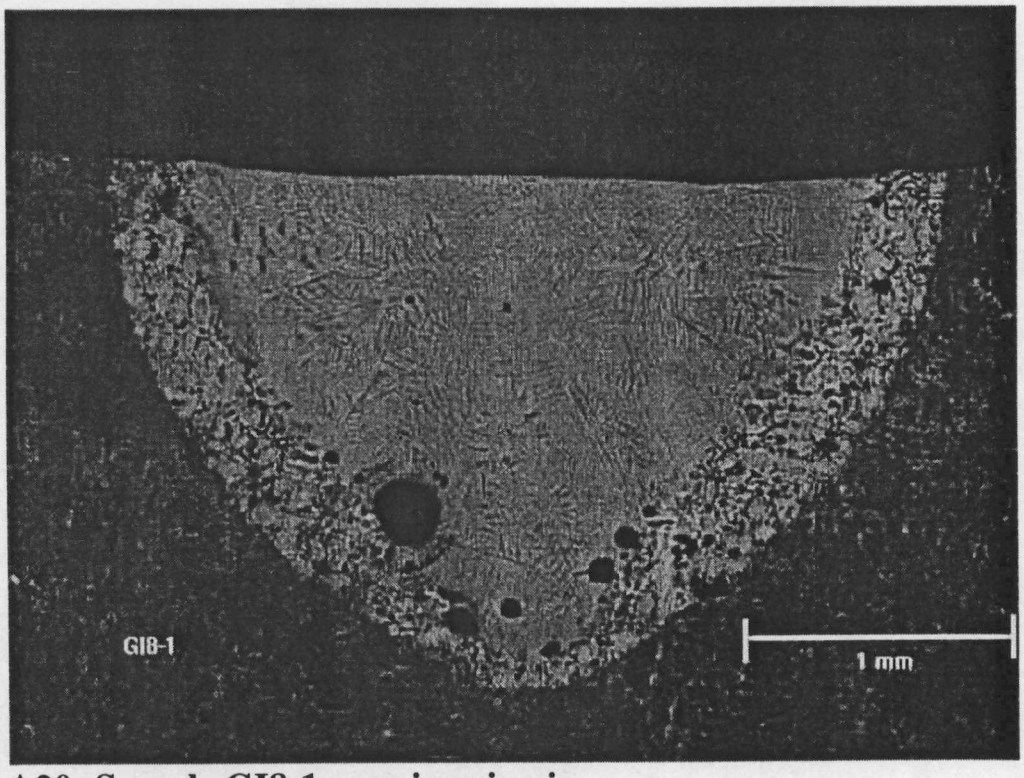
A17: Sample GI5-3 gray iron in argon



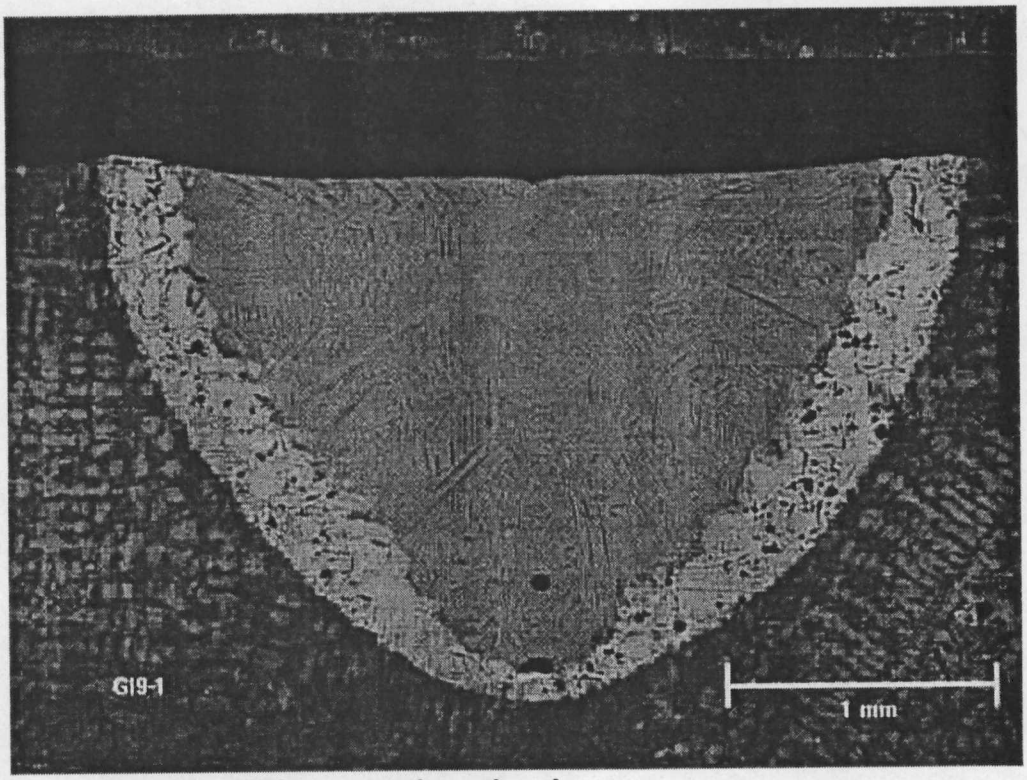
A18: Sample GI6-3 gray iron in argon



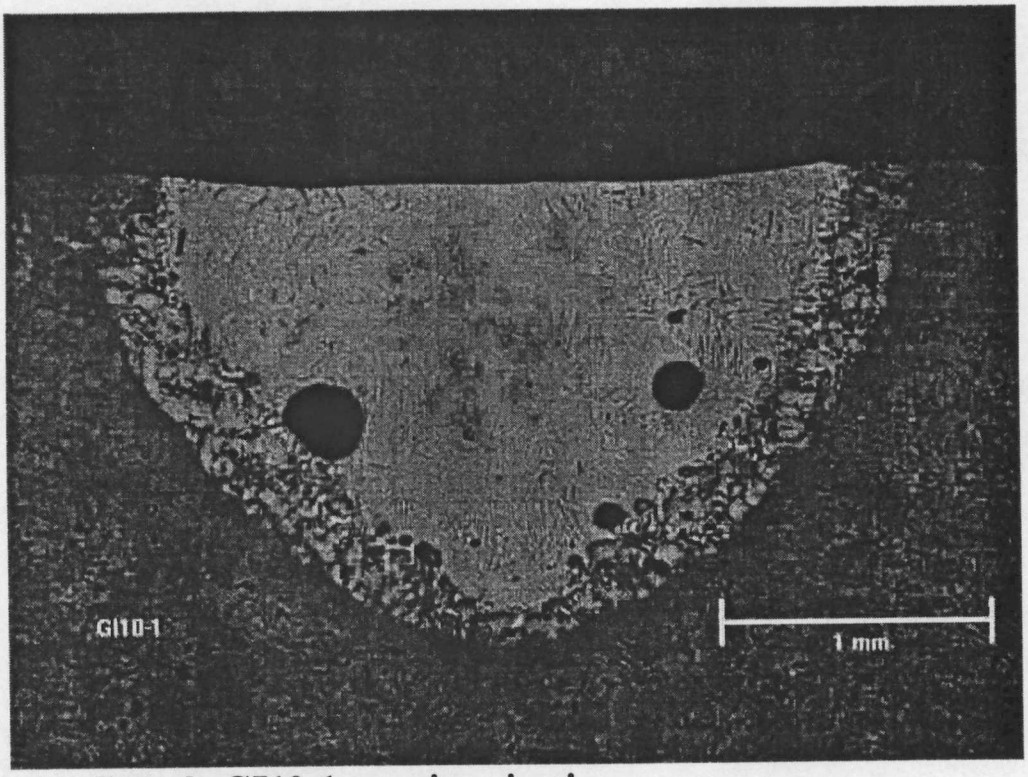
A19: Sample GI7-1 gray iron in air



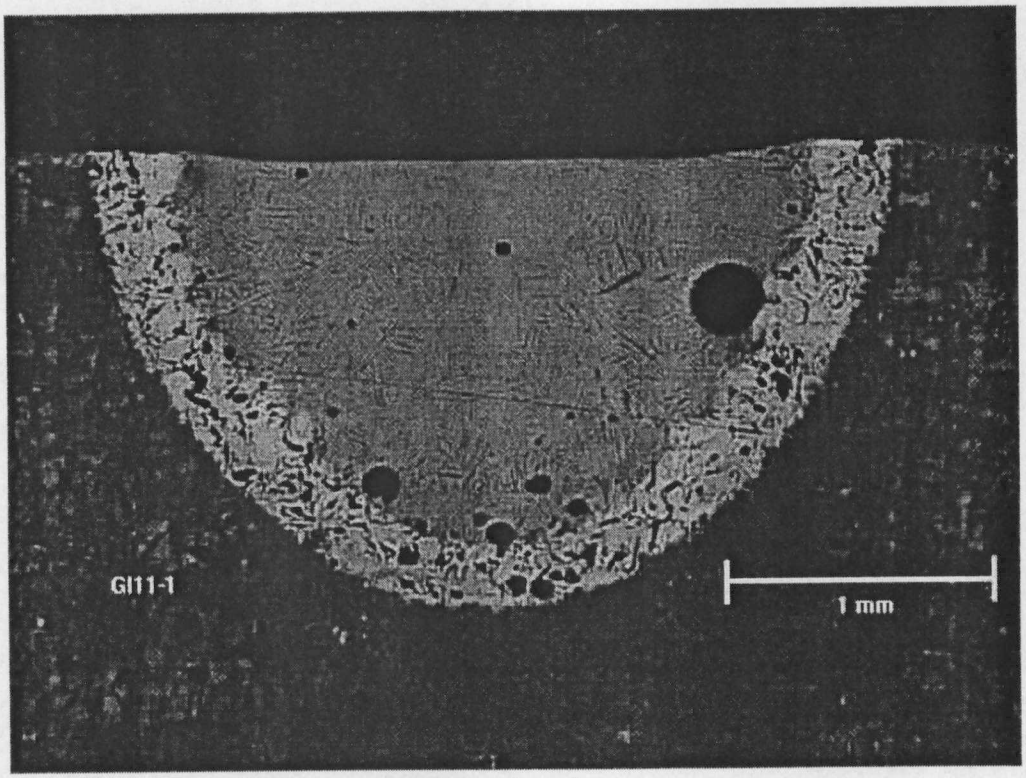
A20: Sample GI8-1 gray iron in air



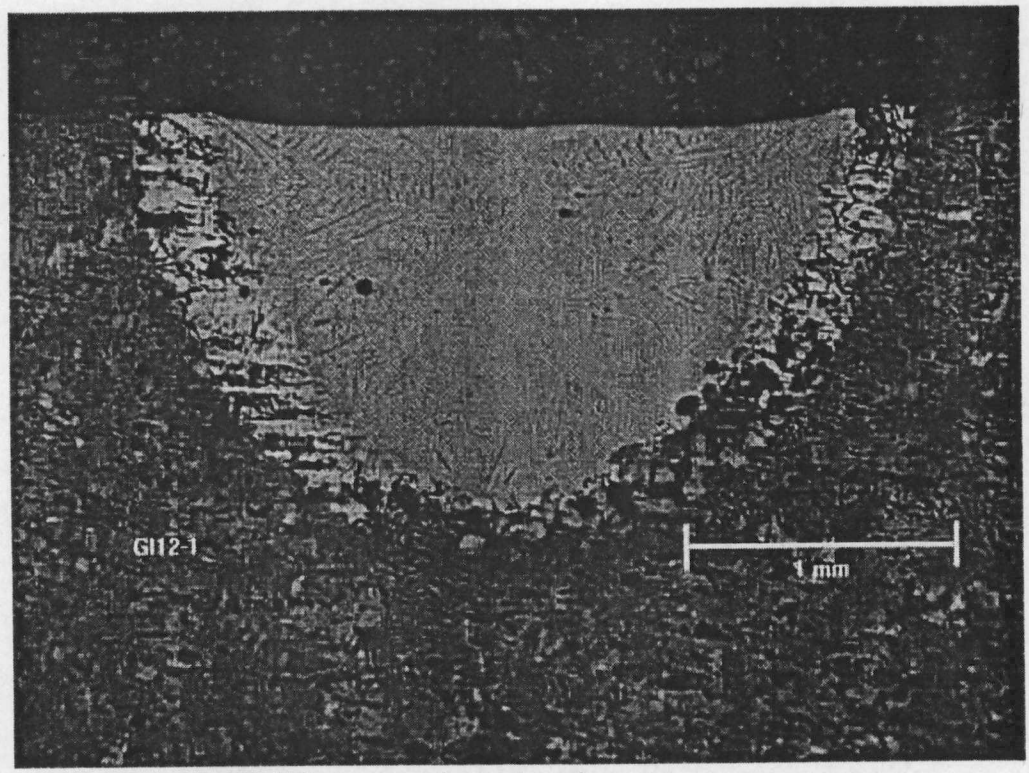
A21: Sample GI9-1 gray iron in air



A22: Sample GI10-1 gray iron in air

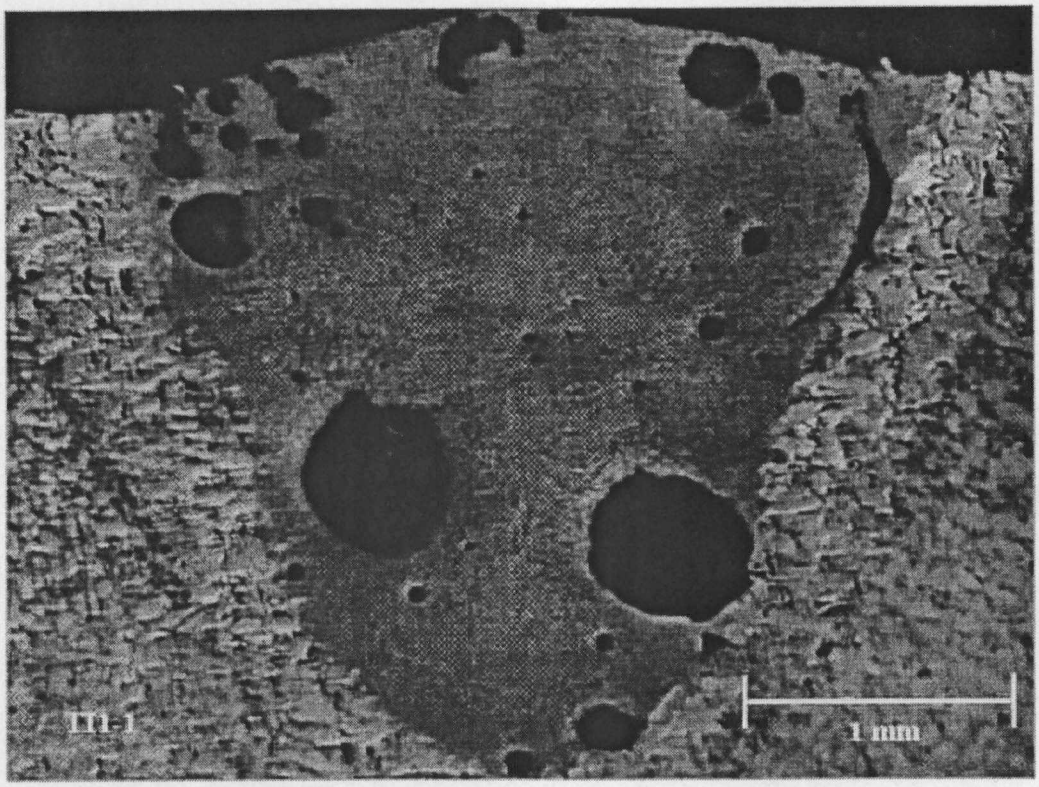


A23: Sample GI11-1 gray iron in air

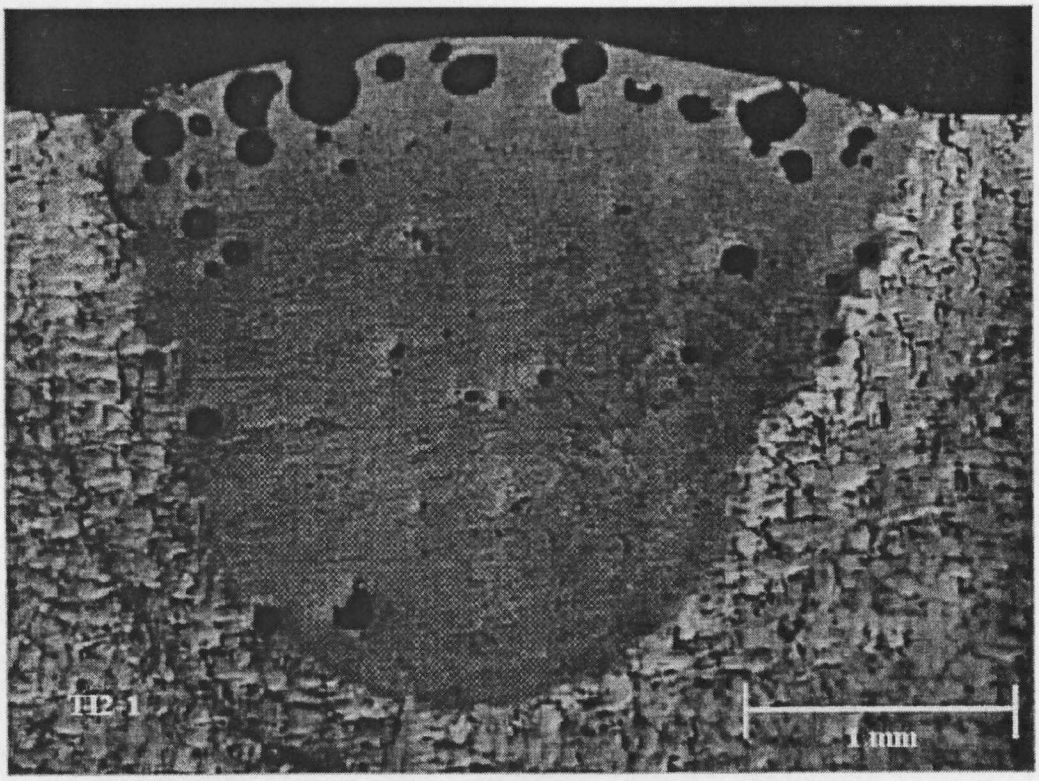


A24: Sample GI12-1 gray iron in air

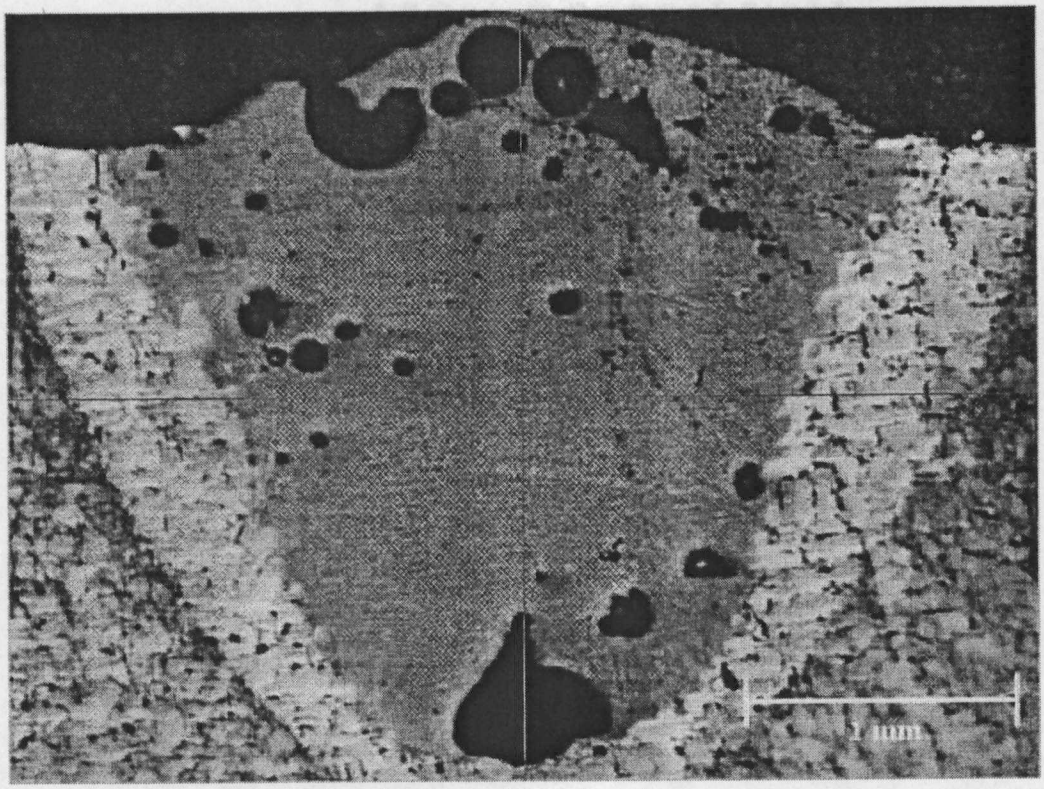
Appendix B
Cross-sectional Photos of Titanium on Iron (TI) Samples



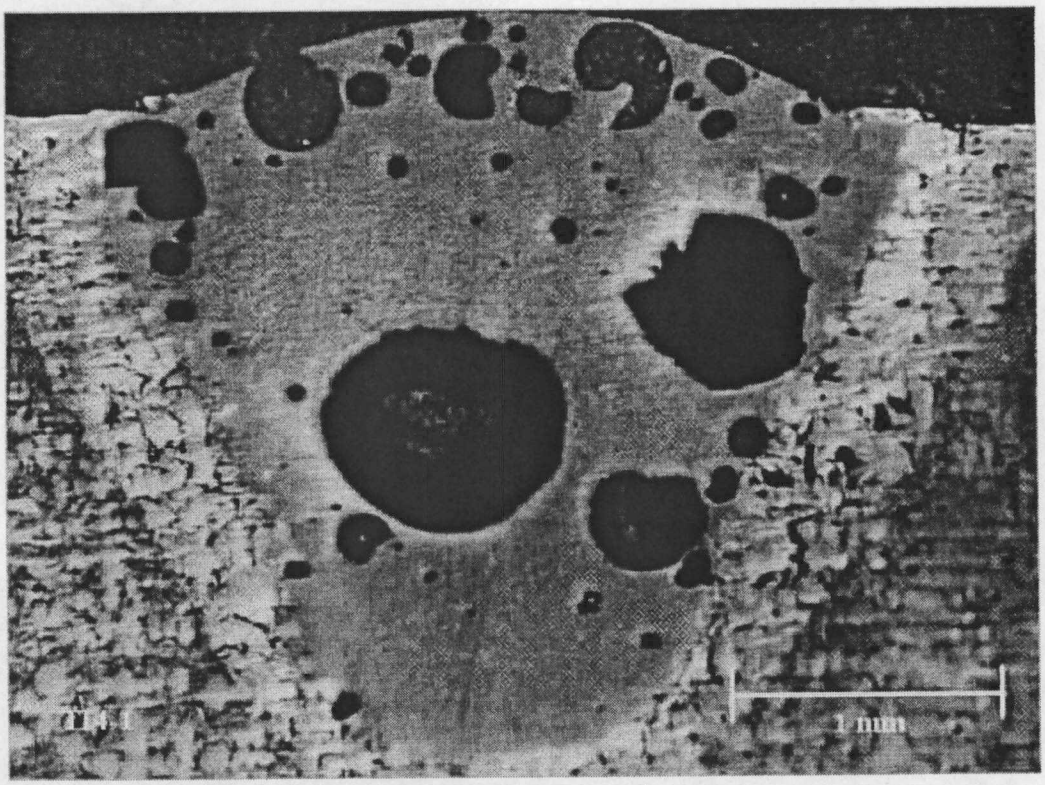
B1: Sample TI1-1 titanium on iron in air



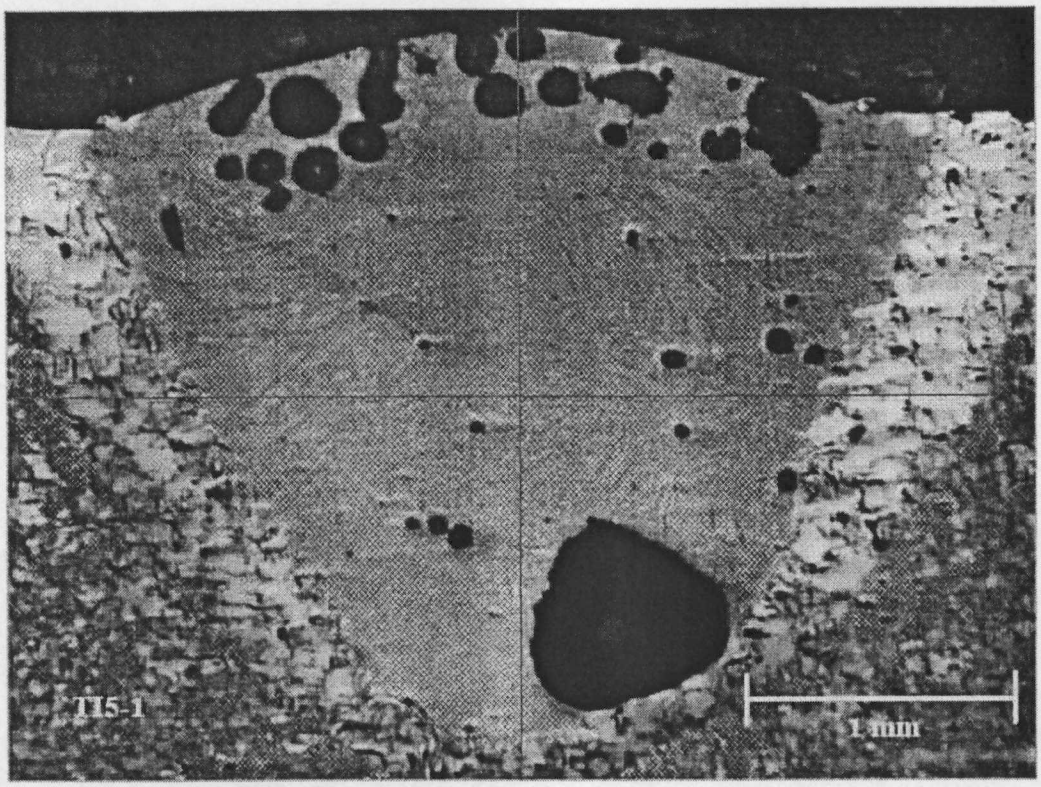
B2: Sample TI2-1 titanium on iron in air



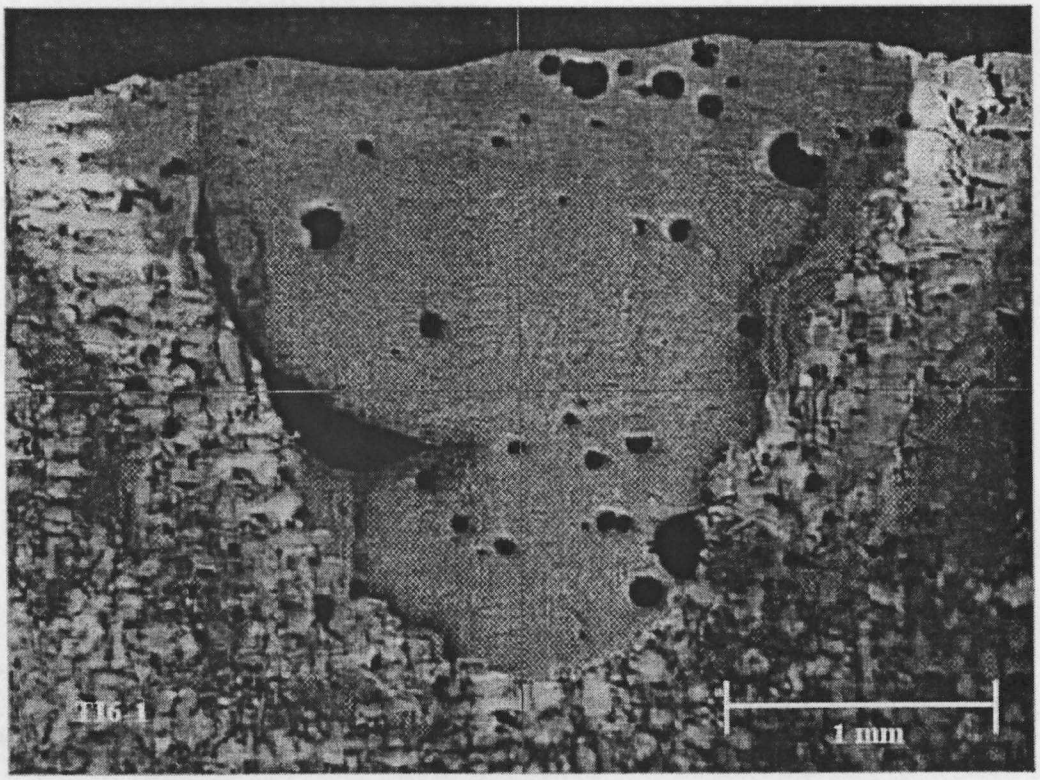
B3: Sample TI3-1 titanium on iron in air



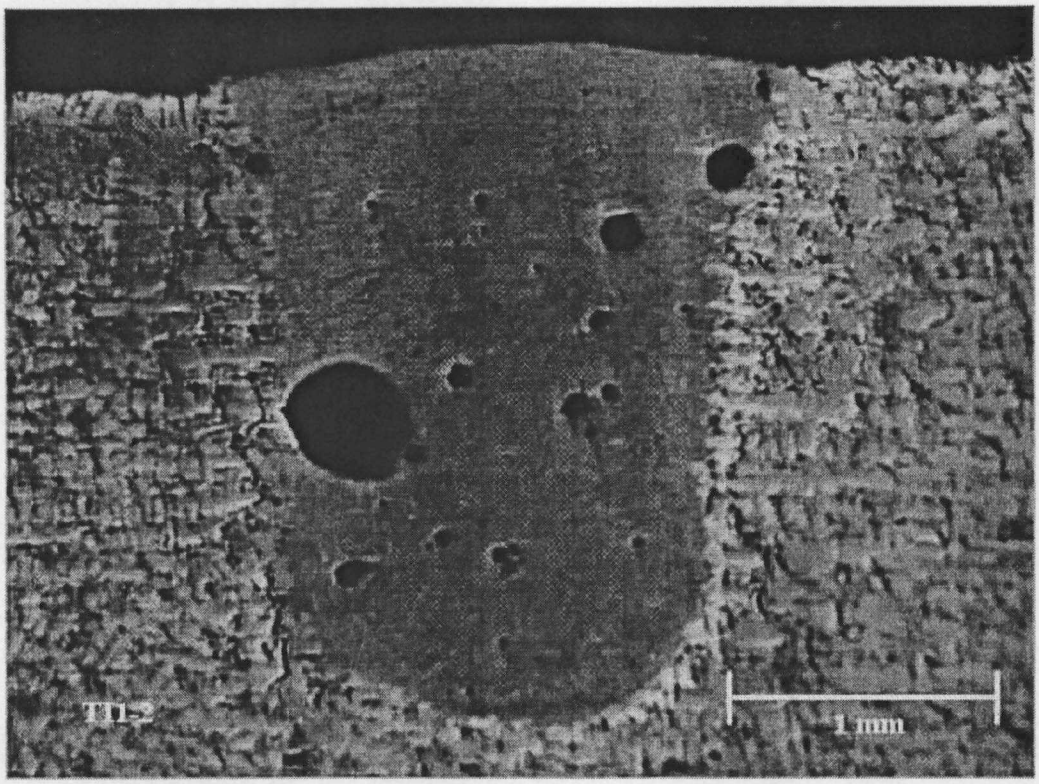
B4: Sample TI4-1 titanium on iron in air



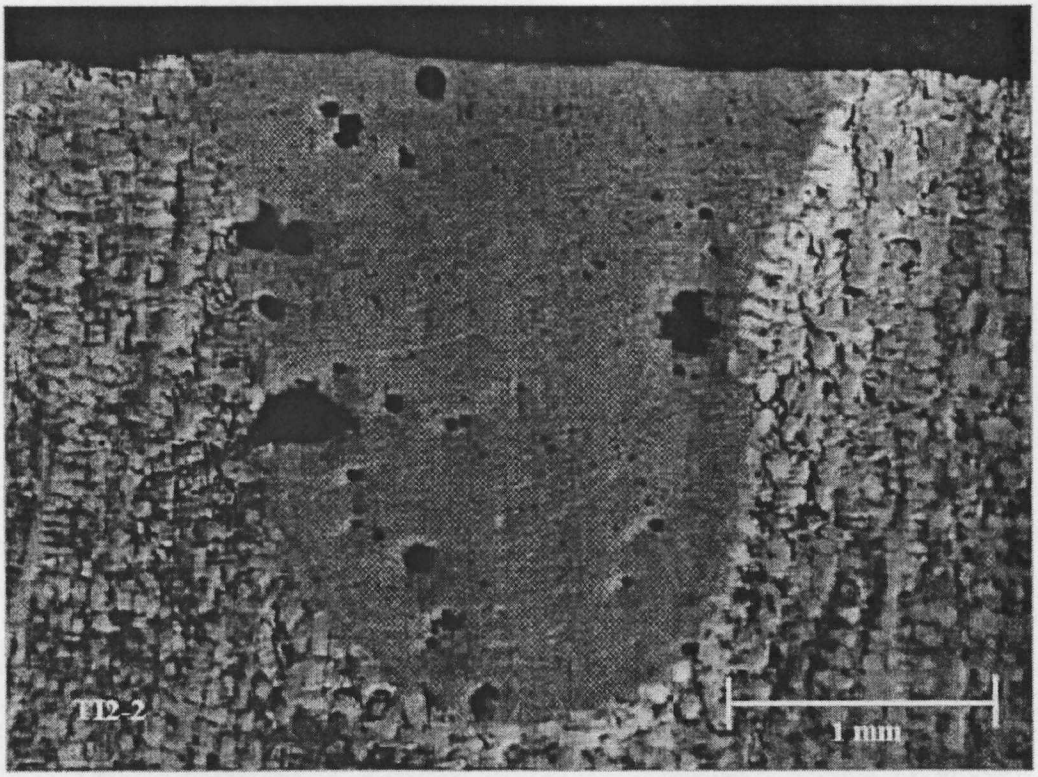
B5: Sample TI5-1 titanium on iron in air



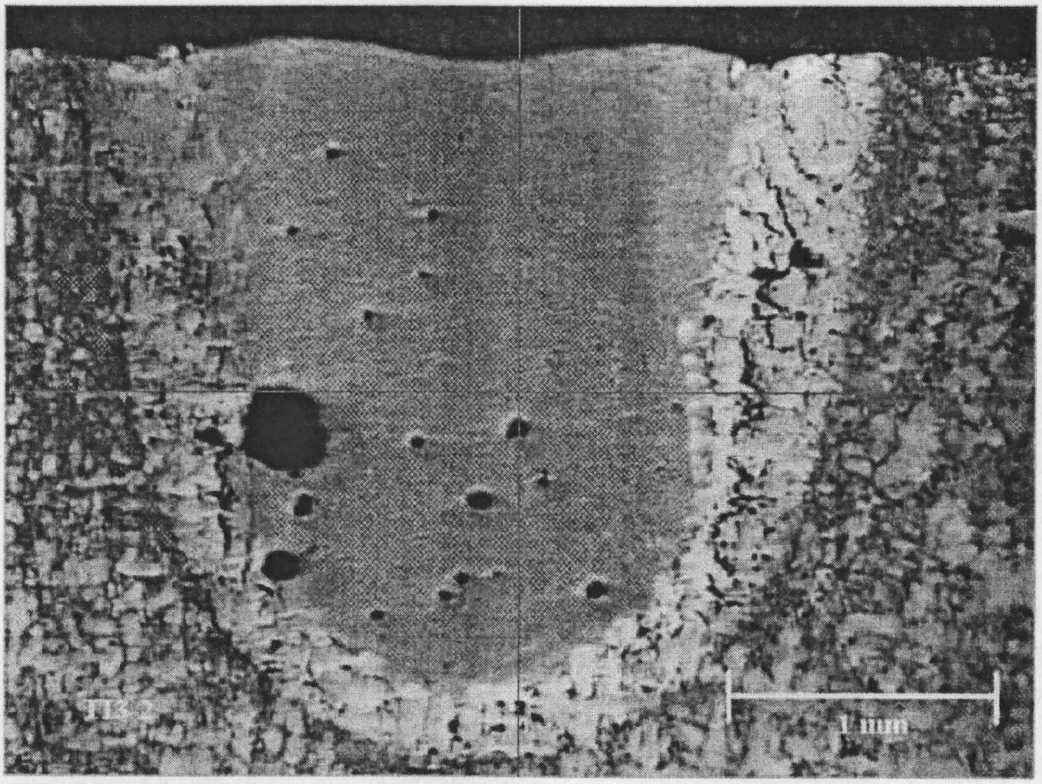
B6: Sample TI6-1 titanium on iron in air



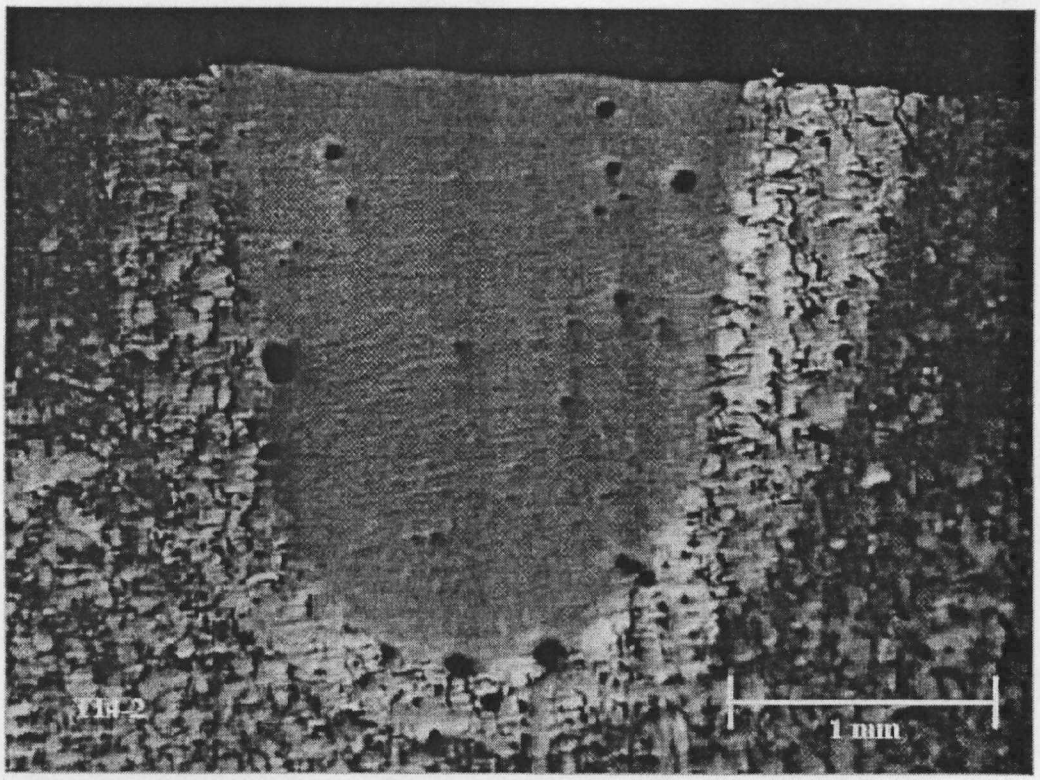
B7: Sample TI1-2 titanium on iron in nitrogen



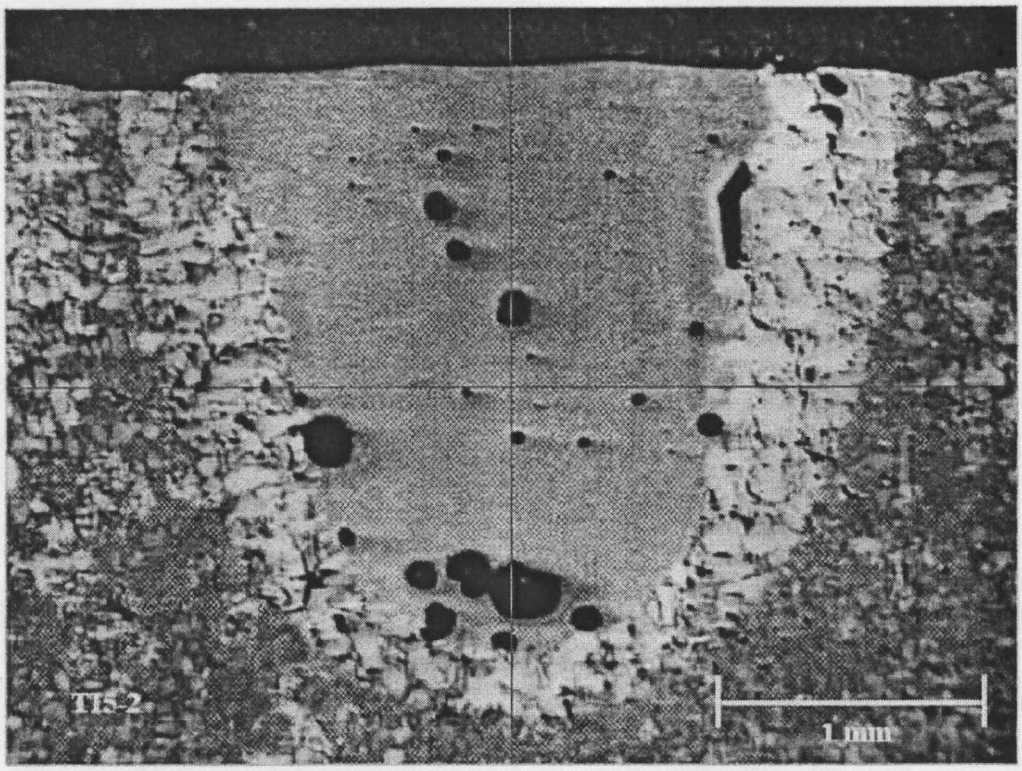
B8: Sample TI2-2 titanium on iron in nitrogen



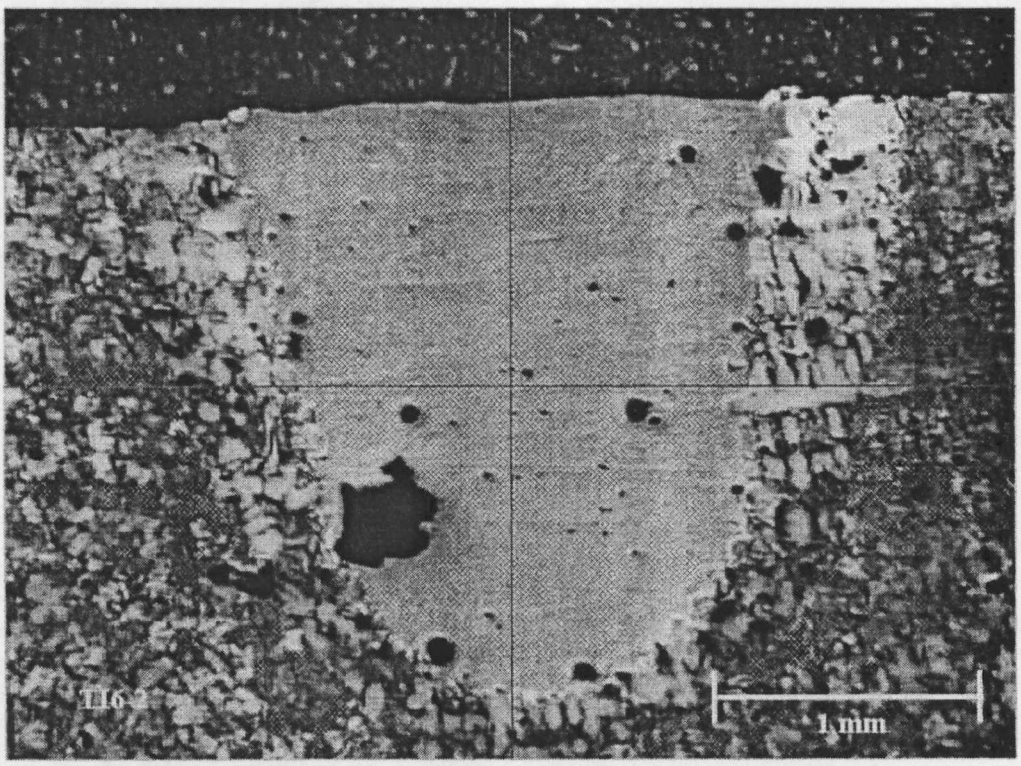
B9: Sample TI3-2 titanium on iron in nitrogen



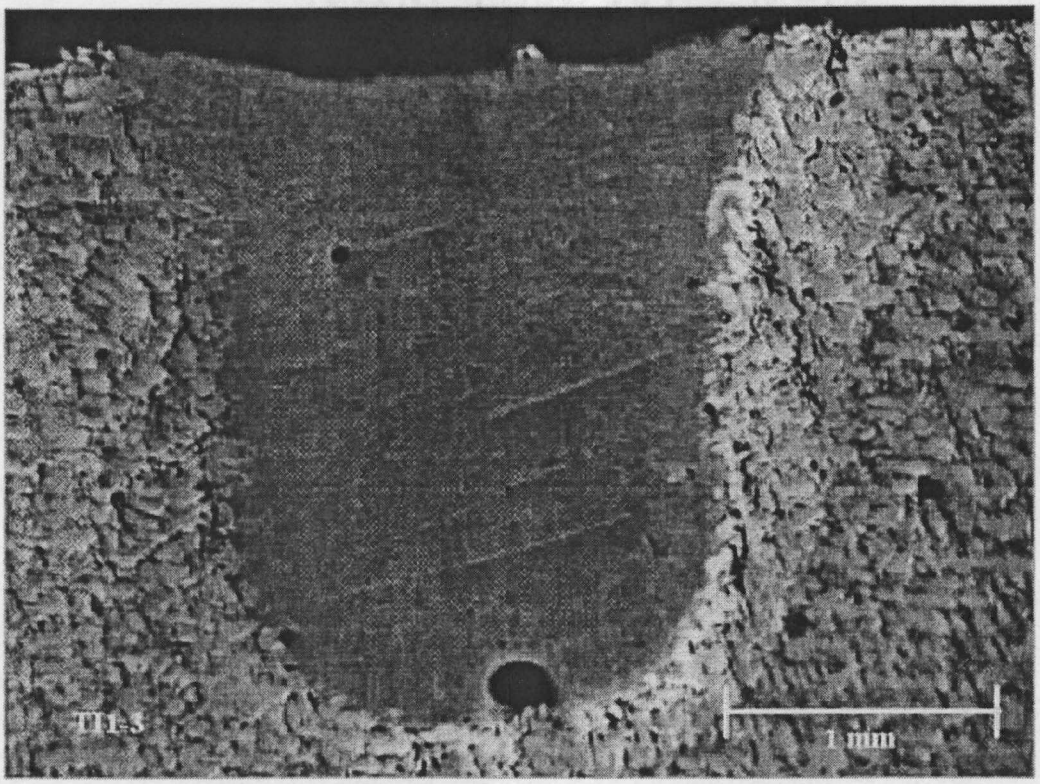
B10: Sample TI4-2 titanium on iron in nitrogen



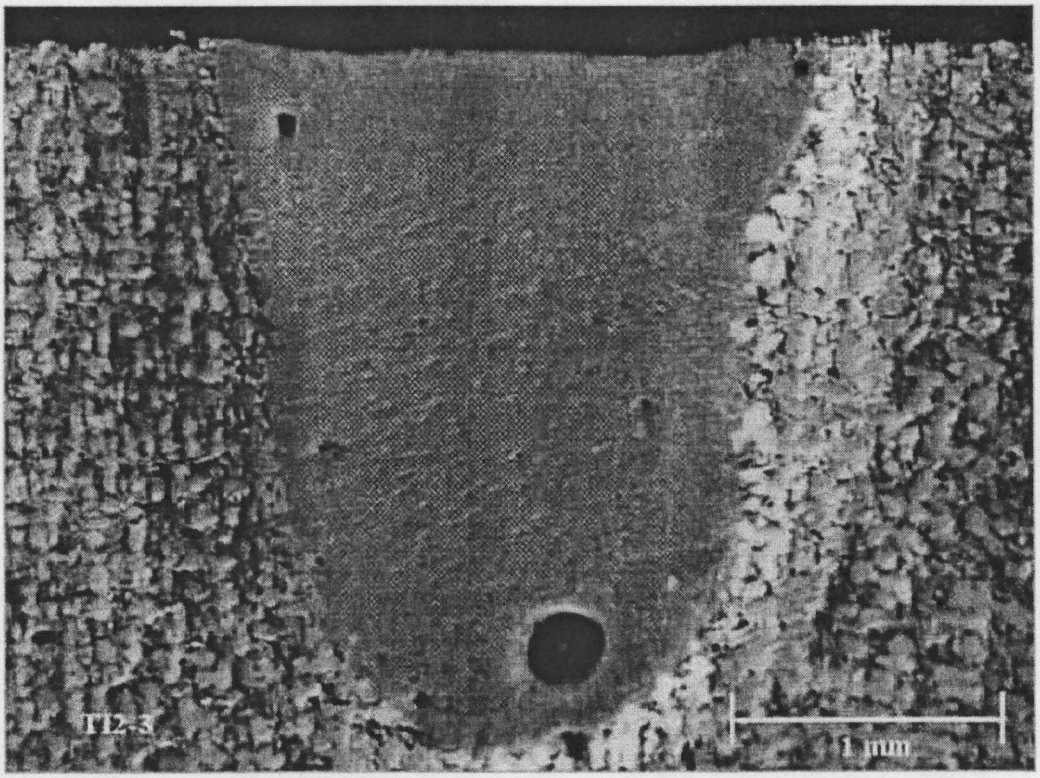
B11: Sample TI5-2 titanium on iron in nitrogen



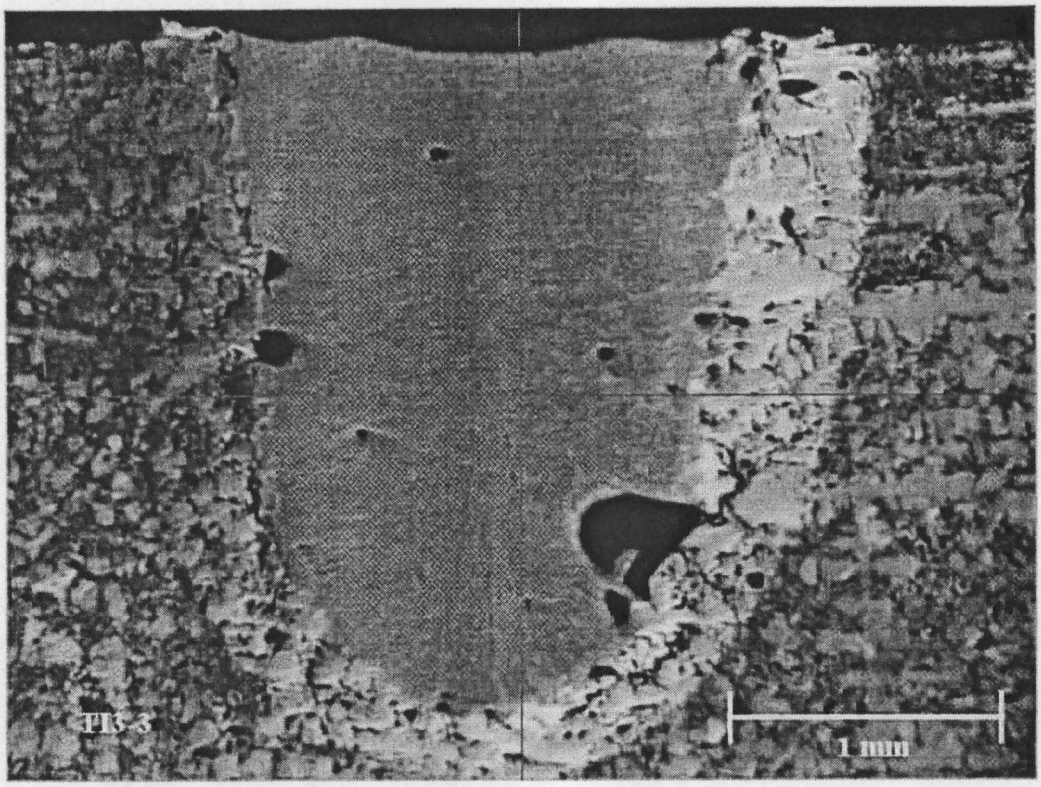
B12: Sample TI6-2 titanium on iron in nitrogen



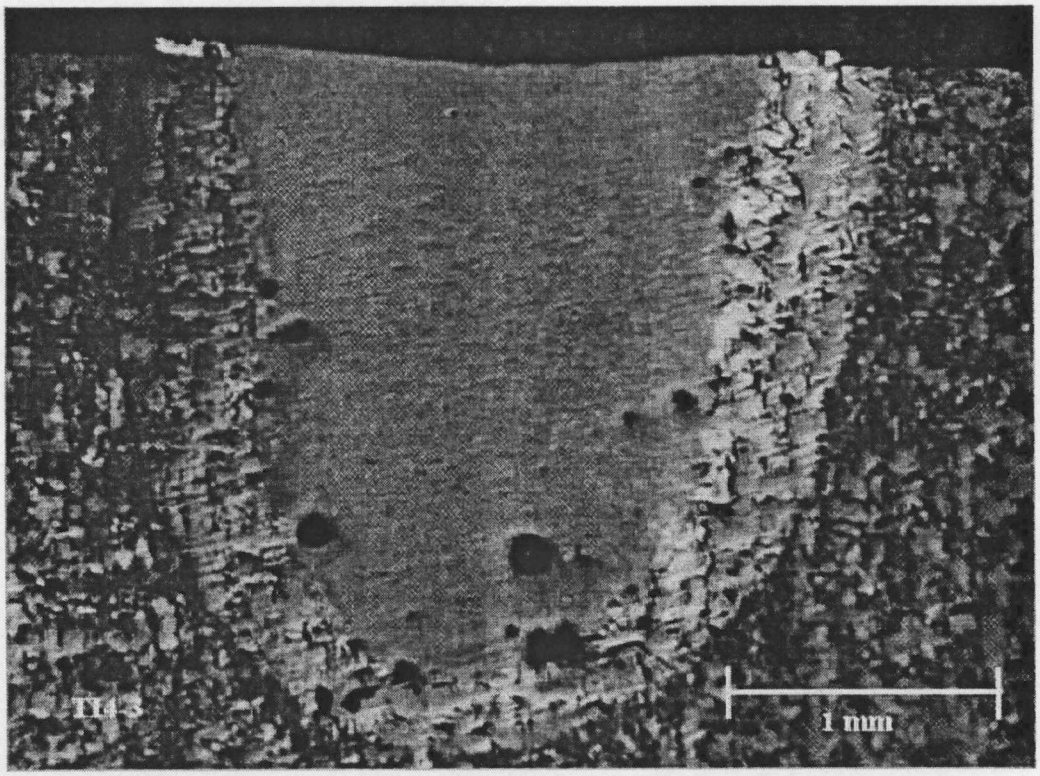
B13: Sample TI1-3 titanium on iron in argon



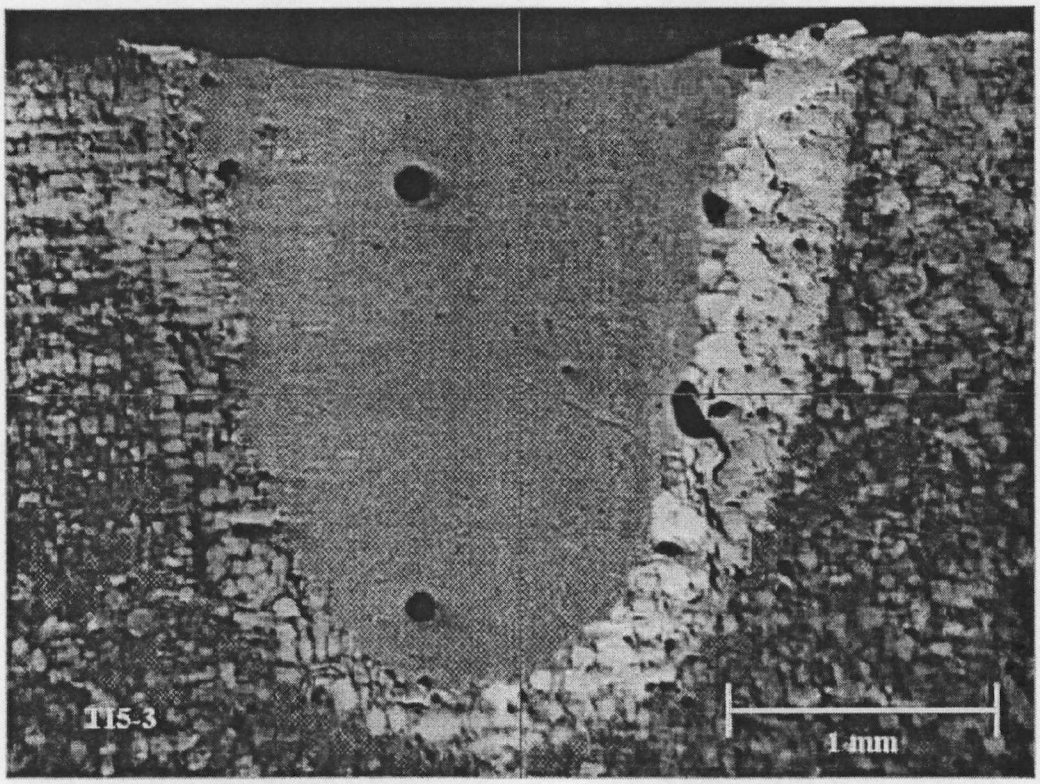
B14: Sample TI2-3 titanium on iron in argon



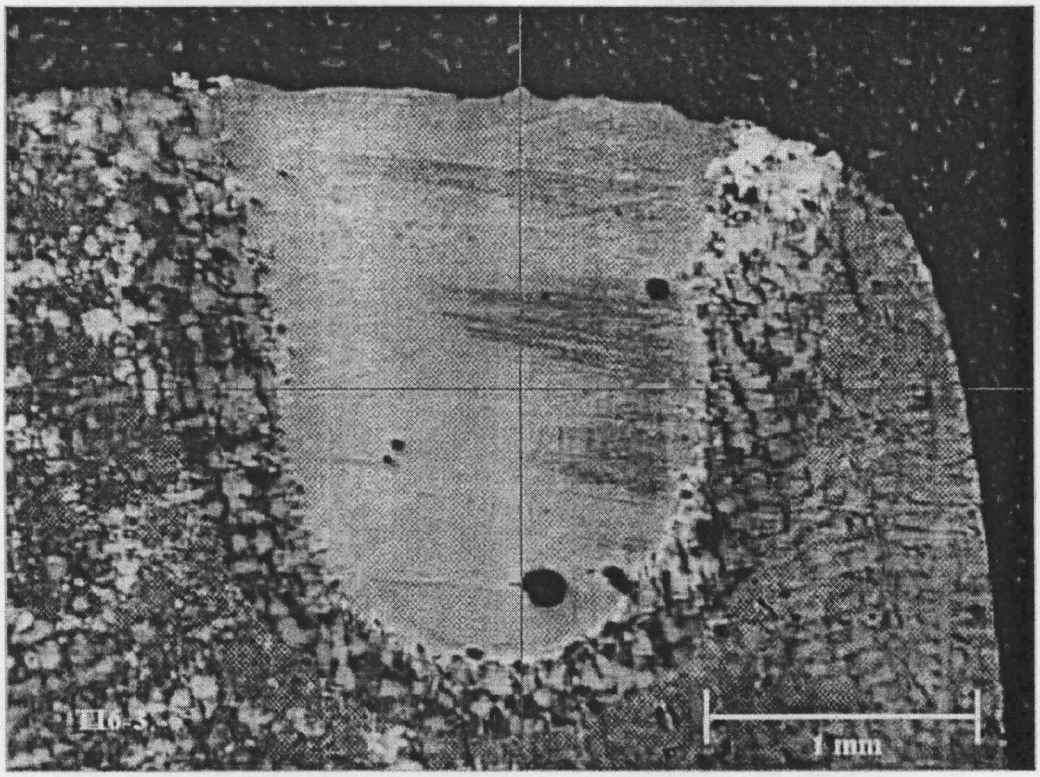
B15: Sample TI3-3 titanium on iron in argon



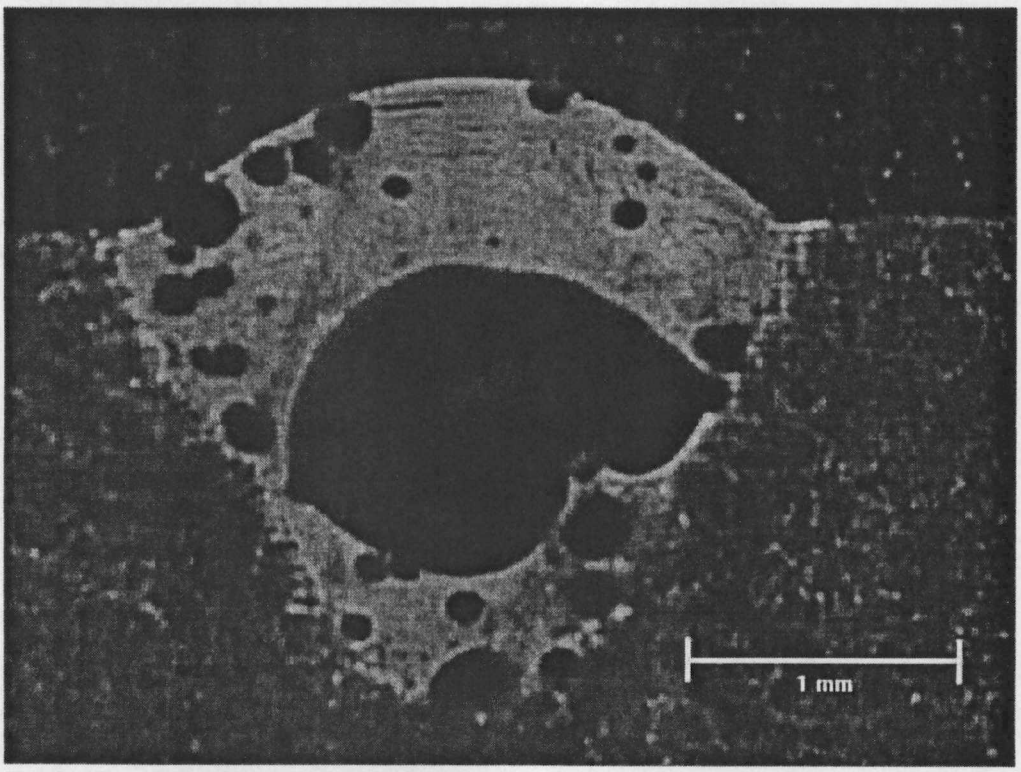
B16: Sample TI4-3 titanium on iron in argon



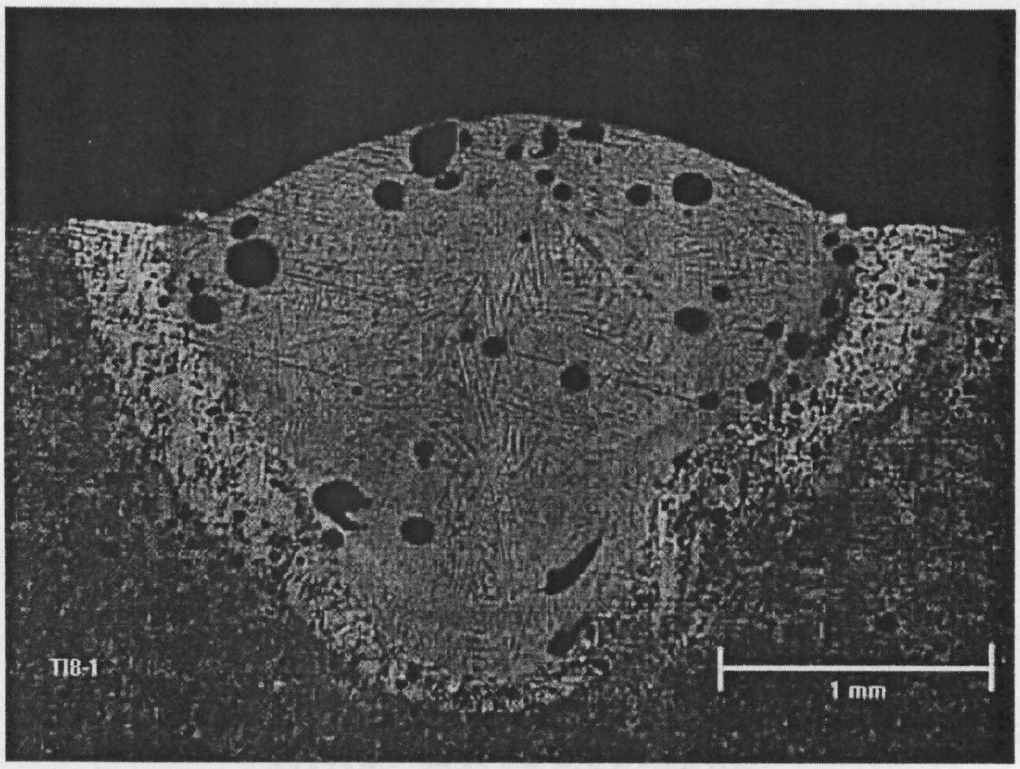
B17: Sample TI5-3 titanium on iron in argon



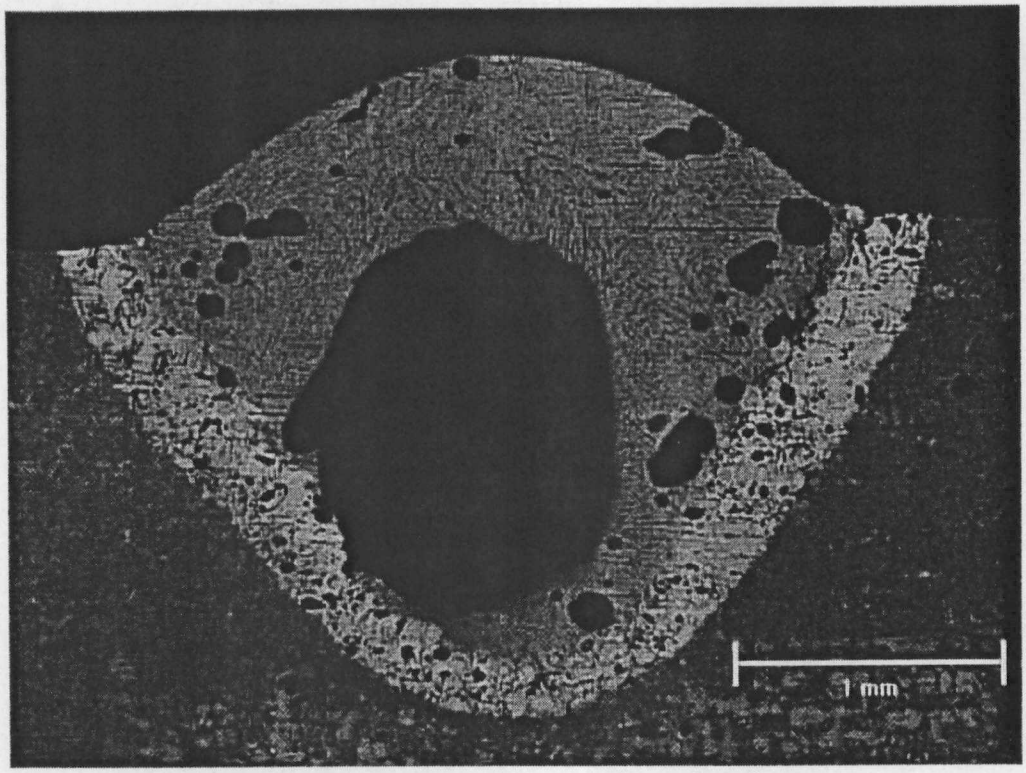
B18: Sample TI6-3 titanium on iron in argon



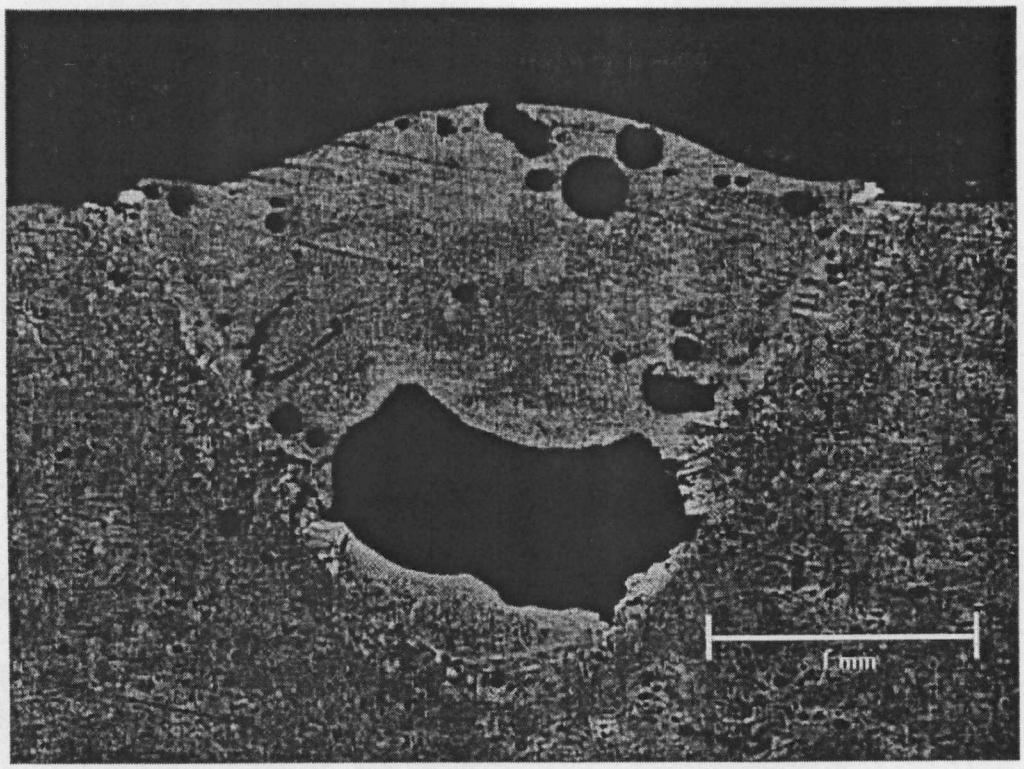
B19: Sample TI7-1 Titanium on gray iron in air



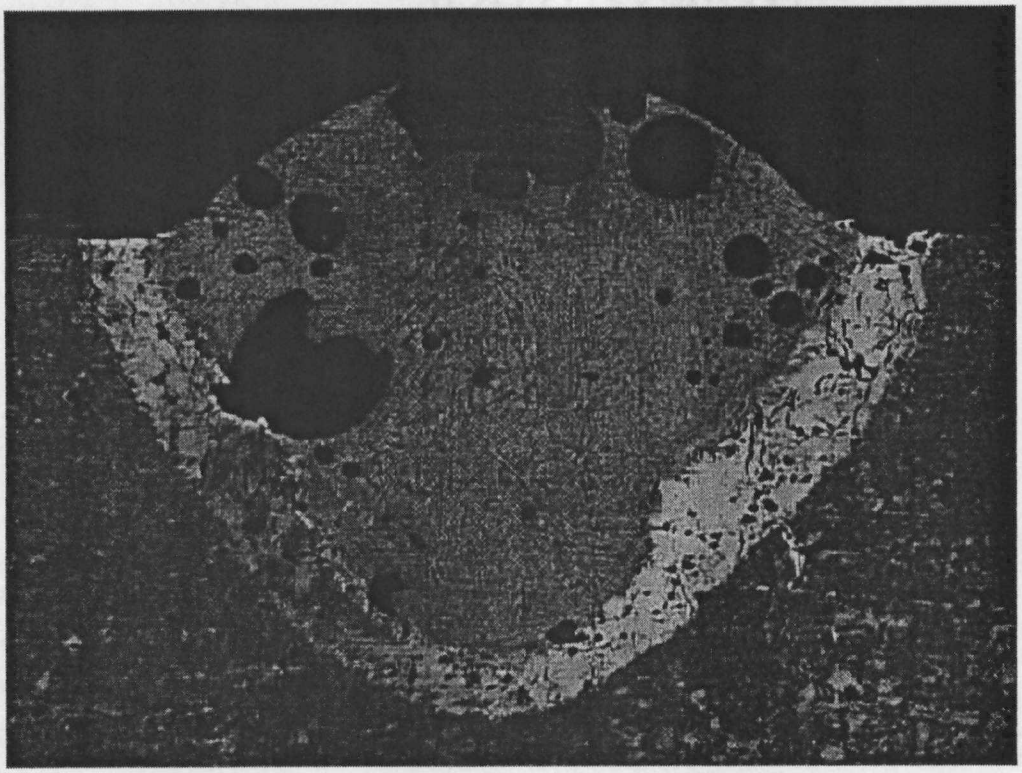
B20: Sample TI8-1 Titanium on gray iron in air



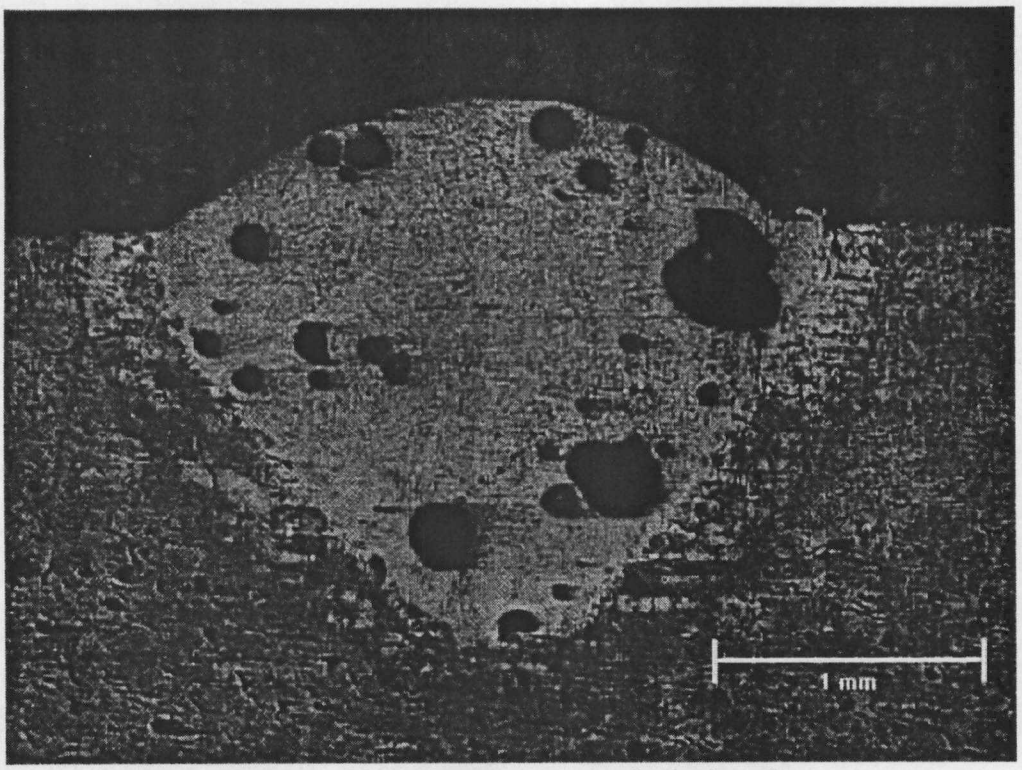
B21: Sample TI9-1 Titanium on gray iron in air



B22: Sample TI10-1 Titanium on gray iron in air

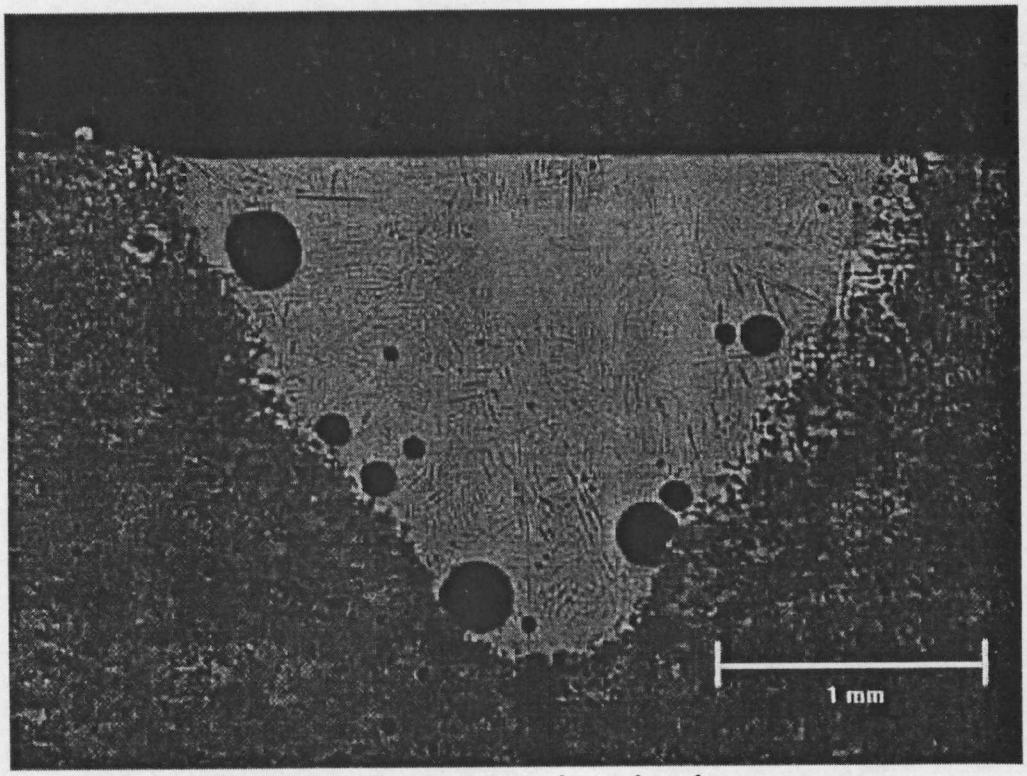


B23: Sample TI11-1 Titanium on gray iron in air

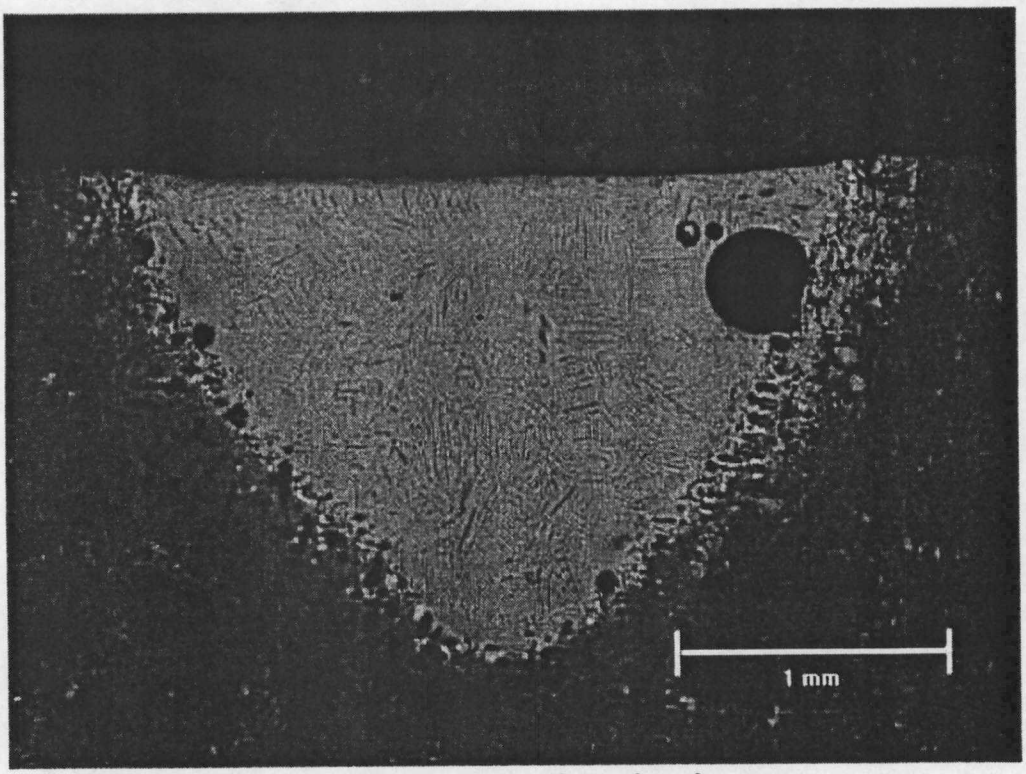


B24: Sample TI12-1 Titanium on gray iron in air

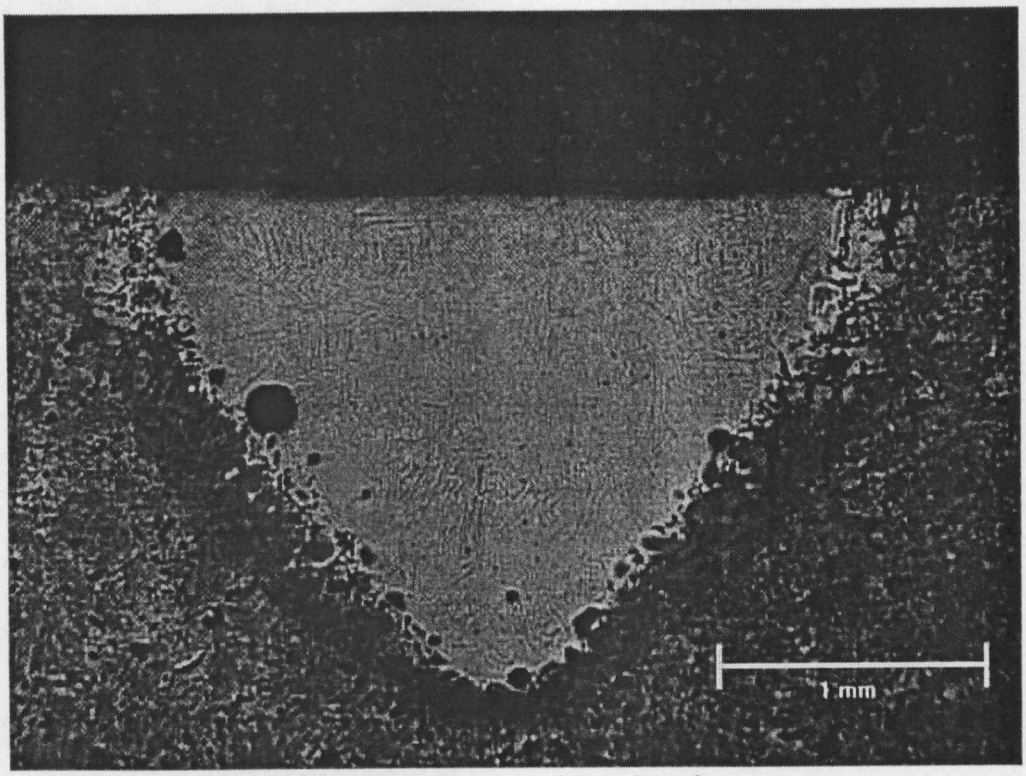
Appendix C
Cross-sectional Photos of Binder on Iron (BI) Samples



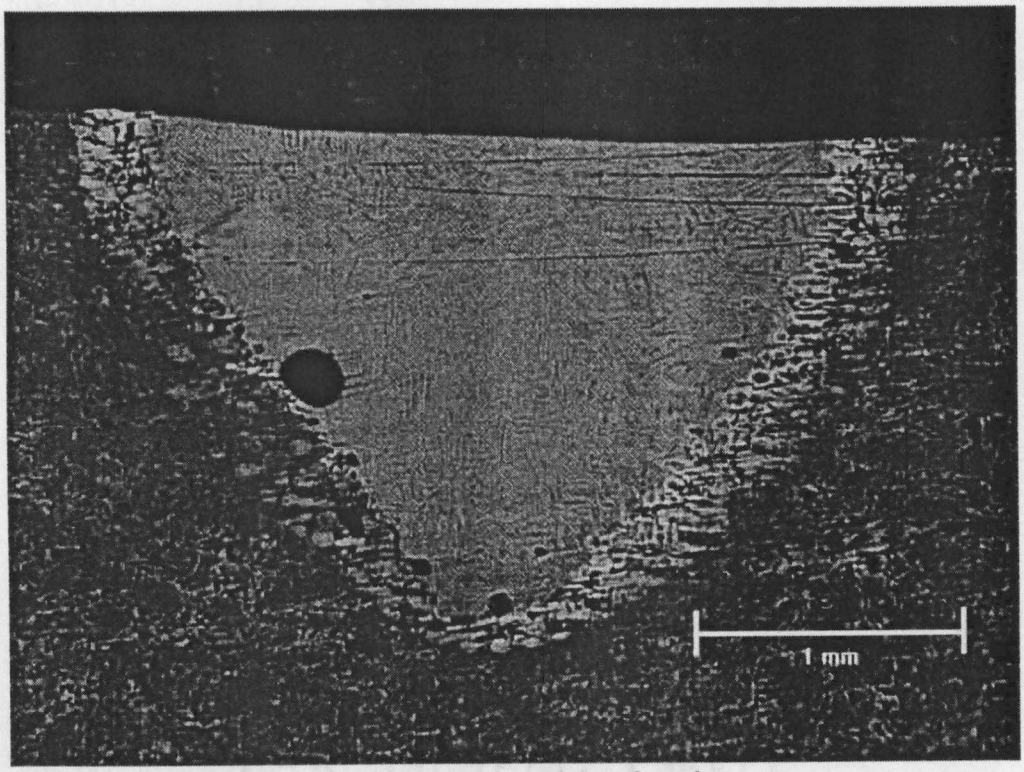
C1: Sample BI1-1 binder on gray iron in air



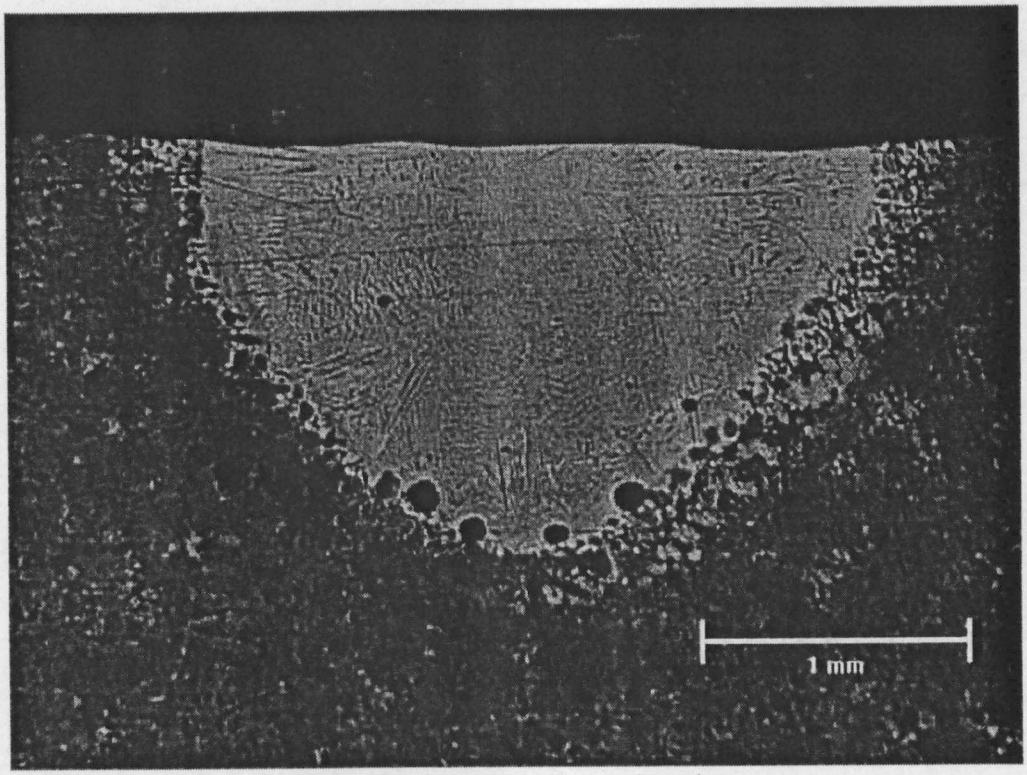
C2: Sample BI2-1 binder on gray iron in air



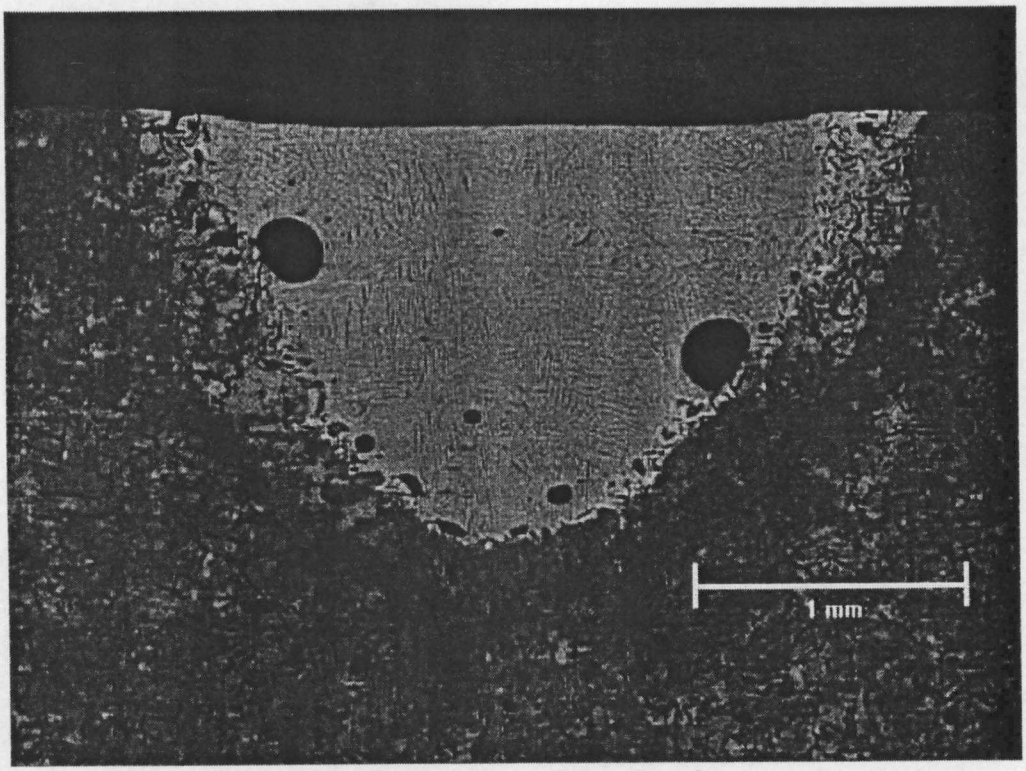
C3: Sample BI3-1 binder on gray iron in air



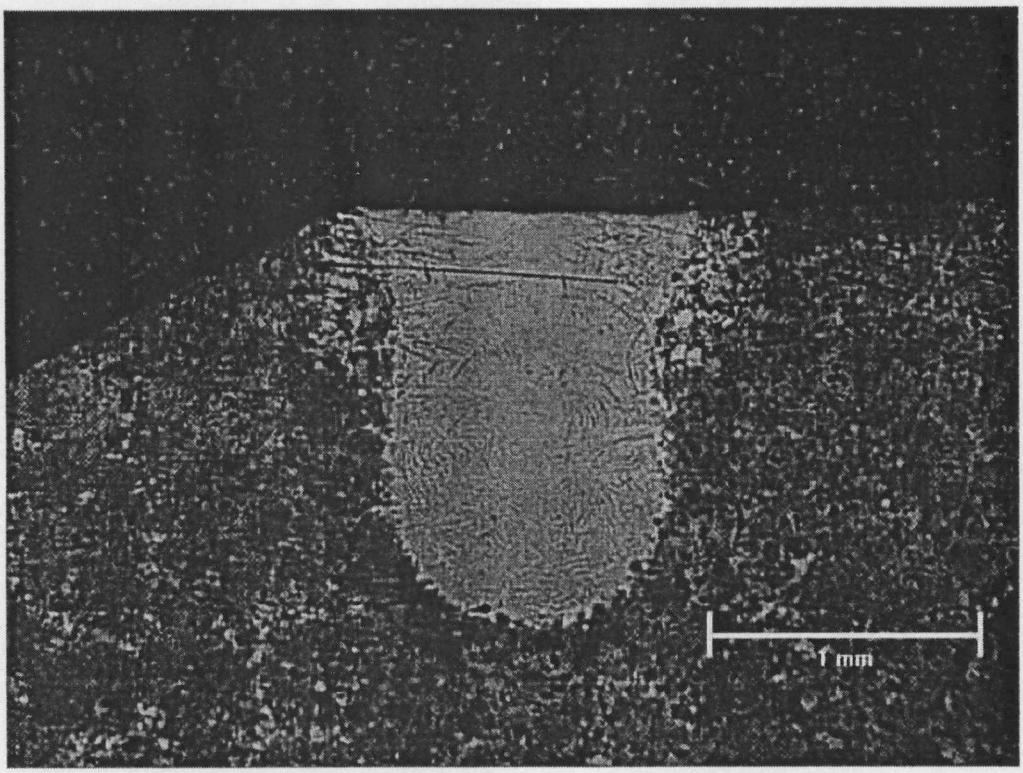
C4: Sample BI4-1 binder on gray iron in air



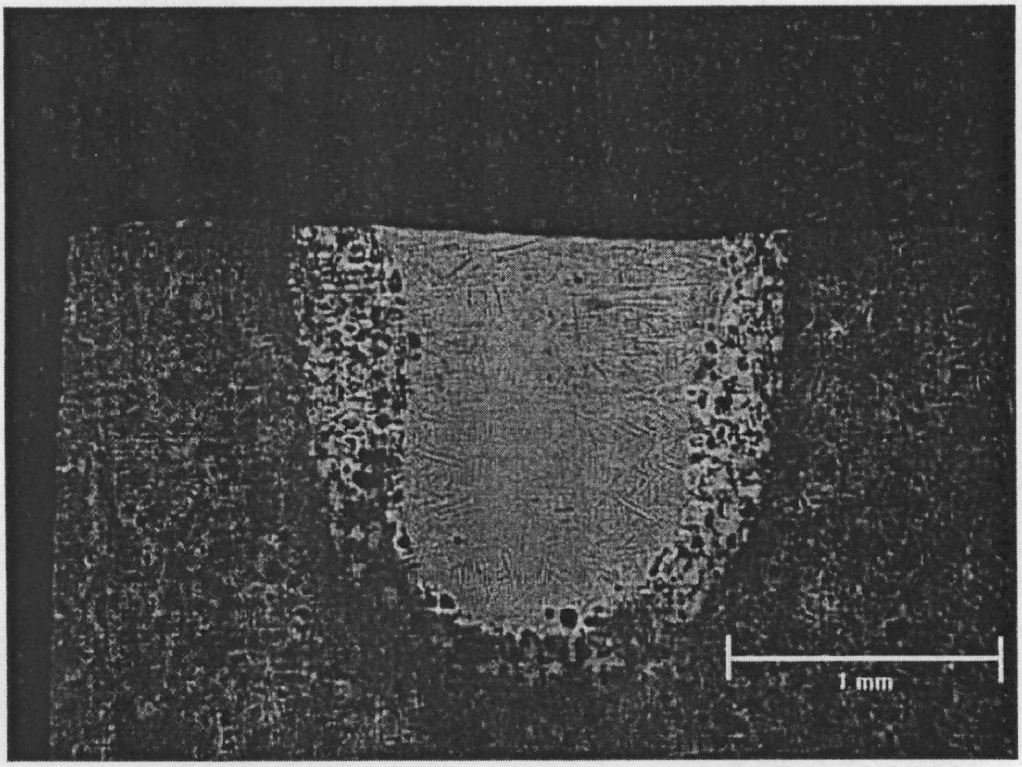
C5: Sample BI5-1 binder on gray iron in air



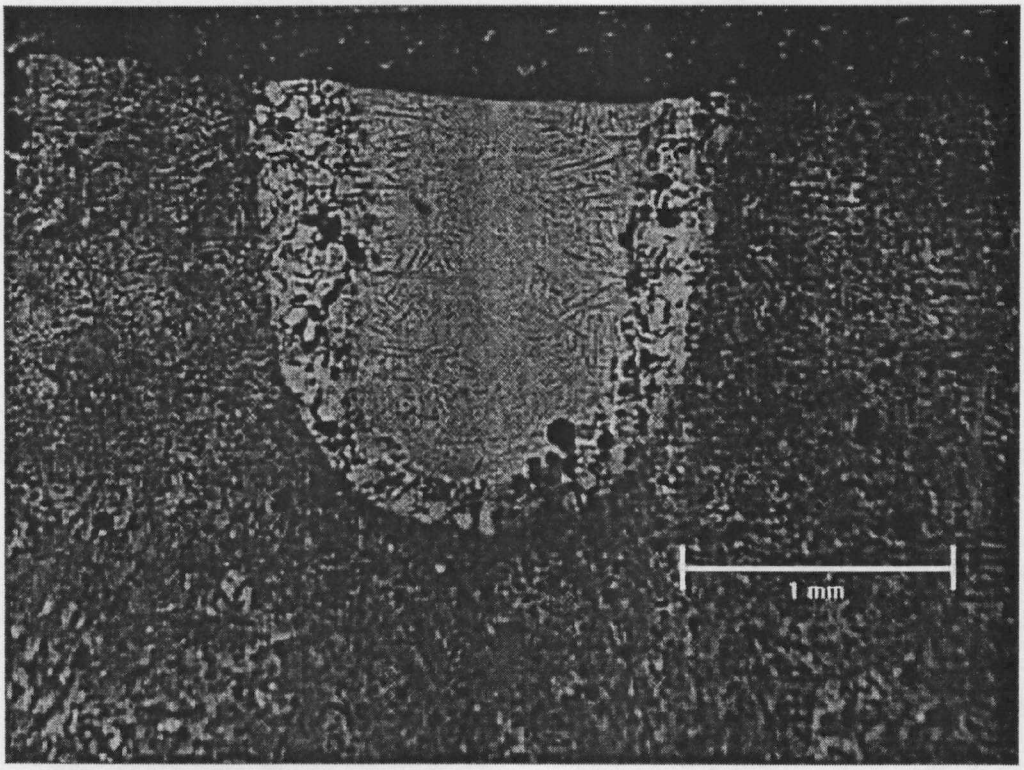
C6: Sample BI6-1 binder on gray iron in air



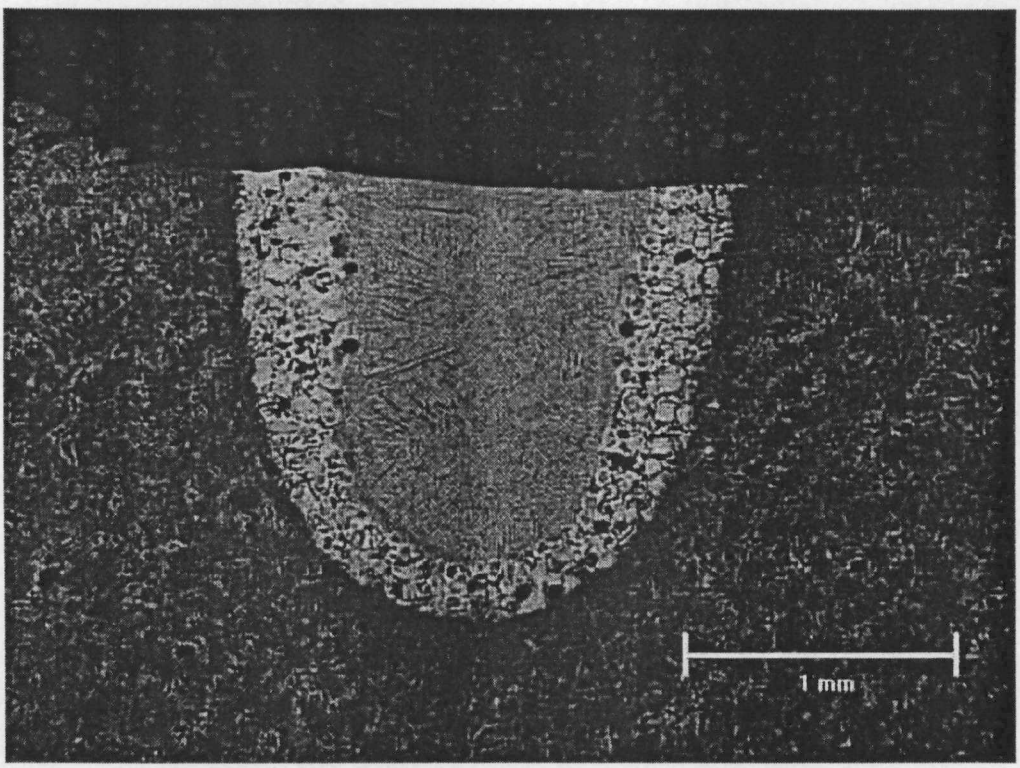
C7: Sample BI1-2 binder on gray iron in nitrogen



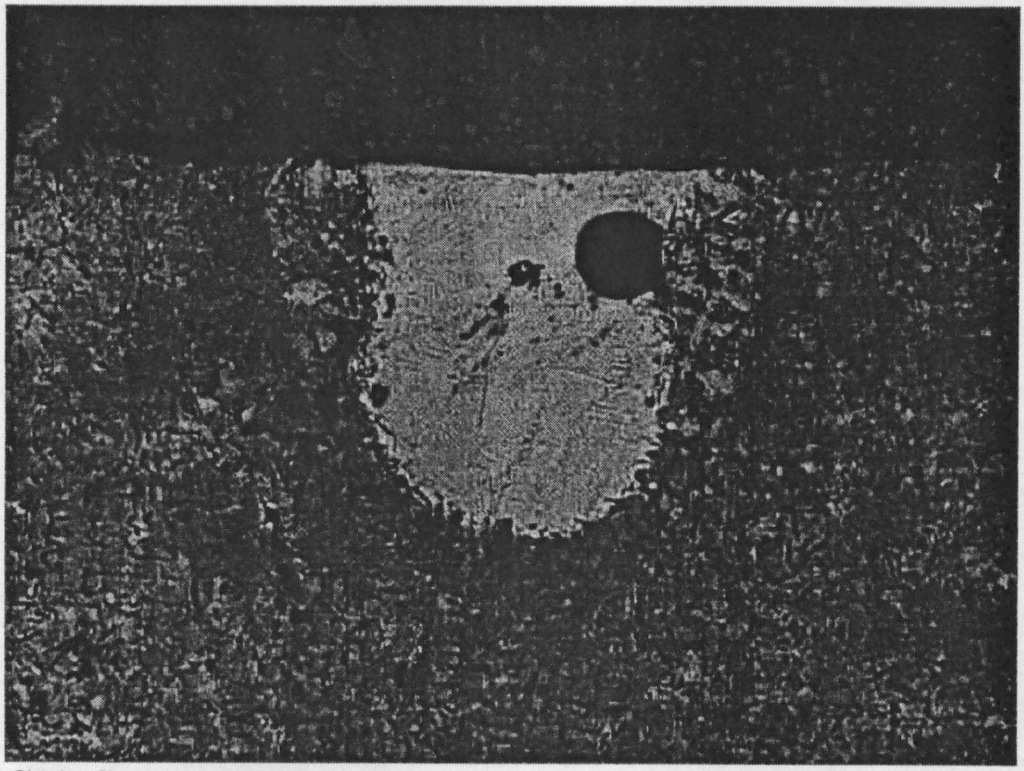
C8: Sample BI2-2 binder on gray iron in nitrogen



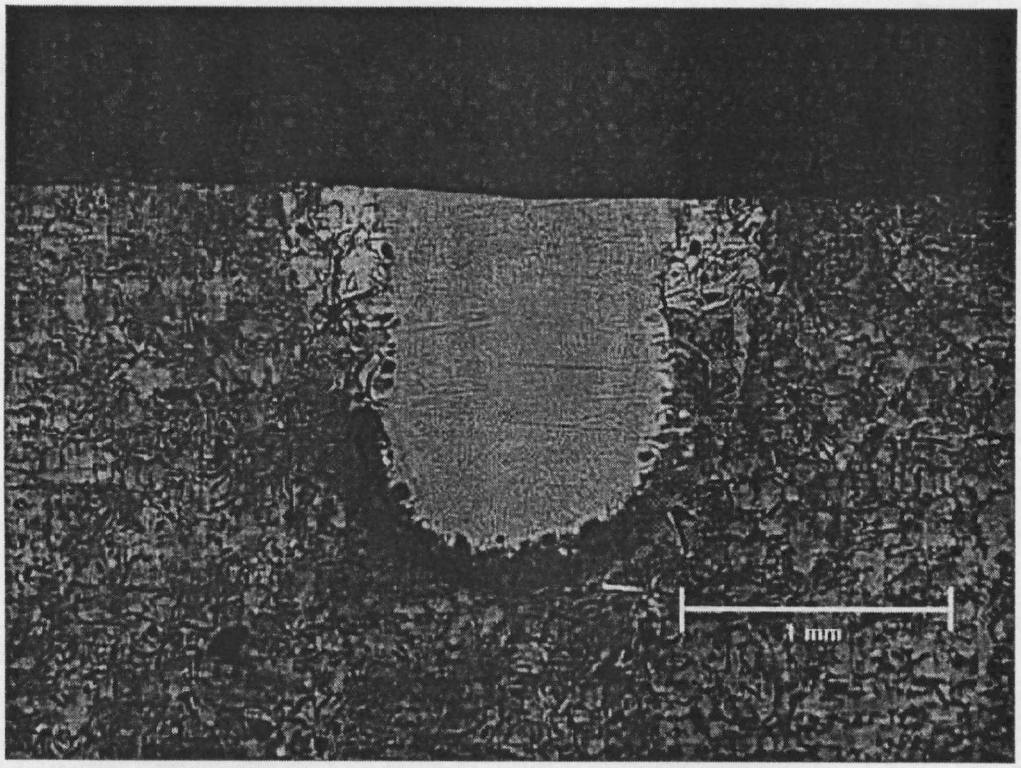
C9: Sample BI3-2 binder on iron in nitrogen



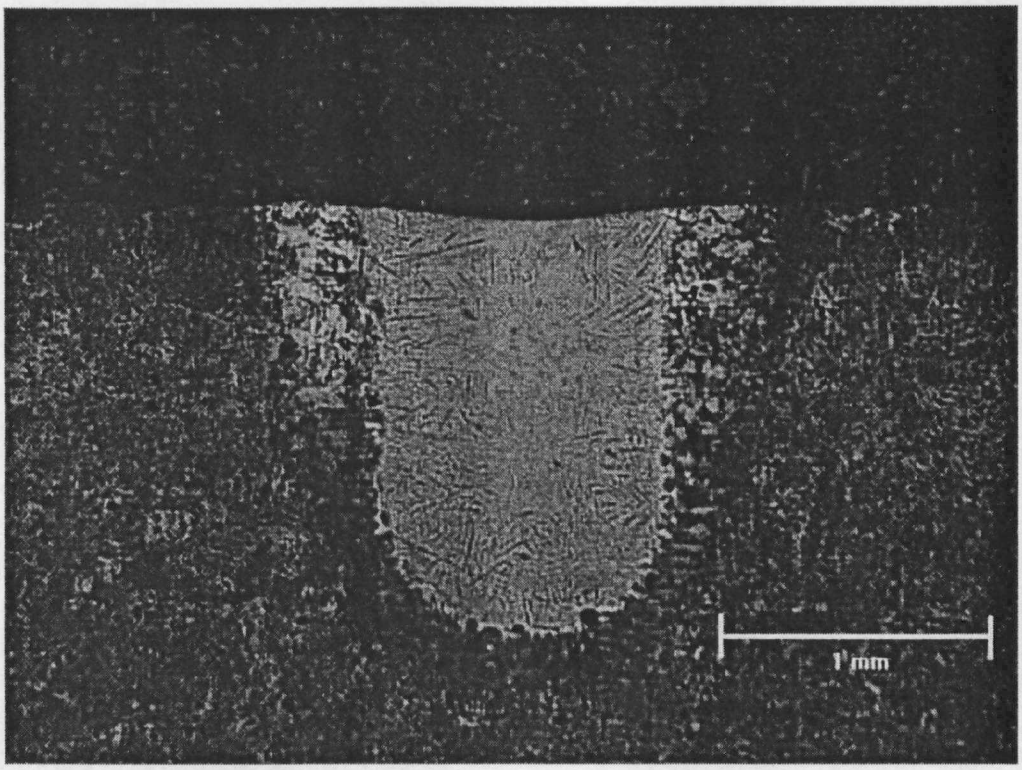
C10: Sample BI4-2 binder on gray iron in nitrogen



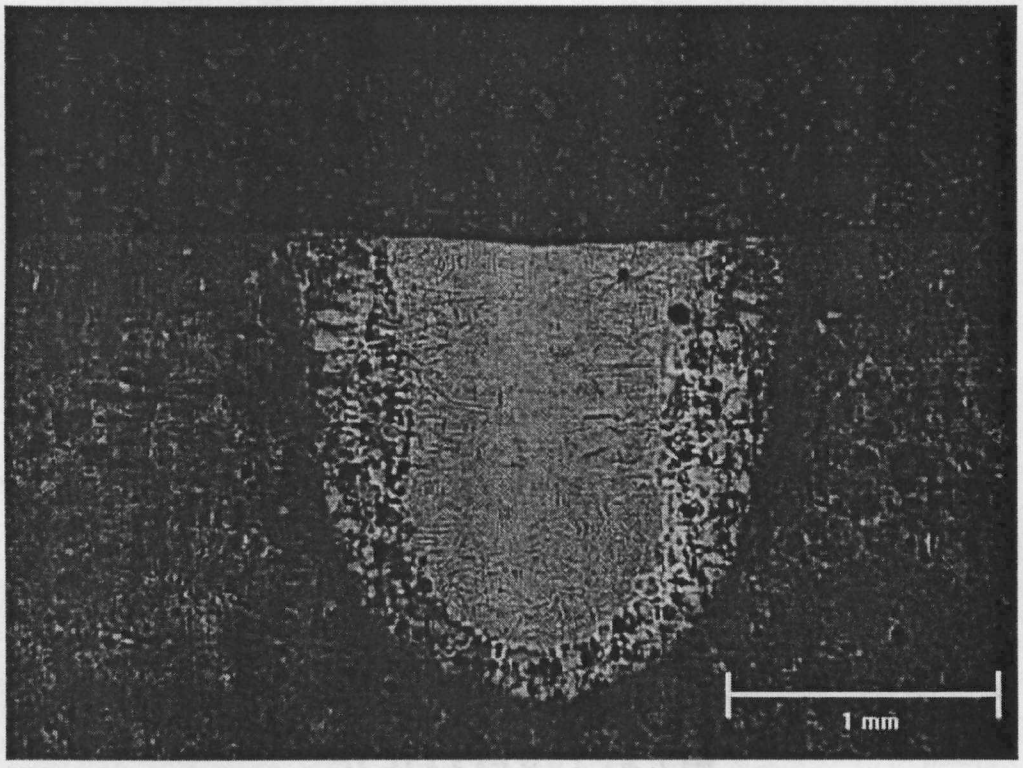
C11: Sample BI5-2 binder on gray iron in nitrogen



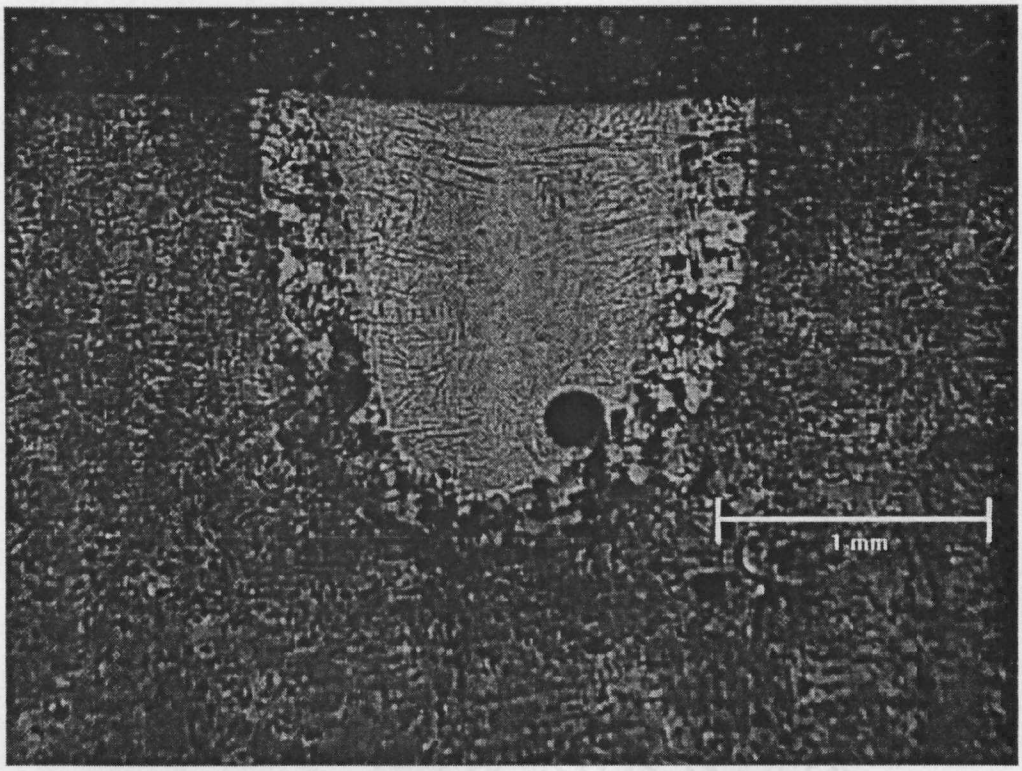
C12: Sample BI6-2 binder on gray iron in nitrogen



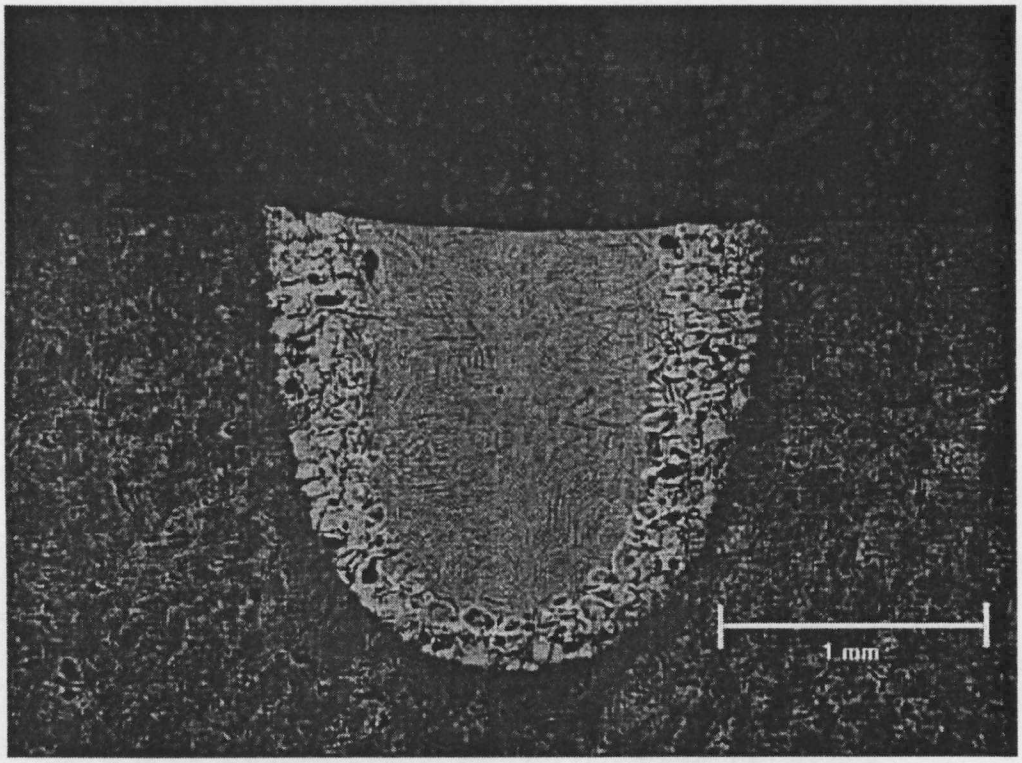
C13: Sample BI1-3 binder on gray iron in argon



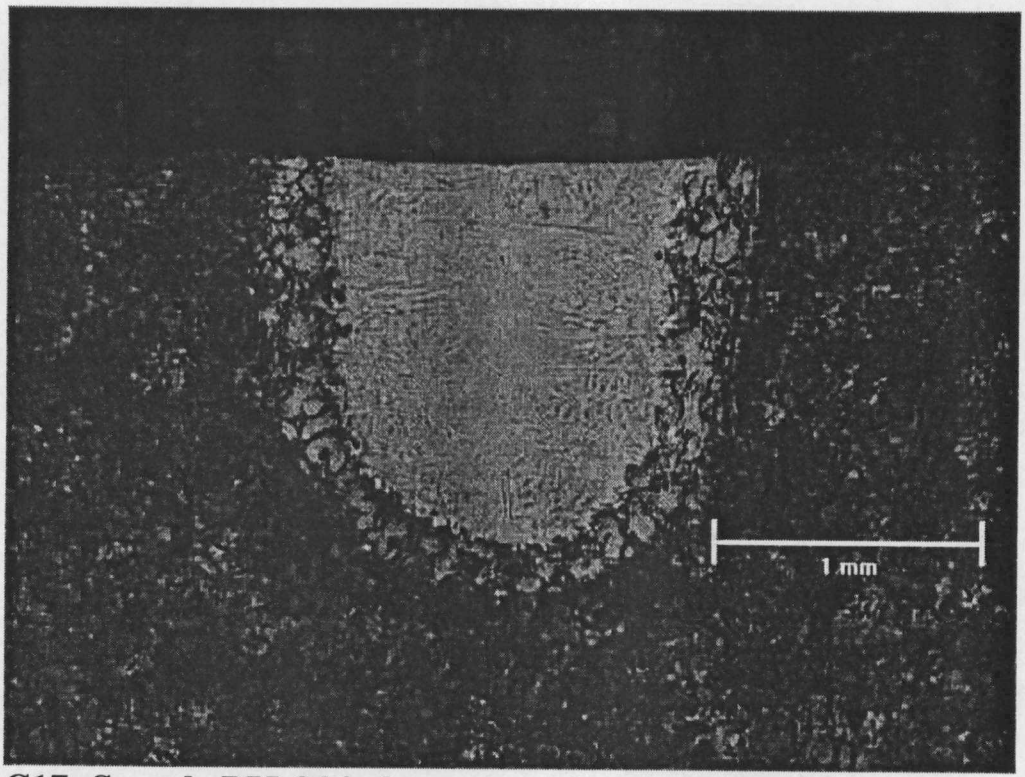
C14: Sample BI2-3 binder on gray iron in argon



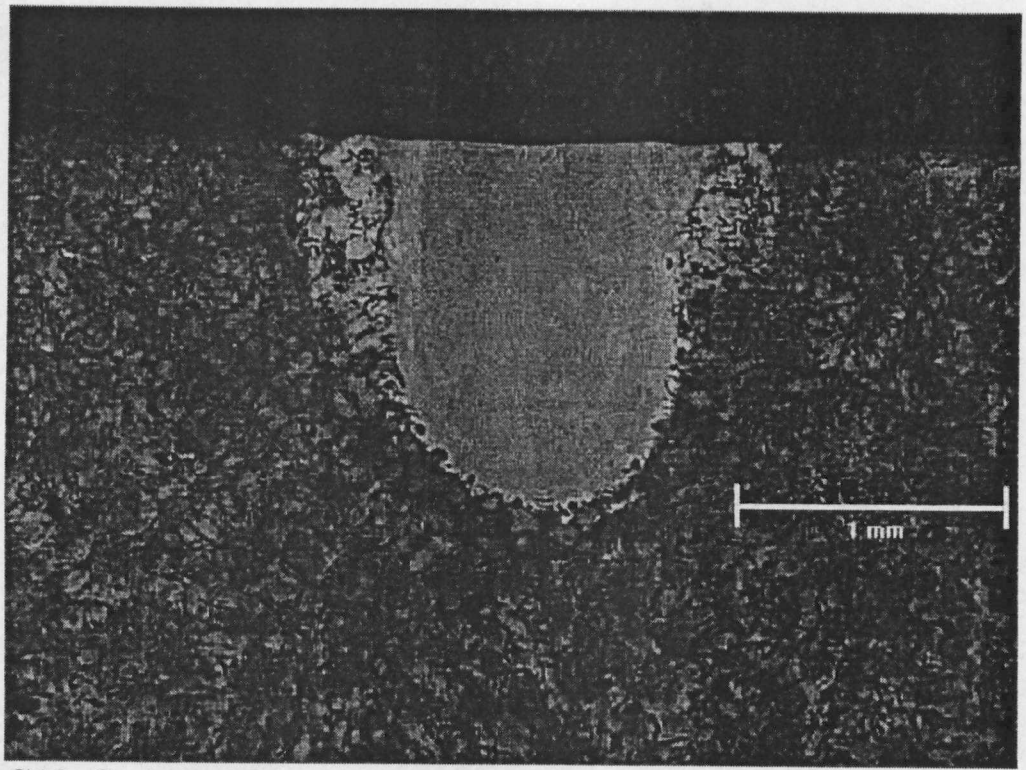
C15: Sample BI3-3 binder on gray iron in argon



C16: Sample BI4-3 binder on gray iron in argon



C17: Sample BI5-3 binder on gray iron in argon



C18: Sample BI6-3 binder on gray iron in argon

Appendix D
X-ray Diffraction Analysis Report

X-ray Diffraction Analysis Report

M White

July 7, 1999

Sample 1: Sample designation GI3, being a grey cast iron having three melt tracks from laser processing in air (GI3-1), in nitrogen (GI3-2), and in argon (GI3-3)

Sample 2: Sample designation TI3, the same grey cast iron having three melt tracks from laser processing in air (TI3-1), in nitrogen (TI3-2), and in argon (TI3-3), all with incorporation of titanium into the melt tracks

Analysis Requested by: Denise Duncan

Objective of Analysis Request: To look for existence of internal oxides, nitrides, or carbides in the melt tracks

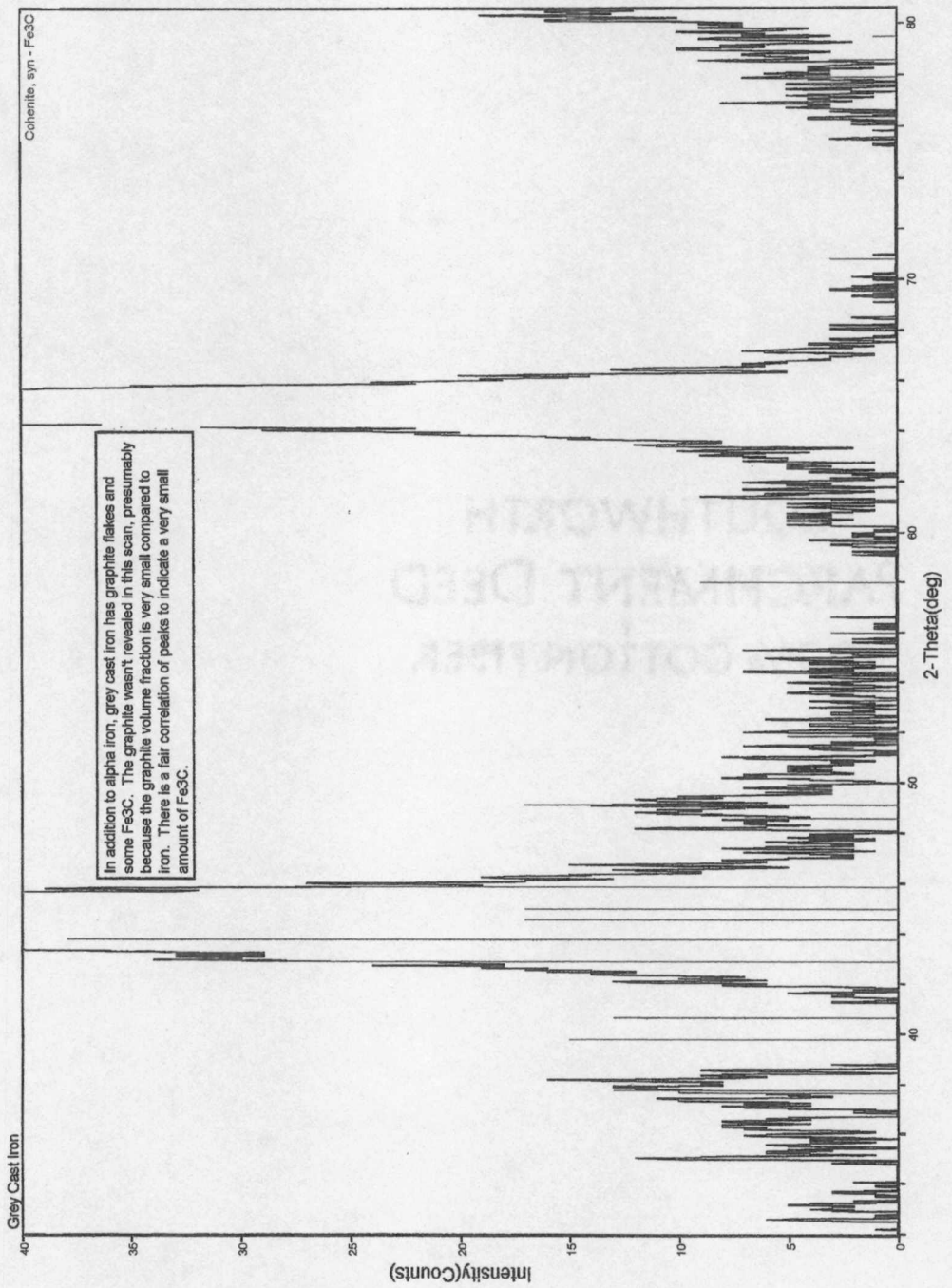
Procedures: Using the Philips Norelco diffractometer, the incident beam divergence slit was narrowed so that the beam just covered the narrowest of the tracks, and a scan was done on each individual track with the fixed divergence slit. The scans were done from 20 to 100 degrees 2Theta in steps of 0.05 degrees with 5 seconds counting time per step. Additionally, a scan was run on the unprocessed grey cast iron for comparison. However, that scan was done with variable divergence slit and with the beam covering a 0.5 inch wide area of the sample.

Conclusions:

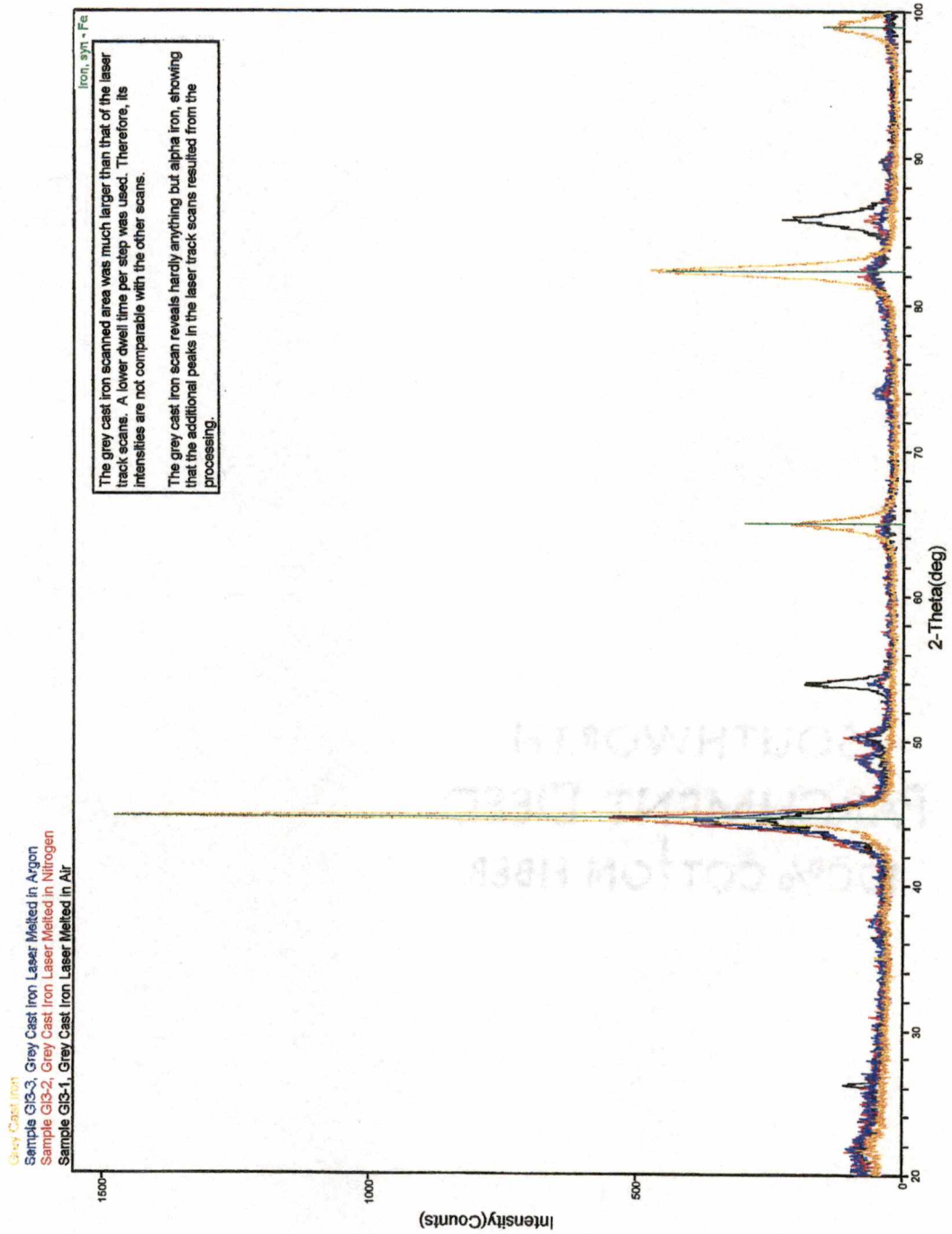
- The area of the melt tracks was too small to get sufficient diffracted intensities to detect minor or trace amounts of internal oxides or nitrides.
- Major differences were revealed between the processed and unprocessed grey cast iron. Whereas the unprocessed material revealed only ferrite and an almost trace amount of Fe3C, the processed samples appeared to have relatively more Fe3C and also to have significant amounts of some other phases which were probably carbides with compositions similar to FeC and Fe5C2.
- Identification of phases by comparison of diffraction peaks with known peak locations and intensities for single phase materials included in the PDF database is quite dependent on the grains in the sample being randomly oriented This is not the case with laser melt tracks, which possess strong preferred orientations. Consequently, some peaks for a given phase will have (perhaps much) greater and some peaks will have (perhaps much) lower intensities than would be the case for a randomly oriented sample. This makes it difficult to identify phases because peak relative intensities are different from the reference phases and some peaks may be missing. Also, it complicates comparison of a scan of one track to a scan of another track, because there is no assurance that both tracks have the same preferred orientation or degree of preferred orientation.
- Another difficulty exists relative to identification of secondary phases such as the carbides present in these samples. The database reference phases are mainly stoichiometric compounds, while the secondary phase compounds in real world samples processed under nonequilibrium conditions are generally everything but stoichiometric. Additionally, the composition of a particular secondary phase is probably highly variable within the analyzed

volume, and what is observed is the effect of the average composition Consequently, it is frustratingly seldom that such phases can be unambiguously identified. Such is the case with these samples. Something approximating Fe3C is certainly present, but it's not stoichiometric Fe3C. Also, phases are probably present with compositions similar to FeC and Fe5C2.

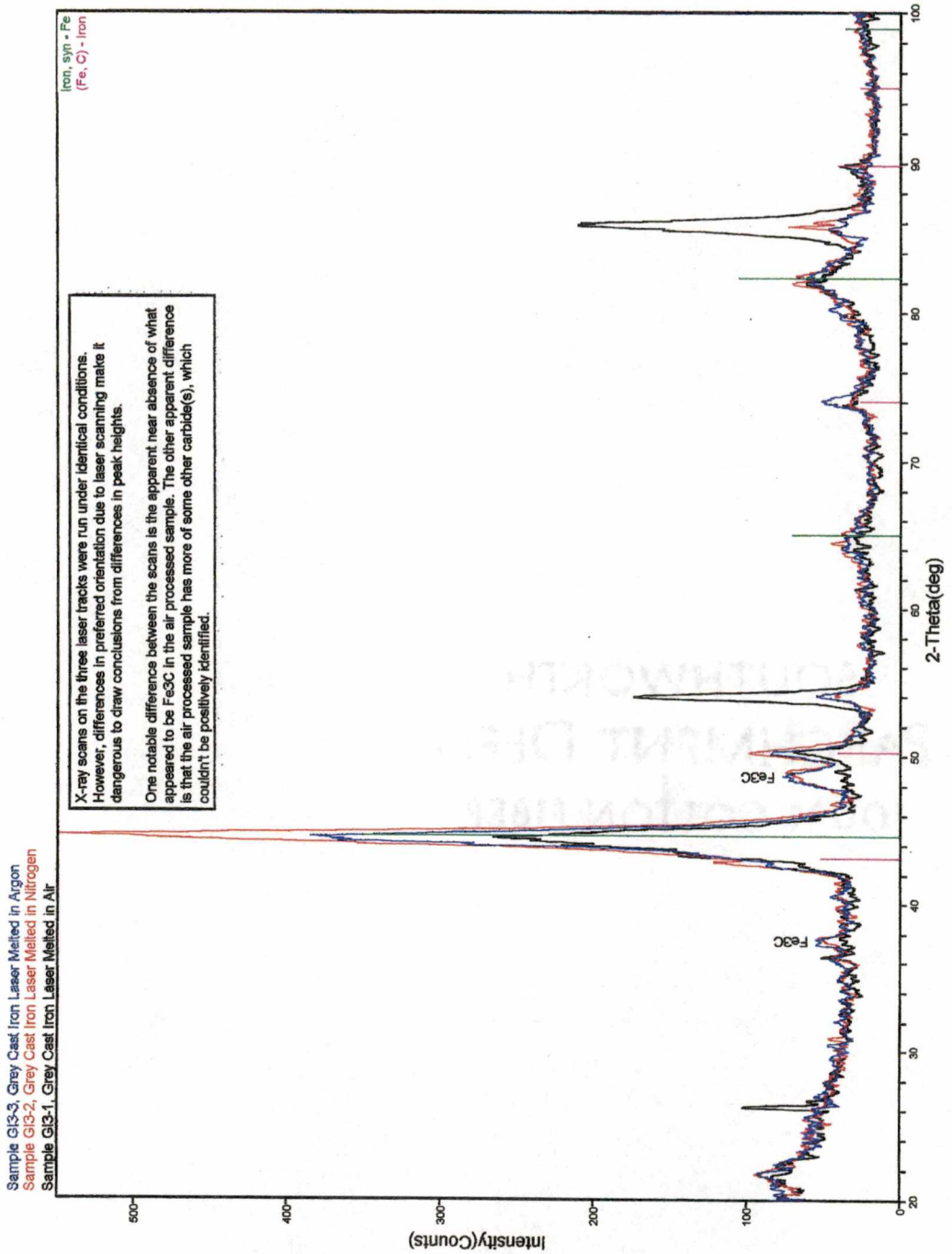
- The predominant crystalline phase indicated in all tracks is alpha iron (ferrite).
- All tracks contained some retained austenite as a result of quenching the high carbon-content iron. A nitrogen atmosphere seemed to result in more retained austenite while air resulted in least. Air perhaps oxidized surface carbon, resulting in less retained austenite in the surface layer. A nitrogen purge will yield a faster quench than argon, accounting perhaps for more retained austenite.
- Air processed tracks showed hardly any Fe3C, while nitrogen processed tracks showed most. In the GI3 sample, much more of other carbides was indicated with air processing. Just the opposite was the case in the TI3 sample, with least of other carbides with air processing.
- Comparison of scans for air processed samples with and without Ti revealed less retained austenite with Ti addition, as well as much less carbides. The two seem at odds. If Ti took carbon out of solution, it would be expected to be present as carbides.
- Comparison of scans for nitrogen processed samples with and without Ti revealed little difference
- Comparison of scans for argon-processed samples with and without Ti revealed that Ti addition resulted in less retained austenite, less Fe3C, and more of other carbides.



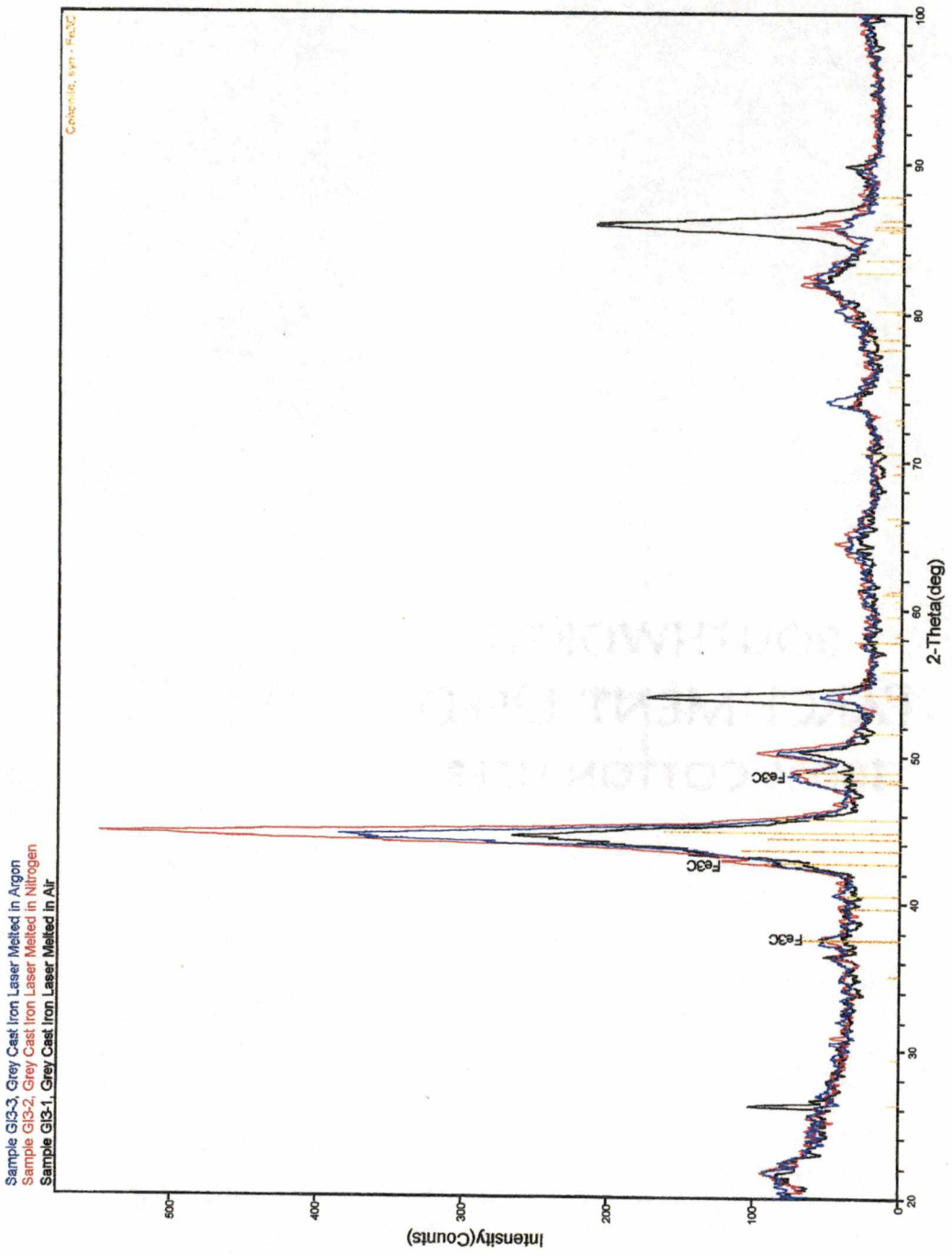
D1: X-ray trace of gray iron



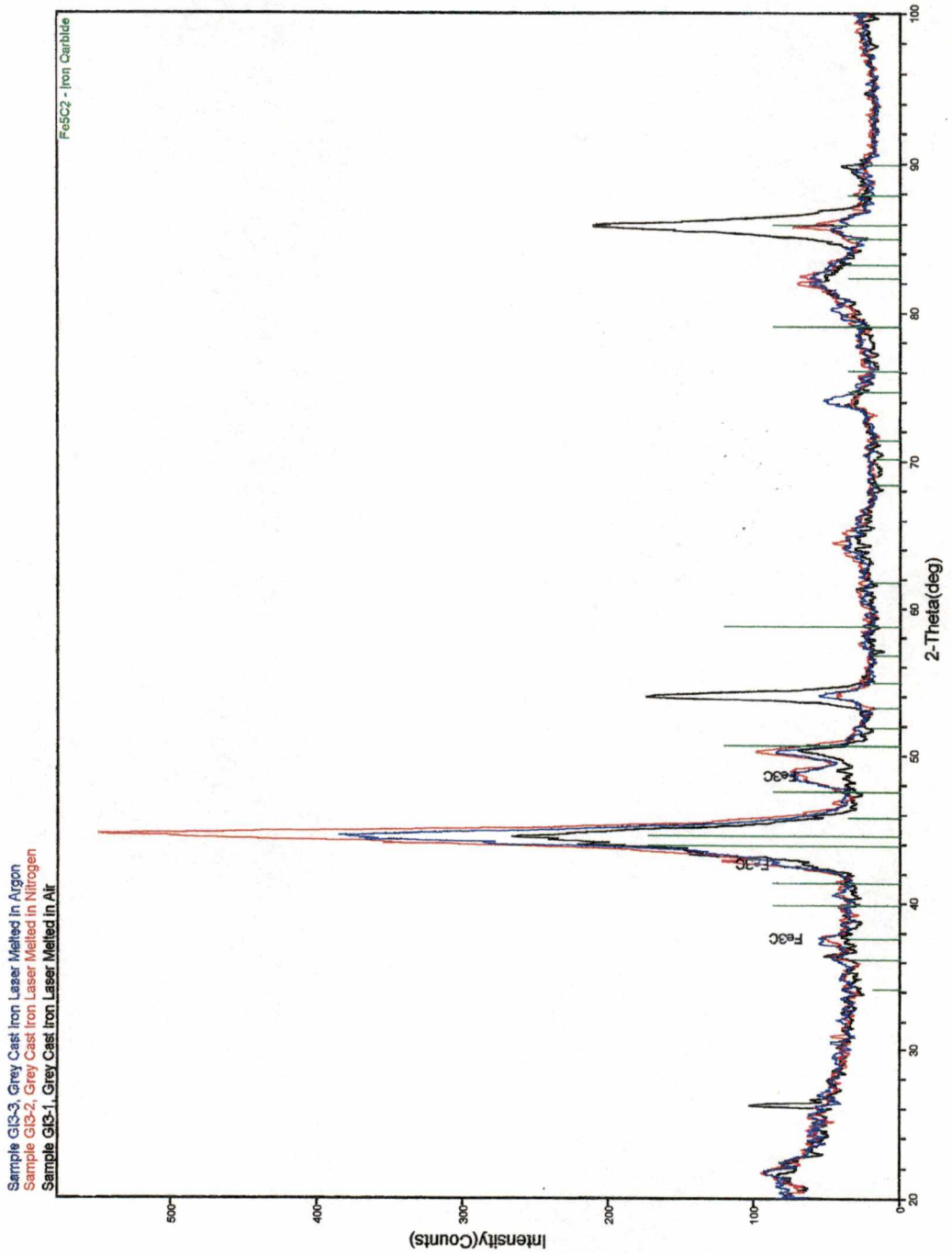
D2: X-ray trace of gray iron and sample GI3



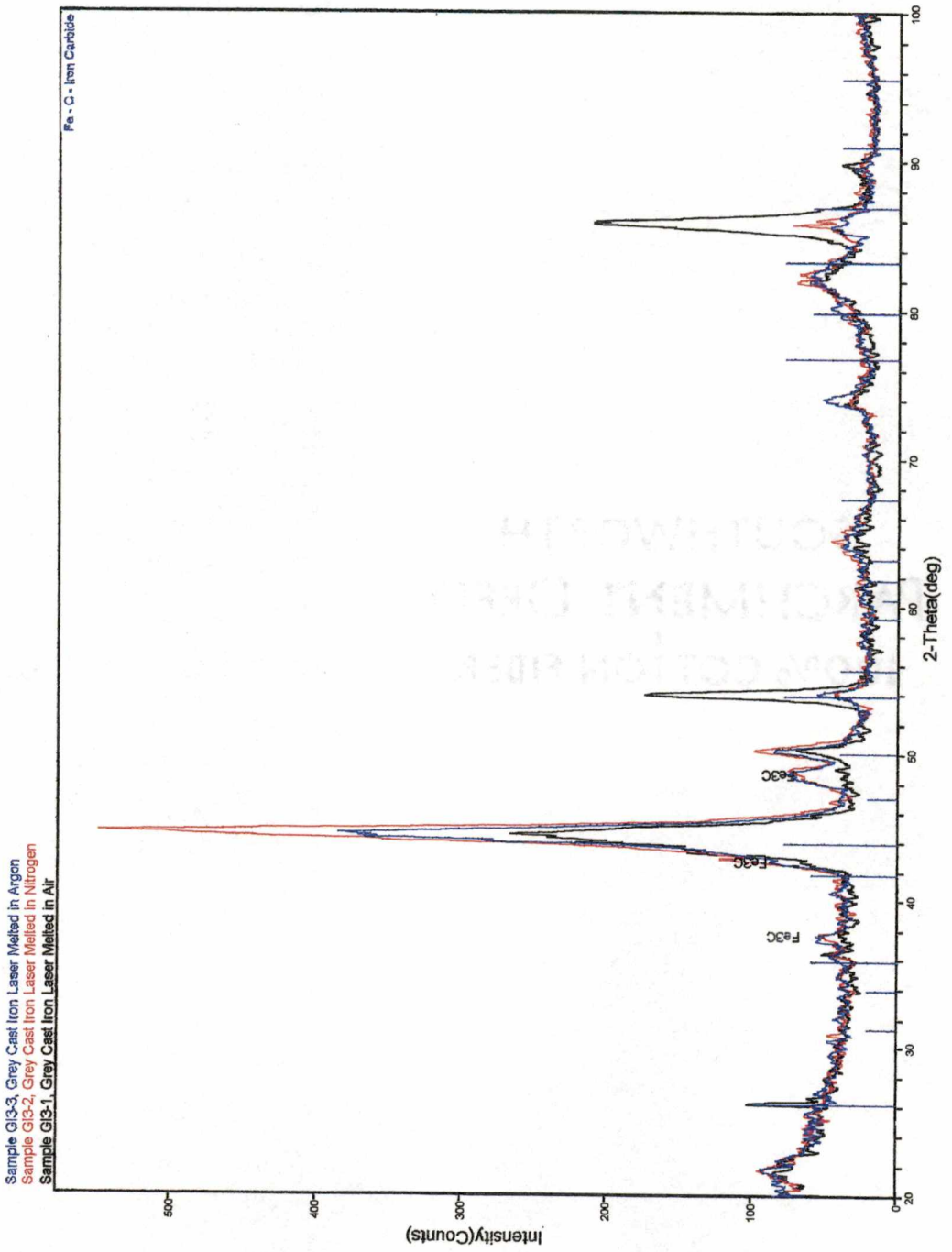
D3: X-ray Trace of sample GI3 – Iron



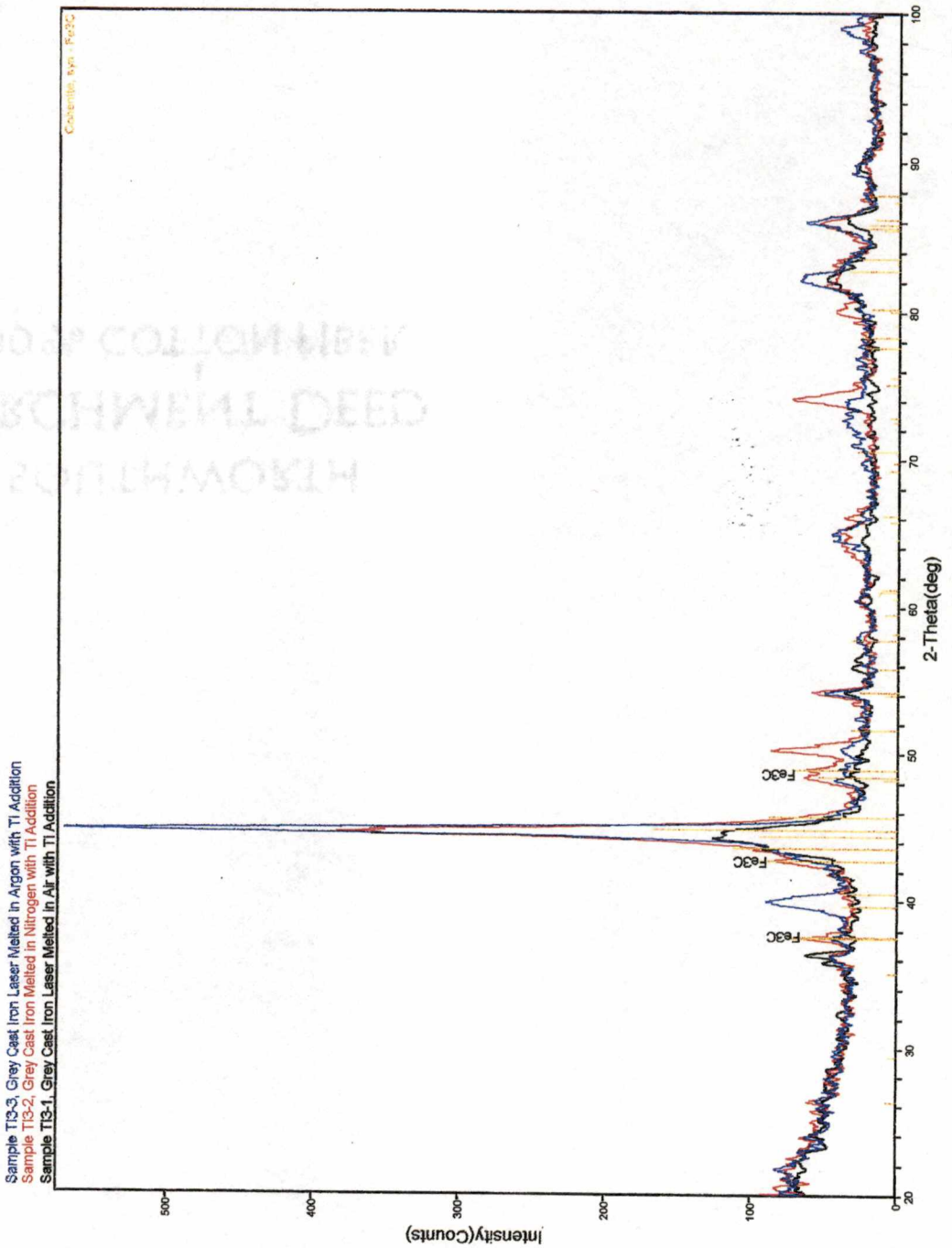
D4: X-ray trace of sample GI3 – Fe_3C



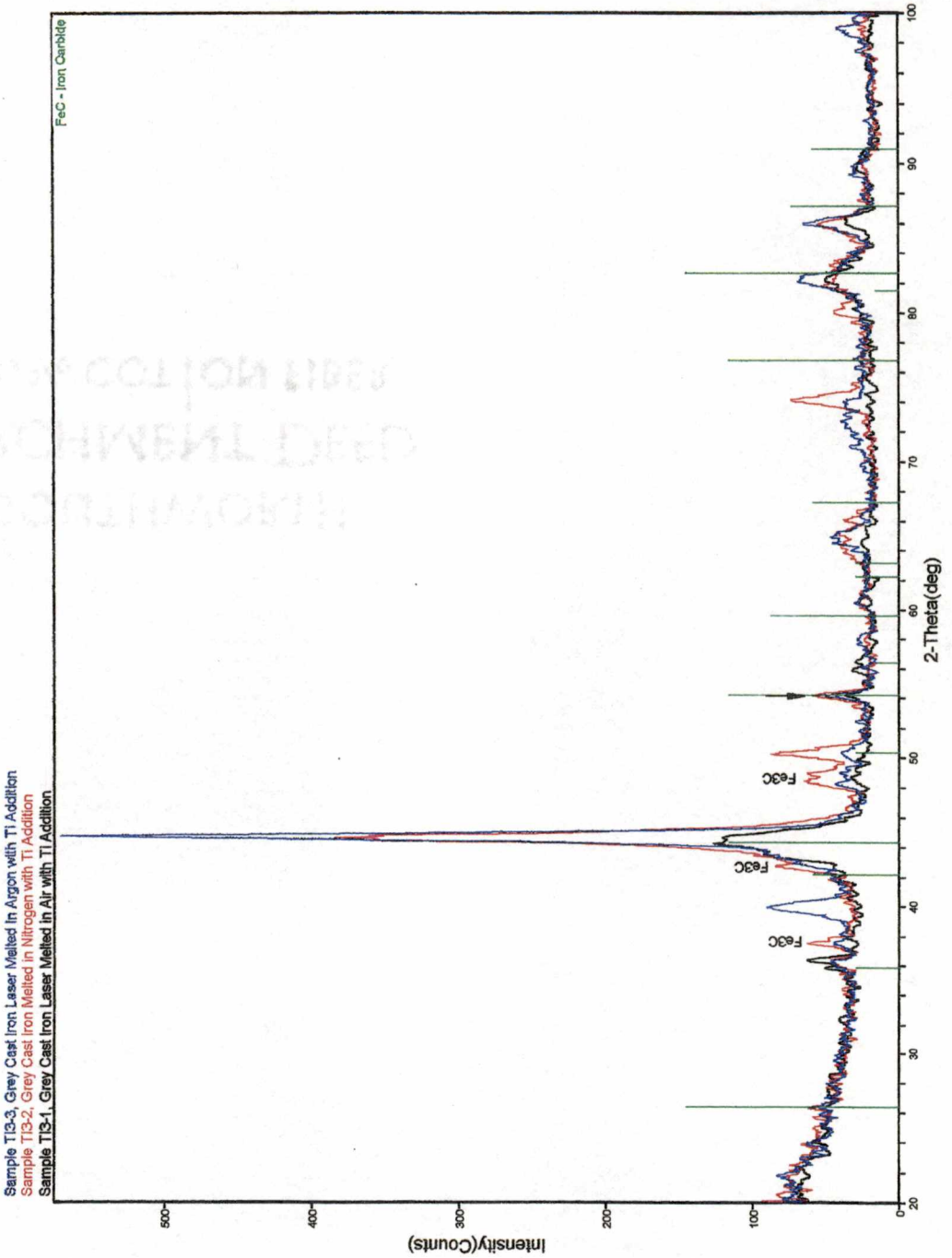
D5: X-ray trace of sample GI3 – Fe_5C_2



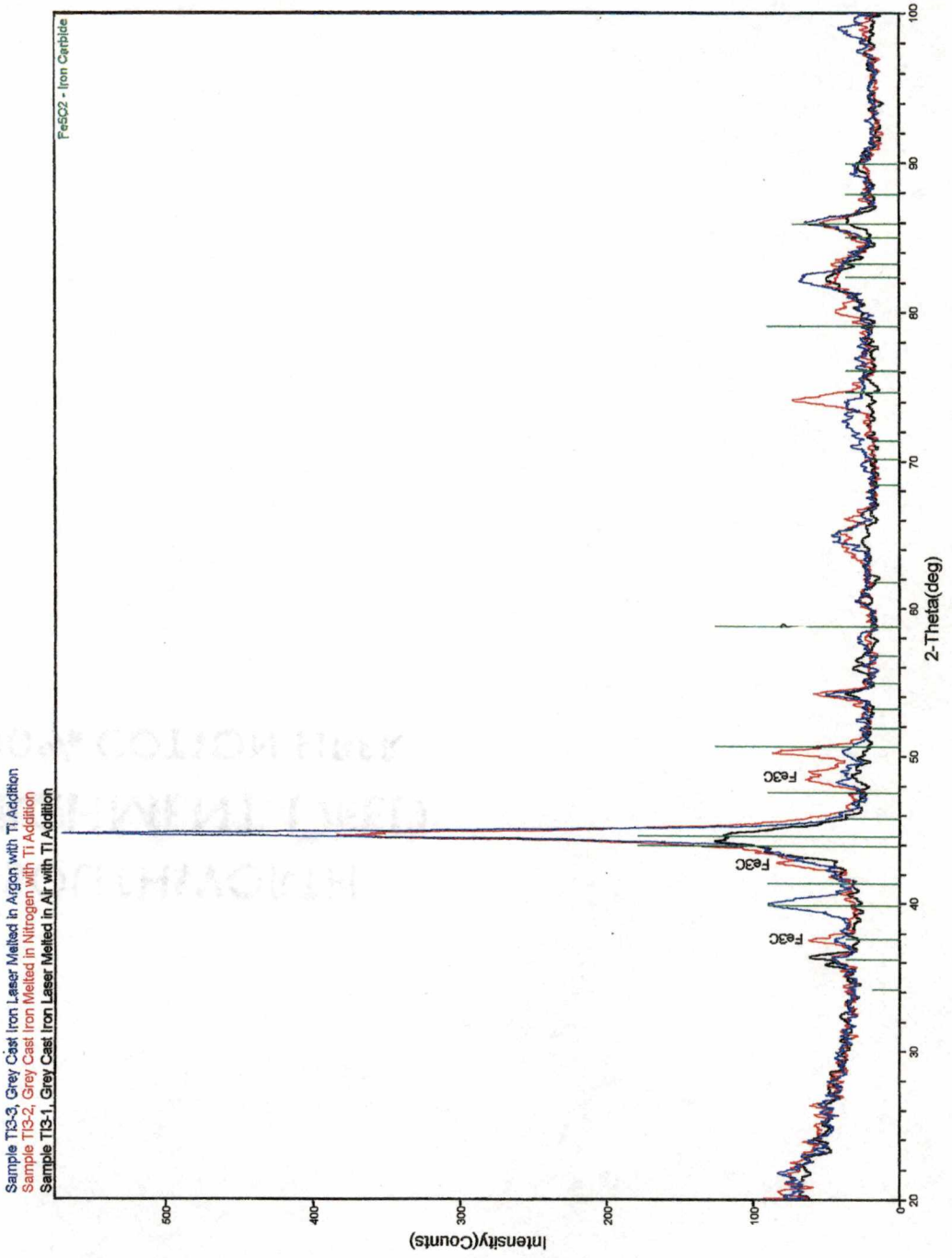
D6: X-ray trace of sample GI3 – FeC



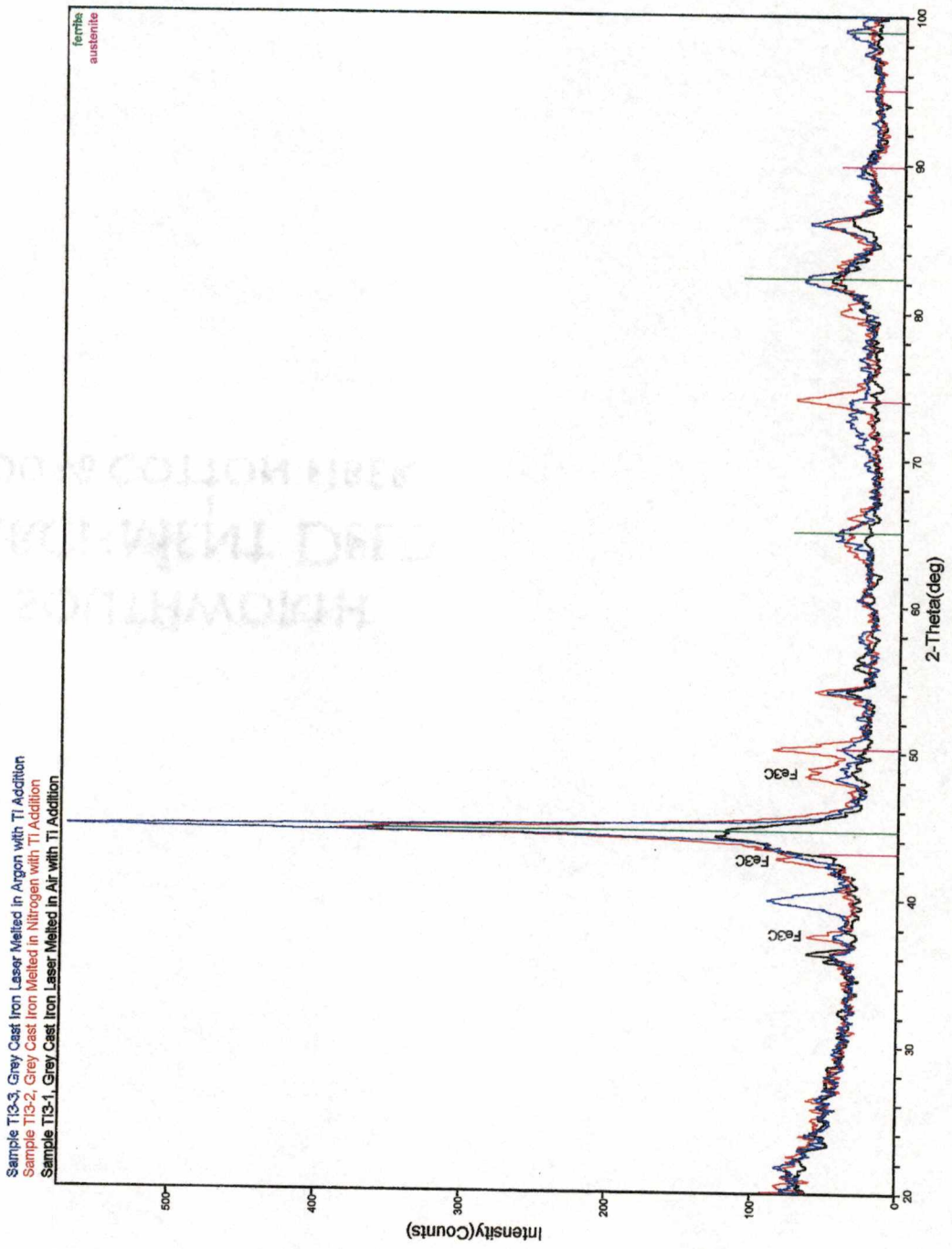
D7: X-ray trace of sample TI3 – Fe_3C



D8: X-ray trace of sample TI3 – FeC



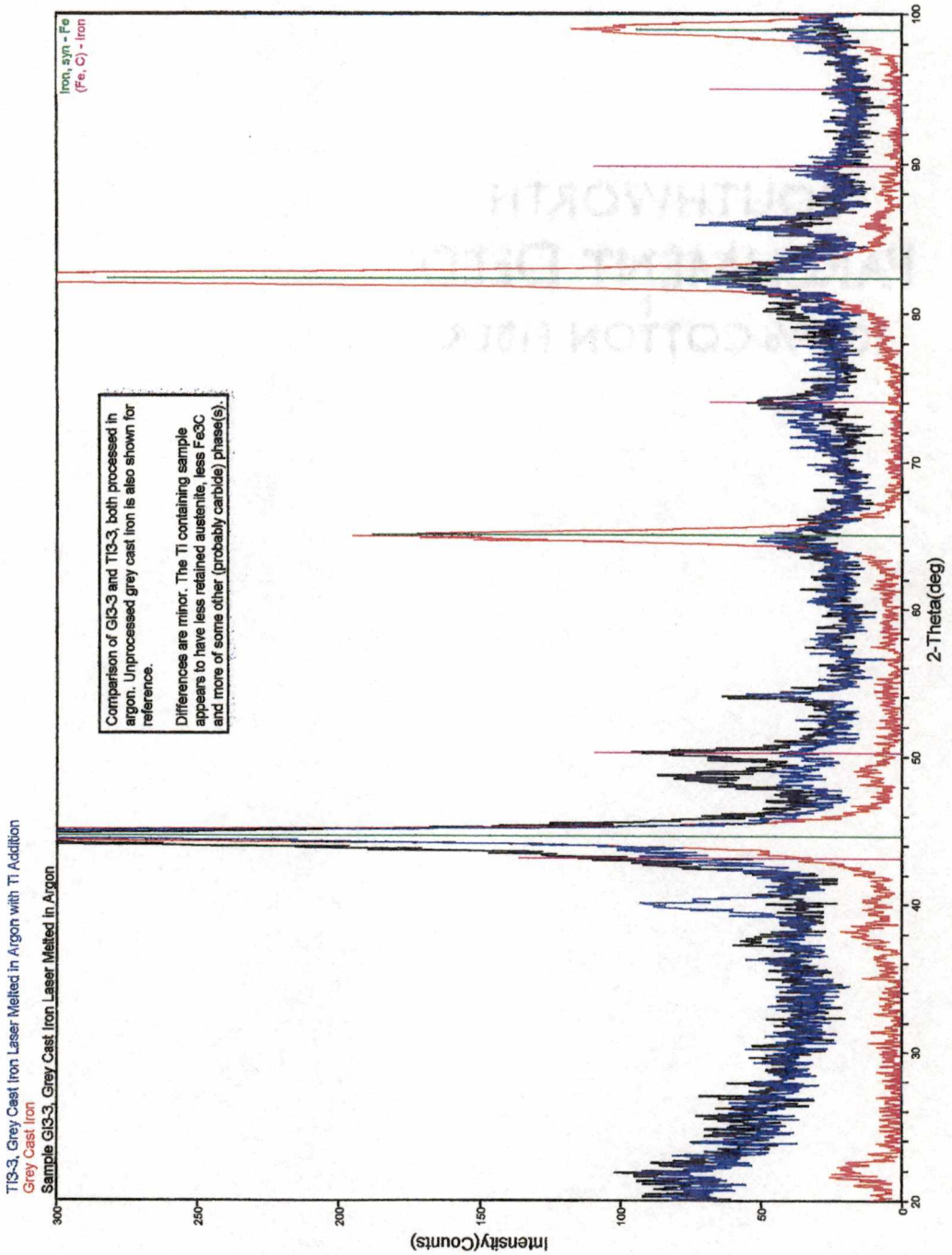
D9: X-ray trace of TI3 – Fe_5C_2



D10: X-ray trace of sample TI3 – iron phases

D11: X-ray trace comparison in air

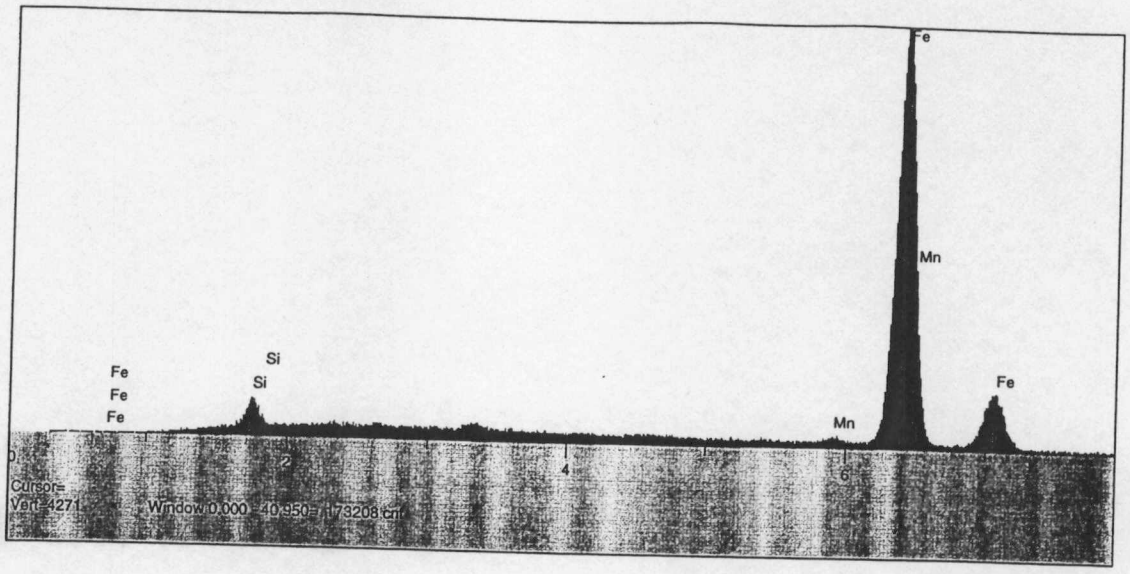
D12: X-ray trace comparison in nitrogen



D13: X-ray trace comparison in argon

Appendix E
SEM Analyses

Spectrum: Ti4-base.SP0



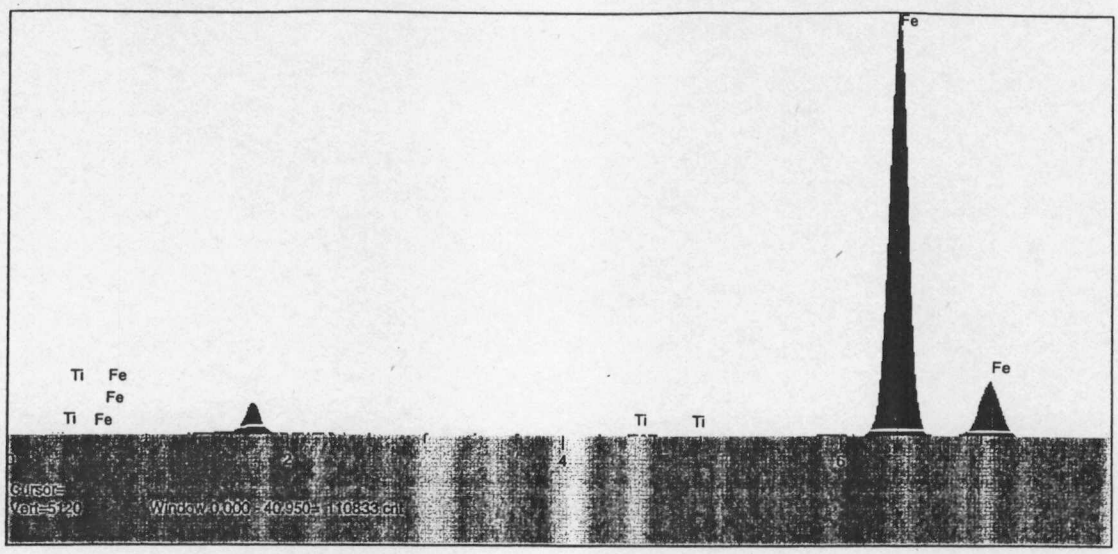
Ti4-base
June 08, 1999. 11:35 AM

Component	Type	Mole Wt %	Conc.	
Si	Calc	4.629	2.383	wt.%
Mn	Calc	0.613	0.618	wt.%
Fe	Calc	94.758	96.999	wt.%

Elt.	Line	Intensity (c/s)	Error 2-sig	Low keV	High keV	Quant	Atomic Wt %	Atomic Ratio	Conc
Si	Ka	33.98	1.449	1.685	1.795	ZAF	4.629	1.0000	2.383
Mn	Ka	7.61	1.121	5.823	5.974	ZAF	0.613	0.1325	0.618
Fe	Ka	680.92	5.300	6.326	6.481	ZAF	94.758	20.4715	96.999

E1: SEM analysis of sample TI4 on base iron

Spectrum: Ti4-11.sp0



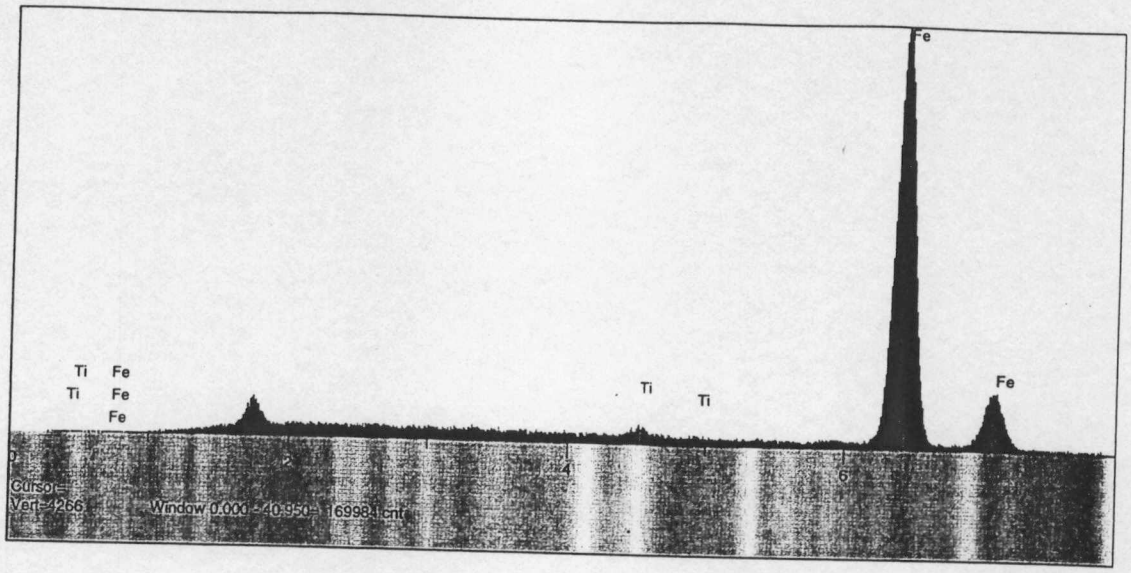
Ti4-11
June 08, 1999. 11:15 AM

Component	Type	Mole Wt %	Conc.	
Ti	Calc	0.272	0.234	wt.%
Fe	Calc	99.728	99.766	wt.%

Elt.	Line	Intensity (c/s)	Error 2-sig	Low keV	High keV	Quant	Atomic Wt %	Atomic Ratio	Conc
Ti	Ka	4.03	1.230	4.442	4.580	ZAF	0.272	1.0000	0.234
Fe	Ka	830.89	5.847	6.326	6.481	ZAF	99.728	366.4275	99.766

E2: SEM analysis of sample TI4-1, point 1

Spectrum: Ti4-12.sp0



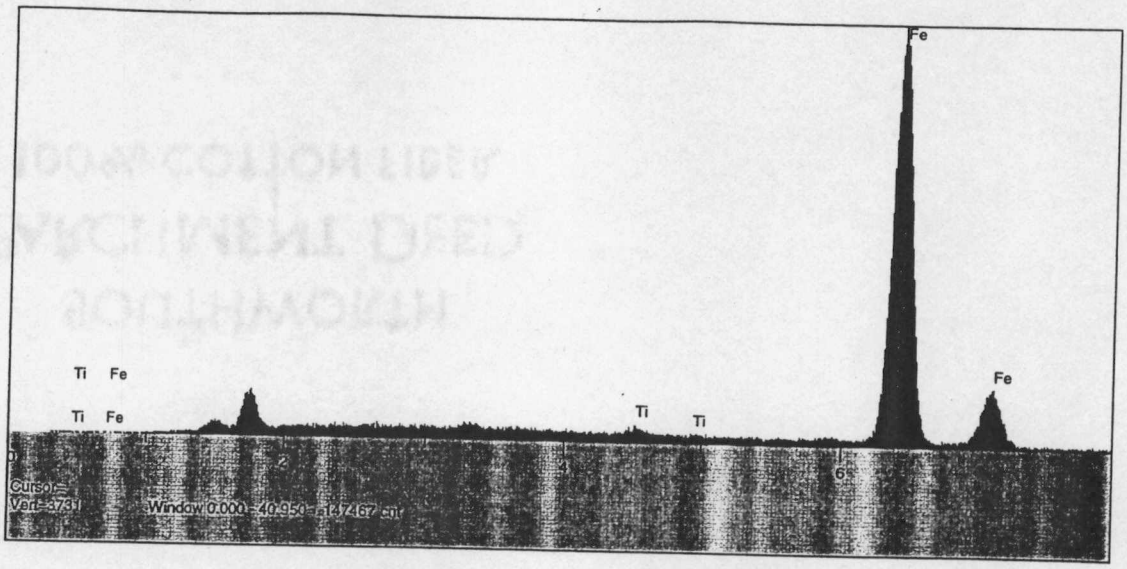
Ti4-12
June 08, 1999. 11:16 AM

Component	Type	Mole Wt %	Conc.	
Ti	Calc	1.134	0.975	wt.%
Fe	Calc	98.866	99.025	wt.%

Elt.	Line	Intensity (c/s)	Error 2-sig	Low keV	High keV	Quant	Atomic Wt %	Atomic Ratio	Conc
Ti	Ka	13.83	1.291	4.442	4.580	ZAF	1.134	1.0000	0.975
Fe	Ka	680.69	5.295	6.326	6.481	ZAF	98.866	87.1456	99.025

E3: SEM Analysis of sample TI4-1, point 2

Spectrum: Ti4-13.sp0



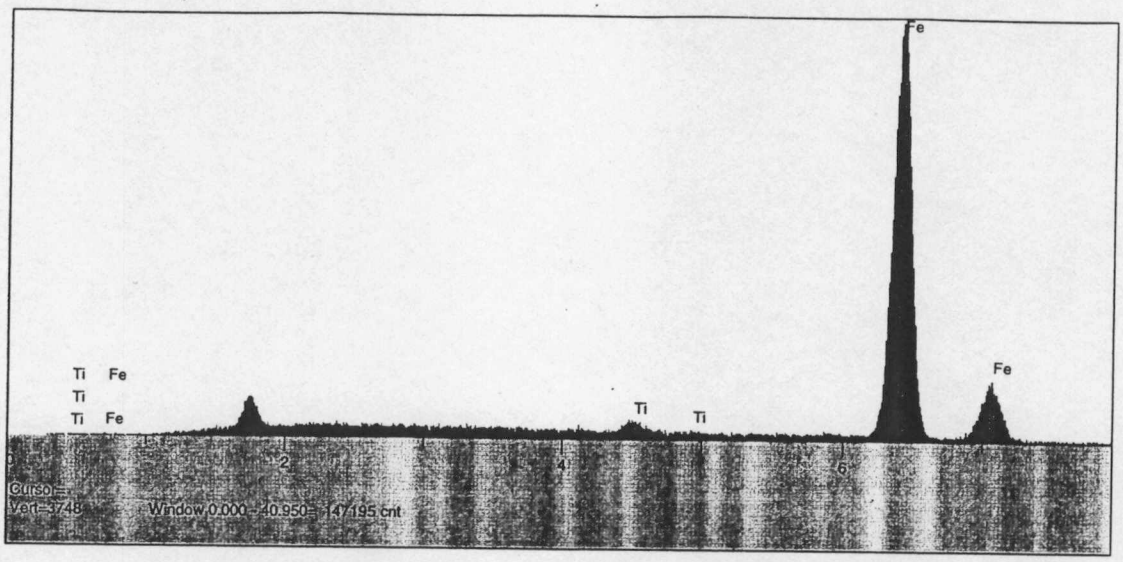
Ti4-13
June 08, 1999. 11:17 AM

Component	Type	Mole Wt %	Conc.	
Ti	Calc	0.711	0.610	wt.%
Fe	Calc	99.289	99.390	wt.%

Elt.	Line	Intensity (c/s)	Error 2-sig	Low keV	High keV	Quant	Atomic Wt %	Atomic Ratio	Conc
Ti	Ka	7.40	1.137	4.442	4.580	ZAF	0.711	1.0000	0.610
Fe	Ka	582.91	4.907	6.326	6.481	ZAF	99.289	139.7384	99.390

E4: SEM Analysis of Sample TI4-1, point 3

Spectrum: Ti4-14.sp0



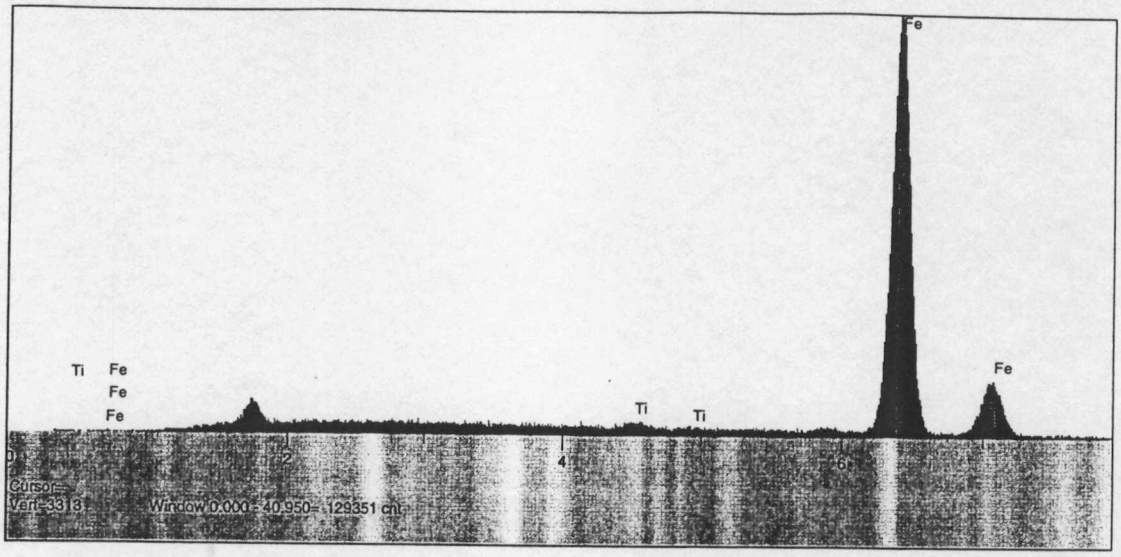
Ti4-14
June 08, 1999. 11:18 AM

Component	Type	Mole Wt %	Conc.	
Ti	Calc	1.342	1.153	wt.%
Fe	Calc	98.658	98.847	wt.%

Elt.	Line	Intensity (c/s)	Error 2-sig	Low keV	High keV	Quant	Atomic Wt %	Atomic Ratio	Conc
Ti	Ka	14.28	1.232	4.442	4.580	ZAF	1.342	1.0000	1.153
Fe	Ka	593.24	4.949	6.326	6.481	ZAF	98.658	73.4975	98.847

E5: SEM Analysis of sample TI4-1, point 4

Spectrum: Ti4-15.sp0



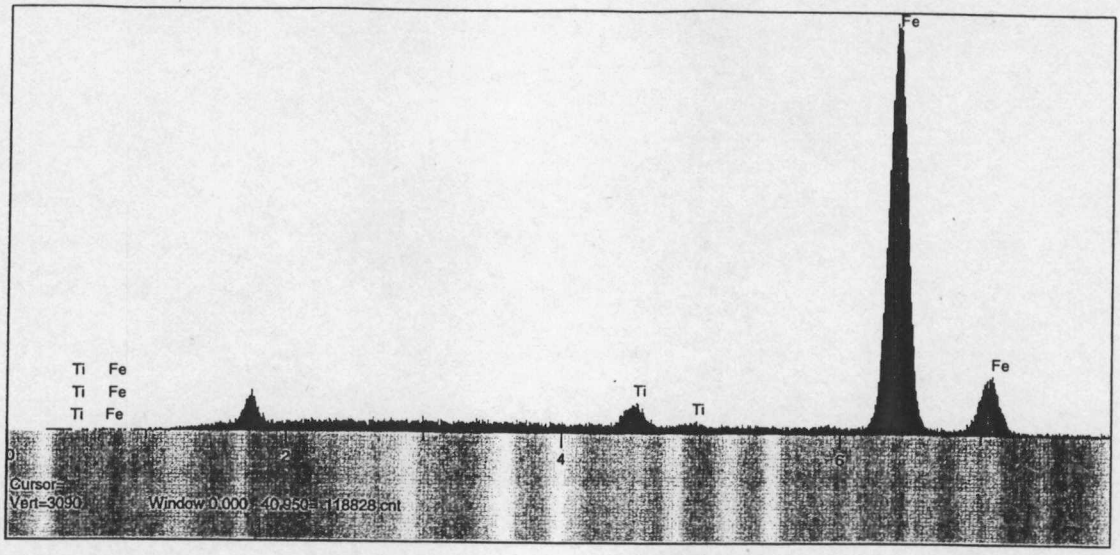
Ti4-15
June 08, 1999. 11:18 AM

Component	Type	Mole Wt %	Conc.	
Ti	Calc	0.982	0.844	wt.%
Fe	Calc	99.018	99.156	wt.%

Elt.	Line	Intensity (c/s)	Error 2-sig	Low keV	High keV	Quant	Atomic Wt %	Atomic Ratio	Conc
Ti	Ka	9.21	1.081	4.442	4.580	ZAF	0.982	1.0000	0.844
Fe	Ka	523.80	4.648	6.326	6.481	ZAF	99.018	100.8112	99.156

E6: SEM analysis of sample TI4-1, point 5

Spectrum: Ti4-16.sp0



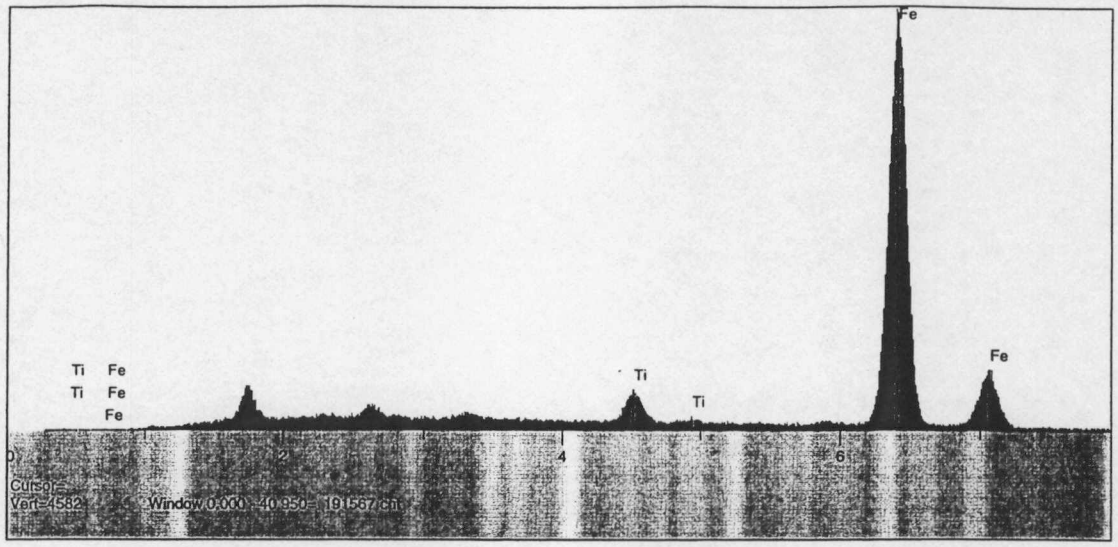
Ti4-16
June 08, 1999. 11:19 AM

Component	Type	Mole Wt %	Conc.	
Ti	Calc	2.781	2.394	wt.%
Fe	Calc	97.219	97.606	wt.%

Elt.	Line	Intensity (c/s)	Error 2-sig	Low keV	High keV	Quant	Atomic Wt %	Atomic Ratio	Conc
Ti	Ka	24.02	1.326	4.442	4.580	ZAF	2.781	1.0000	2.394
Fe	Ka	477.49	4.442	6.326	6.481	ZAF	97.219	34.9632	97.606

E7: SEM analysis of sample TI4-1, point 6

Spectrum: Ti4-2-1.sp0



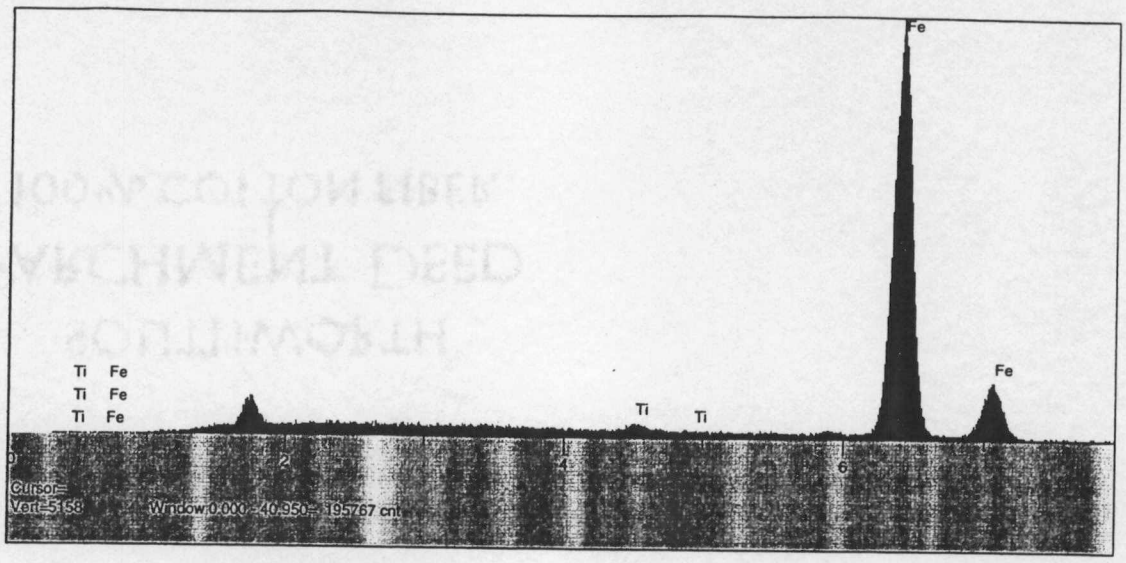
Ti4-2-1
June 08, 1999. 11:22 AM

Component	Type	Mole Wt %	Conc.	
Ti	Calc	3.630	3.130	wt.%
Fe	Calc	96.370	96.870	wt.%

Elt.	Line	Intensity (c/s)	Error 2-sig	Low keV	High keV	Quant	Atomic Wt %	Atomic Ratio	Conc
Ti	Ka	46.98	1.774	4.442	4.580	ZAF	3.630	1.0000	3.130
Fe	Ka	711.54	5.423	6.326	6.481	ZAF	96.370	26.5463	96.870

E8: SEM analysis of sample TI4-2, point 1

Spectrum: Ti4-2-2.sp0



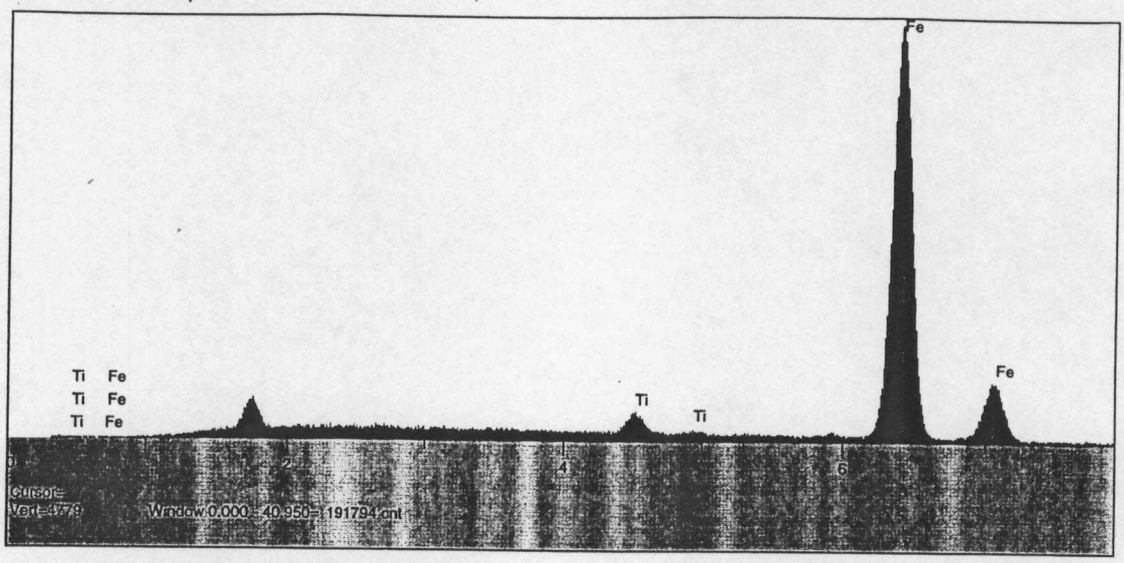
Ti4-2-2
June 08, 1999. 11:22 AM

Component	Type	Mole Wt %	Conc.	
Ti	Calc	0.787	0.676	wt.%
Fe	Calc	99.213	99.324	wt.%

Elt.	Line	Intensity (c/s)	Error 2-sig	Low keV	High keV	Quant	Atomic Wt %	Atomic Ratio	Conc
Ti	Ka	11.18	1.305	4.442	4.580	ZAF	0.787	1.0000	0.676
Fe	Ka	794.08	5.721	6.326	6.481	ZAF	99.213	125.9863	99.324

E9: SEM analysis of sample TI4-2, point 2

Spectrum: Ti4-2-3.sp0



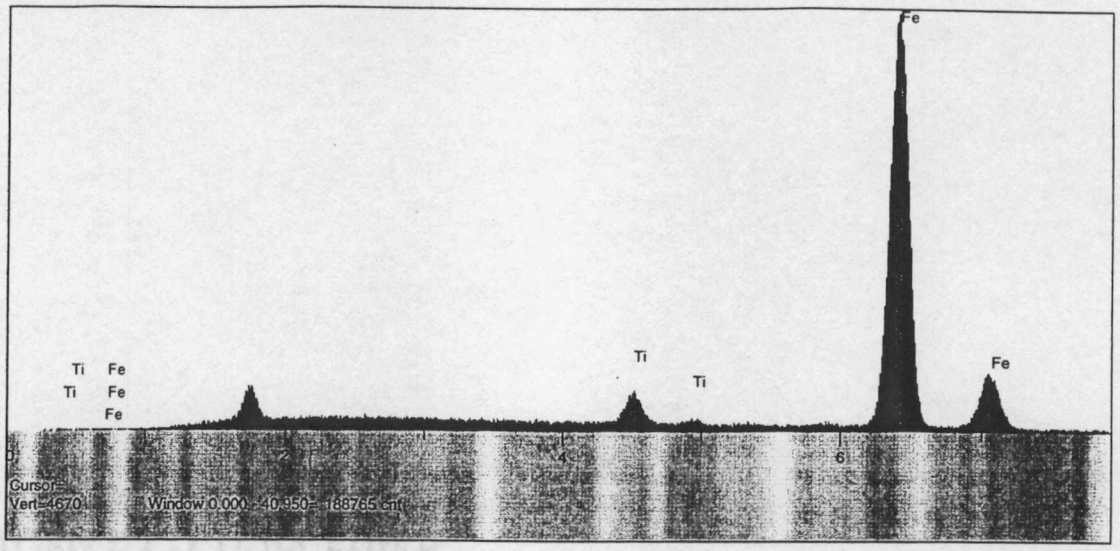
Ti4-2-3
June 08, 1999. 11:23 AM

Component	Type	Mole Wt %	Conc.	
Ti	Calc	2.153	1.852	wt.%
Fe	Calc	97.847	98.148	wt.%

Elt.	Line	Intensity (c/s)	Error 2-sig	Low keV	High keV	Quant	Atomic Wt %	Atomic Ratio	Conc
Ti	Ka	29.39	1.566	4.442	4.580	ZAF	2.153	1.0000	1.852
Fe	Ka	757.35	5.588	6.326	6.481	ZAF	97.847	45.4447	98.148

E10: SEM analysis of sample TI4-2, point 3

Spectrum: Ti4-2-4.sp0



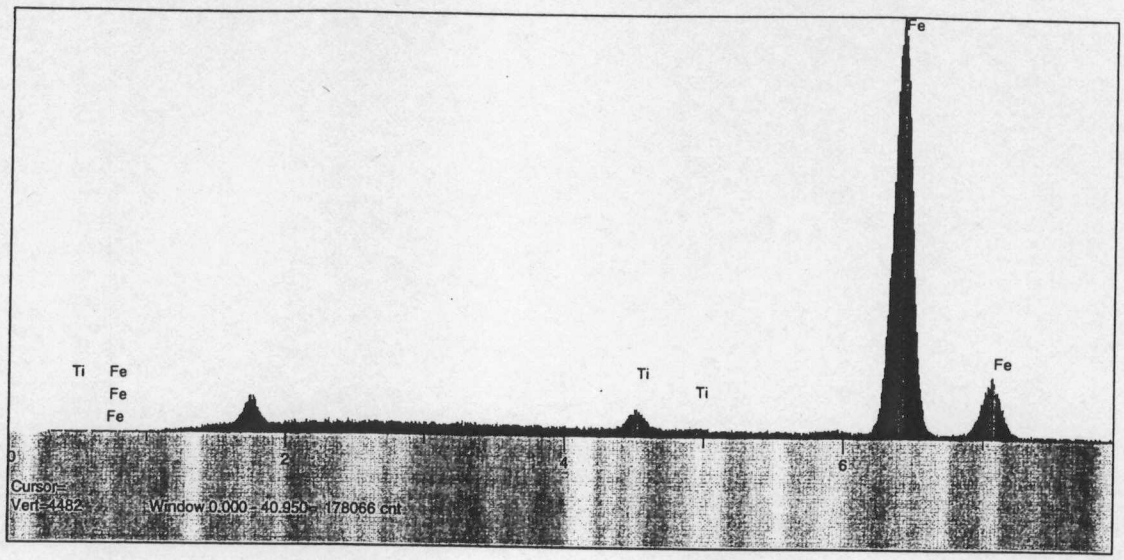
Ti4-2-4
June 08, 1999. 11:23 AM

Component	Type	Mole Wt %	Conc.	
Ti	Calc	3.529	3.042	wt.%
Fe	Calc	96.471	96.958	wt.%

Elt.	Line	Intensity (c/s)	Error 2-sig	Low keV	High keV	Quant	Atomic Wt %	Atomic Ratio	Conc
Ti	Ka	47.27	1.765	4.442	4.580	ZAF	3.529	1.0000	3.042
Fe	Ka	736.91	5.512	6.326	6.481	ZAF	96.471	27.3383	96.958

E11: SEM analysis of sample TI4-2, point 4

Spectrum: Ti4-2-5.sp0



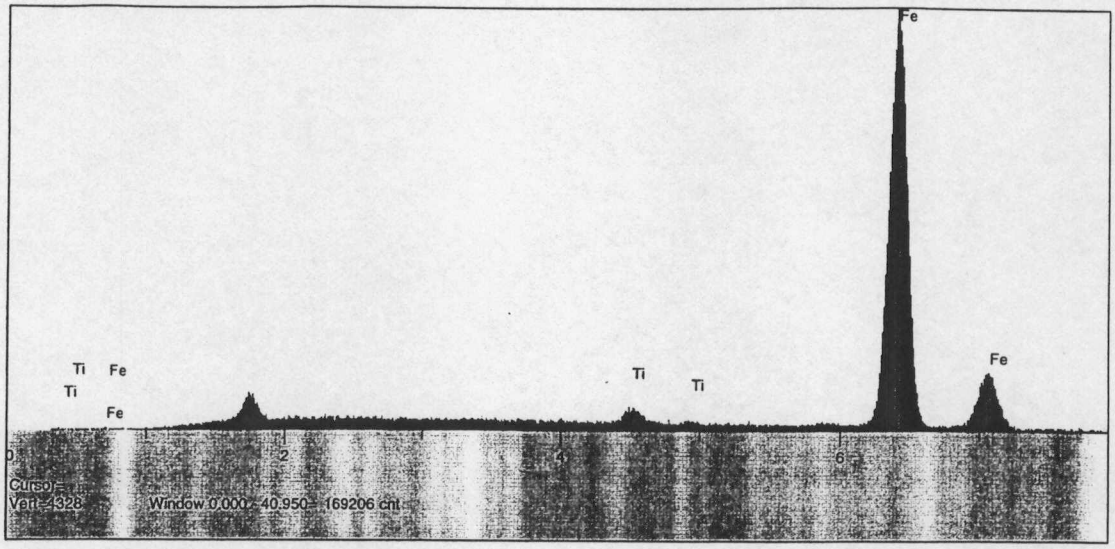
Ti4-2-5
June 08, 1999. 11:24 AM

Component	Type	Mole Wt %	Conc.	
Ti	Calc	2.213	1.904	wt.%
Fe	Calc	97.787	98.096	wt.%

Elt.	Line	Intensity (c/s)	Error 2-sig	Low keV	High keV	Quant	Atomic Wt %	Atomic Ratio	Conc
Ti	Ka	28.27	1.529	4.442	4.580	ZAF	2.213	1.0000	1.904
Fe	Ka	708.46	5.407	6.326	6.481	ZAF	97.787	44.1849	98.096

E12: SEM analysis of sample TI4-2, point 5

Spectrum: Ti4-2-6.sp0



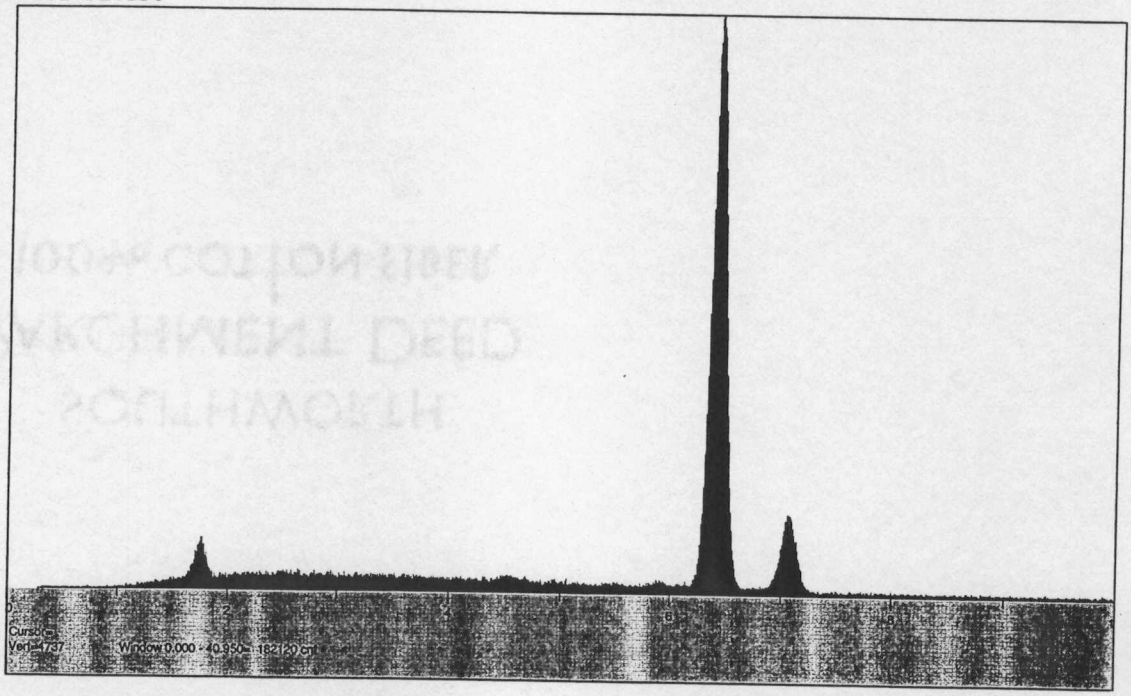
Ti4-2-6
June 08, 1999. 11:25 AM

Component	Type	Mole Wt %	Conc.	
Ti	Calc	1.712	1.472	wt.%
Fe	Calc	98.288	98.528	wt.%

Elt.	Line	Intensity (c/s)	Error 2-sig	Low keV	High keV	Quant	Atomic Wt %	Atomic Ratio	Conc
Ti	Ka	20.74	1.390	4.442	4.580	ZAF	1.712	1.0000	1.472
Fe	Ka	673.81	5.271	6.326	6.481	ZAF	98.288	57.4021	98.528

E13: SEM analysis of sample TI4-2, point 6

Ti41-31.SP0



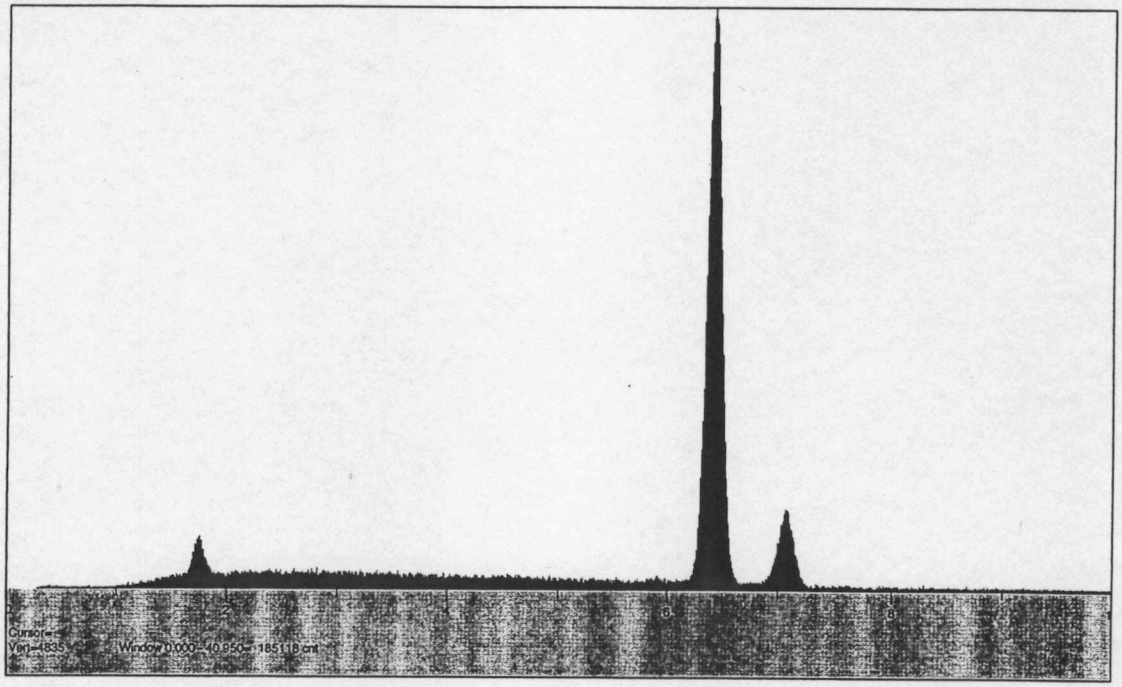
Position: 1. Location: 593, 245. Report: ti41-31.rpt
November 08, 1999. 11:4

Component	Type	Mole Wt %	Conc.	
Fe	Calc	99.480	99.553	wt.%
Ti	Calc	0.520	0.447	wt.%

Elt.	Line	Intensity (c/s)	Error 2-sig	Low keV	High keV	Quant	Atomic Wt %	Atomic Ratio	Conc
Ti	Ka	6.63	1.214	4.442	4.580	ZAF	0.520	1.0000	0.447
Fe	Ka	722.95	5.467	6.326	6.481	ZAF	99.480	191.1492	99.553

E14: SEM analysis of sample TI4-3, point 1

Ti41-32.SP0



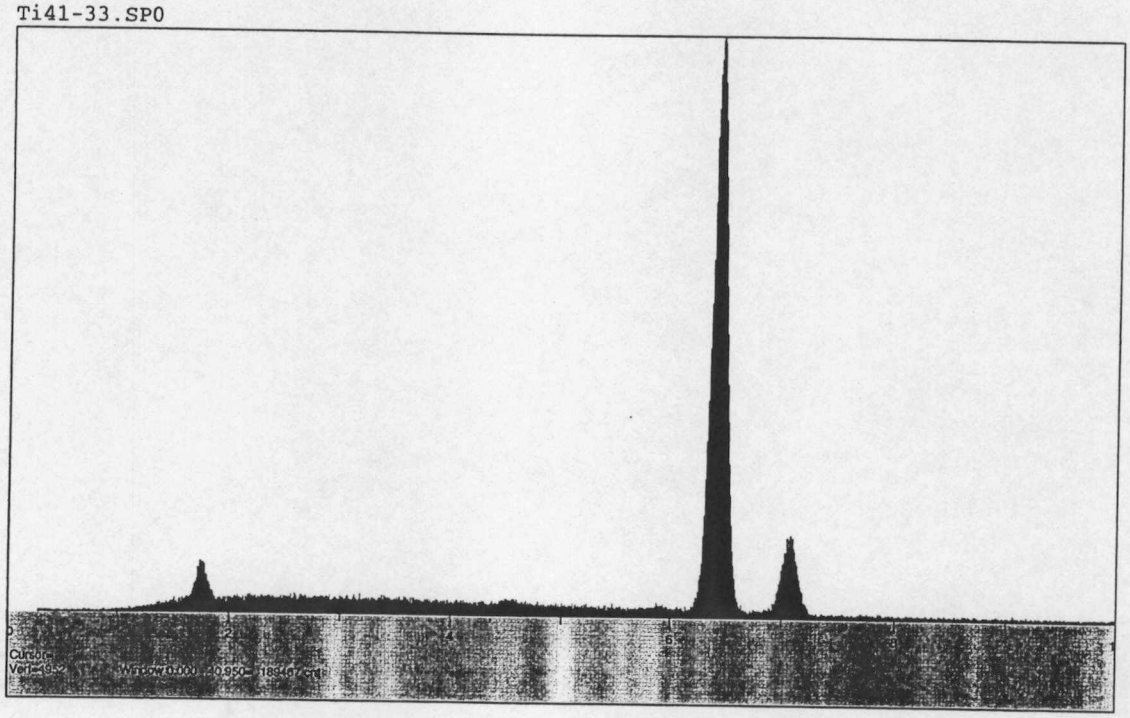
Position: 2. Location: 563, 317. Report: ti41-32.rpt
November 08, 1999. 11:4

Component	Type	Mole Wt %	Conc.	
Fe	Calc	99.764	99.797	wt.%
Ti	Calc	0.236	0.203	wt.%

Elt.	Line	Intensity (c/s)	Error 2-sig	Low keV	High keV	Quant	Atomic Wt %	Atomic Ratio	Conc
Ti	Ka	2.99	1.153	4.442	4.580	ZAF	0.236	1.0000	0.203
Fe	Ka	718.34	5.446	6.326	6.481	ZAF	99.764	422.0889	99.797

E15: SEM analysis of sample TI4-3, point 2

Ti41-33.SP0



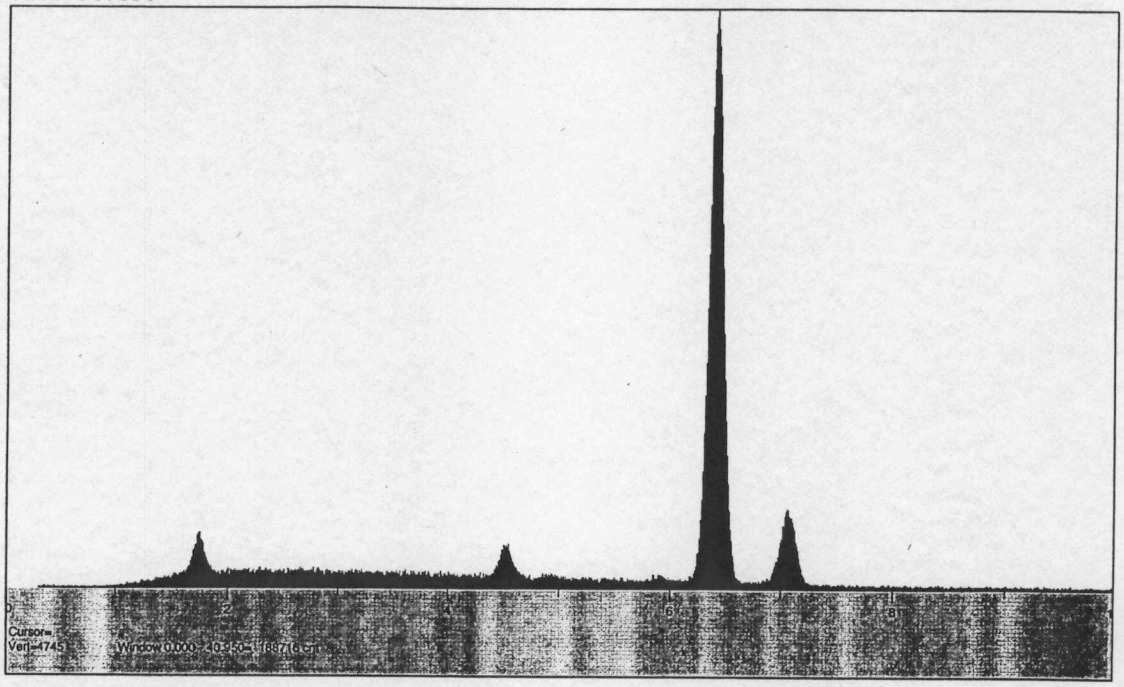
Position: 3. Location: 520, 419. Report: ti41-33.rpt
November 08, 1999. 11:4

Component	Type	Mole Wt %	Conc.	
Fe	Calc	99.466	99.542	wt.%
Ti	Calc	0.534	0.458	wt.%

Elt.	Line	Intensity (c/s)	Error 2-sig	Low keV	High keV	Quant	Atomic Wt %	Atomic Ratio	Conc
Ti	Ka	6.98	1.233	4.442	4.580	ZAF	0.534	1.0000	0.458
Fe	Ka	741.91	5.535	6.326	6.481	ZAF	99.466	186.3139	99.542

E16: SEM analysis of sample TI4-3, point 3

Ti41-34.SP0



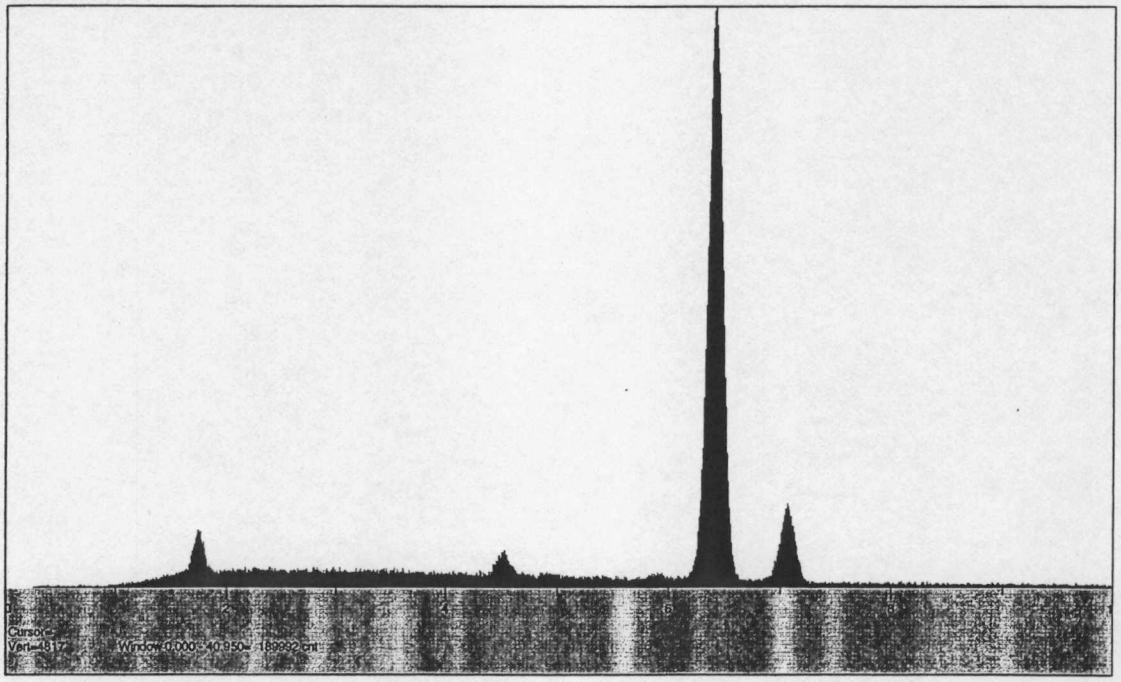
Position: 4. Location: 492, 508. Report: ti41-34.rpt
November 08, 1999. 11:4

Component	Type	Mole Wt %	Conc.	
Fe	Calc	97.130	97.529	wt.%
Ti	Calc	2.870	2.471	wt.%

Elt.	Line	Intensity (c/s)	Error 2-sig	Low keV	High keV	Quant	Atomic Wt %	Atomic Ratio	Conc
Ti	Ka	37.31	1.640	4.442	4.580	ZAF	2.870	1.0000	2.471
Fe	Ka	726.80	5.477	6.326	6.481	ZAF	97.130	33.8490	97.529

E17: SEM analysis of sample TI4-3, point 4

Ti41-35.SP0



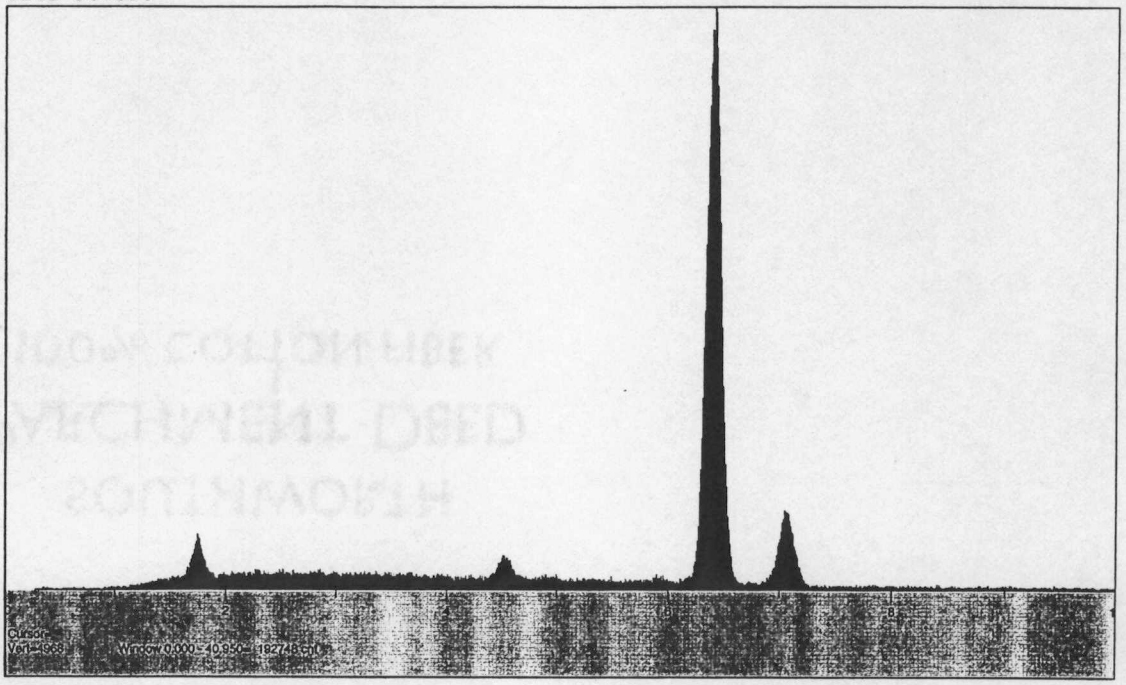
Position: 5. Location: 427, 650. Report: ti41-35.rpt
November 08, 1999. 11:4

Component	Type	Mole Wt %	Conc.	
Fe	Calc	98.119	98.382	wt.%
Ti	Calc	1.881	1.618	wt.%

Elt.	Line	Intensity (c/s)	Error 2-sig	Low keV	High keV	Quant	Atomic Wt %	Atomic Ratio	Conc
Ti	Ka	24.71	1.492	4.442	4.580	ZAF	1.881	1.0000	1.618
Fe	Ka	738.88	5.522	6.326	6.481	ZAF	98.119	52.1536	98.382

E18: SEM analysis of sample TI4-3, point 5

Ti41-36.SP0



Position: 6. Location: 377, 780. Report: ti41-36.rpt
November 08, 1999. 11:4

Component	Type	Mole Wt %	Conc.	
Fe	Calc	97.834	98.137	wt.%
Ti	Calc	2.166	1.863	wt.%

Elt.	Line	Intensity (c/s)	Error 2-sig	Low keV	High keV	Quant	Atomic Wt %	Atomic Ratio	Conc
Ti	Ka	29.19	1.542	4.442	4.580	ZAF	2.166	1.0000	1.863
Fe	Ka	757.03	5.586	6.326	6.481	ZAF	97.834	45.1749	98.137

E19: SEM analysis of sample TI4-3, point 6

Ti7-1
September 24, 1999 12 2

Component	Type	Mole Wt %	Conc	
Ti	Calc	2 698	2 323	wt %
Fe	Calc	97.302	97 677	wt %

Elt	Line	Intensity (c/s)	Error 2-sig	Low keV	High keV	Quant	Atomic Wt %	Atomic Ratio	Conc
Ti	Ka	26 20	1 362	4 442	4 580	ZAF	2 698	1 0000	2 323
Fe	Ka	537 11	4 710	6 326	6 481	ZAF	97 302	36 0670	97 677

Ti7-2
September 24, 1999 12 3

Component	Type	Mole Wt %	Conc	
Ti	Calc	2 837	2 443	wt %
Fe	Calc	97 163	97 557	wt %

Elt	Line	Intensity (c/s)	Error 2-sig	Low keV	High keV	Quant	Atomic Wt %	Atomic Ratio	Conc
Ti	Ka	29 09	1 451	4 442	4 580	ZAF	2 837	1 0000	2 443
Fe	Ka	566 57	4 840	6 326	6.481	ZAF	97 163	34 2427	97 557

Ti7-3
September 24, 1999 12 4

Component	Type	Mole Wt %	Conc	
Ti	Calc	1 108	0 952	wt %
Fe	Calc	98 892	99 048	wt %

Elt	Line	Intensity (c/s)	Error 2-sig	Low keV	High keV	Quant	Atomic Wt %	Atomic Ratio	Conc
Ti	Ka	9 21	0 846	4 442	4 580	ZAF	1 108	1 0000	0 952
Fe	Ka	463 73	3 571	6 326	6 481	ZAF	98 892	89 2260	99 048

E20: SEM analysis of sample TI7 in air, points 1, 2, 3

Ti7-4
September 24, 1999 12 5

Component	Type	Mole Wt %	Conc	
Ti	Calc	3 097	2 668	wt %
Fe	Calc	96 903	97 332	wt %

Elt	Line	Intensity (c/s)	Error 2-sig	Low keV	High keV	Quant	Atomic Wt %	Atomic Ratio	Conc
Ti	Ka	26 03	1 109	4 442	4 580	ZAF	3 097	1 0000	2 668
Fe	Ka	463 64	3 573	6 326	6 481	ZAF	96 903	31 2871	97 332

Ti7-5
September 24, 1999 01 (

Component	Type	Mole Wt %	Conc	
Ti	Calc	4 244	3 662	wt %
Fe	Calc	95 756	96 338	wt %

Elt	Line	Intensity (c/s)	Error 2-sig	Low keV	High keV	Quant	Atomic Wt %	Atomic Ratio	Conc
Ti	Ka	81 06	2 258	4 442	4 580	ZAF	4 244	1 0000	3 662
Fe	Ka	1045 98	6 573	6 326	6 481	ZAF	95 756	22 5624	96 338

Ti7-6
September 24, 1999 01 (

Component	Type	Mole Wt %	Conc	
Ti	Calc	3 265	2 813	wt %
Fe	Calc	96 735	97 187	wt %

Elt	Line	Intensity (c/s)	Error 2-sig	Low keV	High keV	Quant	Atomic Wt %	Atomic Ratio	Conc
Ti	Ka	24 68	1 359	4 442	4 580	ZAF	3 265	1 0000	2 813
Fe	Ka	416 70	4 157	6 326	6 481	ZAF	96 735	29 6305	97 187

E21: SEM analysis of sample TI7 in air, points 4, 5, 6

Ti7-base
September 24, 1999 03 (

Component	Type	Mole Wt %	Conc	
Si	Calc	5 833	3 022	wt %
Mn	Calc	0 643	0 652	wt %
Fe	Calc	93 523	96 326	wt %

Elt	Line	Intensity (c/s)	Error 2-sig	Low keV	High keV	Quant	Atomic Wt %	Atomic Ratio	Conc
Si	Ka	91 37	2 330	1 685	1 795	ZAF	5 833	1 0000	3 022
Mn	Ka	16 90	1 611	5 823	5 974	ZAF	0 643	0 1103	0 652
Fe	Ka	1429 70	7 680	6 326	6 481	ZAF	93 523	16 0328	96 326

E22: SEM analysis of sample TI7 in air, base iron

Spec4 Titanium std Check of calibration of system
September 24, 1999 10 (

Component	Type	Mole Wt %	Conc	
Al	Calc	8 604	5 248	wt %
Si	Calc	9 846	6 252	wt %
Ti	Calc	78 645	85 156	wt %
V	Calc	2 905	3 345	wt %

Elt	Line	Intensity (c/s)	Error 2-sig	Low keV	High keV	Quant	Atomic Wt %	Atomic Ratio	Conc
Al	Ka	72 33	1 939	1 433	1 540	ZAF	8 604	1 0000	5 248
Si	Ka	106 27	2 278	1 685	1 795	ZAF	9 846	1 1442	6 252
Ti	Ka	993 04	6 396	4 442	4 580	ZAF	78 645	9 1401	85 156
V	Ka	34 18	1 509	4 881	5 023	ZAF	2 905	0 3376	3 345

Al 6.08%
V 3.96%
balance Titanium
} What the sample is supposed to be.

E23: SEM calibration check with titanium standard

Ti10base base iron
September 24, 1999 12 (

Component	Type	Mole Wt %	Conc	
Si	Calc	7 411	3 870	wt %
Fe	Calc	92 589	96 130	wt %

Elt	Line	Intensity (c/s)	Error 2-sig	Low keV	High keV	Quant	Atomic Wt %	Atomic Ratio	Conc
Si	Ka	38 96	1 471	1 685	1 795	ZAF	7 411	1 0000	3 870
Fe	Ka	473 16	4 417	6 326	6 481	ZAF	92 589	12 4931	96 130

E24: SEM analysis of sample TI10 in air, base iron

Ti10-1 same as Ti10
September 24, 1999 10 :

Component	Type	Mole Wt %	Conc	
Al	Calc	3 333	1 724	wt %
Si	Calc	8 812	4 745	wt %
Ti	Calc	3 417	3 138	wt %
Fe	Calc	84 438	90 394	wt %

Elt	Line	Intensity (c/s)	Error 2-sig	Low keV	High keV	Quant	Atomic Wt %	Atomic Ratio	Conc
Al	Ka	4 08	0 330	1 433	1 540	ZAF	3 333	1 0000	1 724
Si	Ka	15 30	0 516	1 685	1 795	ZAF	8 812	2 6436	4 745
Ti	Ka	9 82	0 452	4 442	4 580	ZAF	3 417	1 0253	3 138
Fe	Ka	141 16	1 394	6 326	6 481	ZAF	84 438	25 3320	90 394

Ti10-2
September 24, 1999 10 :

Component	Type	Mole Wt %	Conc	
Ti	Calc	12 797	11 179	wt.%
Fe	Calc	87 203	88 821	wt %

Elt	Line	Intensity (c/s)	Error 2-sig	Low keV	High keV	Quant	Atomic Wt %	Atomic Ratio	Conc
Ti	Ka	80 54	0 907	4 442	4 580	ZAF	12 797	1 0000	11 179
Fe	Ka	322 24	1 641	6 326	6 481	ZAF	87 203	6 8143	88 821

Ti10-3
September 24, 1999 11 :

Component	Type	Mole Wt %	Conc	
Ti	Calc	12 581	10 987	wt %
Fe	Calc	87 419	89 013	wt %

Elt	Line	Intensity (c/s)	Error 2-sig	Low keV	High keV	Quant	Atomic Wt %	Atomic Ratio	Conc
Ti	Ka	20 12	0 451	4 442	4 580	ZAF	12 581	1 0000	10 987
Fe	Ka	82 06	0 827	6 326	6 481	ZAF	87 419	6 9483	89 013

E25: SEM analysis of sample TI10 in air, points 1, 2, 3

Ti10-4
September 24, 1999 11 5

Component	Type	Mole Wt %	Conc	
Ti	Calc	11 511	10 037	wt %
Fe	Calc	88 489	89 963	wt %

Elt	Line	Intensity (c/s)	Error 2-sig	Low keV	High keV	Quant	Atomic Wt %	Atomic Ratio	Conc
Ti	Ka	56 40	0 980	4 442	4 580	ZAF	11 511	1 0000	10 037
Fe	Ka	253 71	1 874	6 326	6 481	ZAF	88 489	7 6874	89 963

Ti10-5
September 24, 1999. 12 (

Component	Type	Mole Wt %	Conc	
Ti	Calc	2.357	2.029	wt %
Fe	Calc	97 643	97 971	wt %

Elt	Line	Intensity (c/s)	Error 2-sig	Low keV	High keV	Quant	Atomic Wt %	Atomic Ratio	Conc
Ti	Ka	26 93	1 471	4 442	4 580	ZAF	2 357	1 0000	2 029
Fe	Ka	633 10	5 104	6 326	6 481	ZAF	97 643	41 4186	97.971

E26: SEM analysis of sample TI10 in air, points 4, 5

Appendix F
Table of Past Experiments

Table of Past Experiments on Laser Processed Iron-based Materials

Type of Material	Laser Process	Type of Laser	Laser Power (kW)	Beam diameter mm	Proccessing Speed (m/min)	Power Density (W/cm^2)	Shielding gas	Porosity	Research study	Vol Energy Input (J/cm / cm^2)
spheroidal graphite cast iron	electron beam welding	NA	6		NA	NA	none mentioned	y	ref 1 Shibata	
nodular cast iron	hardening	1 5 KW CWCO2	0 4 - 1	8	(int time 0 7-5 1 s)	795 8 - 1989 4	no	none mentioned ?	ref 5 Farias, Denis,Simon	
steel		7 5 kW CO2 biannular mode	0 8-1 6	4 - 7	(int time 0 05 s) 1 5 - 6	6366 2 - 4157 5	No	none mentioned	ref 5 Farias, Denis, Simon	2,546 5 - 415 75
pearlitic nodular cast iron	melting	CO2	1 - 3		0 3-0 96	8,330 - 31,200	none mentioned	none mentioned	ref 6 Guangjun, Zhuchang Weirong, Wenlogn	5,206 25 - 62,400
pearlitic grey cast iron	melting	2 kW CWCO2	1 2 1 7	2 1 5	54 60	31,831 113,177 96,200	none mentioned	? No	ref 7 Straus, Szylar, Golebiewski	353 7 1131 8 962
cast iron & steel	melting		0 8	3	0 125,0 25 0 5	11,318	none mentioned	yes	ref 8 Samsonov, An, Shnypkin Boitsov	54,326 4 - 27,163 2 13,581 60
hypereutectic ductile iron	transformation hardening & melting	5 kW CCO2 400 W Nd YAG	1 - 2 5	1 - 2	0 3-3	127,324 - 79,577	none mentioned	? No	ref 9 Gadag, Srinivasan, Mordike	15,915 4 - 254,648
spherical graphitic cast iron	melting	CWCO2	0 5-2 0	0 2-2 0	0 21-0 33	1,591,549 - 63,662	Argon, Nitrogen	Yes	ref 11 Luft, Reitzenstein, Zarubova, Cermak	4,547,283 - 115,749
gray cast iron	hardening	1 2 kW CWCO2	0 95	4	1 26	7560	none mentioned	none mentioned	ref 12 Shen, Li	3600
low carbon steel (AISI 1018)	alloying	10 kW CWCO2	2 - 6	2,4 mm doughnut	0 3804 - 3 810	15,900 - 95,500	Argon	none mentioned	ref 13 Nagaratham, Komvopoulos	2,503 9 - 150,630 9
ductile cast iron									ref 14 Chen, Rigsbee Keshavan, Altstetter	
	alloying	CWCO2							ref 15 Chande, Ghose, Mazumder	
nodular cast iron pearlitic gray cast iron		10KW CWCO2	0 5 - 4	1	1.266 - 25 02	500,000	Helium	yes?	Chen, Altstetter, Rigsbee	236966 8 - 11990 4
	cladding								ref 17 Li, Mazunder	
	cladding	CO2							ref 18 Mazumder, Singh	
pearlitic gray cast iron	melting	'5 KW, 15KW CO	2 5 , 15	6		8842 - 53,052	Helium	yes	ref 19 Riccardi, Pasquini, Tiziani Rudilosso	
pearlitic cast iron	transformation hardening	1 5 KW CWCO2 3 0 KW CO2	1 1 5 2 6	5 0	6 8 6	5093 7639 13,242	none	none	ref 20 Kogan, Sazonova, Zelenov Aleksandrov	509 3 572 93 1324 2
steel	hardening melting	6 KW CWCO2 TEM 20		35 (5 x 7)			Argon	?No (corrosion pitting)	ref 21 Moisio, Pederson Sorensen, Hansson	
cast iron	transformation hardening	3 4 kW CO2 TEM 01 pulsed or cont	1 - 2	1-2 5	? 30-480	127,324 - 40,744	Nitrogen	? No empty graphite nodules	ref 27 Papaphilippou, Jeandin Vardevoulias	2546 5 - 50 93
ductile cast iron	melting	1 kW pulsed Nd YAG	0 8 - 1 1	5 5	0 05 -0 75 0 1	13,200 - 38,700	none	?none (graphitization)	Wang, Bergmann	10,560 - 464,400
	melting & annealing	1 kW pulsed Nd YAG	1 1	5 5	0 1 0 3-0 8	4630	none	?none (graphitization)	Wang, Bergmann	9260 - 3472 5

Type of Material	Laser Process	Type of Laser	Laser Power (kW)	Beam diameter mm	Proccessing Speed (m/min)	Power Density (W/cm^2)	Shielding gas	Porosity	Research study	Vol Energy Input (J/cm / cm^2)
gray, ductile and malleable cast iron	hardening melting alloying	2 5 kw CO2	1 57 2 4 2 4	8 x 8 2 2	0 7 2 2 1 0 , 1 5	3123 76,394	Nitrogen Helium Argon	none mentioned	ref 29 Magnusson, Wiklund Vourinen, Engstrom Pedersen	2676 9 20834 7 45836 4, 30557 6
mild steel (AISI 1020)	cladding	2 5, 10 KW CO2		12 x 12		23,000, 6000	N2, Argon			
pearlitic grey iron (ASTM A40)	hardening melting	CWCO2	2 5 , 5	10 mm sq	1- 5 95 0 3 - 1 8	1600, 2600	none	none mentioned	ref 30 Ruiz, Lopez, Fernandez	161 3, 1560
pearlite & lamellar graphite cast iron	alloying	CWCO2	1 2 - 1 35	3 0 - 4 0	0 198-0 3	16,977 - 10,743	Argon	none mentioned	ref 33 Jianglong Peidao, Gongqi	51,445 5 - 21,486
low carbon steel	alloying	10 kW CWCO2 defocused TEM01	up to 4 5 kW 7	4 12 mm sq	0 798 0 498	35,810 - 74,272	Argon	none mentioned	ref 35 Ion, Thorstensen Sorensen, Hansson	43144 6 - 89484 3
mild steel, ANSI 1020	cladding	CO2 multi, CO2 TEM01	2 5 1 5			12 5 - 30 8	Argon - Nitrogen	none mentioned	ref 38 Engstrom, Hansson, Johansson, Sorensen	
20Cr2Ni4WA steel	cladding	CWCO2	1 1 - 2	3	0 15-0 18	15,562 - 28,294	Nitrogen	none mentioned	ref 39 Jianglong, Chuanguang Peidao	51,873 3 - 113,176
plain carbon steels		5 5 kW CO2	1 4, 2 9	8, 15	0 25 0 27-0 3	2785 - 1641	not mentioned	none mentioned	ref 41 Shwager, Sholtes Mordike, Macherauch	6188 9 - 3282
ductile iron	melting	10 kW CO2	1 - 5	min diam 1 0 mm	1 02-15	500,000 @ 4kW	Helium	none mentioned	ref 43 Chen, Ju, Rigsbee	294,117 6 - 20,000
cast iron	melting					80,000			ref 44 Bergmann, Mordike, Bell	
cast iron	melting	CO2				300K-1mill			ref 46 Mordike, Fntsch, Bergmann	
		Nd YAG semicont	0 15		0 2-1 0	20,000		y	ref 48? Sivakumar	60,000 - 12,000
	melting, alloying, cladding	Nd YAG CO2	over view not specific study				y		ref 49 Burchards, Mordike	
plain carbon steel	hardening		0 6		0 5-0 7		Helium, Argon	none mentioned	ref 50 Haulk, Macherauch	
SG iron grey iron	melting	CO2 TEM 00	0 5				N2, CO2, Argon, He	microporosity mentioned	ref 51 Bergmann, Henning Mordike	
nodular cast iron grey cast iron	melting	CO2				500,000			ref 52 Chen, Alstetter, Rigsbee	
SG iron	melting	CO2, 5 kW CO2	0 7 kW cont 4 kW pulsed		1		Argon	yes	Mordike, Bergmann	
ceramic coatings	melting over plasma spray	CWCO2 pulsed CO2 Nd YAG		0 4	0 5-3 0 05 - 2	50,000 100,000 - 1,000,000 20,000	no	some mention	Sivakumar, Mordike ref 48?	60,000 - 10,000 30,000 - 12,000,000
Steel	transformation hardening		0 6	0 3	0 7 0 5	848,826	Argon + CH4 Helium	yes	Sholtes, Mordike	727,565 10
iron + steel			0 5		6			none mentioned yes?	Bergmann, Mordike	
grey iron pearlitic, ferritic nodular AISI 1045 Steel	melting	CWCO2	0 7	0 2	24	2,228,169	Argon	no? graphite nodules	Bamberger, Boas, Akin	55,704

Type of Material	Laser Process	Type of Laser	Laser Power (kW)	Beam diameter mm	Proccessing Speed (m/min.)	Power Density (W/cm^2)	Shielding gas	Porosity	Research study	Vol. Energy Input (J/cm / cm^2)
pearlite gray iron 200 ferrite-pearl nod 400		CO2	0.45		0.12 - 2.52	35,700	none	no	Grum, Sturm	178,500
grey iron HT25-47		CWCO2	2		0.2 - 1.5	29,000	none	no	Wang Maocai, Wu Weitao	87,000 - 11,600
flake graphite CI nodular graphite CI		CWCO2		2	(int t 0.15-1.25 s)	20,000	none	no	Leech	
pearlitic grey iron		CWCO2	0.3-3		0.006 - 18		Argon	no	Fouquet, Renard, Nicot,Merlin	
low carbon steel medium carbon steel	alloying, cladding		0.76	4 - 16	1.2 - 10.2	1000 - 10^9	no	no	Pelletier, Vannes, Vincent	10 - 1000
steel, SG and grey iron	cladding	5 kW CO2	1.5-3	3-4.5	0.462 - 1.842		Argon	no	Yellup	
grey iron	remelting alloying	CWCO2 Nd:YAG	1.85	2.3	1	44,527	N2, Argon	yes	UTSI	26716.2

Vita

Margaret Denise Duncan was born in East Chicago, Indiana on March 3, 1973 She was raised by her parents, Jerry L and Sandra J Duncan in Calumet Township Denise was the 1991 valedictorian of Calumet High School.

After high school Denise pursued an engineering degree at Purdue University where she received several Dean's List and Semester Honors designations She was initiated into Chi Epsilon, a civil engineering honor society, and Tau Beta Pi, an all engineering honor society while at Purdue She was a participant in the Cooperative Education Program She also qualified for and completed the Purdue Grand Prix go-kart race in 1995 as an independent driver Denise graduated with a Bachelor of Science in Civil Engineering, with Distinction, in 1995 She was offered a GAANN fellowship to continue graduate studies at Purdue

Denise returned to graduate school at the University of Tennessee Space Institute to pursue a master's degree in engineering She became president of the UTSI Soaring Club and started flying gliders She volunteered part of her time with the Dossett Chapel Youth Program and coached girls basketball for Kings Cross Church Denise received a Master of Science in Mechanical Engineering in 2000 from the University of Tennessee